This is an authorized facsimile
of the original book,
and was produced in 1975 by microfilm-xerography
by Xerox University Microfilms,
Ann Arbor, Michigan, U.S.A.

INFORMATION TO USERS

This material was produced from a microfilm copy of the original document. While the most advanced technological means to photograph and reproduce this document have been used, the quality is heavily dependent upon the quality of the original submitted.

The following explanation of techniques is provided to help you understand markings or patterns which may appear on this reproduction.

1. The sign or "target" for pages apparently lacking from the document photographed is "Missing Page(s)". If it was possible to obtain the missing page(s) or section, they are spliced into the film along with adjacent pages. This may have necessitated cutting thru an image and duplicating adjacent pages to insure you complete continuity.

2. When an image on the film is obliterated with a large round black mark, it is an indication that the photographer suspected that the copy may have moved during exposure and thus cause a blurred image. You will find a good image of the page in the adjacent frame.

3. When a map, drawing or chart, etc., was part of the material being photographed the photographer followed a definite method in "sectioning" the material. It is customary to begin photoing at the upper left hand corner of a large sheet and to continue photoing from left to right in equal sections with a small overlap. If necessary, sectioning is continued again – beginning below the first row and continuing on until complete.

4. The majority of users indicate that the textual content is of greatest value, however, a somewhat higher quality reproduction could be made from "photographs" if essential to the understanding of the dissertation. Silver prints of "photographs" may be ordered at additional charge by writing the Order Department, giving the catalog number, title, author and specific pages you wish reproduced.

5. PLEASE NOTE: Some pages may have indistinct print. Filmed as received.

Xerox University Microfilms
300 North Zeeb Road
Ann Arbor, Michigan 48106

75-8248

OSBORNE, Alfred Richard, 1942-
THE MULTIPLE SCATTERING OF COSMIC RAY
MUONS ABOVE 2.5 GeV/c.

University of Houston, Ph.D., 1974
Physics, elementary particles

Xerox University Microfilms, Ann Arbor, Michigan 48106

THE MULTIPLE SCATTERING OF COSMIC RAY MUONS ABOVE 2.5 GeV/c

A Dissertation

Presented to

the Faculty of the Department of Physics

University of Houston

In Partial Fulfillment

of the Requirements for the Degree

Doctor of Philosophy

By

Alfred Richard Osborne

May 1974

ACKNOWLEDGEMENTS

I would like to express my appreciation to Dr. William R. Sheldon for his excellent counsel throughout my graduate career. I would also like to thank Dr. James R. Benbrook for his many hours of patient advice about the rigors of experimental physics. Thanks must go to Mr. Mohamed S. Abdel-Monem for his assistance in the data analysis.

THE MULTIPLE SCATTERING OF COSMIC RAY MUONS ABOVE 2.5 GeV/c

An Abstract of a Dissertation

Presented to

the Faculty of the Department of Physics

University of Houston

In Partial Fulfillment

of the Requirements for the Degree

Doctor of Philosophy

By

Alfred Richard Osborne

May 1974

ABSTRACT

The multiple scattering of cosmic ray muons in a magnetic momentum spectrometer has been investigated both theoretically and experimentally. Theoretically, the multiple scattering theory of Molière has been modified to account for observations made with magnetic spectrometers. Experimentally, 8000 muon events have been analyzed in the momentum region 2.5 GeV/c to 200 GeV/c for a target thickness of one meter of iron. Good agreement is found between the theoretical and experimental results.

TABLE OF CONTENTS

ABSTRACT

LIST OF TABLES

LIST OF FIGURES

CHAPTER I. INTRODUCTION

CHAPTER II. THE EXPERIMENTAL APPARATUS

2.1 The Magnetic Spectrometer

2.2 The Digitizing Apparatus

CHAPTER III. DATA REDUCTION AND ANALYSIS

3.1 Introduction

3.2 An Overview of the Reconstruction of a Muon Trajectory into Real Space

3.3 Analysis of the Spectrometer Optics

3.3.1 Measurement of Muon Events

3.3.2 Geometry of the Optical Configuration

3.3.3 Determination of the Lens Position Vector

3.3.4 Estimation of the Magnification Parameter

3.3.5 Chi-Square Fit to the Spectrometer Optical Parameters

3.4 Reconstruction of a Muon Trajectory into Real Space

3.4.1 Clock Frame-To-Digitizer Frame Transformation

3.4.2 Determination of the Position and Angle of the Muon Spark in the Digitizer Frame

3.4.3 Corrections Due to Non-Linear Optics

3.4.4 Determination of Two Points on the Muon Spark in the Spectrometer Frame

3.4.5 Determination of the Plane Formed by the Particle Line and the Lens Point

3.4.6 Determination of the Muon Position Vector

3.4.7 Unit Momentum Vector of the Muon

TABLE OF CONTENTS CONTINUED

3.4.8 Sample of Reconstructed Events

3.5 Determination of the Muon Charge and Momentum

3.5.1 Muon Charge Determination

3.5.2 Determination of the Muon Momentum

3.5.2.1 Numerical Integration of the Muon Trajectory Through the Spectrometer

CHAPTER IV. MOLIÈRE'S THEORY OF MULTIPLE SCATTERING

4.1 Introduction

4.2 The Projected Angle Density

4.3 The Wentzel Summation Method

4.4 The Single Scattering Law

4.5 The Derivation of the Multiple Scattering Density

4.6 Width of the Multiple Scattering Probability Density

CHAPTER V. MODIFICATION TO THE THEORY OF MULTIPLE SCATTERING

5.1 Statement of the Problem

5.2 Modification of the Simple Gaussian Theory

5.2.1 Introduction

5.2.2 Uncertainty in Momentum

5.2.3 The Momentum and Total Angle Probability Densities

5.2.3.1 Approximate Forms for the Momentum and Total Angle Densities

5.2.3.2 Exact Forms for the Momentum and Total Angle Densities

5.2.4 The Effects of Momentum Loss

5.2.5 Modification of the Gaussian Theory

5.2.6 The Effects of Uncertainty in Angle Measurement

5.2.7 Integration over the Cosmic Ray Spectrum

TABLE OF CONTENTS CONTINUED

5.3 Modification of the Molière Theory

5.3.1 Introduction

5.3.2 Momentum Uncertainty Due to Multiple Scattering

5.3.3 The Total Angle Density

5.3.4 Modification to the Molière Density

5.3.4.1 Integral Formulation

5.3.4.2 Semi-Analytic Formulation

5.3.5 The Effects of Uncertainty in Angle Measurement

5.3.6 Integration over the Cosmic Ray Spectrum

CHAPTER VI. EXPERIMENTAL RESULTS

6.1 Introduction

6.2 Assumptions of the Molière Theory

6.3 Assumptions Made in the Modification to the Molière Theory

6.4 Experimental Error and Instrument Resolution

6.5 Preparation of the Data for Analysis; the Data Analysis

APPENDIX I The Cosmic Ray Muon Momentum Spectrum

APPENDIX II Correction of the Cosmic Ray Muon Momentum Spectrum for Multiple Scattering

REFERENCES

LIST OF FIGURES

		Page
2.1	The Magnetic Spectrometer Telescope	2.1.2
2.2	Spectrometer Control Schematic	2.1.4
2.3	Configuration of Spectrometer Optical System	2.1.6
2.4	UH Track Measuring Apparatus	2.2.2
2.5	Schematic of Digitizing Apparatus	2.2.4
3.1	Reconstruction of a Muon Trajectory	3.1.2
3.2	Table, Digitizer and Clock Frame Coordinates	3.3.1.2
3.3	Measurement of an Event	3.3.1.4
3.4	Optical Reconstruction Geometry	3.3.2.4
3.5	Field View Lens Coordinate Geometry	3.3.3.2
3.6	No-Field View Lens Coordinate Geometry	3.3.3.3
3.7	Geometry of the Magnification Parameter	3.3.4.3
3.8.a	Fiducial Wire Slopes in the Field View, Bottom Chamber	3.3.5.9
3.8.b	Fiducial Wire Slopes in the Field View, Top Chamber	3.3.5.10
3.9	Histogram of "Infinite Momentum Events" as Viewed by the Spectrometer	3.3.5.12
3.10	Clock Frame to Digitizer Frame Transformation	3.4.1.2
3.11.a	Position and Angle of Muon Spark in Digitizer Frame	3.4.2.2
3.11.b	Determination of two Points on the Muon Spark	3.4.4.1
3.12.a	Momentum Histogram From a Sample of 1023 Events	3.5.1.2

LIST OF FIGURES CONTINUED

		Page
3.12.b	Middle Chamber Scattering Position Distribution	3.5.1.3
3.12.c	Bottom Chamber Scattering Position Distribution	3.5.1.4
3.12.d	Middle Chamber Scattering Angle Distribution	3.5.1.5
3.12.e	Bottom Chamber Scattering Angle Distribution	3.5.1.6
3.12.f	Distribution of Events in Field View Top Scintillator Plane	3.5.1.7
3.12.g	Distribution of Events in No-Field Top Scintillator Plane	3.5.1.8
3.12.h	Distribution of Events in Field View Bottom Scintillator Plane	3.5.1.9
3.12.i	Distribution of Events in No-Field View Bottom Scintillator Plane	3.5.1.10
3.13	Muon Charge Determination	3.5.1.12
3.14	Typical Muon Trajectory in the Spectrometer	3.5.2.1.2
3.15	Flowchart of the Program 'TRAJEC'	3.5.2.1.3
3.16.a	Projected Angles of the Muon Momentum Vector	3.5.2.1.6
3.16.b	Determination of the Normal Vectors $\hat{n}_x$ and $\hat{n}_y$	3.5.2.1.6
3.17	Muon Energy Loss Rate in Iron	3.5.2.1.11
4.1	Geometry of the Spatial Angle θ, and the Projected Angles θ_x and θ_y.	4.2.3
4.2	Molière Multiple Scattering Density	4.5.11
5.1	Ideal Multiple Scattering Experiment Using a Particle Accelerator	5.1.2

LIST OF FIGURES CONTINUED

		Page
5.2	Measurement of Multiple Scattering Variables	5.1.4
5.3.a	Projected Multiple Scattering Angles for no Magnetic Field	5.2.3.2
5.3.b	Projected Angles When a Magnetic Field is Present	5.2.3.2
5.4	Bending and Scattering Angles	5.2.3.1.2
5.5	Experimentally Determined Momentum	5.2.3.1.4
5.6	Momentum Distribution Due to Multiple Scattering, σ = .2	5.2.3.1.7
5.7	The Multiple Scattering Density and Total Angle Density as a Function of Projected Scattering Angle	5.2.3.2.2
5.8	Total Angle Density: The Sum of Two Gaussian Densities	5.2.3.2.4
5.9	Monte Carlo Momentum Distribution for the Magnetic Spectrometer	5.2.4.8
5.10	Spectrometer Field and No-Field View Scattering Variables	5.2.5.7
5.11	Domain of (ϕ_S,ϕ_T) Integration	5.2.5.7
5.12	Modification to the Simple Gaussian Theory, σ = .2	5.2.5.9
5.13	Field View and No-Field View Angle Variables	5.2.6.2
5.14	Spectrometer Noise as a Function of Momentum	5.3.1.4
5.15	Comparison of Molière and Corrected Molière Densities	5.3.4.2.10
5.16	Corrected Molière Densities: Semi-Analytic vs. Numerically Integrated	5.3.5.2

LIST OF FIGURES CONTINUED

		Page
5.17	Multiple Scattering Curves at Characteristically Determined Momenta of 50 GeV/c, 100 GeV/c, ∞	5.3.5.9
5.18	Multiple Scattering Curves	5.3.5.10
6.1	Multiple Scattering Fit to Data Contaminated by Knock-on Electrons, $\alpha = \frac{1}{\sigma}\frac{\phi}{\phi_T}$	6.5.4
6.2	Multiple Scattering Fit to Data with Knock-on Electrons Removed, $\alpha = \frac{1}{\sigma}\frac{\phi}{\phi_T}$	6.5.5
6.3	Comparison of Curve of Fig. 6.2 With Data Histogramed via $\alpha = f(p)p\phi$	6.5.6

LIST OF TABLES

		Page
1.1	Summary of Multiple Scattering Experiments	1.3
3.1	Particle Event Information Codes	3.3.2.2
3.2	Measured Optical Parameters	3.3.3.5

CHAPTER I

INTRODUCTION

This dissertation is devoted to the investigation of the multiple scattering of cosmic ray muons in large, solid iron, magnetic momentum spectrometers. The motivation for this research has a dual purpose: (1) magnetic spectrometers allow multiple scattering to be investigated at far greater energies and target thicknesses than those examined previously, and (2) precise, accurate measurements of the cosmic ray muon momentum spectrum require an understanding of multiple scattering in magnetic spectrometers.

We shall be interested primarily in a two-fold problem: (1) the theoretical investigation of the behavior of multiple scattering in magnetic spectrometers, and subsequently the modification of existing theories to account for spectrometer observations, and (2) the comparison of the theoretical result with experimental data. We do not imply here that multiple scattering, a clearly defined physical phenomenon, occurs differently in one experimental appratus as compared to another. What we do imply is that we shall <u>interpret</u> multiple scattering in spectrometers by means of a different approach; the reason for this approach will not become clear until the first section of Chapter V, after discussions on the experimental apparatus and the theory of multiple scattering. Our course of action will be to introduce, in subsequent chapters, the following topics:

Chapter II - A description of the experimental apparatus

Chapter III - Data reduction and analysis techniques required for an investigation of multiple scattering

Chapter IV - A description of the Molière theory of multiple scattering

Chapter V - The modification of the Molière theory to account for multiple scattering in solid iron magnetic spectrometers.

Chapter VI - Comparison of theoretical and experimental results.

Table 1.1 gives a review of several experimental results on multiple scattering. We shall refer back to this table at a later time.

In this work we often speak of a "probability density" as being a function, f(x), with the properties

$$f(x) \geq 0 \; ; \int_{-\infty}^{\infty} f(x)dx = 1$$

The function f(x) is often referred to as a "probability distribution"; however, we shall use probability density or "density" to refer to functions of this type.

TABLE 1.1 MULTIPLE SCATTERING PAPERS

TABLE 1.1

MULTIPLE SCATTERING PAPERS

AUTHOR(S)	INCIDENT BEAM	INCIDENT BEAM ENERGY	TARGET MATERIAL	TARGET THICKNESS	NUMBER OF EVENTS	RESULTS
Hungerford[1] et al. (1972)	Protons	600 MeV	C,AL,Cd,Pb	<20 gm/cm²	~200,000	Molière fits well except at large angles due to nuclear force
Bhattacharyya[2] (1970)	Cosmic Ray Muon	1.7 GeV	Copper	10.7 gm/cm²	4000	Compares to Cooper and Rainwater
Ayre et al.[3] (1973)	Cosmic Ray Muon	10-70 GeV	Iron	~3000 gm/cm	10,000	Investigates only RMS scattering displacement, finds agreement
Torsti[4] (1973)	Cosmic Ray Muon	10-100 GeV	Iron	~3000 gm/cm²	10,000	Investigates only RMS scattering displacement, finds agreement
Whittemore & Shutt[5] (1952)	Cosmic Ray Protons & Muons	1-4.8 GeV	Lead	~70 gm/cm²	-	Molière fits well
Meyer et al.[6] (1953)	Cosmic Ray Muons	<1 GeV	Pb,Sn,Fe	27 gm/cm²	10,000	Agreed with Cooper and Rainwater
Bichsel[7] (1958)	Protons	<4.8 MeV	Al,Ni,Ag,Au	~mg/cm²	-	Agreed with Molière
Lloyd & Wolfendale[8] (1955)	Cosmic Ray Muons	<2 GeV	Pb,Fe	50 gm/cm²	2600	Agreed with Molière

CHAPTER II

THE EXPERIMENTAL APPARATUS

2.1 THE MAGNETIC SPECTROMETER

The multiple scattering of cosmic ray muons has been investigated with a magnetic momentum spectrometer, which is the heart of a collaborative effort in cosmic ray physics between the University of Houston and Texas A&M University. The instrument is operated at the Airforce annex near College Station, Texas. Bateman[9] has given a detailed account of the spectrometer and the interested reader is referred to his work. Here we only briefly review the operation of the instrument.

A schematic of the apparatus is shown in Fig. 2.1. The instrument consists of three basic elements: (1) solid iron magnets, (2) plastic scintillators and (3) wide-gap spark chambers. The magnets are constructed of 1.27 cm laminae of low-carbon soft steel of high permeability; the magnets weigh a total of about 8 tons. They are gapless d.c. electromagnets and their construction is somewhat like that of large transformers. The magnetic field of each magnet was measured using a Grassot fluxmeter connected to search coils placed uniformly throughout each magnet volume. The average measured magnetic field was 17.4 kilogauss and was uniform to within 1.5% throughout the entire volume of the iron. A magnetizing current of

FIG. 2.1 THE MAGNETIC SPECTROMETER TELESCOPE

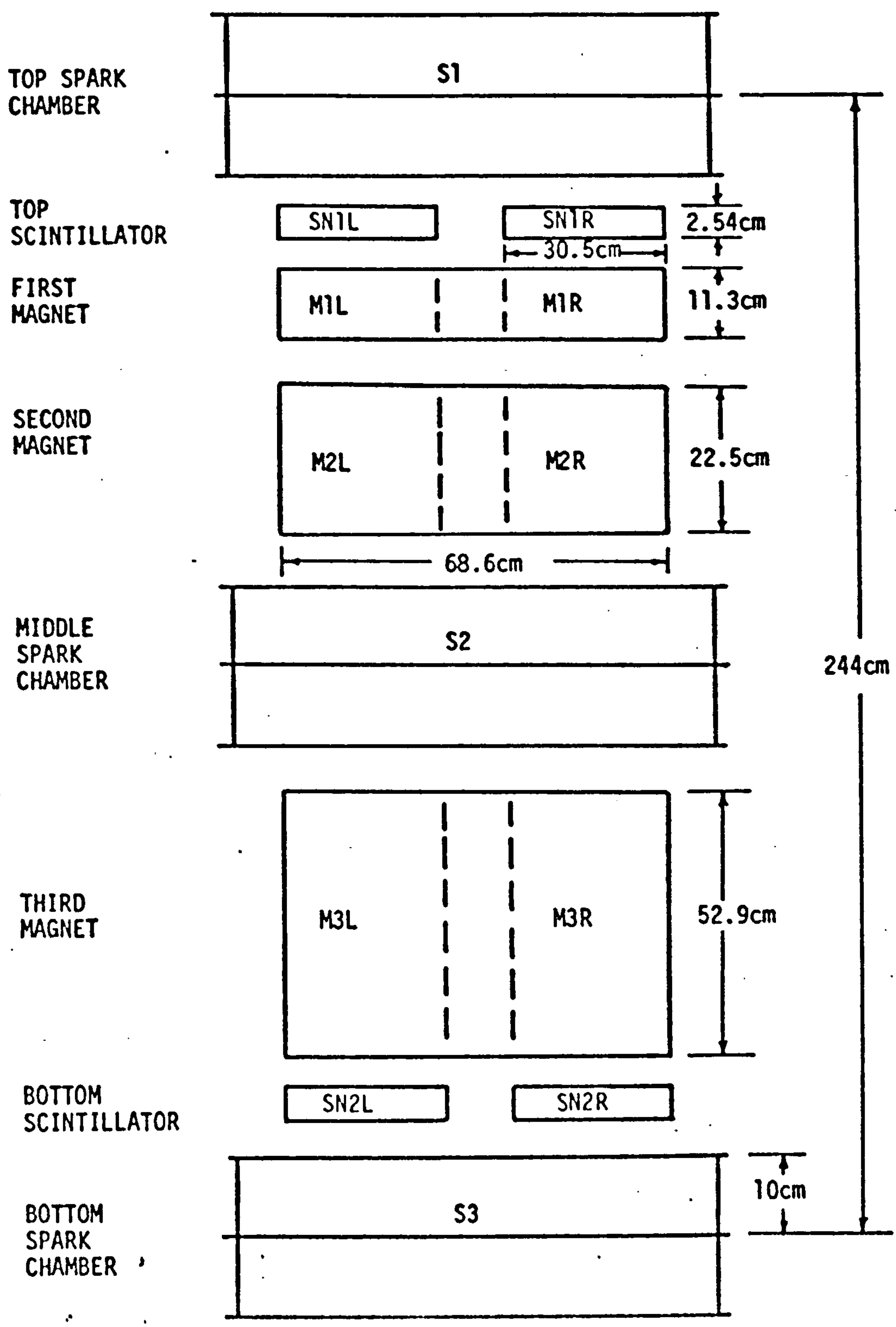
TOP SPARK CHAMBER
S1
TOP SCINTILLATOR
SN1L
SN1R
2.54cm
30.5cm
FIRST MAGNET
M1L
M1R
11.3cm
SECOND MAGNET
M2L
M2R
22.5cm
68.6cm
MIDDLE SPARK CHAMBER
S2
244cm
THIRD MAGNET
M3L
M3R
52.9cm
BOTTOM SCINTILLATOR
SN2L
SN2R
BOTTOM SPARK CHAMBER
S3
10cm

11 amps was used; however there is little dependence on current in the highly saturated operating region. The total thickness of all the magnets is 86.6 cm.

In order to detect the passage of a muon through the instrument two plastic scintillators (of dimensions 2.54 cm X 30.5 cm X 61 cm) are placed immediately above and below the magnet sections. Acrylic plastic light pipes couple both ends of each scintillator to photomultiplier tubes which detect the passage of fast charged particles. The scintillator planes define a "telescope" which is sensitive only to particles traversing both scintillators (SN1R and SN2R in Fig. 2.1) and all three magnets (M1R, M2R, M3R). A two-fold coincidence between both scintillators in a telescope results from the passage of a muon, the only known charged elementary particle which can traverse a meter of iron. Thus penetration of both SN1R and SN2R by a muon generates a coincidence which triggers the voltage pulse to the spark chambers, allowing the muon sparks to be subsequently photographed.

The three spark chambers S1, S2 and S3 are constructed of polished aluminum plates (of thickness .318 cm and area 1 m^2 which are separated by 10 cm gaps. The sides of the chambers are formed from transparent acrylic plastic 1.27 cm thick. The complete unit forms a gas-tight module which is

FIG. 2.2 SPECTROMETER CONTROL SCHEMATIC

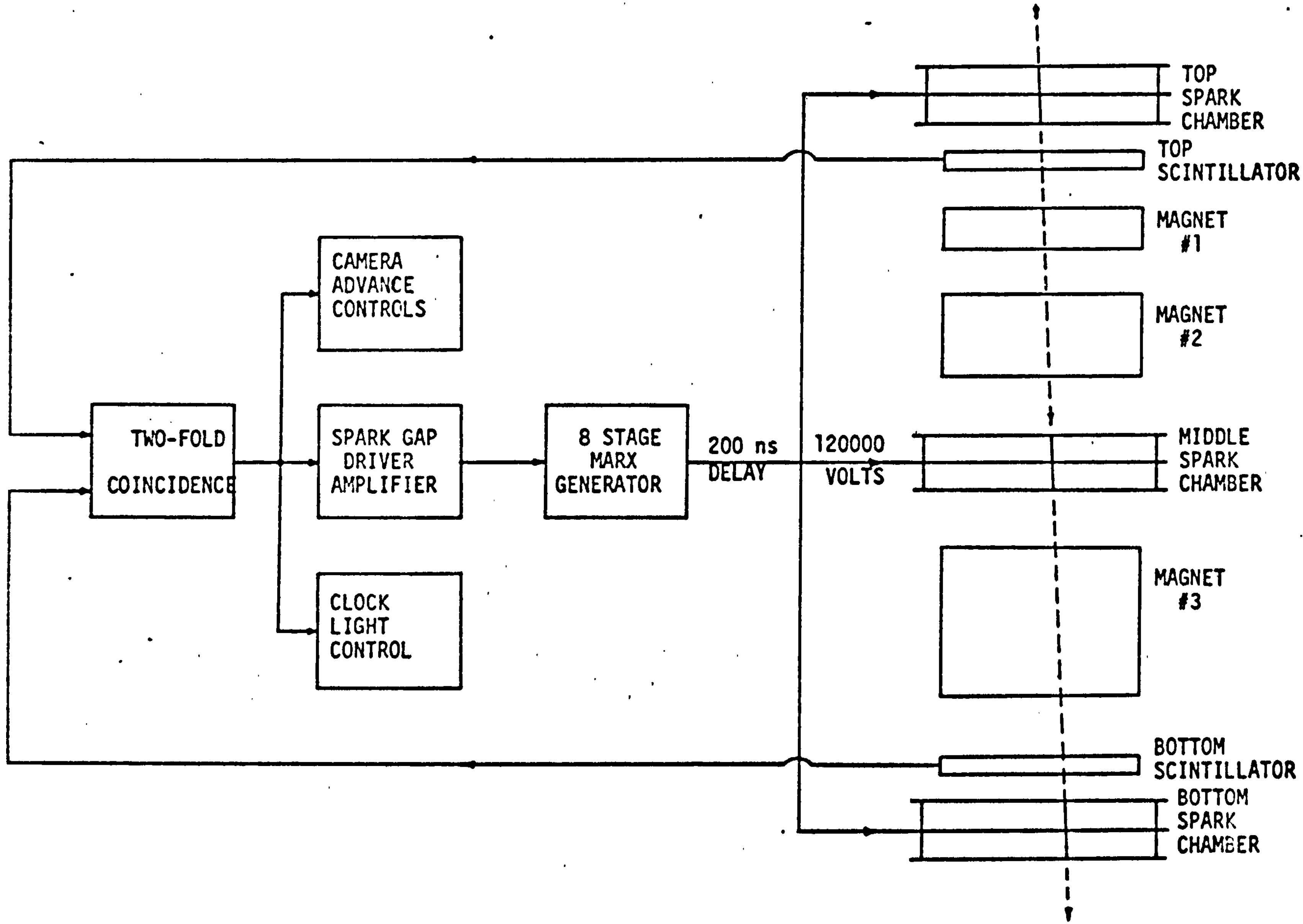

TOP SPARK CHAMBER
TOP SCINTILLATOR
MAGNET #1
MAGNET #2
CAMERA ADVANCE CONTROLS
TWO-FOLD COINCIDENCE
SPARK GAP DRIVER AMPLIFIER
8 STAGE MARX GENERATOR
200 ns DELAY
120000 VOLTS
MIDDLE SPARK CHAMBER
MAGNET #3
CLOCK LIGHT CONTROL
BOTTOM SCINTILLATOR
BOTTOM SPARK CHAMBER

continuously flushed with helium-isobutane (99.05% helium and .95% isobutane) at slightly above atmospheric pressure. The top and bottom plates of each chamber are grounded to the spectrometer frame while the center plate is insulated from the others. When a voltage pulse is applied to the center plate the chambers become large capacitors which subsequently break down along the ionized tracks left behind by charged particles. The high voltage necessary for the operation of these spark chambers is applied with an eight-stage Marx generator (a device consisting of high-voltage capacitors, spark gaps, and resistors which allows the capacitors to be charged in parallel and then to be discharged in series).

When a particle traverses either the left or right channel of the spectrometer (labeled L and R in Fig. 2.1) a signal is generated which initiates operation of the system. This trigger pulse (caused by a two-fold coincidence between both scintillators of the channel) nominally occurs within 200 nanoseconds of the particle traversal (see Fig. 2.2). Subsequently the Marx generator is fired, the camera is advanced and the clocks are illuminated. A 1.48 second dead-time is built into the system so that no other trigger can occur for this length of time; this allows time for the Marx generators to recharge and the cameras to advance.

2,1,6

FIG. 2.3 CONFIGURATION OF SPECTROMETER OPTICAL SYSTEM

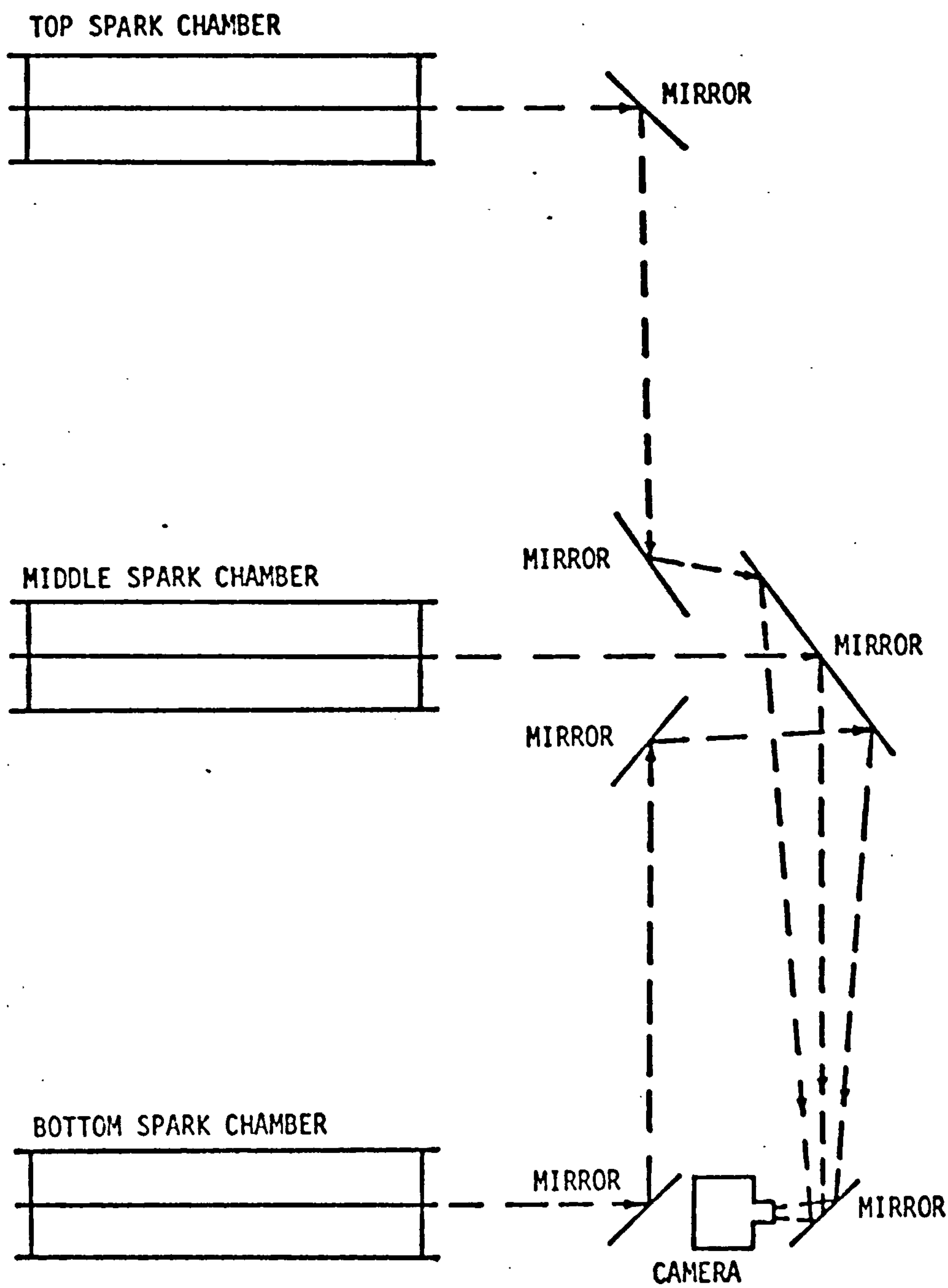
TOP SPARK CHAMBER
MIRROR
MIDDLE SPARK CHAMBER
MIRROR
MIRROR
MIRROR
BOTTOM SPARK CHAMBER
MIRROR
MIRROR
CAMERA

The spark images and clock time are recorded by two 16 mm cameras, one with film plane perpendicular to the magnetic field (which we shall call the "field view"), and one with film plane parallel to the magnetic field (the "no-field view"). The cameras photograph all three chambers simultaneously by means of an optical system of mirrors as shown in Fig. 2.3 A roll of 16 mm film contains about 4000 events; however, since each event is photographed simultaneously in the field and no-field views one obtains two rolls of film, one from each view.

2.2 THE DIGITIZING APPARATUS

Each measured muon event is recorded on film and must therefore be reduced to digital form for computer analysis. To this end an electronic digitizing apparatus was designed and built at the University of Houston. The apparatus allows the photographed event to be projected onto an analysis table (via an overhead mirror) where spatial coordinates (x,y) and angle coordinate (θ) can be simultaneously measured and electronically digitized.

The analysis table is essentially a drafting machine with x and y degrees of freedom (see Fig. 2.4). The linear motion of the drafting head is facilitated by linear bearings mounted in cast aluminum blocks which roll on two parallel steel rods. The result is a drafting machine of extreme rigidity and accuracy. Each axis is

FIG. 2.4 UH TRACK MEASURING APPARATUS

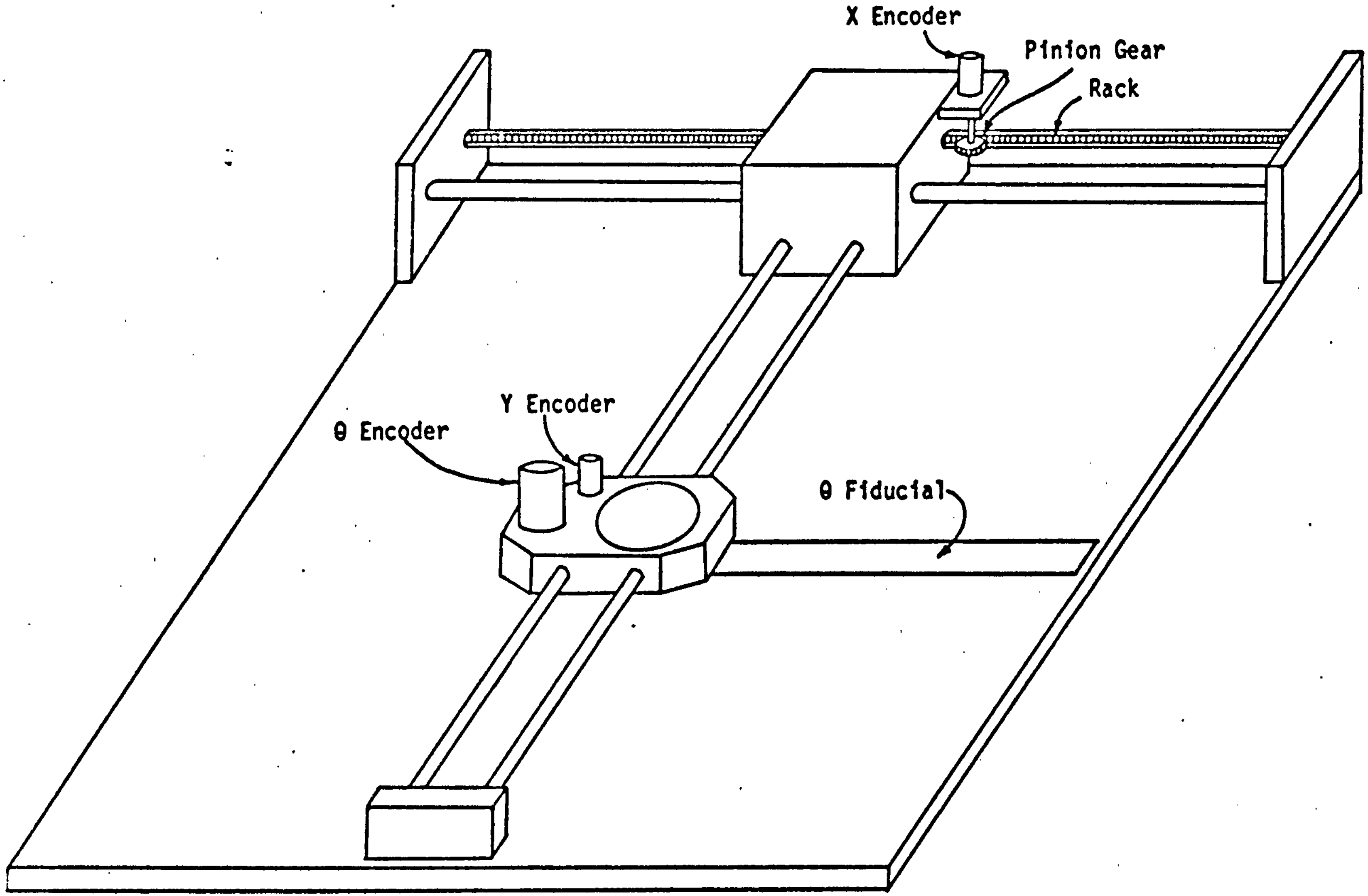

X Encoder
Pinion Gear
Rack
Y Encoder
θ Encoder
θ Fiducial

connected mechanically (via rack and pinion) to an optical encoder, an electronic device which generates digital pulses when its input shaft is rotated. The encoders used for the x and y axes have $2^{12} = 4096$ pulses/revolution. These pulses are summed electronically by binary coded decimal (BCD) up-down counters. The net x or y axis displacement is a number in "counts" where each count is .00146 cm. In a similar way the digitizer can measure angles via a geared-down encoder with $2^{16} = 65{,}536$ counts/revolution (1 count ≈ .1 milliradian).

Fig. 2.5 shows a simple schematic of the digitizing apparatus. The optical encoders for x,y and θ provide digital waveforms to electronic circuits which sum total coordinate displacements in BCD up-down counters. The displacements are then stored into 20 bit buffers at a 10 kHz rate. Each coordinate can be read directly by nixie tube displays. Depression of x,y or θ buttons mounted on the main drafting head results in the initiation of a sequence of logic which punches the corresponding x,y or θ coordinate onto paper tape. Additional information about an event may be punched onto paper tape via a set of 20 thumb switches mounted on the main console. The measuring procedure, which has been developed for the digitizing of muon events, is presented in Sec. 3.3.1; operation of the apparatus is described in that section.

FIG. 2.5 SCHEMATIC OF DIGITIZING APPARATUS

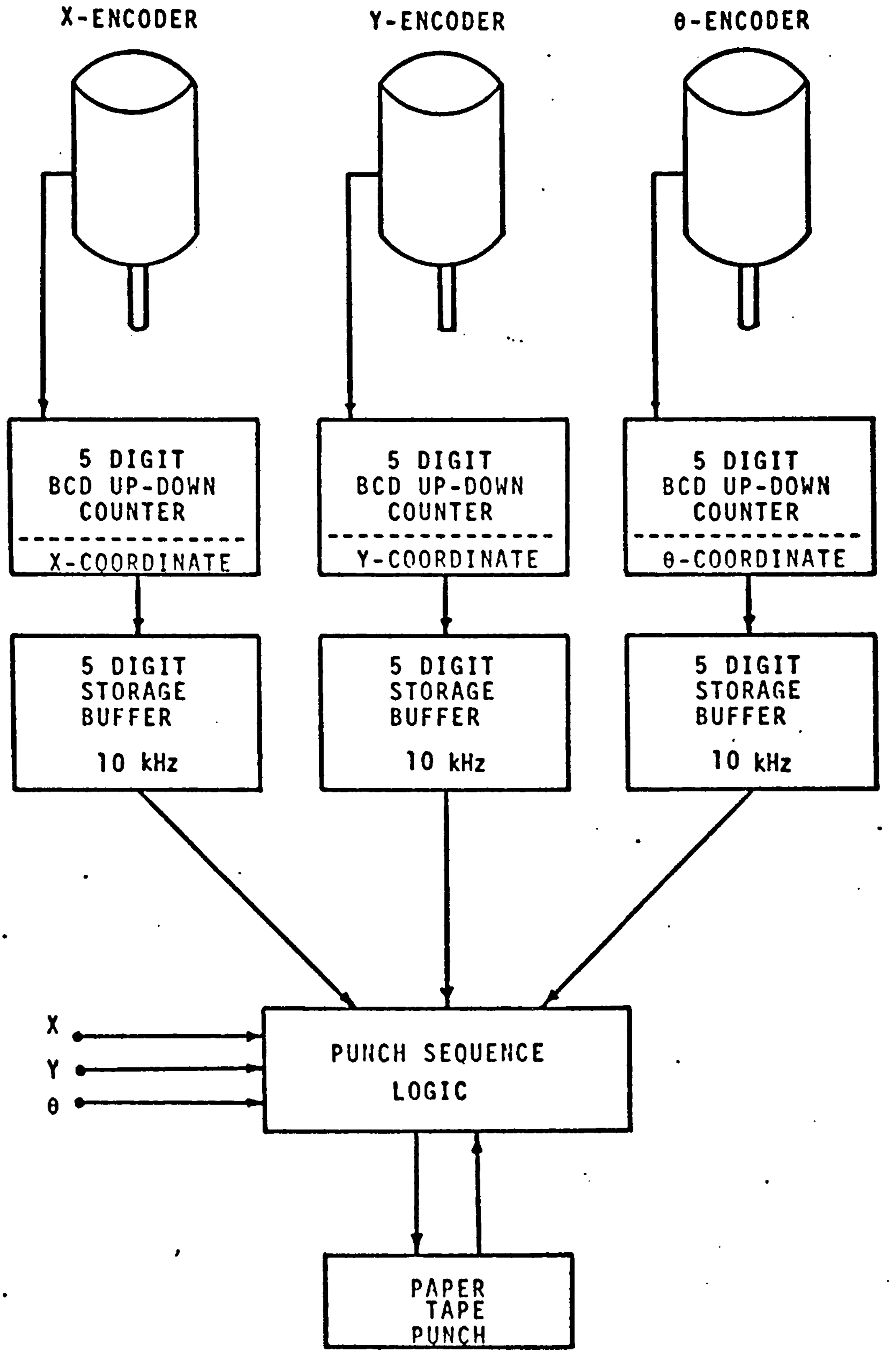
X-ENCODER
Y-ENCODER
θ-ENCODER
5 DIGIT
BCD UP-DOWN
COUNTER
X-COORDINATE
5 DIGIT
BCD UP-DOWN
COUNTER
Y-COORDINATE
5 DIGIT
BCD UP-DOWN
COUNTER
θ-COORDINATE
5 DIGIT
STORAGE
BUFFER
10 kHz
5 DIGIT
STORAGE
BUFFER
10 kHz
5 DIGIT
STORAGE
BUFFER
10 kHz
X
Y
θ
PUNCH SEQUENCE
LOGIC
PAPER
TAPE
PUNCH

CHAPTER III
DATA REDUCTION AND ANALYSIS

3.1 INTRODUCTION

This chapter covers the data reduction and analysis techniques which were used to analyze single muon events from the AMH magnetic spectrometer. Specifically the following topics are discussed: (1) the spectrometer optical system, (2) the reconstruction of a muon trajectory into real space, and (3) determination of the muon momentum, charge, and scattering angle.

3.2 AN OVERVIEW OF THE RECONSTRUCTION OF A MUON TRAJECTORY INTO REAL SPACE

While the reconstruction of a muon trajectory into real space requires a thorough knowledge of the spectrometer optical system, we shall ignore, for the moment, the details of the optics and consider only the essentials of the reconstruction process.

Raw data in the form of muon spark images are photographed in orthogonal views, one parallel, the other perpendicular to the magnetic fields of the solid iron magnets. The optical reconstruction process provides a means of determining, in real space, the position and angles of the muon spark, given the spark images on film, and a knowledge of the optical parameters of the instrument. Figure 3.1 is a simplified schematic of the spectrometer where only the elements necessary in the reconstruction process are shown. Here the entire

FIG. 3.1 RECONSTRUCTION OF A MUON TRAJECTORY

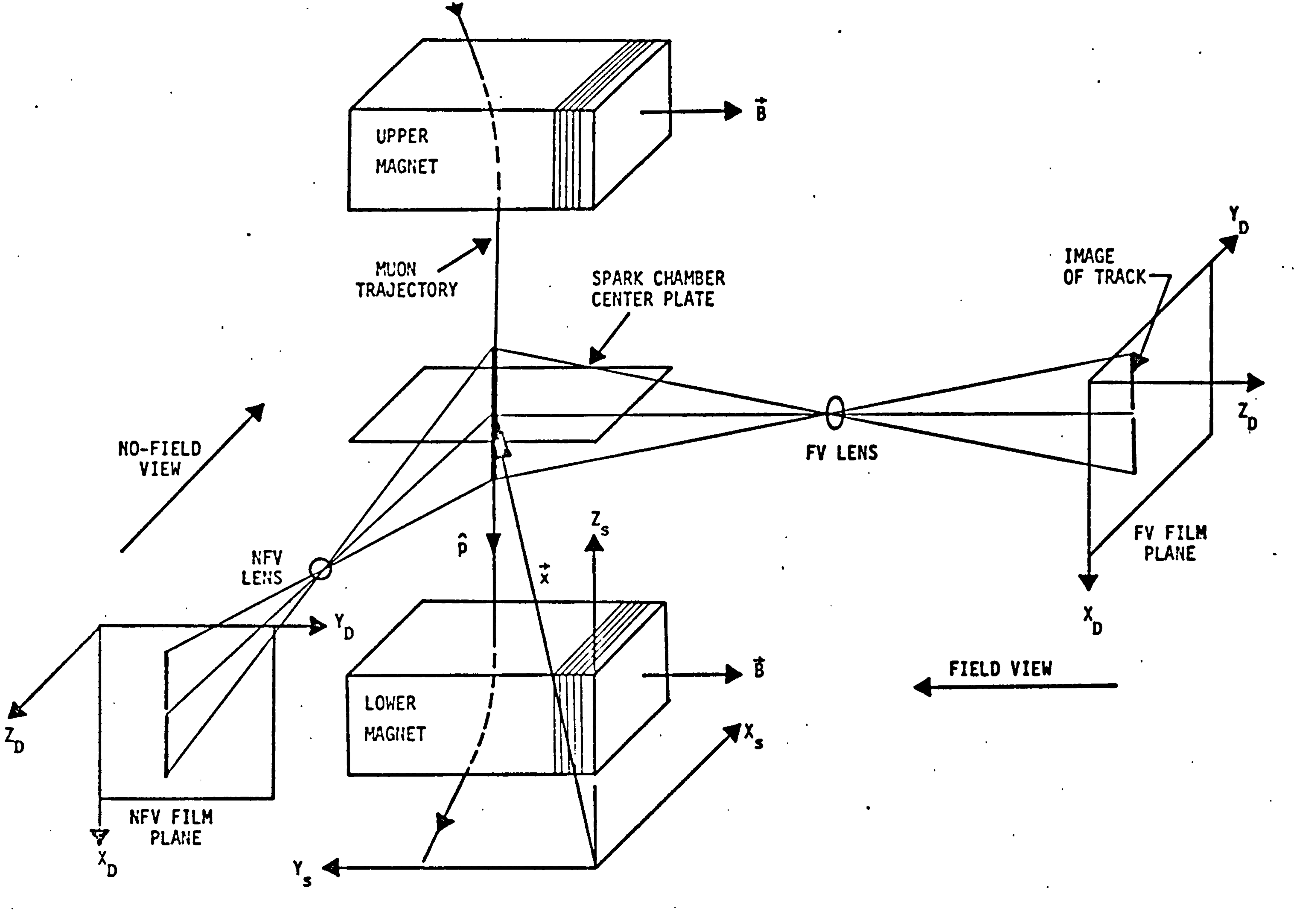

$\vec{B}$
UPPER
MAGNET
MUON
TRAJECTORY
SPARK CHAMBER
CENTER PLATE
IMAGE
OF TRACK
Y_D
Z_D
X_D
FV LENS
FV FILM
PLANE
NO-FIELD
VIEW
NFV
LENS
$\hat{p}$
$\vec{x}$
Z_s
Y_D
Z_D
X_D
NFV FILM
PLANE
$\vec{B}$
LOWER
MAGNET
X_s
Y_s
FIELD VIEW

optical system (i.e. lenses, cameras, mirrors, etc.) is represented by a single lens and a film plane for both the field view (film plane perpendicular to the magnetic field) and the no-field view (film plane parallel to the magnetic field). All components of the spectrometer have well-defined positions in the spectrometer coordinate frame which is labeled X_s, Y_s, Z_s. Thus accurately measured positions and orientations of the magnets, spark chambers, lenses, etc. are known in this coordinate frame fixed relative to the spectrometer.

When a muon traverses the spectrometer, the resultant spark is imaged through the optical system (i.e. through the fictitious "lenses" of Fig. 3.1) onto the field-view and no-field-view film planes. The track image on the film plane is a line which is well-defined in the spectrometer frame. This line, together with the point occupied by the lens, determines a vertical plane in space containing the muon spark. The two vertical planes from the field and no-field view images intersect inside the spark chamber along the muon spark; thus the intersection of these planes defines the muon trajectory inside the chamber.

In light of the above discussion it should be clear that, to reconstruct a muon track into real space, one must execute the following steps:

(1) Measure the coordinates of the track in both orthogonal views by means of the scanning table described in the previous chapter.

(2) From a knowledge of the positions and orientations of the components of the optical system, determine the equations of the lines defined by the track images on the film planes.

(3) Use the line equations found above, together with the lens points, to determine two vertical planes whose intersection is the muon spark.

(4) Determine the downward-pointing unit vector defined by the intersection. This vector is the unit momentum vector of the muon.

(5) Determine the point of intersection of the muon trajectory with the center spark chamber plate. This point defines the position of the muon in the chamber.

The above procedure must be repeated for each of the three spark chambers. One obtains finally three position vectors and three unit momentum vectors above, between, and below the two solid iron magnets; thus the muon spark images have been reconstructed into real space.

The next step is to determine the muon momentum by fitting a "best" trajectory through the three muon positions and unit momentum vectors. However, before discussing momentum determination we shall cover, in the following sections, the details of optical reconstruction.

This will involve a considerable elaboration on the five steps discussed only briefly above.

3.3 ANALYSIS OF THE SPECTROMETER OPTICS

3.3.1 MEASUREMENT OF MUON EVENTS

The muon data is recorded on two rolls of film, one for the field view, the other for the no-field view. For every muon event there is a frame on the field-view roll and a corresponding frame on the no-field-view roll. Each film roll consists of about 8 "batches" of approximately 500 events each. The batches vary in length from 20 minutes to 59 minutes depending upon zenith angle. This is due to the fact that the cosmic ray muon intensity is a decreasing function of zenith angle; thus a longer time is required to obtain 500 events per batch at larger zenith angles. The beginning of each batch is characterized by several frames of fiducial wires; also the film roll number, batch number, zenith angle and azimuth angle are provided.

Before measuring muon data with the analyzing table the electronic counters are "reset" so that all measurements (x-y and θ) are positive definite. This is accomplished by moving the drafting head as far down and to the left as possible; additionally the angle goniometer is rotated clockwise as far as possible (about 45° below horizontal). The RESET button on the analyzer console is then depressed, setting all counters to zero. This configuration of the apparatus defines the "table coordinate frame", which has axes X_T, Y_T, and Z_T. The X_T and Y_T axes are defined by the analyzer X and Y axes (see Figure 3.2). The Z_T axis points out of the table.

Another coordinate frame of interest is the "digitizer coordinate frame" designated by X_D, Y_D and Z_D. This frame is defined relative to the image of the fiducial wires at the beginning of a batch; here the edges of the spark chamber plates are also visible. From Figure 3.2 we see that the digitizer coordinate frame has its origin (and X_D-Y_D plane) in the plane of the table at the point where the images of the center fiducial wire and the center spark chamber plate cross. The X_D-axis points to the right along the center fiducial wire. The Y_D-axis points upward along the center plate of the spark chamber.

In addition to the fiducial wires and spark chambers, the clock is also visible at the beginning of a batch. It is now in order to define a "clock coordinate frame" which is labeled X_c, Y_c, and Z_c (see Figure 3.2). The clock frame has its X_c-Y_c plane in the plane of the analyzer table. Its origin lies at the 30 second mark on the clock. The X_c-axis points to the right through

FIG. 3.2 TABLE, DIGITIZER, AND CLOCK COORDINATE FRAMES

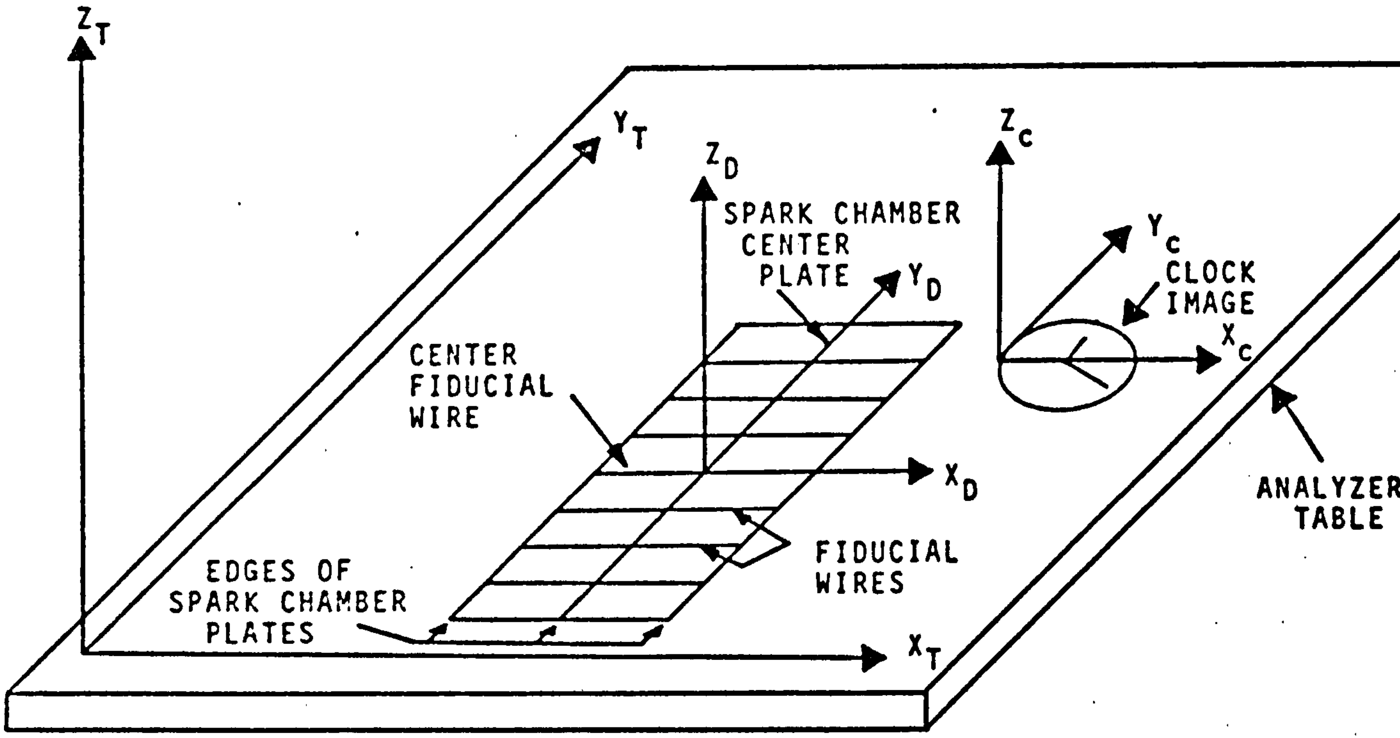

Z_T
Y_T
Z_D
SPARK CHAMBER
CENTER
PLATE
Y_D
Z_c
Y_c
CLOCK
IMAGE
X_c
CENTER
FIDUCIAL
WIRE
X_D
ANALYZER
TABLE
FIDUCIAL
WIRES
EDGES OF
SPARK CHAMBER
PLATES
X_T

the 0 second mark on the clock and the Y_c-axis points upward in the plane of the table, perpendicular to X_c. The Z_c axis points out of the table. At a later time the relative positions and orientations of the three coordinate frames presented here will be developed, i.e. the table frame, digitizer frame and clock frame. Additionally a detailed analysis of the spectrometer optical system, obtained by directly measuring the fiducial wires, will be discussed. We now describe the measuring procedure of a single event.

Figure 3.3 shows how a typical event appears when projected onto the analyzing table. Arranged left to right on the film are the bottom, middle and top spark chambers. While the spark chambers are not visible their center plates are easily located by the central gap in each muon spark. Normally, a single muon track appears in each chamber (however up to 9 tracks per chamber have been observed); the image of the clock is also visible. The fiducial wires are not illuminated during a muon event and are thus not visible.

The measurement of a single event consists of the following four steps:

(1) Entering the "event definition" into the console thumb switches, i.e. number of particles present, time on the clock, whether knock-on electrons or particle showers are present, etc.

3.3.1.4

FIG. 3.3 MEASUREMENT OF AN EVENT

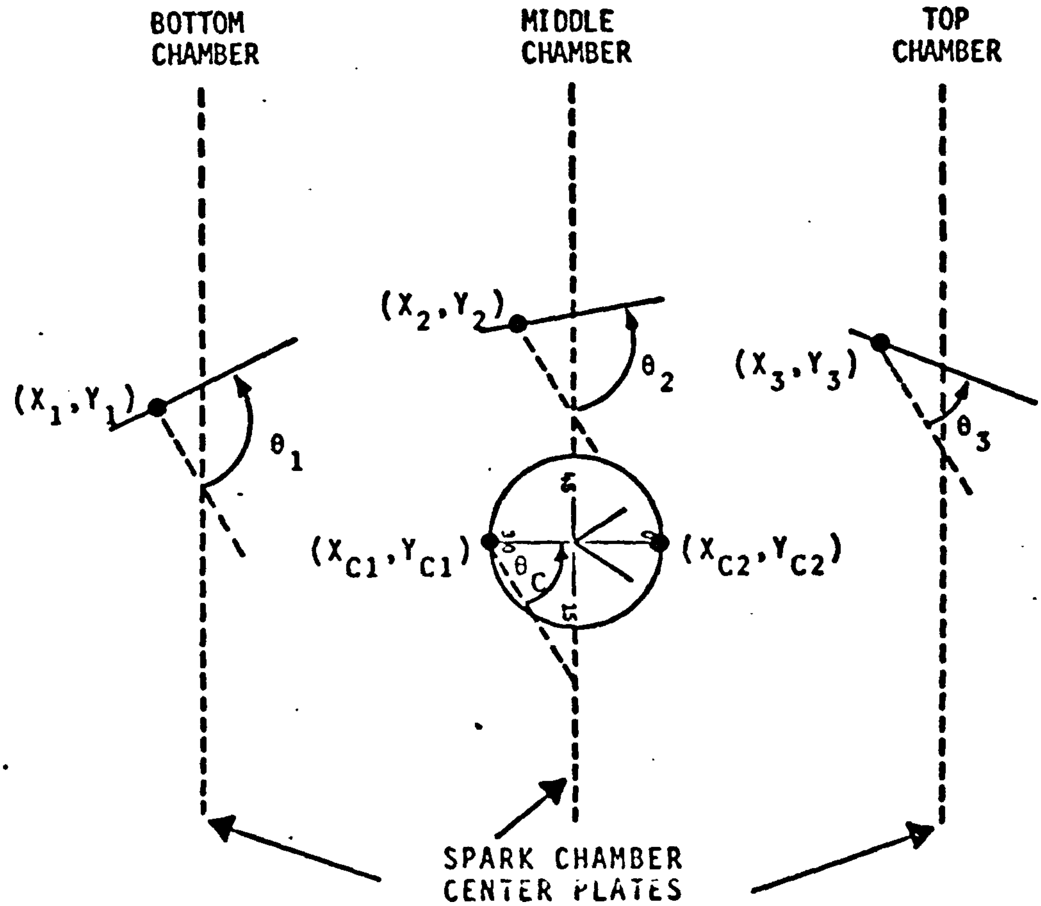

BOTTOM CHAMBER
MIDDLE CHAMBER
TOP CHAMBER
(X_2, Y_2)
θ_2
(X_3, Y_3)
(X_1, Y_1)
θ_1
θ_3
(X_{C1}, Y_{C1})
θ_C
(X_{C2}, Y_{C2})
SPARK CHAMBER CENTER PLATES

(2) Measuring two points and an angle on the clock.

(3) Measuring a point and an angle for each particle observed.

(4) Depressing the "END" button on the console.

What follows is an elaboration on the above points.

The event definition of step (1) above is entered into a 20-digit thumb switch which is on the analyzer console. The following inputs are required.

(a) A two-digit identification number designating the person operating the machine.

(b) Two-digit bottom chamber particle definition, XY; X = number of particles in the bottom chamber, Y = number of the particle judged to be the muon (numbered from the highest particle in the chamber).

(c) Two-digit middle chamber particle definition, defined as in (b) above.

(d) Two-digit top chamber particle definition, defined as in (b) above.

(e) Four-digit information code. This code is a number from 1-6 which is used to characterize the type of event being analyzed. Ninety per cent of all events were classified as "normal" (information code 0001); these are events in which only one muon is observed in each spark chamber. Occasionally more than one muon were observed and the event was then judged to belong to one of the categories of Table 3.1. These classifications should not be taken literally (a "shower event" may not be discernable from a "nuclear event"), but are used primarily as a check on the analyzing personnel and as rough estimates of the number and types of events in the data.

(f) Six digit time code, XXYYYY. XX = time in minutes on the event clock, YYYY = time on the clock in centi-seconds, i.e. a time of 231960 is 23 min. 19.6 sec.

The second step in the track measuring procedure is measurement of the clock coordinates. In order to determine the position and orientation of the "clock coordinate frame" we measure the X-Y coordinates of the 0 and 30 second marks on the clock (see Figure 3.3). Also the angle that the clock diameter makes through the 0 and 30 second marks is measured.

To accomplish the third step in the measurement procedure, one point (X-Y) and one angle (θ) are measured on each particle track. This is sufficient to determine the line associated with each track.

3.3.2 GEOMETRY OF THE OPTICAL CONFIGURATION

The magnetic spectrometer has six distinct optical systems, one for each spark chamber for both the field and no-field views. Each optical system contains the following elements:

3.3.2.2

TABLE 3.1

PARTICLE EVENT INFORMATION CODES

INFORMATION CODE	DESCRIPTION	EXAMPLE OF EVENT TYPE
0001	"NORMAL EVENT"	
0002	"SPURIOUS EVENT"	NO PARTICLES
0003	"NUCLEAR EVENT"	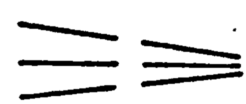
0004	"SHOWER EVENT"	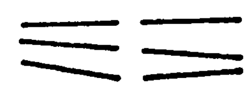
0005	"KNOCK-ON EVENT"	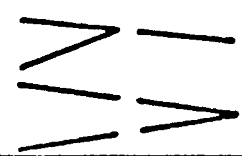
0006	"PAIR PRODUCTION EVENT"	

(1) spark chamber.

(2) mirrors to deflect the optical path into the camera.

(3) lens and film plane of the camera.

(4) lens and light source of the film projector used in the data analyzer.

(5) overhead mirror of the data analyzer.

(6) measuring table.

Analysis of all the above optical elements is not a simple task nor even a desirable one. We do not require knowledge of the effects of each of the optical elements; only the total effect of all the elements is required. In this light we point out that an optical system may (1) translate, (2) rotate and (3) generate non-linear effects such as "barrel", "astigmatic" , and "pin cushion" distortions. Normally we do not expect an optical system (if adequately designed and built) to be a source of non-linear distortions. Even though an optical system is never completely linear, we expect the non-linearities to be small. Thus, we may assume the optical systems of the spectrometer to be linear to first order. This allows the entire optical system to be replaced by a single simple lens and a "film plane" (which here we take to be the plane of the analyzing table). We have previously shown this simplified view of the optics in Figure 3.1.

In Figure 3.4 the optical reconstruction geometry is shown where the fictitious "lens" of our optical system is located by the vector $\vec{X}_{lens}$. In the following

3,3,2,4

FIG. 3.4 OPTICAL RECONSTRUCTION GEOMETRY

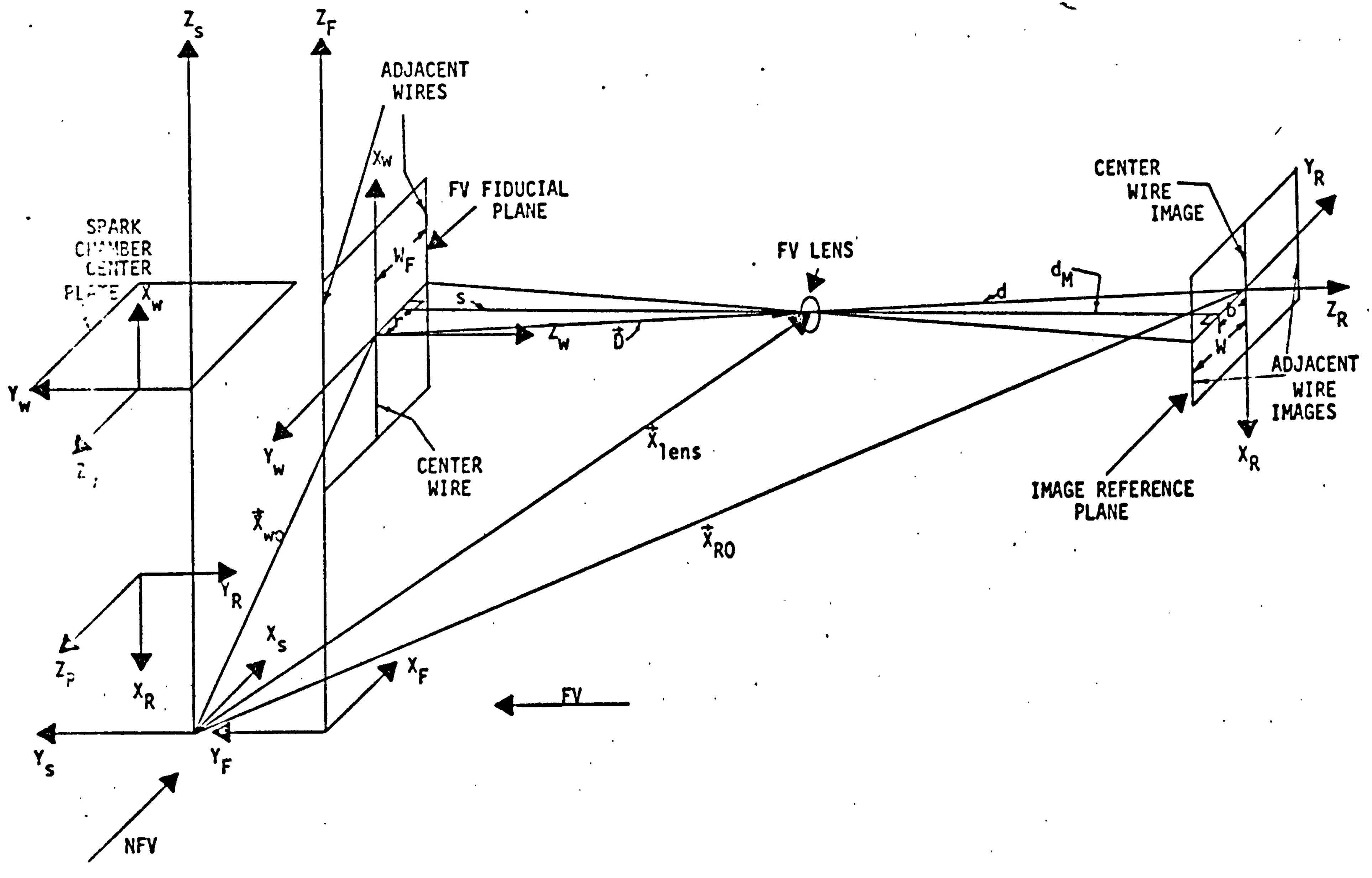

Z_s
Z_F
ADJACENT WIRES
X_W
FV FIDUCIAL PLANE
SPARK CHAMBER CENTER PLATE
X_W
W_F
s
Z_W
$\vec{D}$
FV LENS
d
d_M
CENTER WIRE IMAGE
Y_R
Z_R
b
W
ADJACENT WIRE IMAGES
X_R
IMAGE REFERENCE PLANE
Y_W
Y_W
CENTER WIRE
$\vec{X}_{lens}$
$\vec{X}_{wc}$
$\vec{X}_{RO}$
Y_R
Z_P
X_R
X_s
X_F
FV
Y_s
Y_F
NFV

development all vectors and matrices are assumed to be relative to the "spectrometer coordinate frame" labeled X_s, Y_s, Z_s. This frame has its origin and X_s-Y_s plane in the middle plate of the bottom spark chamber. All three spectrometer axes are parallel to the edges of the solid iron magnets. The spectrometer is contained in the first octant of this frame (see Figure 3.1). The Y_S-axis is parallel (or antiparallel) to the magnetic field. The Z_s-axis points upward along a magnet edge, and the X_s axis completes the right-handed triad. The "fiducial coordinate frame" (X_F,Y_F,Z_F) has axes parallel to the spectrometer-frame axes. Actually there are two sets of fiducial axes, one for the field view, the other for the no-field view. The field view set is obtained by translating the spectrometer axes in the direction of $-Y_s$ through a distance sufficient to place the X_F-Z_F plane in the field view fiducial plane (see Figures 3.5,3.6) In a similar way the no-field view fiducial frame (X_{FN},Y_{FN},Z_{FN}) is displaced so that the Y_{FN}-Z_{FN} plane lies in the no-field view fiducial plane (see Figures 3.5,3.6).

Next in order is the "wire coordinate frame" (labeled X_w,Y_w,Z_w) which also is defined differently in the field and no-field views. This frame has its origin in the plane of a center chamber plate with X_w-Y_w plane in the fiducial plane as shown in Figure 3.5. The

X_w-axis is parallel to the Z_s-axis and lies along the center fiducial wire.

Another coordinate frame of interest is the "image reference frame", labeled (X_R,Y_R,Z_R) in Figure 3.4. To define this frame it is assumed that the lens position, $\vec{X}_{lens}$, is well known. The origin of the image reference frame is then found by

$$\vec{X}_{RO} = \vec{X}_{wo} + (D + d)\,\frac{(\vec{X}_{lens} - \vec{X}_{wo})}{|\vec{X}_{lens} - \vec{X}_{wo}|} \tag{1}$$

where $\vec{X}_{wo}$ is the position vector of the wire frame origin, D is the distance from the wire frame origin to the lens, and d is the distance from the lens to the origin of the image reference frame. All of the variables on the right of equation (1) are measured ones except for d. This parameter is related to the optical magnification and must be determined from a χ^2 fitting procedure. The definition of the image reference frame is now clear. Its origin lies at the point defined by equation (1) and its orientation is found by rotating the wire frame through an angle of 180° about the Z_w-axis. The motivation behind the above definition comes from the fact that simple lenses (1) rotate and (2) translate images by conic projection. This means that all points in space which lie on a line through the lens point must map onto a single point on some specified plane. Here the specified plane (which we shall call the image reference plane) is parallel to the fiducial plane and a distance $(s + d_M)$ from it (see Fig. 3.4). Here s is the perpendicular distance from the fiducial plane to the lens, and d_M is the distance from the lens to the image reference plane. Thus the image reference frame X_R-Y_R plane is the conic projection of the wire frame X_W-Y_W plane onto the image reference plane. In the same way the fiducial plane maps onto the image reference plane by conic projection. Since the fiducial plane is parallel to the image reference plane the fiducial wire images must be parallel and equally spaced. If $s \neq d_M$ then we expect the image of be magnified $(d_M > s)$ or demagnified $(d_M < s)$ and thus the spacing between the imaged wires and the wires themselves is not the same. In any case the spacing between the wire images leads to a geometrical derivation of the parameter d_M (or equivocally the parameter, d), (see section 3.3.4).

Now consider what happens when the fiducial wires are mapped onto a plane not parallel to the fiducial plane. In this case the fiducial images are not parallel or equally spaced. This is, in fact, what we see when the fiducials are projected onto the analyzing table. If the plane of the analyzing table were parallel to the fiducial plane (optically speaking, of course) then all fiducial images would appear parallel and equally spaced in the absence of non-linear effects. The image reference plane and the plane of the analyzing table would be superimposed. Likewise the digitizer coordinate frame and the image reference frame would coincide. Because the fiducial wires are not observed to be parallel and equally spaced the digitizer and image frames must be related by a rotation matrix describing their relative orientations. This leads to the matrix equation

$$[SD] = [RD][SR] \tag{2}$$

where

[SD] = spectrometer-to-digitizer rotation matrix

[RD] = image reference-to-digitizer rotation matrix

[SR] = spectrometer-to-image reference frame rotation matrix

It is clear that [RD] is a unit matrix when the fiducial images are parallel and equally spaced. In reality we do not expect [RD] to be much different from unity because the fiducial images are observed to be nearly parallel and equally spaced.

It will be shown in a later section that the matrix [RD] may be represented by three infinitesimal rotations about the X_R, Y_R, and Z_R axes through angles

θ_x θ_y, and θ_z. The angles are adjustable parameters (along with d) which must be determined by a χ^2 fitting technique to best describe the conic projection of the fiducial wires onto the digitizer plane. How these four parameters affect the fit is easily seen. Physically if the parameter d is varied, then the magnification (and also the distance between the imaged fiducial wires) must change. When the angle θ_y is non-zero the fiducial images become non-parallel and when θ_x is non-zero the spacing between the fiducial lines becomes unequal. Finally if θ_z is non-zero, then the fiducial images are rotated in the digitizer plane. It will be shown in later sections how these results may be determined quantitatively. First, however, expressions will be developed for the lens positions. Additionally estimates of the four parameters d, θ_x, θ_y, and θ_z will be made. Then these estimated results will be used as starting values in a numerical χ^2 fitting procedure which determines the set of (d, θ_x, θ_y, θ_z) best describing the optical projection of the fiducial wires onto the digitizer plane for each of the six optical systems of the spectrometer. If any non-linear distortions are present in the optics, then discrepancies (i.e. deviations in the sense of a χ^2 fit) will appear in the projection of the fiducial wires onto the digitizer plane.

3.3.3 DETERMINATION OF THE LENS POSITION VECTOR

Previously the lens position vector was used to determine the origin of the image reference frame. It was assumed that this vector was known, i.e. a measurable quantity of the optical system. Furthermore it is now assumed that the lens lies in the plane of the center plate of a spark chamber and that the lens is a distance s from the fiducial plane (see Figures 3.5 and 3.6). The distance s is taken to be the same as the true distance that the real camera lens lies from the fiducial plane. Thus the lens position can be described in terms of a two dimensional vector, $\vec{D}$, in the Y_W-Z_W plane of the wire coordinate frame. This vector makes an angle δ with the Z_W-axis which was measured by means of a laser beam. The laser was mounted so that (1) the beam was parallel to a spark chamber center plate and as close to the plate as possible without intercepting or reflecting the light, (2) the beam intercepted the center fiducial wire and (3) the beam intercepted the camera lens. Thus the laser beam follows the "optical path" of the spectrometer for a chosen spark chamber. Now define a new set of orthogonal axes, designed "optical axes" (X_O,Y_O,Z_O), which are parallel to the magnet edges and intercept at the geometrical center of the magnet (see Figures 3.5 and 3.6). The distances ΔX and $\Delta X'$ were directly measured

3.3.3.2

FIG. 3.5 FIELD VIEW LENS
COORDINATE GEOMETRY

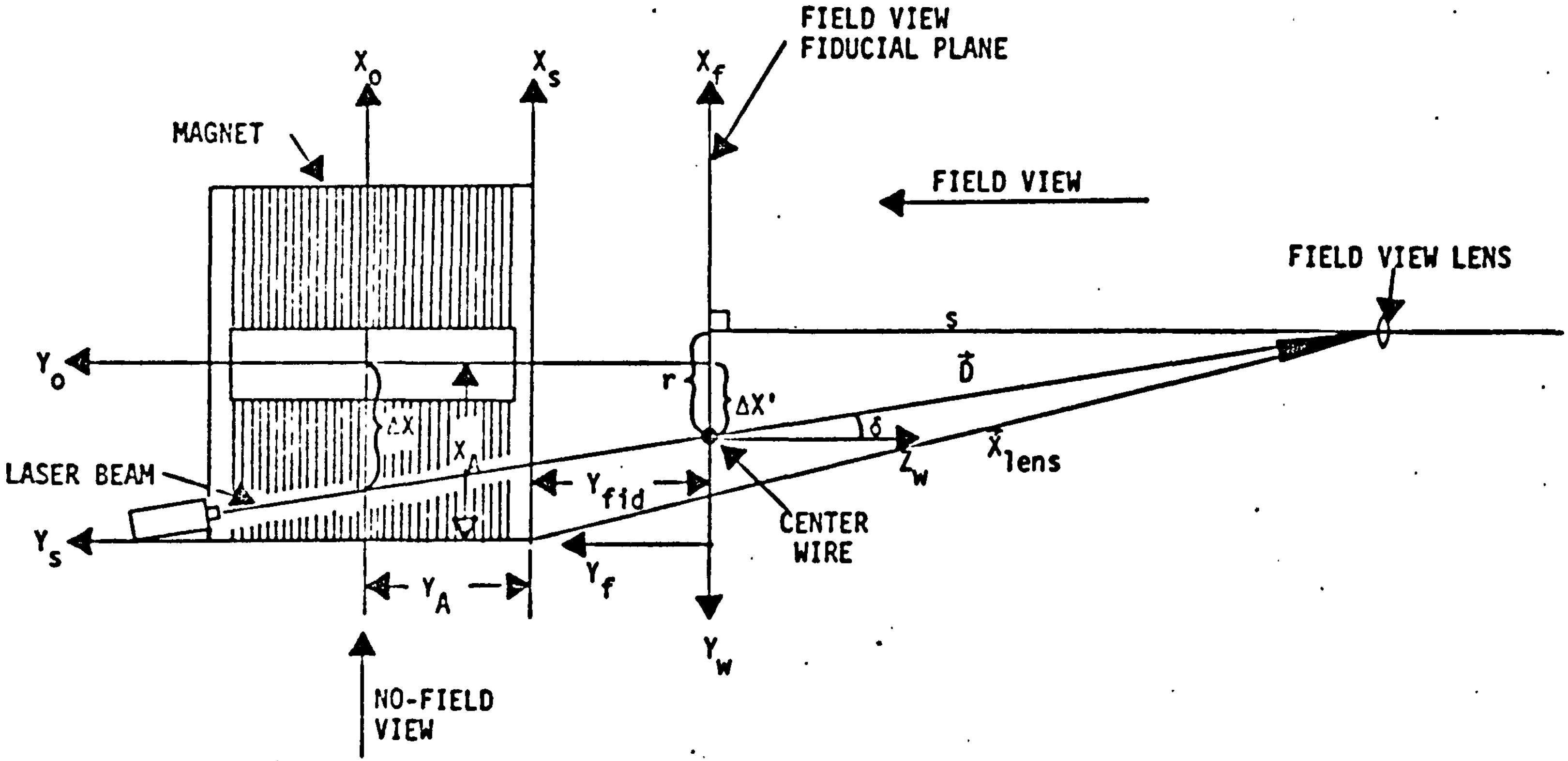

FIELD VIEW
FIDUCIAL PLANE
X_o
X_s
X_f
MAGNET
FIELD VIEW
FIELD VIEW LENS
s
Y_o
r
$\Delta X'$
$\vec{D}$
ΔX
δ
X_A
LASER BEAM
Z_w
$\vec{X}_{lens}$
Y_{fid}
CENTER
WIRE
Y_s
Y_f
Y_A
Y_w
NO-FIELD
VIEW

3.3.3.3

FIG. 3.6 NO-FIELD-VIEW LENS
COORDINATE GEOMETRY

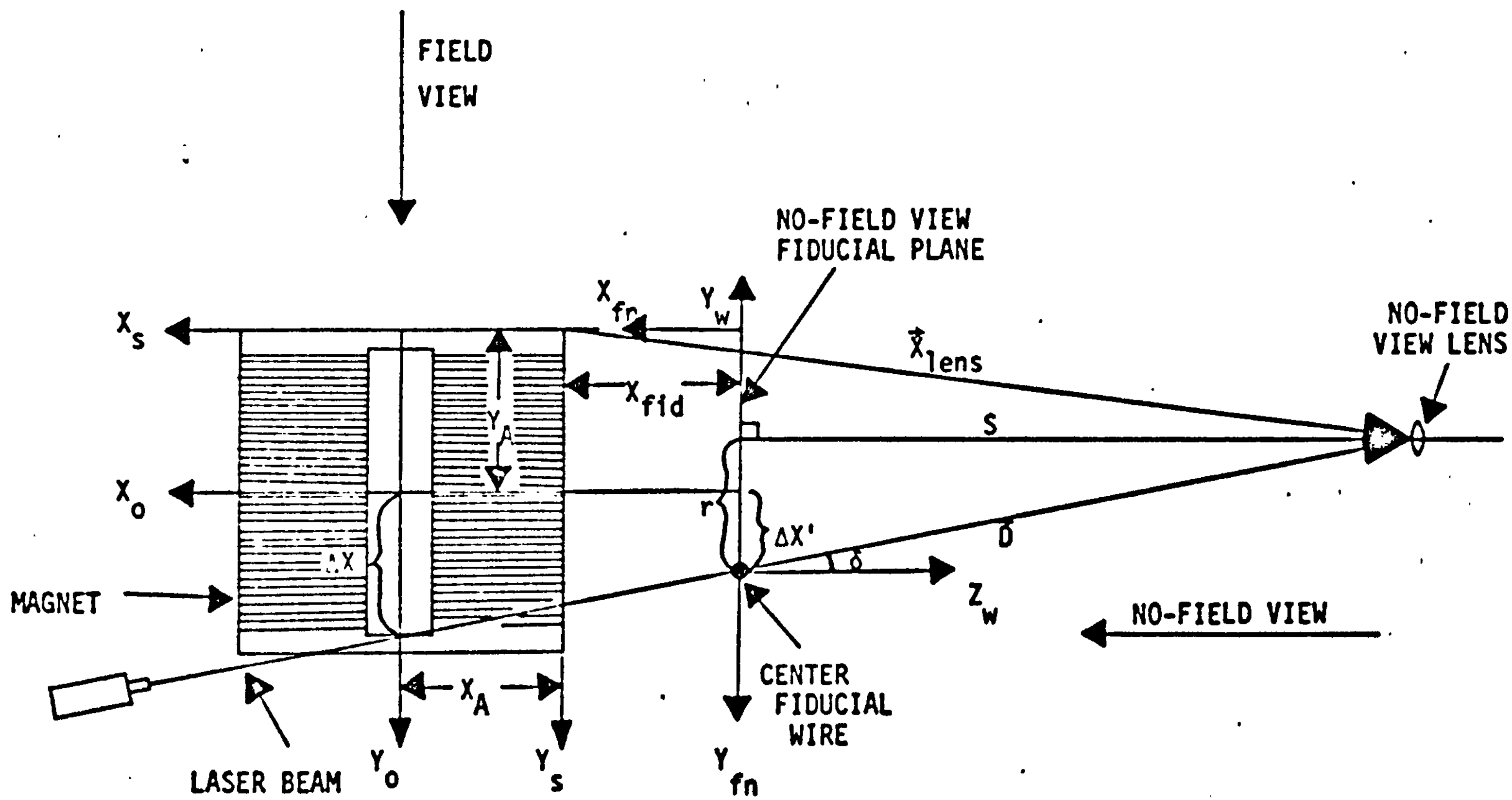

FIELD
VIEW
NO-FIELD VIEW
FIDUCIAL PLANE
X_s
X_{fr}
Y_w
$\vec{X}_{lens}$
NO-FIELD
VIEW LENS
Y_A
X_{fid}
S
X_o
r
ΔX'
$\vec{D}$
ΔX
δ
MAGNET
Z_w
NO-FIELD VIEW
X_A
CENTER
FIDUCIAL
WIRE
LASER BEAM
Y_o
Y_s
Y_{fn}

where in the field view

ΔX = distance from the Y_o-Z_o plane to the laser beam as measured along the X_o-axis

$\Delta X'$ = distance from the Y_o-Z_o plane to the laser beam as measured along the X_F axis

The angle δ is then found, in the field view, from

$$\text{TAN } \delta = \frac{\Delta X - \Delta X'}{Y_A + Y_{fid}} \quad \text{(field view)} \tag{3}$$

where, from Figure 3.5:

Y_A = magnet half-width in the no-field view

Y_{fid} = distance from the magnet face to the fiducial plane in the field view

Correspondingly in the no-field view

$$\text{TAN } \delta = \frac{\Delta X - \Delta X'}{X_A + X_{fid}} \quad \text{(no-field view)} \tag{4}$$

where, from Figure 3.6:

X_A = magnet half-width in the no-field view

X_{fid} = distance from the magnet face to the fiducial plane in the no-field view

Finally the distance D (length of the vector $\vec{D}$) was measured by stretching a string along the laser beam path and then measuring the length of the string. Values of all of the measured optical parameters are presented in Table 3.3.

The lens position vector in the field view may be found from (again see Figure 3.5)

3.3.3.5

TABLE 3.2

MEASURED OPTICAL PARAMETERS

a.) FIELD VIEW DATA

SPARK CHAMBER	D(cm)	TAN δ	ΔX(cm)	Z_{sc}(cm)
TOP	330	.014	2.08	244.039
MIDDLE	218	.0039	.615	126.683
BOTTOM	317	.0048	-.076	0.0

b.) NO-FIELD VIEW DATA

SPARK CHAMBER	D(cm)	TAN δ	ΔX(cm)	Z_{sc}(cm)
TOP	325	.0026	.160	244.039
MIDDLE	231	.0000	.150	126.683
BOTTOM	347	.0087	.524	0.0

$$\vec{X}_{lfv} = \vec{X}_{wo} + \vec{D} \qquad (5)$$

where $\vec{X}_{wo}$ is the position of the wire frame origin in the spectrometer frame:

$$\vec{X}_{wo} = (X_A - \Delta X', -Y_{fid}, Z_{sc}) \text{ (field view)} \qquad (6)$$

where Z_{sc} is the spark chamber Z-coordinate. Also

$$\vec{D} = (D\sin\delta, -D\cos\delta, 0) \text{ (field view)} \qquad (7)$$

Thus the field-view lens vector is

$$\vec{X}_{lfv} = [(X_A-\Delta X')+D\sin\delta, -Y_{fid}-D\cos\delta, Z_{sc}] \qquad (8)$$

For the no-field view we have

$$\vec{X}_{wo} = (-X_{fid}, Y_A + \Delta X', Z_{sc}) \text{ (no-field view)} \qquad (9)$$

$$\vec{D} = (-D\cos\delta, -D\sin\delta, 0) \text{ (no-field view)} \qquad (10)$$

Finally the no-field view lens vector is

$$\vec{X}_{lnv} = [-X_{fid}-D\cos\delta, (Y_A+\Delta X')-D\sin\delta, Z_{sc}] \qquad (11)$$

3.3.4 ESTIMATION OF THE MAGNIFICATION PARAMETER

In section 3.3.2 the position vector of the origin of the image reference frame was developed (eq. 3.1). It has subsequently been necessary to determine the lens position vector, $\vec{X}_{lens}$, the position vector of the wire frame origin, $\vec{X}_{wo}$, and the distance from the wire frame origin to the lens, D. The parameter associated with optical magnification, d, will now be considered. From Figure 3.7 it can be seen how d and D are related to the distance between fiducial wires in the fiducial plane, W_F, and the width between fiducial wires in the digitizer plane, W_D. This figure is a view of the optical geometry as seen from above the spectrometer; thus Figure 3.7 is a "top" view of Figure 3.4. In addition to the fiducial plane and the image reference plane, the dititizer plane is also shown in Figure 3.7. Recall that if the digitizer orientation angles θ_x, θ_y, θ_z are all zero then the digitizer and image reference planes coincide. In this event the magnification parameter obtained is

$$d = \frac{D}{W_F} W_D \tag{1}$$

In actual fact the orientation angles are not zero and a more exact relation than (12) is necessary. Because a simple optical system can only invert images we expect that $\theta_z \sim 0$ (this is consistent with the results of a χ^2 fitting procedure to be discussed in a later section). Additionally a rotation about θ_y does not change the distance between the fiducial wires along the Y_D axis (i.e. along the image of the center spark chamber plate). Hence if we chose to measure (for the purpose of estimating the parameter d) the distance between fiducial wires in the digitizer plane along a center spark chamber plate then W_D is not affected by θ_y and θ_z. The only angle

3.3.4.3

FIG. 3.7 GEOMETRY OF THE MAGNIFICATION PARAMETER

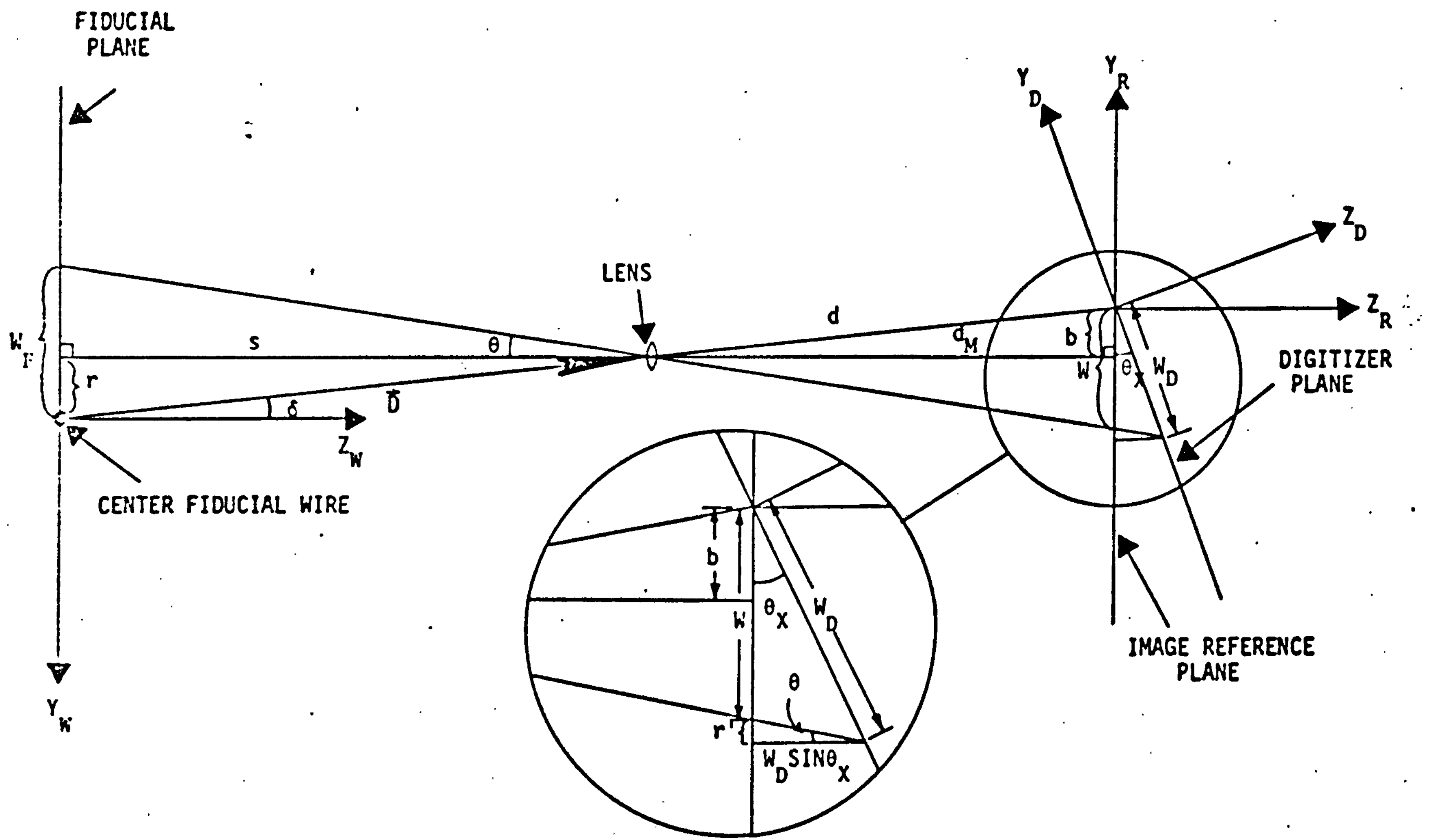

FIDUCIAL PLANE
LENS
CENTER FIDUCIAL WIRE
DIGITIZER PLANE
IMAGE REFERENCE PLANE
s
d
r
b
W
θ
δ
θ_X
W_D
W_F
d_M
$\vec{D}$
Z_W
Y_W
Y_D
Y_R
Z_D
Z_R
$W_D \sin\theta_X$

which affects the determination of d is θ_x which is seen from Figure 3.7. First write

$$d = \frac{DW}{W_F} \tag{2}$$

where W is the distance between fiducial wire images in the image reference plane. From the geometry it is seen that

$$\mathrm{TAN}\ \theta = \frac{W_F - r}{s} \tag{3}$$

where the variable definitions can be easily deduced from the expanded inset of Figure 3.7. Also

$$\mathrm{COS}\ \theta_x = \frac{W + r'}{W_D} \tag{4}$$

where

$$r' = W_D \mathrm{SIN}\ \theta_x\ \mathrm{TAN}\ \theta = W_D \left(\frac{W_F - r}{s}\right) \mathrm{SIN}\ \theta_x \tag{5}$$

Put (5) into (4) and solve for W to get:

$$W = W_D \left[\mathrm{COS}\ \theta_x - \left(\frac{W_F - r}{s}\right) \mathrm{SIN}\ \theta_x\right] \tag{6}$$

where

$$r = D\ \mathrm{SIN}\ \delta \tag{7}$$

Finally if (6) and (7) are used in (8) the following result for the magnification parameter is obtained

$$d = \frac{D}{W_F} W_D \left[\mathrm{COS}\ \theta_x - \left(\frac{W_F - D\mathrm{SIN}\ \delta}{s}\right) \mathrm{SIN}\ \theta_x\right] \tag{8}$$

In the limit as $\theta_x \to 0$ equation (8) becomes (2) as expected.

3.3.5 CHI-SQUARE FIT TO THE SPECTROMETER OPTICAL PARAMETERS

Here we arrive at a method for determining the optical parameters (d, θ_x, θ_y,θ_z) which we have defined previously. In order to accomplish this we need to develop the equations which describe the mapping of the fiducial wires onto the digitizer plane. To this end we may write the position vector, $\vec{X}_s$, of any point, P, in the spectrometer frame as

$$\vec{X}_s = \vec{X}_{DO} + [DS]\vec{X}_D \tag{1}$$

where $\vec{X}_{DO}$ is the position vector of the digitizer frame origin ($\vec{X}_{DO} \equiv \vec{X}_{RO}$), [DS] is the digitizer-to-spectrometer frame matrix and $\vec{X}_D$ is the position vector of P in the digitizer frame. Here $\vec{X}_{DO}$ is given by eq. (3.3.2.1). The matrix [DS] is defined by

$$[DS] = [RS][DR]. \tag{2}$$

The reference-to-digitizer frame matrix is given by

$$[RD] = [DR]^T = [Z][Y][X] \tag{3}$$

where the matrices [X], [Y] and [Z] are Euler angle rotations about the X_D, Y_D and Z_D axes respectively and are given by

$$[X] = \begin{bmatrix} 1 & 0 & 0 \\ 0 & \cos\theta_x & -\sin\theta_x \\ 0 & \sin\theta_x & \cos\theta_x \end{bmatrix} \tag{4}$$

$$[Y] = \begin{bmatrix} \mathrm{COS}\ \theta_y & 0 & -\mathrm{SIN}\ \theta_y \\ 0 & 1 & 0 \\ \mathrm{SIN}\ \theta_y & 0 & \mathrm{COS}\ \theta_y \end{bmatrix} \tag{5}$$

$$[Z] = \begin{bmatrix} \mathrm{COS}\ \theta_z & \mathrm{SIN}\ \theta_z & 0 \\ -\mathrm{SIN}\ \theta_z & \mathrm{COS}\ \theta_z & 0 \\ 0 & 0 & 1 \end{bmatrix} \tag{6}$$

Put (4)-(6) into (3) and obtain

$$[RD] = \begin{bmatrix} C(\theta_z)C(\theta_y) & -C(\theta_z)S(\theta_y)S(\theta_x) + S(\theta_z)C(\theta_x) & -C(\theta_z)S(\theta_y)C(\theta_x) - S(\theta_z)S(\theta_x) \\ -S(\theta_z)C(\theta_y) & S(\theta_z)S(\theta_y)S(\theta_x) + C(\theta_z)C(\theta_x) & S(\theta_z)S(\theta_y)C(\theta_x) - S(\theta_z)S(\theta_x) \\ S(\theta_y) & C(\theta_y)S(\theta_x) & C(\theta_y)C(\theta_x) \end{bmatrix} \tag{7}$$

where S( ) = SIN( ) and C( ) = COS( ).

Inspection of Fig. (3.4) shows that the reference-to-spectrometer frame matrix is given by (for the field view)

$$[RS] = \begin{bmatrix} 0 & 1 & 0 \\ 0 & 0 & -1 \\ -1 & 0 & 0 \end{bmatrix} \tag{8}$$

Use (7) and (8) in (2) to get, finally, in the field view:

$$[DS]_{FV} = \begin{bmatrix} C(\theta_z)S(\theta_y)S(\theta_x) + S(\theta_z)C(\theta_x) & S(\theta_z)S(\theta_y)S(\theta_x) + C(\theta_z)C(\theta_x) & C(\theta_y)S(\theta_x) \\ C(\theta_z)S(\theta_y)C(\theta_x) + S(\theta_z)S(\theta_x) & -S(\theta_z)S(\theta_y)C(\theta_x) + C(\theta_z)S(\theta_x) & -C(\theta_y)C(\theta_x) \\ -C(\theta_z)C(\theta_y) & S(\theta_z)C(\theta_y) & -S(\theta_y) \end{bmatrix} \tag{9}$$

In the no-field view we likewise find

$$[DS]_{NV} = \begin{bmatrix} C(\theta_z)S(\theta_y)C(\theta_x) & -S(\theta_z)S(\theta_y)C(\theta_x) & -C(\theta_y)C(\theta_x) \\ +S(\theta_z)S(\theta_x) & +C(\theta_z)S(\theta_x) & \\ C(\theta_z)S(\theta_y)S(\theta_x) & -S(\theta_z)S(\theta_y)S(\theta_x) & -C(\theta_y)S(\theta_x) \\ -S(\theta_z)C(\theta_x) & -C(\theta_z)C(\theta_x) & \\ -C(\theta_z)C(\theta_y) & S(\theta_z)C(\theta_y) & -S(\theta_y) \end{bmatrix} \quad (10)$$

Eqs. (9) and (10) give us all the information we need to calculate the coordinates of a point in space, P, either in the spectrometer frame ($\vec{X}_s$) or the digitizer frame ($\vec{X}_D$) by means of eq. (1).

We now develop a procedure by which we determine the conic projection of the fiducial wires from the wire frame onto the digitizer frame. In the wire frame each fiducial wire lies in the x_w-y_w plane with a slope and intercept

$$m_w = 0 \quad (11)$$

$$b_w = y_w \quad (12)$$

Hence we may select two points on some particular wire to be

$$(o, y_w) \text{ and } (a, y_w) \quad (13)$$

where "a" is an arbitrary distance from the origin. We may transform these points to the spectrometer frame for the field view

$$\vec{X}_{sw1} = \vec{X}_{wo} + \begin{bmatrix} -y_w \\ 0 \\ 0 \end{bmatrix} \qquad \text{(FIELD VIEW)} \qquad (14)$$
$$\vec{X}_{sw1} = \vec{X}_{wo} + \begin{bmatrix} -y_w \\ 0 \\ a \end{bmatrix}$$

For the no-field-view we have

$$\vec{X}_{sw1} = \vec{X}_{wo} + \begin{bmatrix} 0 \\ y_w \\ 0 \end{bmatrix} \qquad \text{(NO FIELD VIEW)} \qquad (15)$$
$$X_{sw2} = X_{wo} + \begin{bmatrix} 0 \\ y_w \\ a \end{bmatrix}$$

It is clear that the two points on a fiducial wire (given by (14) for the field view or (15) for the no-field-view) and the lens point, $\vec{X}_{lens}$, define a plane. The intersection of this plane with the digitizer x-y plane defines the conic projection of the fiducial wires. Using eq. (1) we have the three points which determine the plane defined by a fiducial wire and the lens point:

$$\begin{aligned} \vec{X}_{D1} &= [SD]\ (\vec{X}_{wo}-\vec{X}_{DO} + [-y_w,o,o]) \\ \vec{X}_{D2} &= [SD]\ (\vec{X}_{wo}-\vec{X}_{DO} + [-y_w,o,a]) \\ \vec{X}_{D3} &= [SD]\ (\vec{X}_{lens} - \vec{X}_{DO}) \end{aligned} \qquad \text{(FIELD VIEW)} \qquad (16)$$

or

$$\begin{aligned} \vec{X}_{D1} &= [SD]\ (\vec{X}_{wo}-\vec{X}_{DO} + [o,y_w,o]) \\ \vec{X}_{D2} &= [SD](\vec{X}_{wo}-\vec{X}_{DO} + [o,y_w,a]) \\ \vec{X}_{D3} &= [SD]\ (\vec{X}_{lens}-\vec{X}_{DO}) \end{aligned} \qquad \text{(NO FIELD VIEW)} \qquad (17)$$

These three points in space determine a plane in the digitizer frame

$$AX+BY+CZ = 1 \tag{18}$$

where A, B and C are the plane parameters found by writing the three points as

$$\begin{aligned} \vec{X}_{D1} &= [x_1, y_1, z_1] \\ \vec{X}_{D2} &= [x_2, y_2, z_2] \\ \vec{X}_{D3} &= [x_3, y_3, z_3] \end{aligned} \tag{19}$$

Then

$$\begin{aligned} A &= \begin{vmatrix} y_2-y_1 & z_2-z_1 \\ y_3-y_1 & z_3-z_1 \end{vmatrix} / D \\ B &= \begin{vmatrix} z_2-z_1 & x_2-x_1 \\ z_3-z_1 & x_3-x_1 \end{vmatrix} / D \\ C &= \begin{vmatrix} x_2-x_1 & y_2-y_1 \\ x_3-x_1 & y_3-y_1 \end{vmatrix} / D \end{aligned} \tag{20}$$

$$D = Ax_1 + By_1 + Cz_1$$

The line of intersection of (18) with the digitizer plane is given by

$$AX + BY = 1 \tag{21}$$

so that

$$Y = -\frac{AX}{B} + \frac{1}{A} \tag{22}$$

Thus the fiducial wires mapped onto the digitizer plane have slopes and intercepts:

$$m_D = -\frac{A}{B} \tag{23}$$

$$b_D = \frac{1}{A} \tag{24}$$

The preceding equations leading up to (23) and (24) allow the fiducial wires to be conically projected onto the digitizer plane provided we select appropriate values of the free parameters $(d, \theta_x, \theta_y, \theta_z)$. Thus these optical parameters can be determined by measuring the fiducial wires in the fiducial plane and in the digitizer plane; then a χ^2 fitting procedure can be used to determine the "best" set of the parameters for a particular optical system. This fitting procedure is discussed in the following paragraphs.

There are six optical systems (2 views and 3 spark chambers). The fiducial wires were photographed for each of these systems. Then the slopes and intercepts of each fiducial were measured 10 times each in the digitizer frame with the optical scanning apparatus. The 10 measurements were averaged for each wire and the corresponding standard deviations calculated (see Figs. 3.8.a and 3.8.b for examples of wire slopes measured in this way). Thus a "measured parameter" vector was formed

$$\vec{X}_m = \begin{bmatrix} m_{D1} \\ b_{D1} \\ m_{D2} \\ b_{D2} \\ \vdots \\ m_{Dn} \\ b_{Dn} \end{bmatrix} \tag{25}$$

Here m_{D1} and b_{D1} are the slope and intercept of the 1st wire as measured in the digitizer frame. Thus $\vec{X}_m$ contains 2n entries, where n is the number of fiducial wires. The "fit parameter" vector is given by

$$\vec{a} = \begin{bmatrix} d \\ \theta_x \\ \theta_y \\ \theta_z \end{bmatrix} \tag{26}$$

The fitting procedure used here calculates the slopes and intercepts of the wires in the digitizer frame using the initially guessed vector $\vec{a}$. In order to minimize χ^2 a "best" set of parameters $\vec{a}^*$ are calculated by the well known χ^2-fit technique. Shown below are the results of fitting the 6 optical systems in the spectrometer:

VIEW	CHAMBER	χ^2_ν	d (cm)	θ_x	θ_y (RADIANS)	θ_z
FV	BOTTOM	.78	286.57	-.0580	.0606	.0025
FV	MIDDLE	2.30	293.69	-.0113	.0077	-.0002
FV	TOP	1.14	308.37	-.0359	-.0357	-.0003
NV	BOTTOM	.81	312.34	-.0327	.1989	.0061
NV	MIDDLE	2.33	303.99	.0024	.0123	.0019
NV	TOP	1.30	302.61	-.0004	-.0746	.0032

χ^2_ν is the reduced value of χ^2 from the fit.

It is perhaps instructive to examine some of the measured fiducial data in light of further corrections which must be made. In Figs 3.8.a and 3.8.b we see the slopes of fiducial wires in the bottom and top chambers. In both cases there is a general trend of changing slope (from positive to negative in Fig. 3.8.a and negative to positive in Fig. 3.8.b). Thus there is a definite indication of a rotation about the y_D-axis. If all of the optical error were due to this rotation then all of the slopes would fall along the straight line drawn through the points. Deviations about the straight line indicate that non-linear optical corrections must be made. In order to account for these non-linear effects linear interpolation is used to correct the slopes and intercepts according to the deviations (in the sense of

FIG.3.8.a FIDUCIAL WIRE SLOPES IN THE FIELD VIEW, BOTTOM CHAMBER

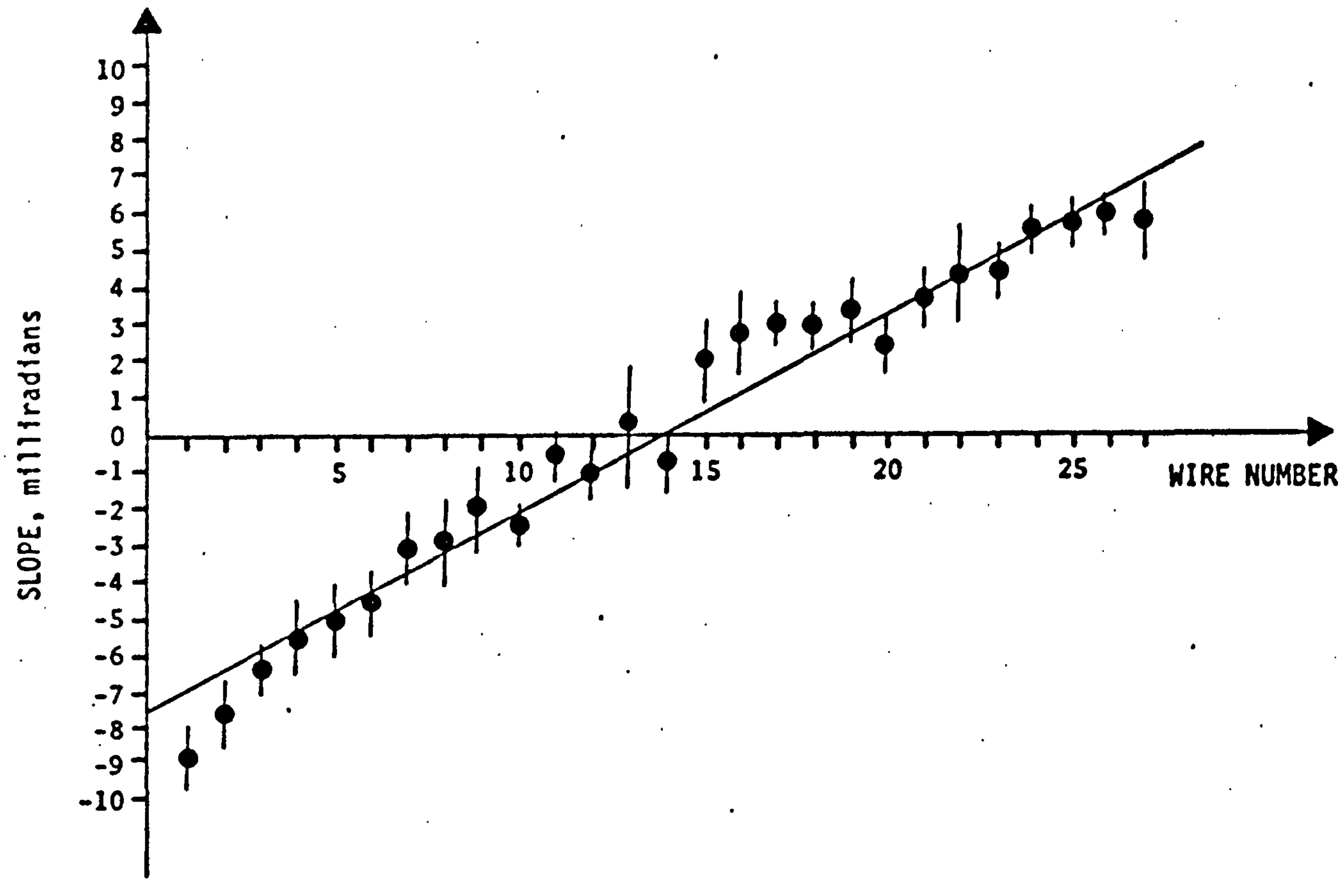

SLOPE, milliradians
10
9
8
7
6
5
4
3
2
1
0
-1
-2
-3
-4
-5
-6
-7
-8
-9
-10
5
10
15
20
25
WIRE NUMBER

FIG. 3.8.b FIDUCIAL WIRE SLOPES IN THE FIELD VIEW, TOP CHAMBER

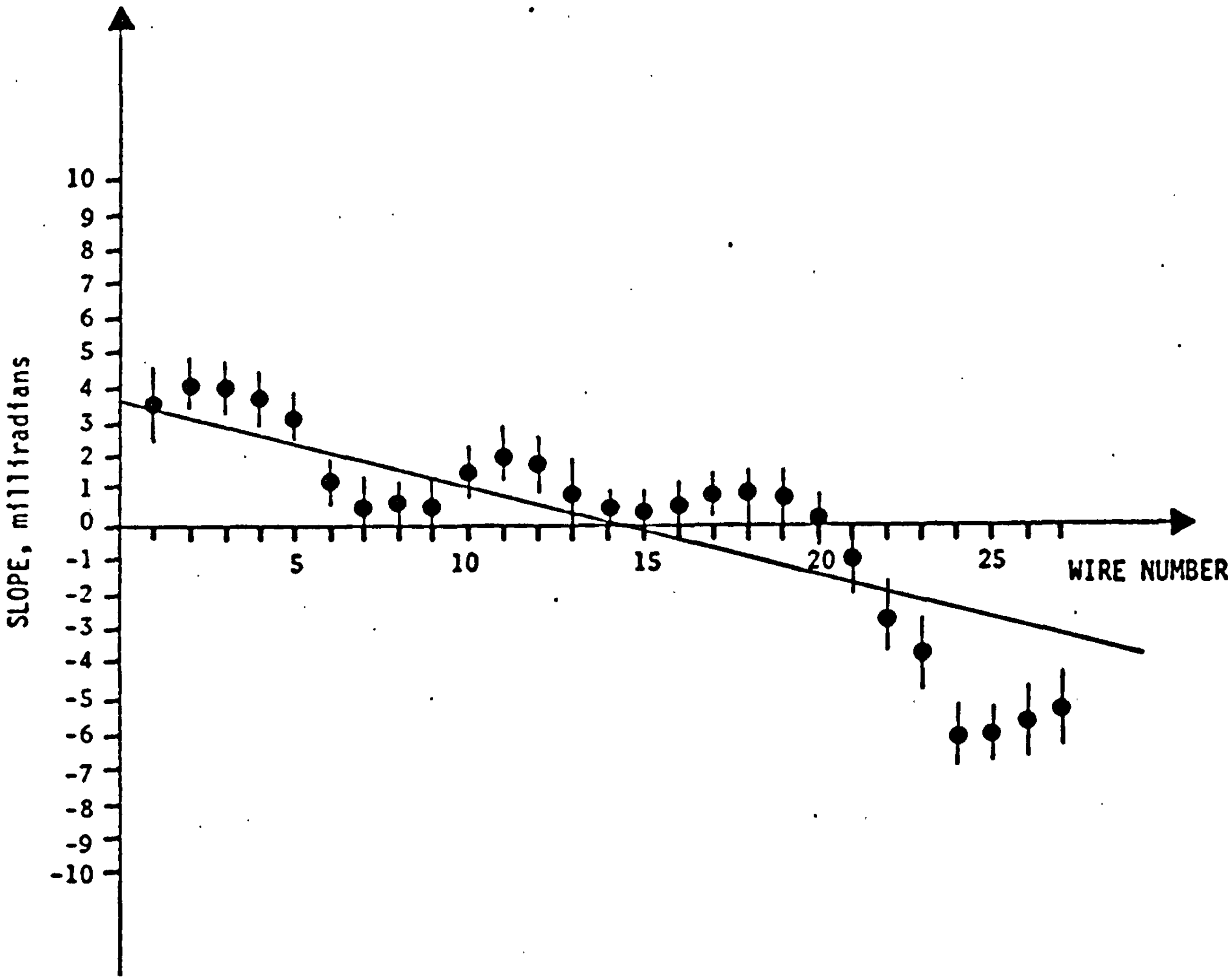
SLOPE, milliradians
10
9
8
7
6
5
4
3
2
1
0
-1
-2
-3
-4
-5
-6
-7
-8
-9
-10
5
10
15
20
25
WIRE NUMBER

a χ^2-fit) between measured and calculated values after the optical parameters $(d, \theta_x, \theta_y, \theta_z)$ have been determined. Thus the deviation vector (between measured and calculated slopes and intercepts) is a measure of the non-linearity of the optics.

In order to make a check on the optical model developed above we devise the following method for determining how "infinite momentum events" are detected. Thus we form various combinations of fiducial wires (which appear as "tracks" on film and which can be viewed as infinite momentum events) as seen in the digitizer frame and assume that the combination of any 3 fiducial wires in the top, middle and bottom spark chambers is an "event". We realize that such "events" are not consistent with real events because their reconstructed positions are a function only of the random selection process. However we shall examine only the angles between the fiducials in the various chambers. If the optical model were perfect then the angle differences would all be zero (since the fiducials stretch the full length of the spectrometer and are parallel to within .01 milliradians). The fiducial events, formed in the above way, were momentum analyzed and the resultant momenta were histogramed as shown in Fig. 3.9. In order to see the significance of this histogram we shall develop the probability density which describes it. We assume that

FIG. 3.9 HISTOGRAM OF "INFINITE MOMENTUM EVENTS" AS VIEWED BY THE SPECTROMETER

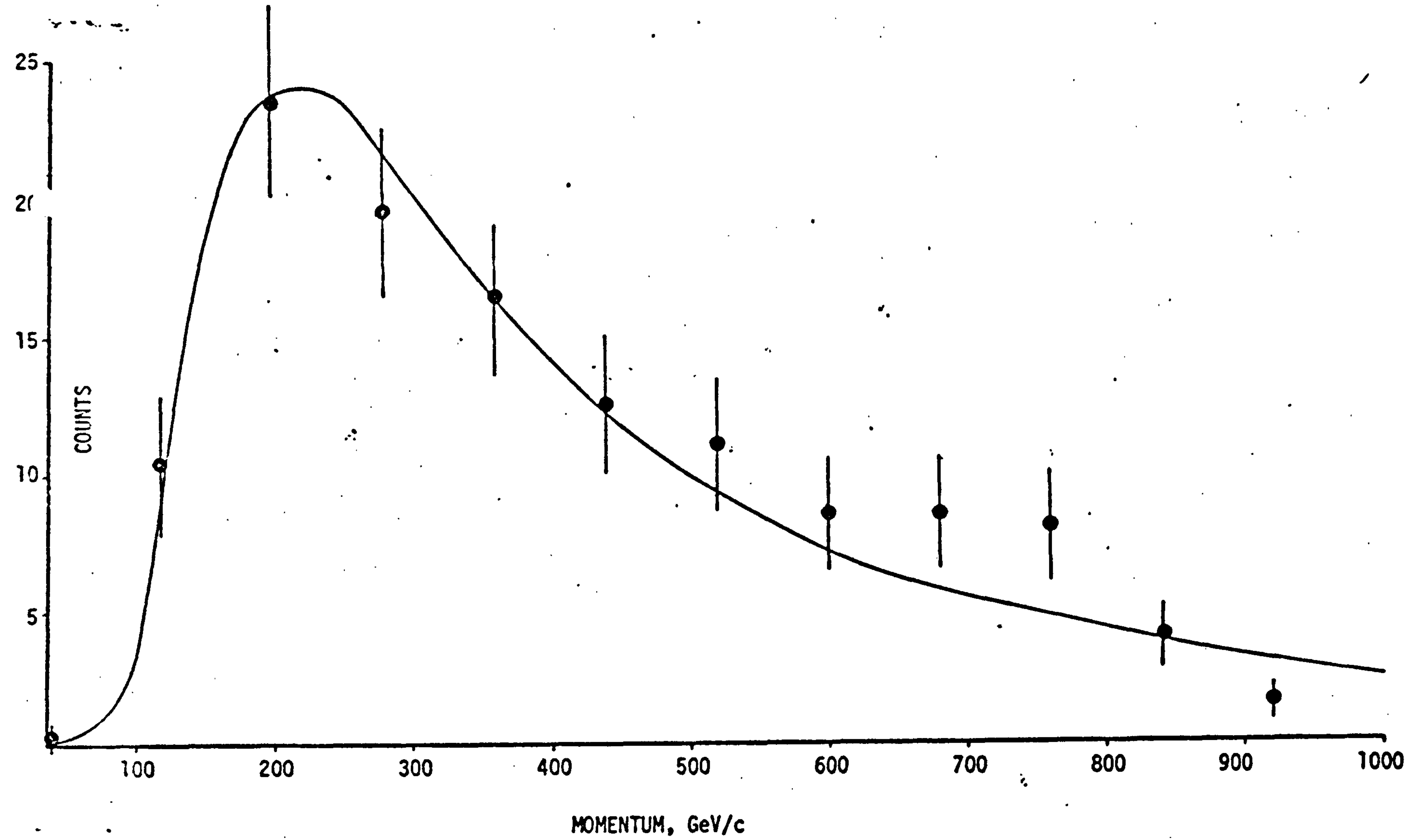

25
20
15
10
5
COUNTS
100
200
300
400
500
600
700
800
900
1000
MOMENTUM, GeV/c

the measured angle difference between any two fiducial wires, $\phi = \phi_1 - \phi_2$, has uncertainty $\Delta\phi$ and is distributed by

$$f(\phi) = \sqrt{\frac{2}{\pi}}\,\frac{1}{\Delta\phi}\; e^{-\frac{1}{2}\left(\frac{\phi}{\Delta\phi}\right)^2} \tag{27}$$

In (27) we are concerned only with the absolute value of ϕ. This is due to the fact that we shall calculate a momentum by

$$p = \frac{k}{\phi} \tag{28}$$

which we require to be positive, hence only the absolute value of ϕ is used. If we introduce the "effective momentum", p_e, by

$$p_e = \frac{k}{\Delta\phi} \tag{29}$$

then we see that p_e corresponds to the angle uncertainty in the reconstruction process. If we use (28) and (29) in (27) we find

$$f(p|p_e) = \sqrt{\frac{2}{\pi}}\,\frac{p_e}{p^2}\; e^{-\frac{1}{2}\left(\frac{p_e}{p}\right)^2} \tag{30}$$

Eq. (30) is a probability density in momentum which is conditionally dependent on the effective momentum. We see that (30) must describe the histogram of Fig. 3.9 for some particular value of p_e. A χ^2-fit of eq. (30) to this data yields a value for the effective momentum of $p_e = 310$ GeV/c; the fitted curve is also shown in Fig 3.9. We conclude that the hypothetical "infinite momentum event" will, on the average be distributed by eq. (30) with an effective momentum of 310 GeV/c.

3.4. RECONSTRUCTION OF A MUON TRAJECTORY INTO REAL SPACE

In this section we derive the equations necessary for the optical reconstruction of a muon event as defined in Sec. 3.2. We begin this task by determining how variables in the clock frame are related to corresponding variables in the digitizer frame.

3.4.1. CLOCK FRAME-TO-DIGITIZER FRAME TRANSFORMATION

The measurement of a single muon event allows the position and orientation of the track to be determined in the clock frame. We now develop equations necessary for transforming the positions and orientations to the digitizer frame. Referring to Fig. 3.10 we see that the origins of the clock frame, $\vec{X}_{C1}$, and the digitizer frame, $\vec{X}_{D1}$, allow the relative origin vector, $\vec{X}_{CD}$, to be calculated.

$$\vec{X}_{CD} = \vec{X}_{D1} - \vec{X}_{C1} \tag{1}$$

The angle between the clock frame X_C-axis and the table frame X_T-axis is seen to be

$$\theta_C = \mathrm{TAN}^{-1} \left[\frac{(\vec{X}_{C2})_y - (\vec{X}_{C1})_y}{(\vec{X}_{C2})_x - (\vec{X}_{C1})_x}\right] \tag{2}$$

while the corresponding angle between the X_D and X_T axes is

3.4.1.2

FIG. 3.10 CLOCK FRAME TO DIGITIZER FRAME TRANSFORMATION

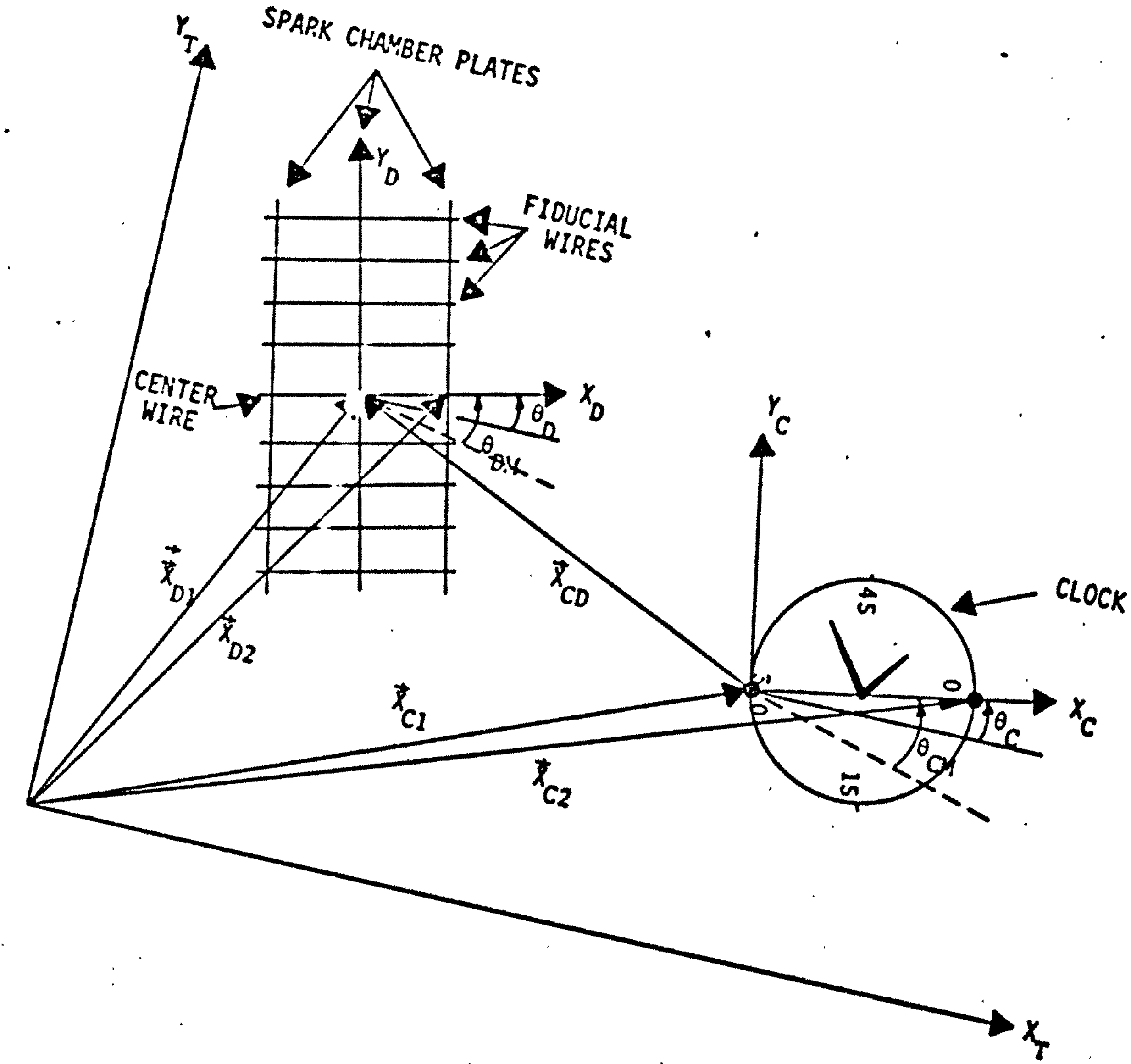

SPARK CHAMBER PLATES
FIDUCIAL WIRES
CENTER WIRE
CLOCK
Y_T
X_T
Y_D
X_D
Y_C
X_C
θ_D
θ_{D1}
θ_C
θ_{C1}
$\vec{X}_{D1}$
$\vec{X}_{D2}$
$\vec{X}_{CD}$
$\vec{X}_{C1}$
$\vec{X}_{C2}$
45
0
15

$$\theta_D = \mathrm{TAN}^{-1}\left[\frac{(\vec{X}_{D2})_y-(\vec{X}_{D1})_y}{(\vec{X}_{D2})_x-(\vec{X}_{D1})_x}\right] \qquad (3)$$

Thus the angle of rotation from the clock frame to the digitizer frame is

$$\theta_{CD} = \theta_D - \theta_C \qquad (4)$$

Any vector in the clock frame, $\vec{R}_C$, has components in the digitizer frame, $\vec{R}_D$, given by

$$\vec{R}_D = [CD][\vec{R}_C-\vec{X}_{CD}] \qquad (5)$$

where the clock-to-digitizer rotation matrix is

$$[CD] = \begin{bmatrix} \mathrm{COS}\ \theta_{CD} & \mathrm{SIN}\ \theta_{CD} & 0 \\ -\mathrm{SIN}\ \theta_{CD} & \mathrm{COS}\ \theta_{CD} & 0 \\ 0 & 0 & 1 \end{bmatrix} \qquad (6)$$

Thus given a point on a muon spark as measured in the clock frame eqs. (5) and (6) can be used to determine this point in the digitizer frame. Likewise any measured angle in the clock frame, θ_{CM}, can be found in the digitizer frame by

$$\theta_{DM} = \theta_{CD} + \theta_{CM} \qquad (7)$$

In order to use (5) - (7) the vector $\vec{X}_{CD}$ and θ_{CD} must be measured for all six optical systems.

3.4.2 DETERMINATION OF THE POSITION AND ANGLE OF THE MUON SPARK IN THE DIGITIZER FRAME

Let $\vec{X}_{PM}$ be a measured position on the muon track in the table frame and $\vec{X}_p$ be the same point as measured in the digitizer frame. From Fig. 3.11.a we see that

$$\vec{X}_p = [TD](\vec{X}_{PM} - \vec{X}_{C1}) - \vec{X}_{CD} \qquad (1)$$

where the table-to-digitizer frame matrix is given by

$$[TD] = \begin{bmatrix} \cos\theta_D & \sin\theta_D & 0 \\ -\sin\theta_D & \cos\theta_D & 0 \\ 0 & 0 & 1 \end{bmatrix} \qquad (2)$$

and

$$\theta_D = \theta_{CM} + \theta_{CD} \qquad (3)$$

The angle of the muon track, θ_p, in the digitizer frame is seen to be

$$\theta_P = \theta_{PM} - \theta_{CM} - \theta_{CD} \qquad (4)$$

A single muon event consists of the measurement of

$$\vec{X}_{PM}, \theta_{PM}, \vec{X}_{C1}, \theta_{CM} \qquad (5)$$

where all variables are measured in the table frame:

$\vec{X}_{PM}$ = position vector of some point on the track

θ_{PM} = angle of the track with some arbitrary reference line

$\vec{X}_{C1}$ = position vector of clock frame origin

θ_{CM} = angle that the X -axis makes with the same arbitrary reference line as θ_{PM}.

3.4.2.2

FIG. 3.11.a POSITION AND ANGLE OF MUON SPARK IN DIGITIZER FRAME

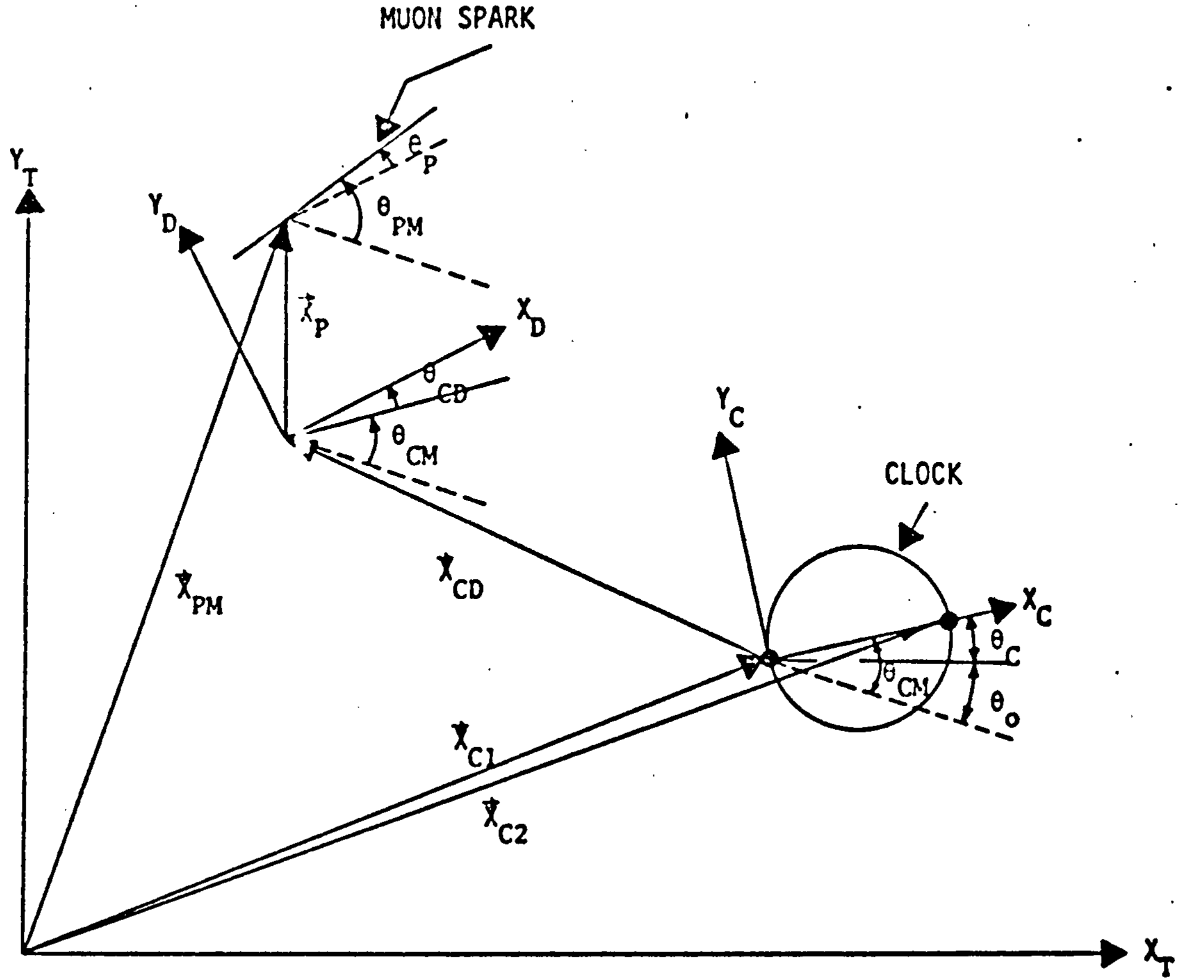

MUON SPARK
θ_P
θ_{PM}
Y_T
Y_D
$\vec{X}_P$
X_D
θ_{CD}
θ_{CM}
Y_C
CLOCK
$\vec{X}_{PM}$
$\vec{X}_{CD}$
X_C
θ_C
θ_{CM}
θ_o
$\vec{X}_{C1}$
$\vec{X}_{C2}$
X_T

We assume that

$$\vec{X}_{CD}, \theta_{CD} \tag{6}$$

are well known constants:

$\vec{X}_{CD}$ = position vector of digitizer frame origin relative to the clock frame with components in the digitizer frame.

θ_{CD} = angle between the X_C-axis and the X_D-axis.

Thus by measurement of the variables (5) and knowing variables (6) one can use eqs. (1) - (6) to establish the particle track coordinates in the digitizer frame.

3.4.3 CORRECTIONS DUE TO NON-LINEAR OPTICS

In the digitizer frame the muon spark has some position, $\vec{X}_p$, and angle, θ_p, determined by the methods of Sec. 3.4.2. The corresponding slope, m_p, and intercept, b_p, of the line are given by

$$m_p = \mathrm{TAN}\ \theta_p \tag{1}$$

$$b_p = y_p - x_p \mathrm{TAN}\ \theta_p \tag{2}$$

Non-linear optical corrections are applied to (1) and (2) using the deviation vector, $\vec{d}$, obtained from the χ^2-fit of the optical parameters as discussed in Sec. 3.3.5.

3.4.4 DETERMINATION OF TWO POINTS ON THE MUON SPARK IN THE SPECTROMETER FRAME

From Fig. 3.11.b we see that two points on the muon

FIG. 3.11.b DETERMINATION OF TWO POINTS ON THE MUON SPARK

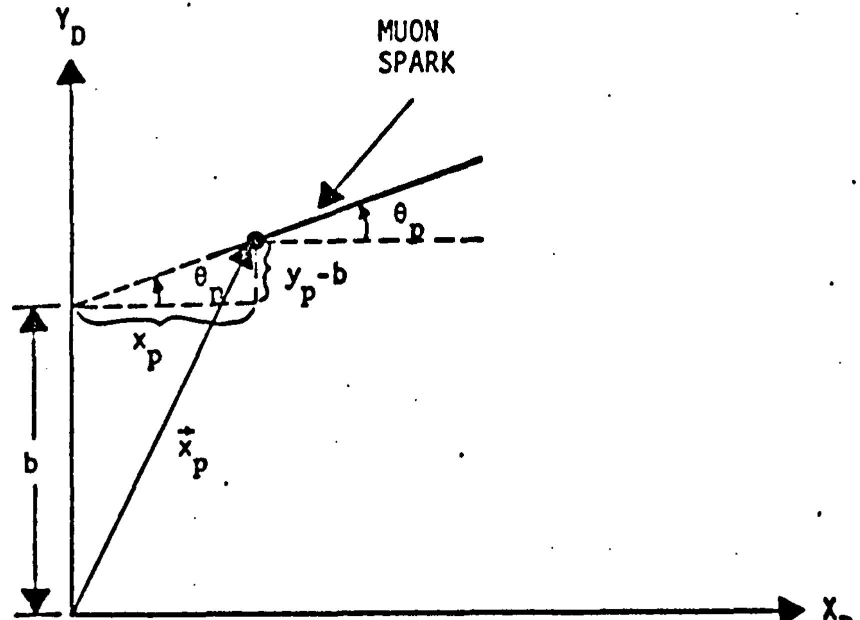

Y_D
MUON
SPARK
θ_p
θ_p
$y_p - b$
x_p
b
$\vec{x}_p$
X_D

spark in the digitizer frame, $\vec{X}_{D1}$, $\vec{X}_{D2}$, are given by

$$\vec{X}_{D1} = \vec{X}_P \tag{1}$$

$$X_{D2} = \vec{X}_P + [X_o, X_o + \mathrm{TAN}\ \theta_P] \tag{2}$$

where X_o is an arbitrary displacement. In the spectrometer frame these points are given by

$$\vec{X}_{S1} = [DS]\vec{X}_{D1} + \vec{X}_{DO} \tag{3}$$

$$\vec{X}_{S2} = [DS]\vec{X}_{D2} + \vec{X}_{DO} \tag{4}$$

where [DS] is the digitizer-to-spectrometer frame matrix given by eqs. (3.3.5.9) and (3.3.5.10). The position vector of the digitizer frame origin is given by (3.3.2.1).

3.4.5 DETERMINATION OF THE PLANE FORMED BY THE PARTICLE LINE AND THE LENS POINT

The two points on the particle line $\vec{X}_{S1}$, and $\vec{X}_{S2}$ (given by (3.4.4.3) and (3.4.4.4)) together with a lens point

$$\vec{X}_{S3} = \vec{X}_{lens} \tag{1}$$

determine a plane which contains the muon spark in real space. The two particle planes, one from the field view, the other from the no-field view, intersect along the muon trajectory in real space. The equation of a plane in three dimensions is given by

$$AX + BY + CZ = D \tag{2}$$

When the plane is determined by three points

$$\vec{X}_{S1} = [x_1, y_1, z_1]$$
$$\vec{X}_{S2} = [x_2, y_2, z_2] \qquad (3)$$
$$\vec{X}_{S3} = [x_3, y_3, z_3]$$

then the plane parameters A,B,C,D are given by

$$A = \begin{vmatrix} y_2 - y_1 & z_2 - z_1 \\ y_3 - y_1 & z_3 - z_1 \end{vmatrix}$$
$$B = \begin{vmatrix} z_2 - z_1 & x_2 - x_1 \\ z_3 - z_1 & x_3 - x_1 \end{vmatrix} \qquad (4)$$
$$C = \begin{vmatrix} x_2 - x_1 & y_2 - y_1 \\ x_3 - x_1 & y_3 - y_1 \end{vmatrix}$$

$$D = Ax_1 + By_1 + Cz_1$$

3.4.6 DETERMINATION OF THE MUON POSITION VECTOR

The muon position vector is defined to be that point in space determined by the intersection of the field view and no-field view particle planes with the center plate of a spark chamber (see Fig. 3.1). Assume that the two particle planes are given by

$$A_1X + B_1Y + C_1Z = D_1' \qquad (1)$$
$$A_2X + B_2Y + C_2Z = D_2' \qquad (2)$$

To find the point of intersection with the constant z-plane of a spark chamber middle plate, set $Z = Z_0$ in (1) and (2) to get

$$A_1X + B_1Y = D_1 \tag{3}$$

$$A_2X + B_2Y = D_2 \tag{4}$$

where

$$D_1 = D_1' - C_1Z_0 \tag{5}$$

$$D_2 = D_2' - C_2Z_0 \tag{6}$$

Now let

$$m_1 = -\frac{A_1}{B_1}; \quad b_1 = \frac{D_1}{B_1} \tag{7}$$

$$m_2 = -\frac{A_2}{B_2}; \quad b_2 = \frac{D_2}{B_2} \tag{8}$$

Thus (3) and (4) become

$$Y = m_1X + b_1 \tag{9}$$

$$Y = m_2X + b_2 \tag{10}$$

The intersection of (9) and (10) is

$$X = \frac{m_1b_2 - m_2b_1}{m_1 - m_2} \tag{11}$$

$$Y = \frac{b_2 - b_1}{m_1 - m_2} \tag{12}$$

Using eqs. (7) and (8) in (11) and (12) we may write the position vector of the muon as

$$\vec{x} = \left[\frac{B_1D_2 - B_2D_1}{A_2B_1 - A_1B_2}, \ \frac{A_2D_1 - D_2A_1}{A_2B_1 - A_1B_2}, \ Z_0\right] \tag{13}$$

3.4.7 UNIT MOMENTUM VECTOR OF THE MUON

The unit momentum vector of the muon is the downward pointing unit vector formed by the intersection of planes

(3.4.6.1) and (3.4.6.2). Normal vectors to these planes are given by

$$\vec{N}_1 = [A_1 , B_1 , C_1] \tag{1}$$

$$\vec{N}_2 = [A_2 , B_2 , C_2] \tag{2}$$

Then the unit momentum vector, $\hat{p}$, is found by

$$\hat{p} = \frac{\vec{N}_1 \times \vec{N}_2}{|\vec{N}_1 \times \vec{N}_2|} \tag{3}$$

To insure that $\hat{p}$ is downward pointing we inspect the z-component, p_z, to see if it is negative; if not the sign of $\hat{p}$ is reversed.

3.4.8 SAMPLE OF RECONSTRUCTED EVENTS

Fig. 3.12.a-i show histograms resulting from the reconstruction of a sample of 1033 muon events. Fig. 3.12.a displays the cosmic ray muon spectrum as observed by the spectrometer where the mean momentum is 15.9 GeV/c. Multiple scattering distributions in lateral displacement and scattering angle (Fig 3.12.b-e) are given for the middle spark chamber (after penetration of about 40 cm of iron) and the bottom spark chamber (after penetration of 95 cm of iron). Histograms of muon positions in the scintillator planes are shown in Fig. 3.12.f-i. The vertical dotted lines indicate the scintillator boundaries. Particles outside the scintillator edges were presumably caused by shower particles from muon collisions in the ceiling or spectrometer structure.

3.5 DETERMINATION OF THE MUON CHARGE AND MOMENTUM

Given the reconstructed muon position vector, $\vec{x}$, (eq. (3.4.6.13)) and the unit momentum vector, $\hat{p}$, (eq. (3.4.7.3)) for each of the three spark chambers we now wish to determine the muon charge and momentum.

3.5.1 MUON CHARGE DETERMINATION

In order to find the muon charge we write the unit momentum vector as

$$\frac{\vec{p}}{p} = [p_x, p_y, p_z] \tag{1}$$

FIG. 3.12.a MOMENTUM HISTOGRAM FROM A SAMPLE OF 1023 EVENTS

WEIGHT = 1023 STANDARD DEVIATION = 52.1 GeV/c MEAN = 15.9 GeV/c

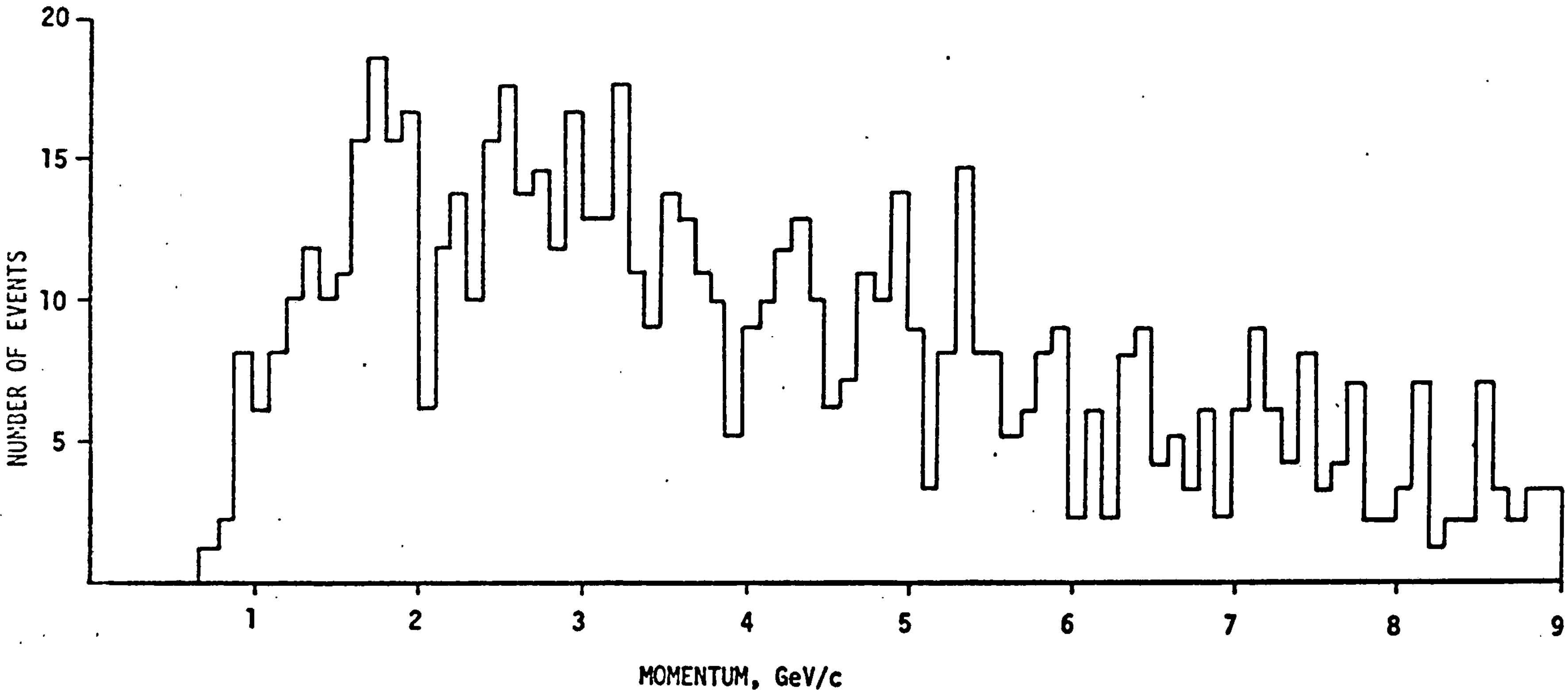

3.5.1.3

FIG 3.12.b MIDDLE CHAMBEP SCATTERING POSITION DISTRIBUTION

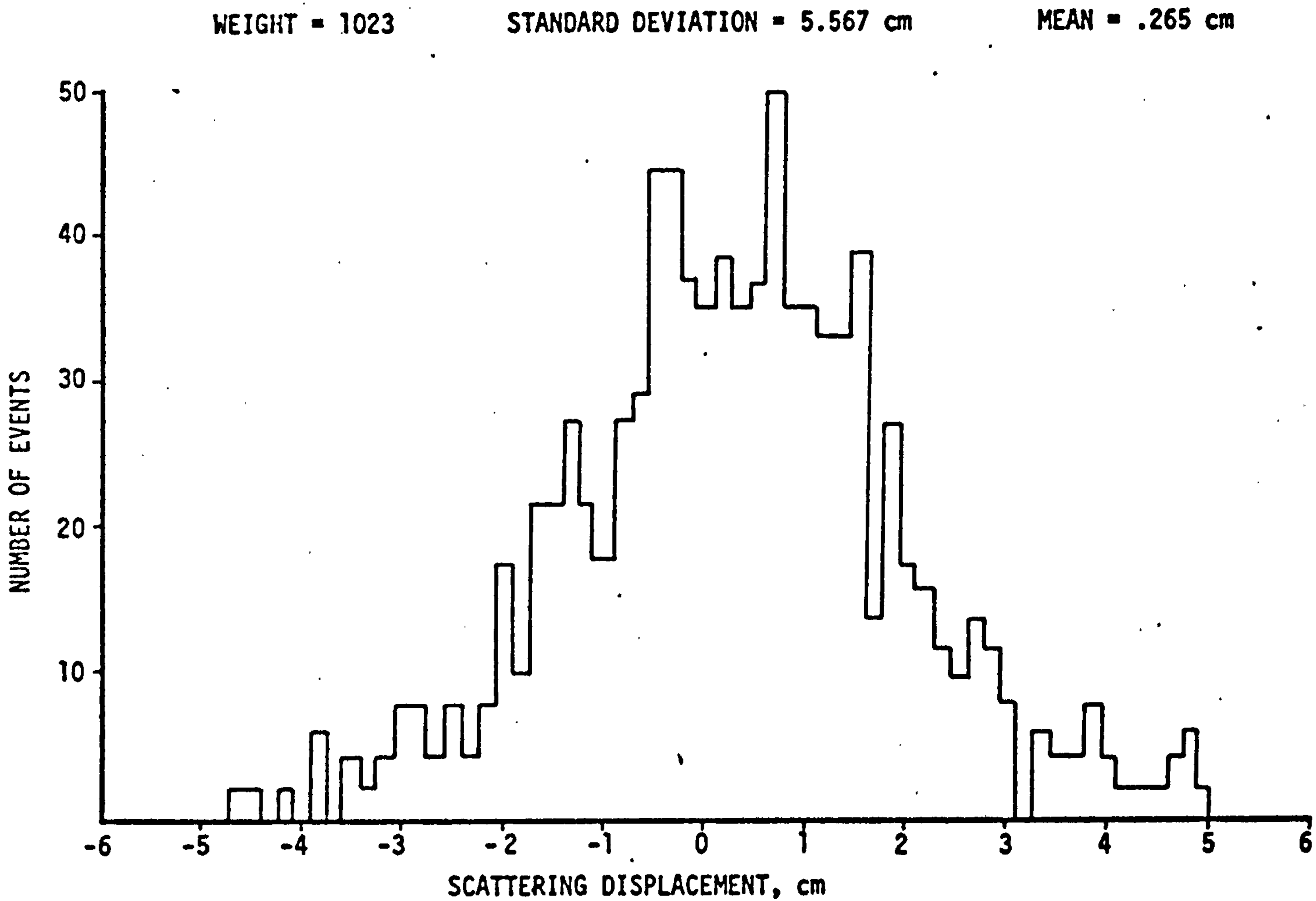
WEIGHT = 1023
STANDARD DEVIATION = 5.567 cm
MEAN = .265 cm
NUMBER OF EVENTS
50
40
30
20
10
-6
-5
-4
-3
-2
-1
0
1
2
3
4
5
6
SCATTERING DISPLACEMENT, cm

3,5,1,4

FIG. 3.12.c BOTTOM CHAMBER SCATTERING POSITION DISTRIBUTION.

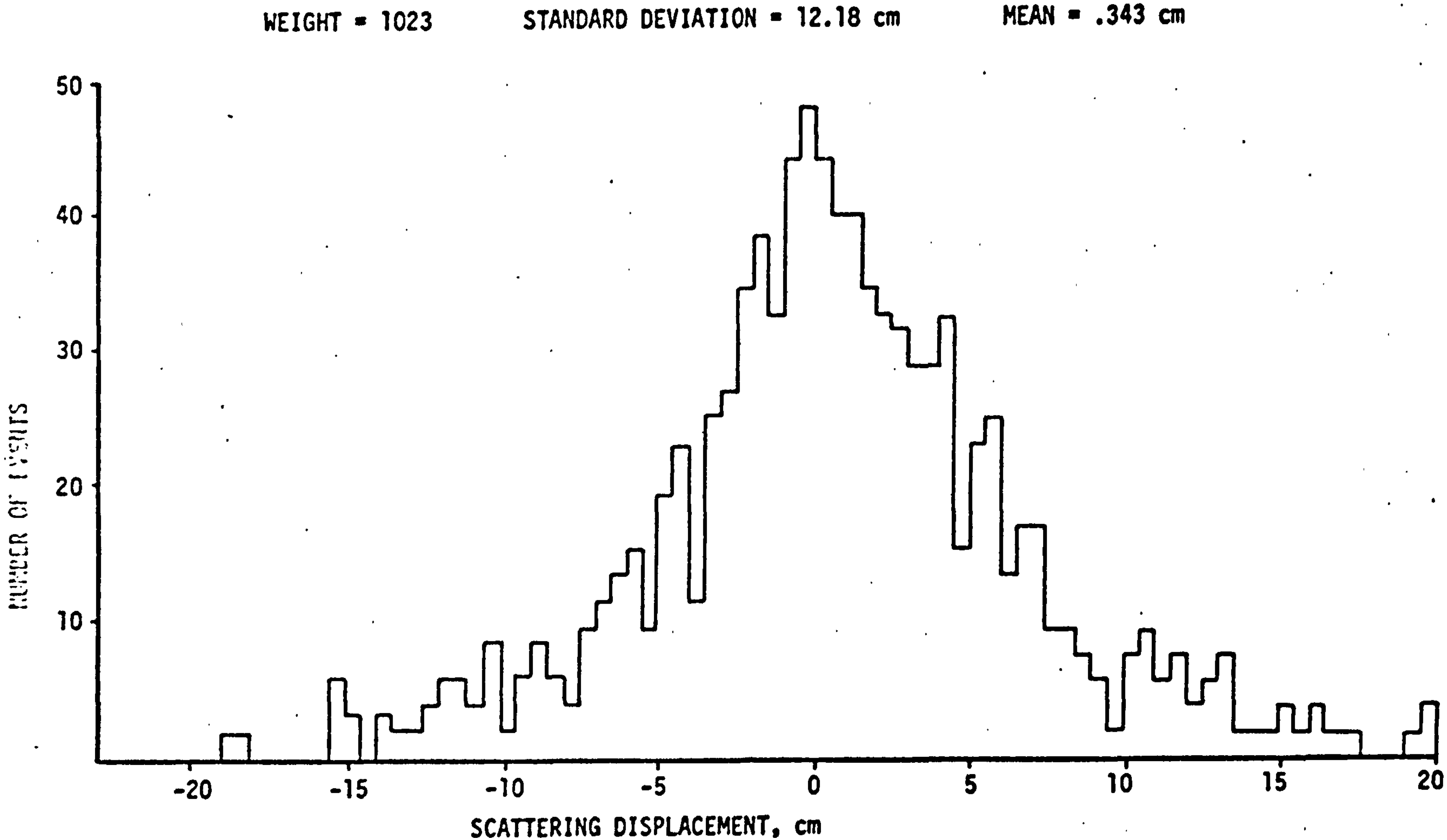
WEIGHT = 1023
STANDARD DEVIATION = 12.18 cm
MEAN = .343 cm
NUMBER OF EVENTS
50
40
30
20
10
-20
-15
-10
-5
0
5
10
15
20
SCATTERING DISPLACEMENT, cm

3.5.1.5

FIG. 3.12.d MIDDLE CHAMBER SCATTERING ANGLE DISTRIBUTION

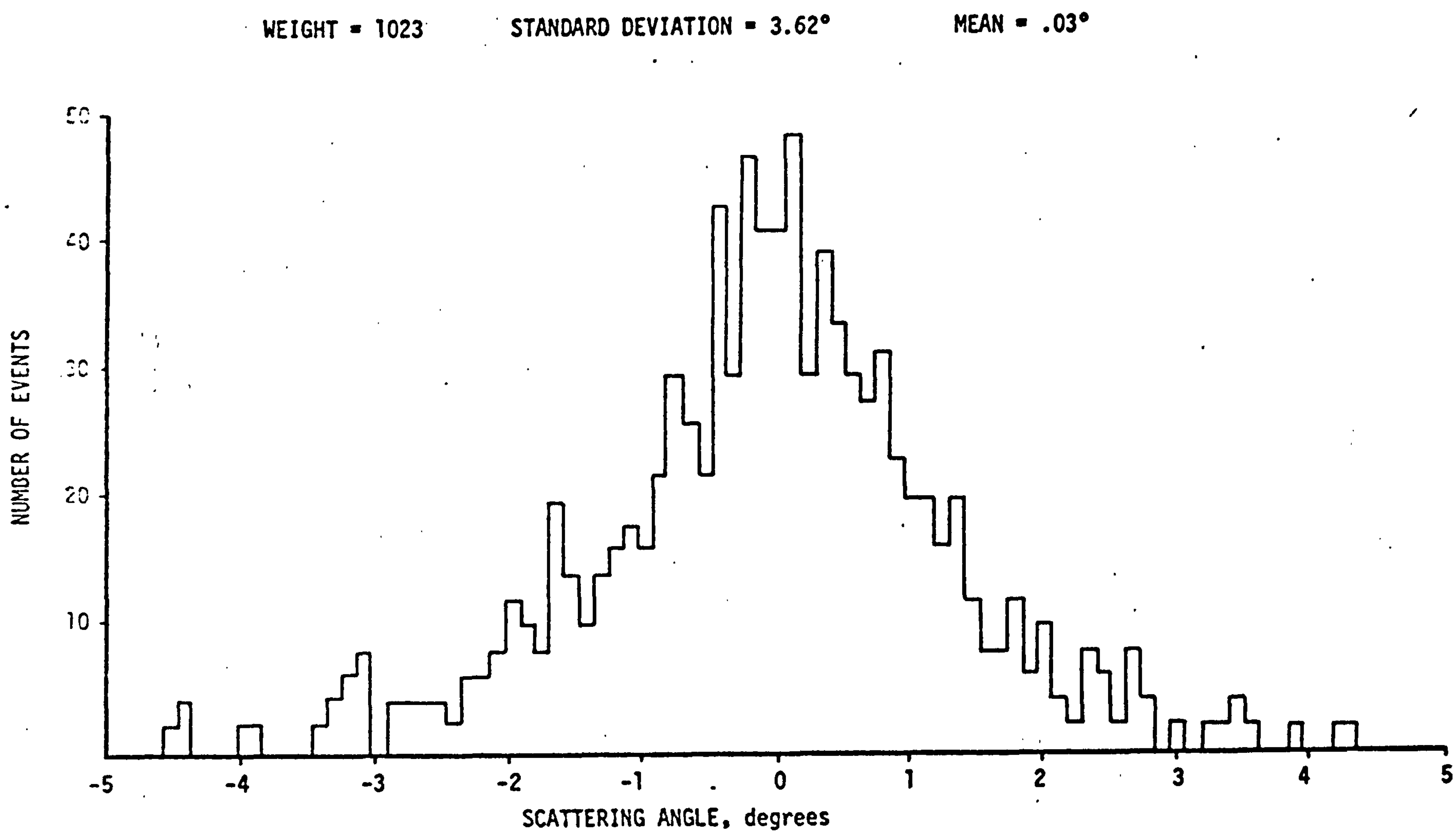
WEIGHT = 1023
STANDARD DEVIATION = 3.62°
MEAN = .03°
NUMBER OF EVENTS
50
40
30
20
10
-5
-4
-3
-2
-1
0
1
2
3
4
5
SCATTERING ANGLE, degrees

FIG. 3.12.e BOTTOM CHAMBER SCATTERING ANGLE DISTRIBUTION

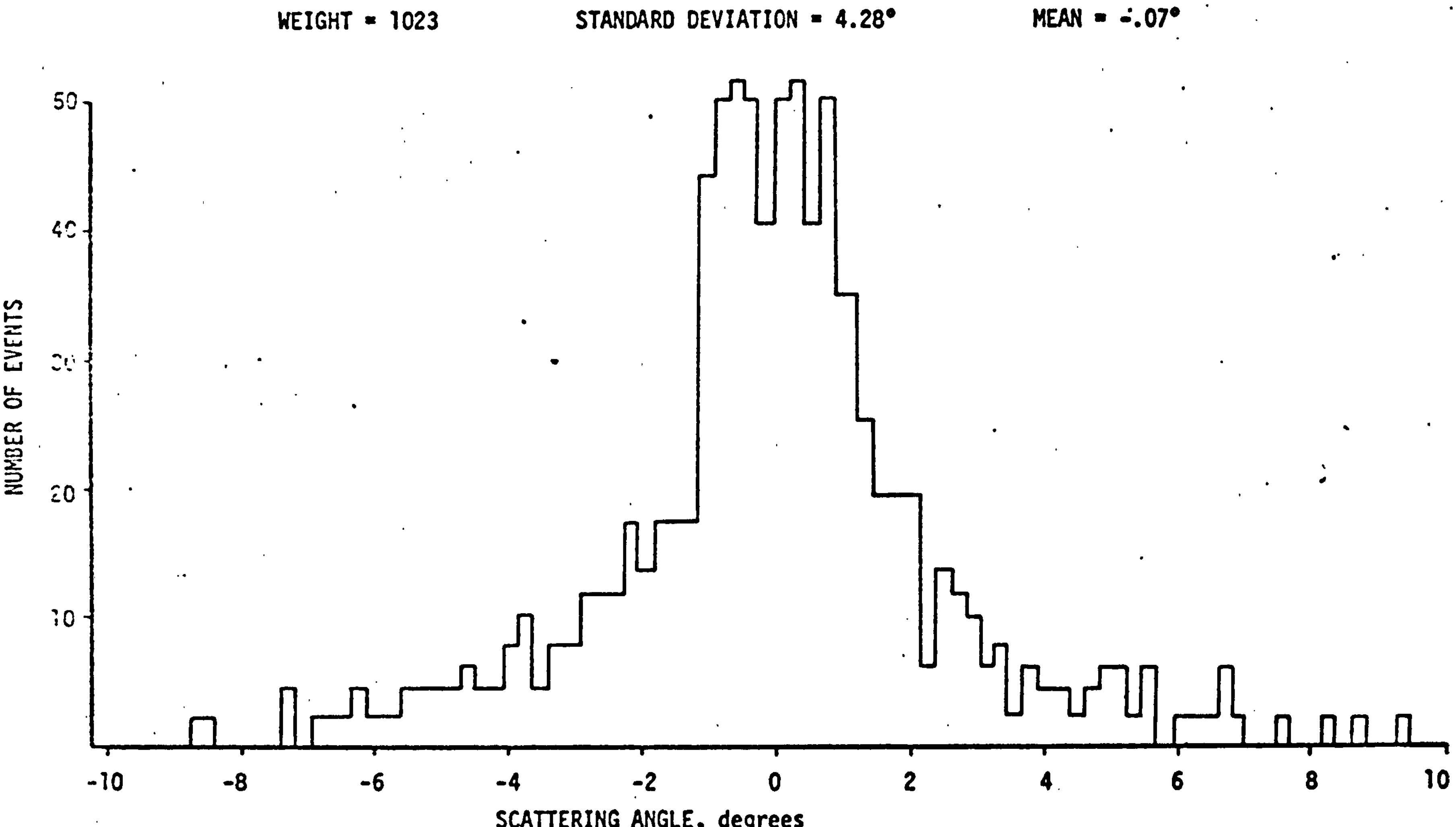

WEIGHT = 1023
STANDARD DEVIATION = 4.28°
MEAN = -.07°
NUMBER OF EVENTS
50
40
20
10
-10
-8
-6
-4
-2
0
2
4
6
8
10
SCATTERING ANGLE, degrees

3.5.1.7

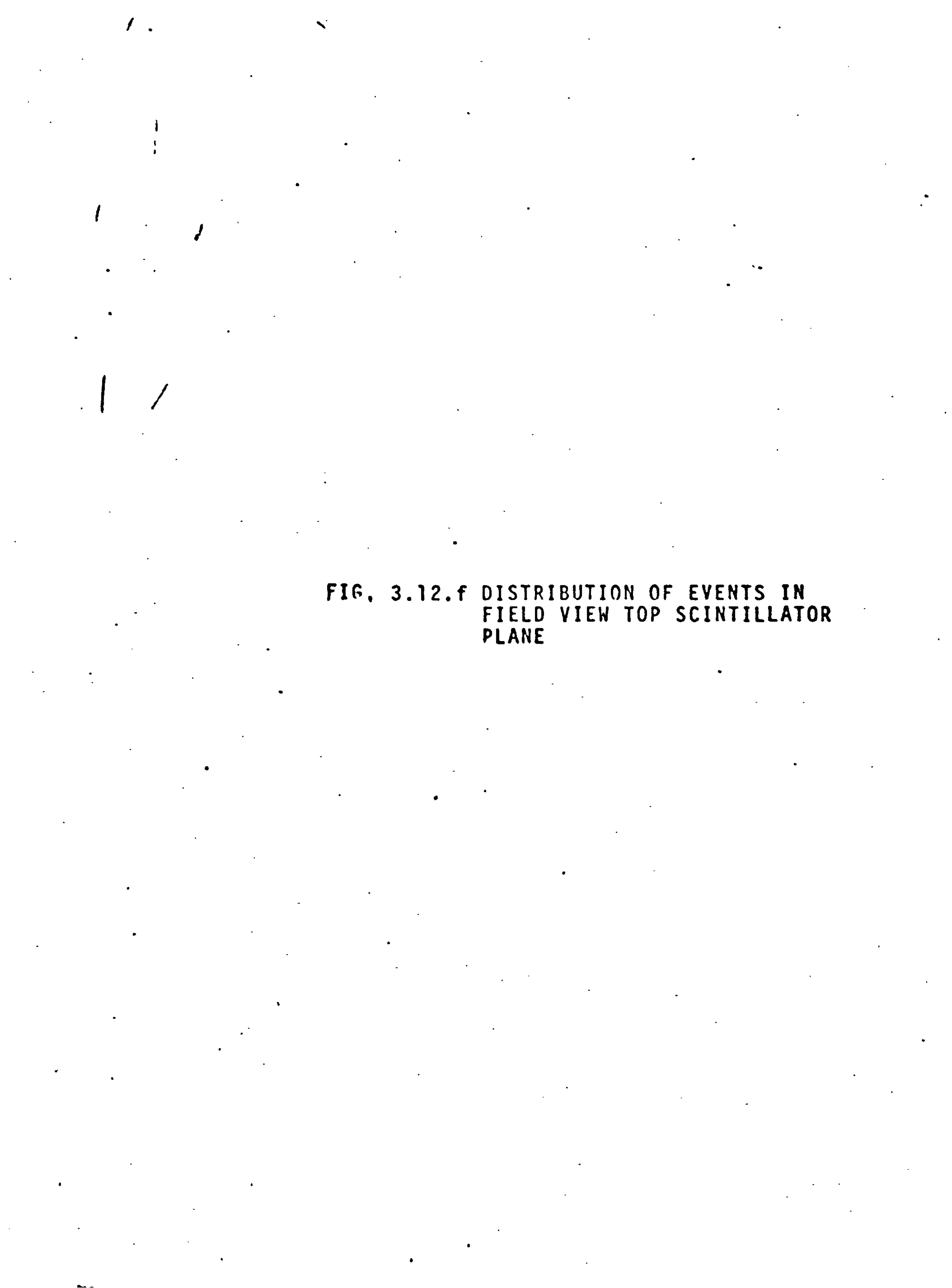

FIG. 3.12.f DISTRIBUTION OF EVENTS IN FIELD VIEW TOP SCINTILLATOR PLANE

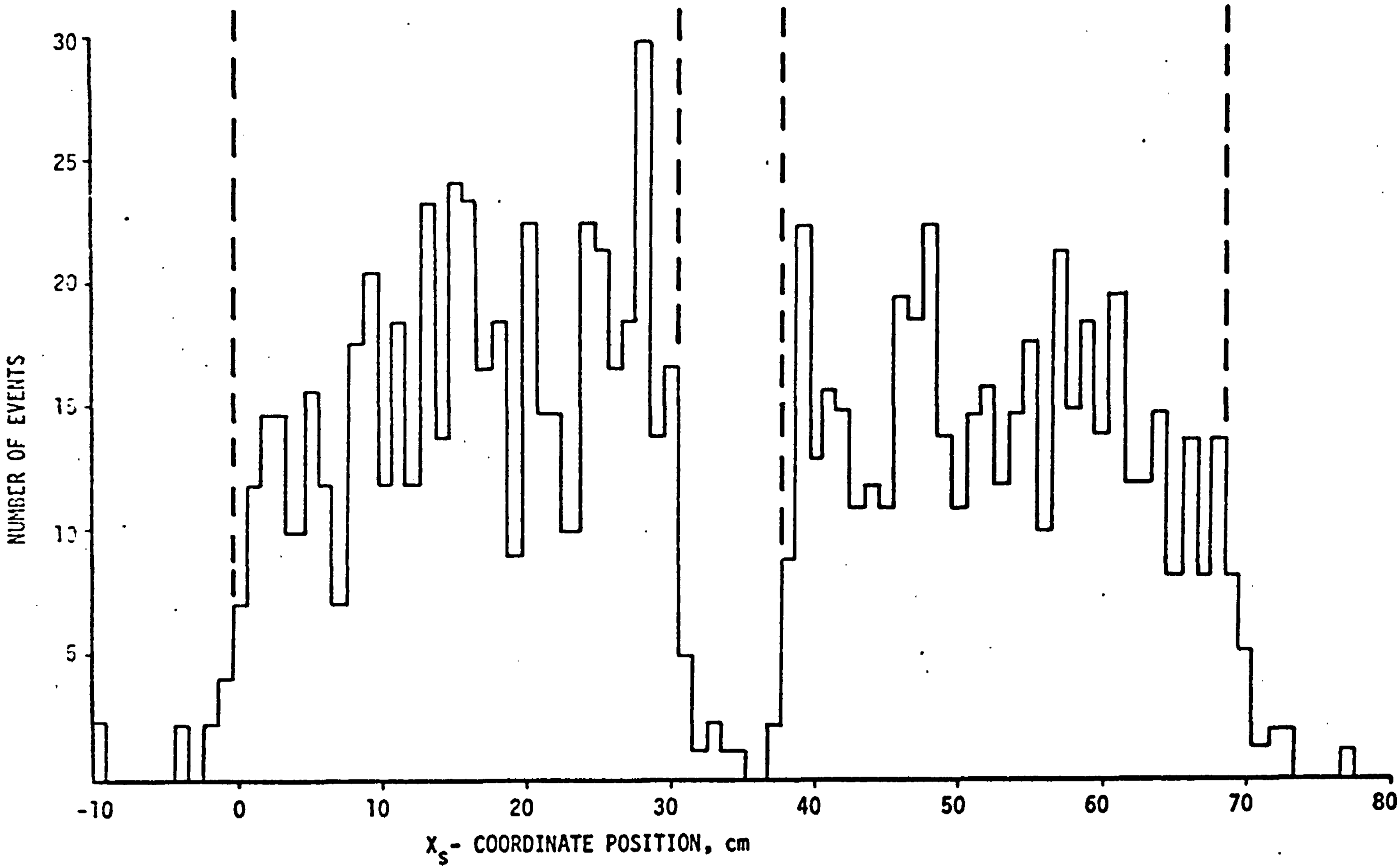

NUMBER OF EVENTS
30
25
20
15
10
5
-10
0
10
20
30
40
50
60
70
80
X_S- COORDINATE POSITION, cm

3.5.1.8

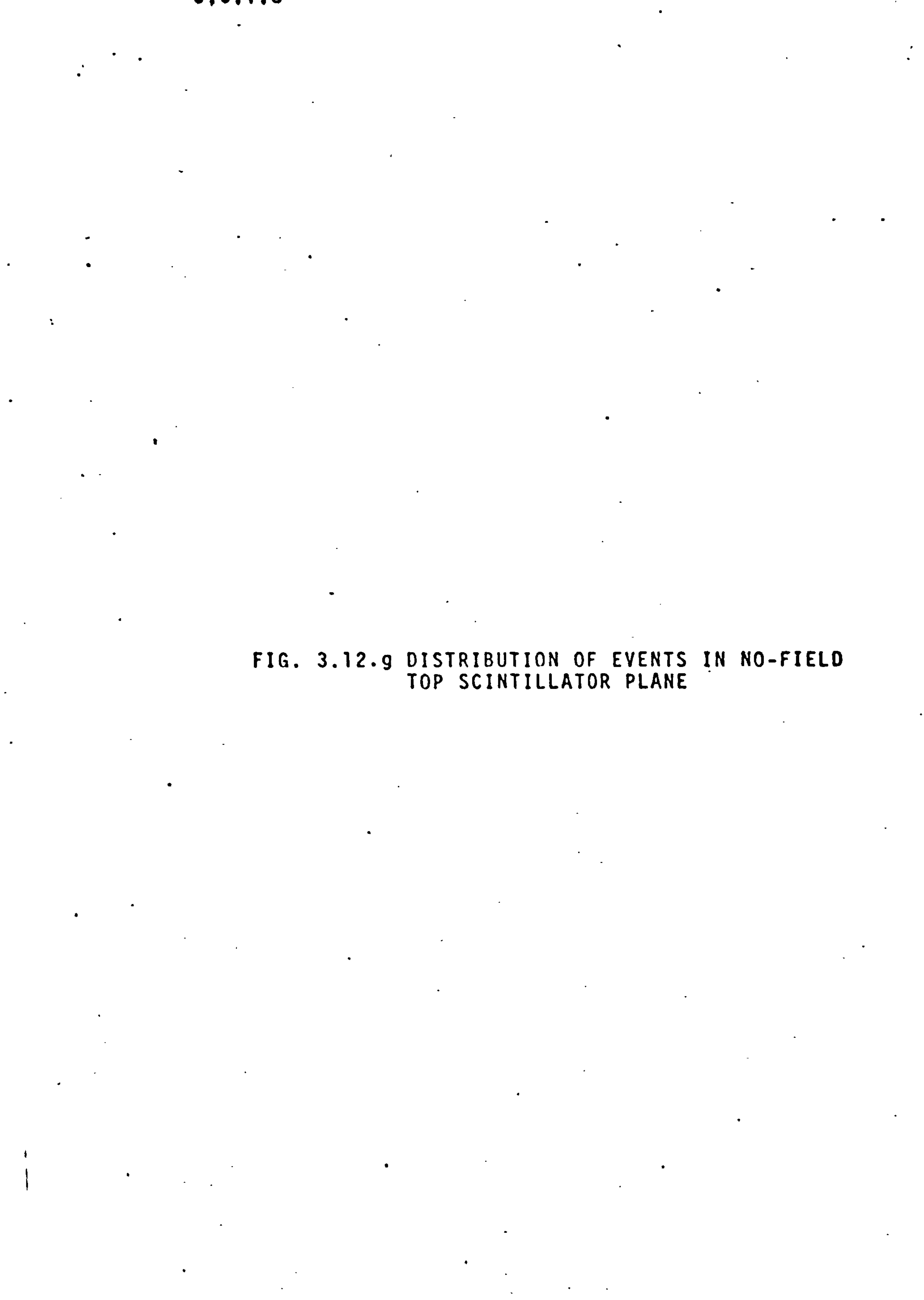

FIG. 3.12.g DISTRIBUTION OF EVENTS IN NO-FIELD TOP SCINTILLATOR PLANE

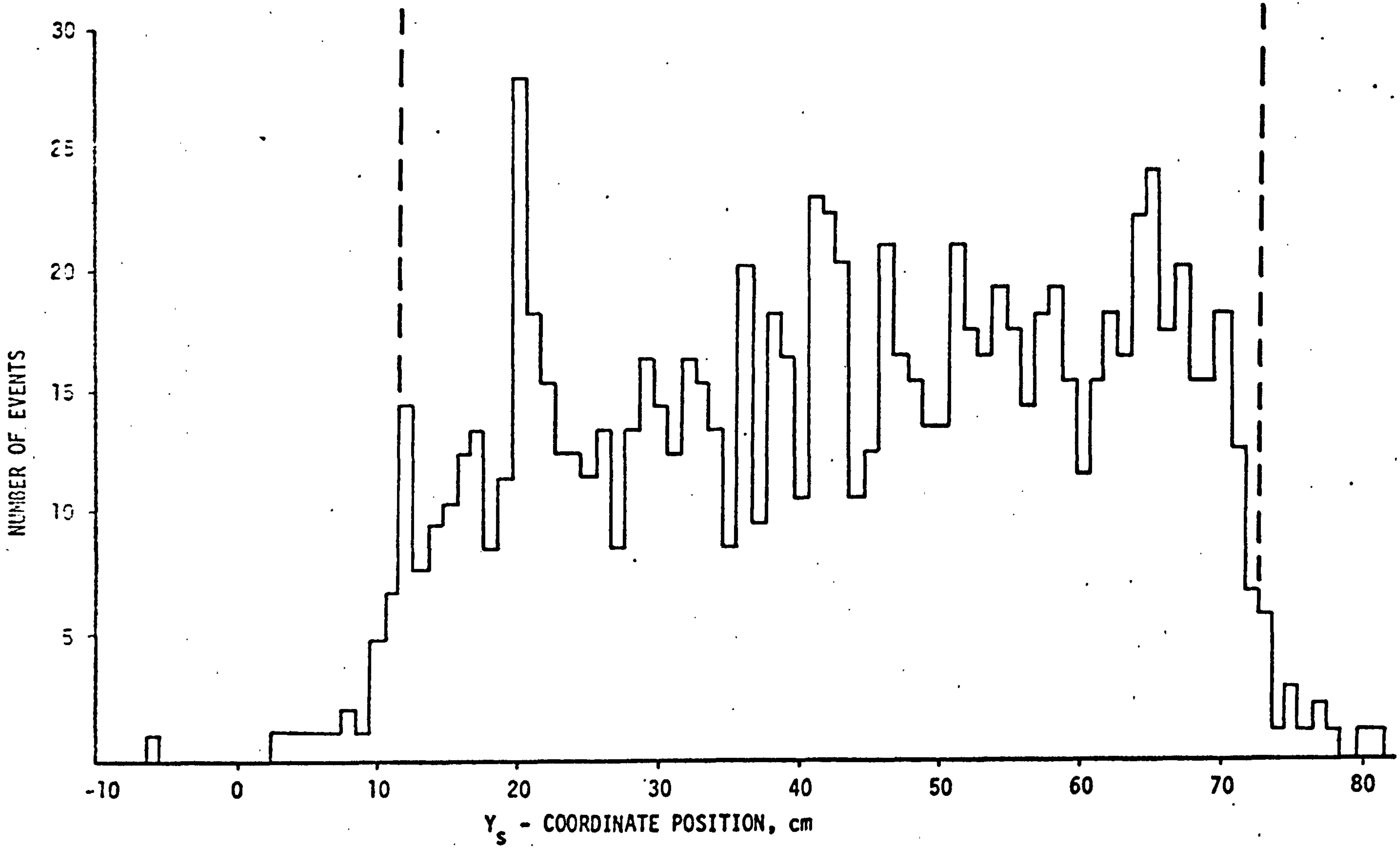

NUMBER OF EVENTS
30
25
20
15
10
5
-10
0
10
20
30
40
50
60
70
80
Y_s - COORDINATE POSITION, cm

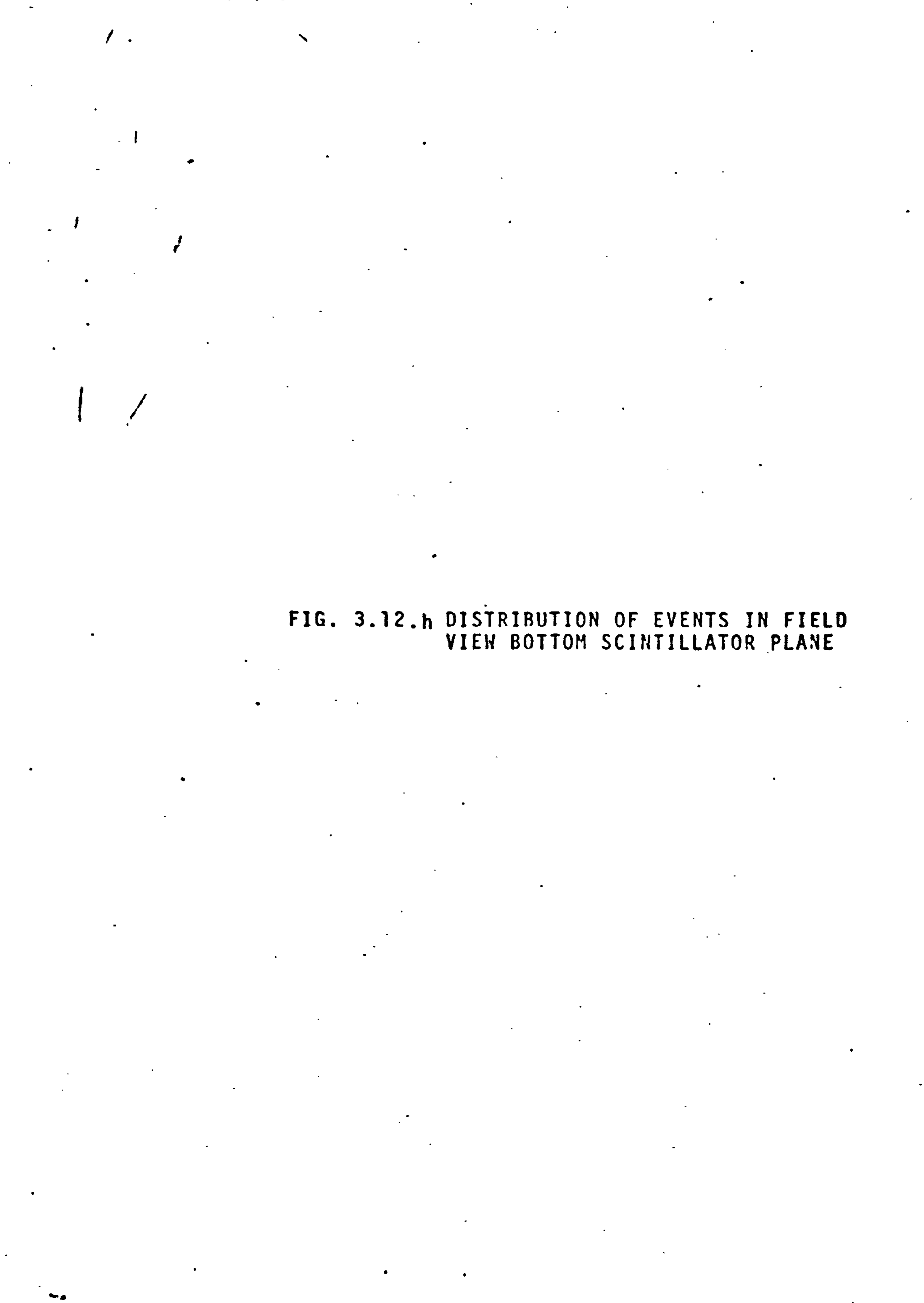

FIG. 3.12.h DISTRIBUTION OF EVENTS IN FIELD VIEW BOTTOM SCINTILLATOR PLANE

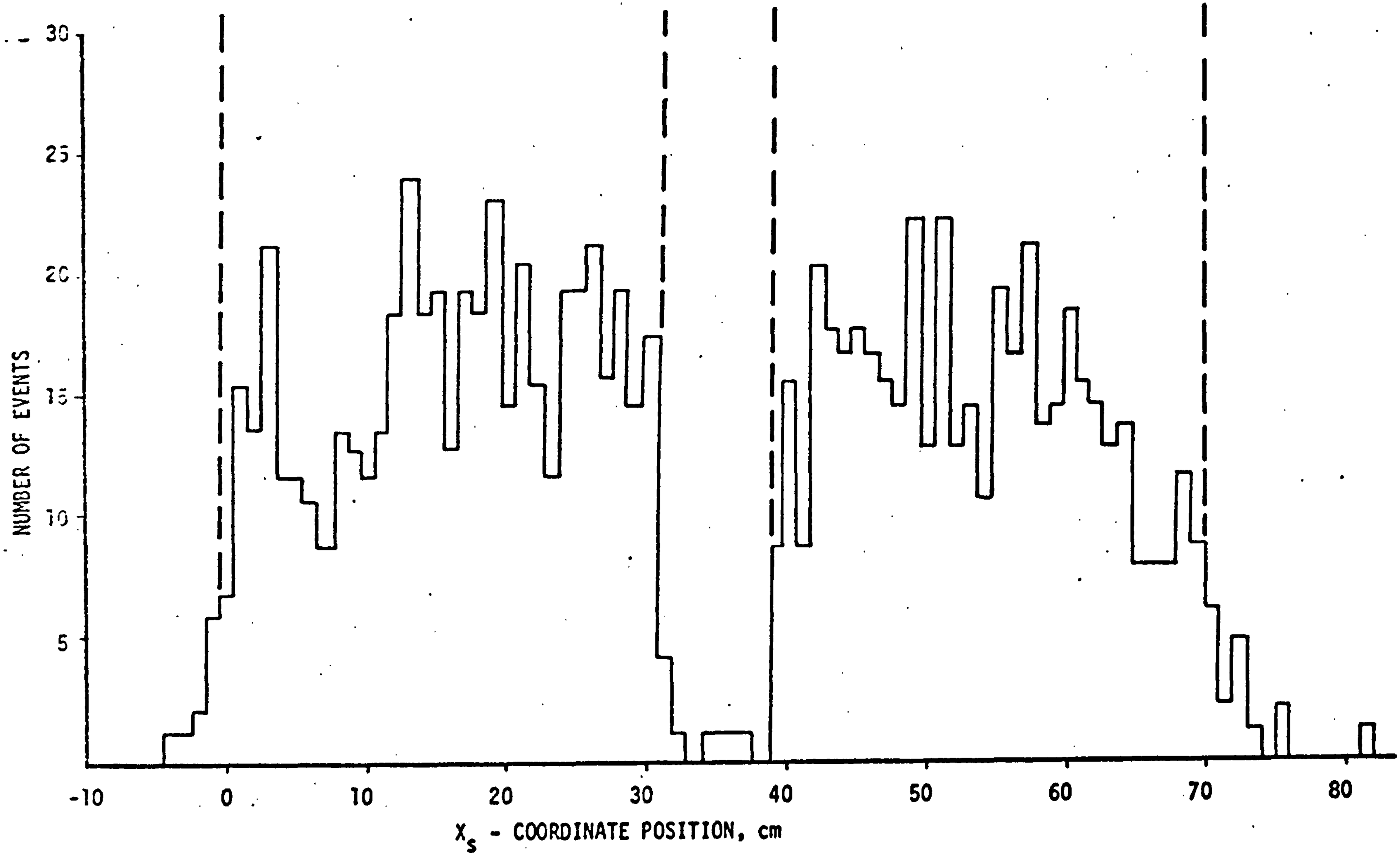
30
25
20
15
10
5
NUMBER OF EVENTS
-10
0
10
20
30
40
50
60
70
80
X_s - COORDINATE POSITION, cm

3,5,1,10

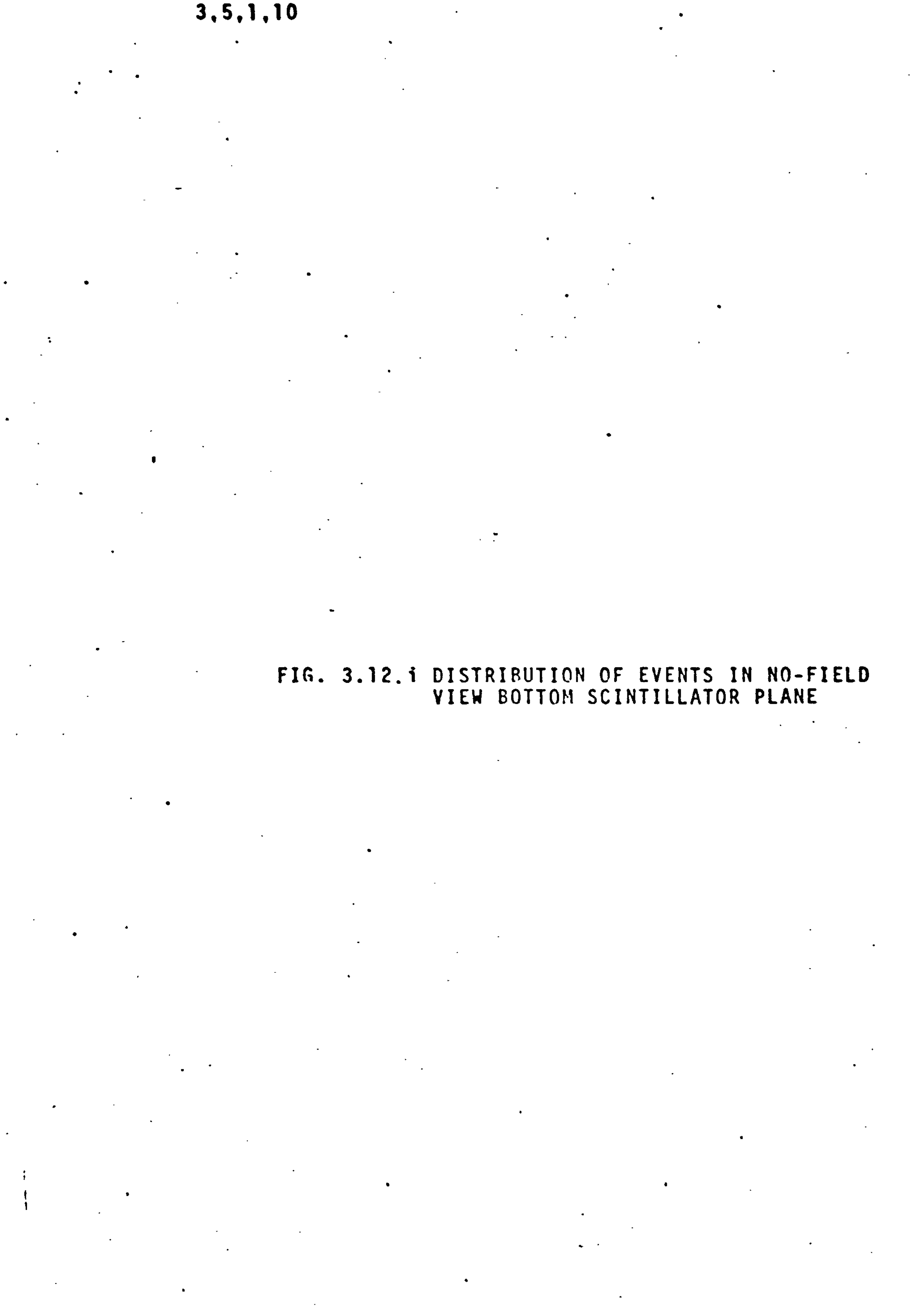

FIG. 3.12.i DISTRIBUTION OF EVENTS IN NO-FIELD
VIEW BOTTOM SCINTILLATOR PLANE

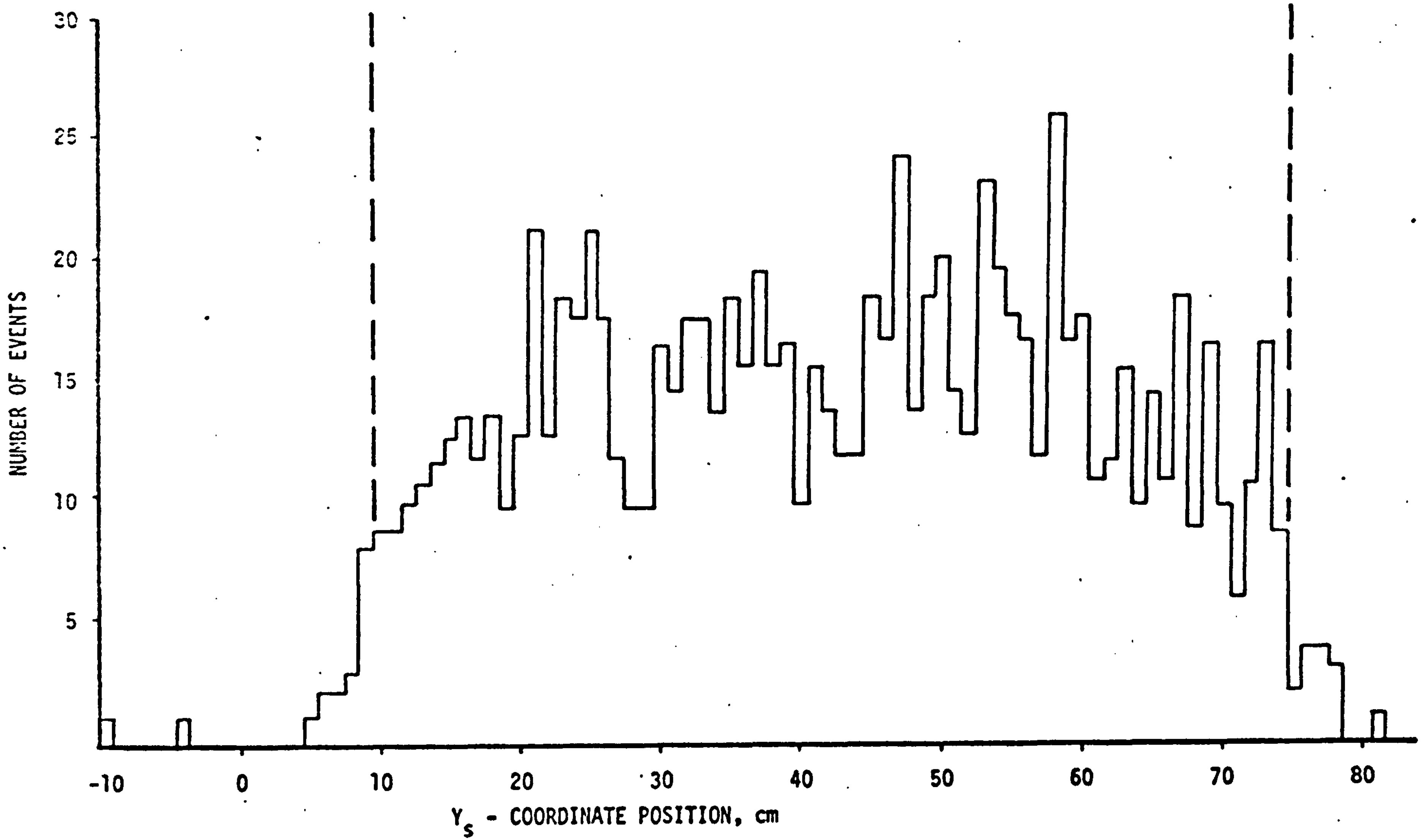

NUMBER OF EVENTS
30
25
20
15
10
5
-10
0
10
20
30
40
50
60
70
80
Y_s - COORDINATE POSITION, cm

(p is the magnitude of the momentum), and then form

$$\vec{u}_1 = [p_{x1},\ 0,\ p_{z2}] \tag{2}$$

$$\vec{u}_2 = [p_{x2},\ 0,\ p_{z2}] \tag{3}$$

where the indices "1" and "2" refer to two points along the trajectory. From Fig. 3.13 we see that $\vec{u}_1$ and $\vec{u}_2$ are vectors in the x_s-z_s plane and are thus perpendicular to the magnetic field $\vec{B} = \pm B_o\vec{j}$. $\vec{u}_1$ has the direction of the entry momentum vector of the muon and $\vec{u}_2$ has the direction of the exit momentum vector in the x_s-z_s plane. From Fig 3.13 we may easily establish that

$$\frac{\vec{u}_1 \times \vec{u}_2}{|\vec{u}_1 \times \vec{u}_2|} = -\frac{q}{|q|}\,\frac{\vec{B}}{|\vec{B}|} \tag{4}$$

If we write the sign of the charge, I_q, as

$$I_q = -\frac{q}{|q|} \tag{5}$$

so that $I_q = 1$ or -1 then

$$\frac{-(\pm B_o\vec{j})I_q}{|\pm B_o|} = \frac{(p_{z1}p_{x2}-p_{x1}p_{z2})\vec{j}}{|p_{z1}p_{x2}-p_{x1}p_{z2}|} \tag{6}$$

or finally

$$I_q = -\frac{I_u}{N_B} \tag{7}$$

where

$$I_u = \frac{p_{z1}p_{x2} - p_{x1}p_{z2}}{|p_{z1}p_{x2} - p_{x1}p_{z2}|} \tag{8}$$

FIG. 3.13 MUON CHARGE DETERMINATION

$\vec{F} = q\vec{v} \times \vec{B}$

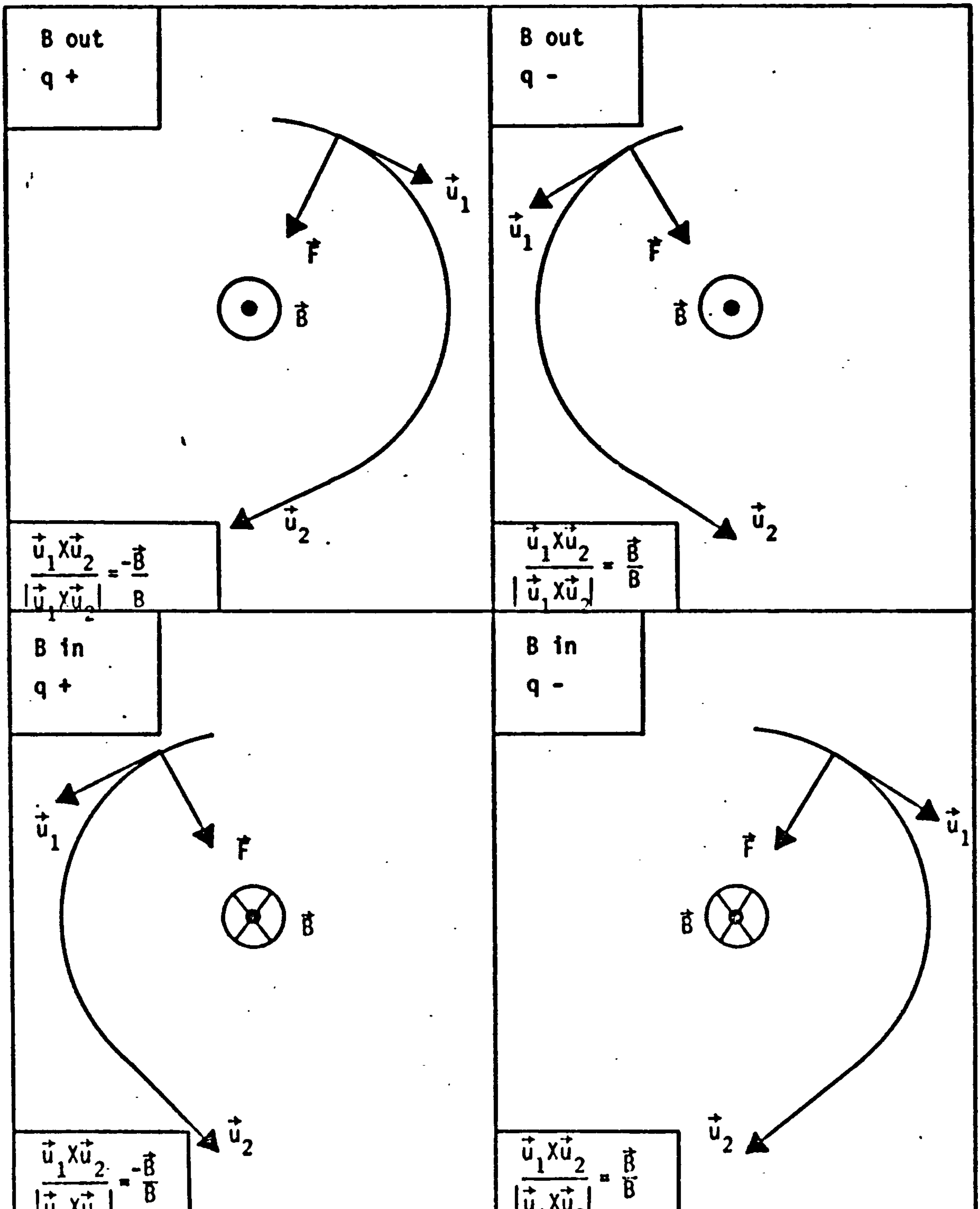

$$N_B = \pm 1, \text{ sign of the } \vec{B} \text{ field.} \tag{9}$$

Thus one uses the proper sign of the magnetic field, calculates (8) from (1) and determines the sign of the muon by (7).

3.5.2 DETERMINATION OF THE MUON MOMENTUM

In order to calculate the incident muon momentum we use the χ^2-fit technique to discover a numerically integrated muon trajectory which best fits the measured data for a single event. Thus we would like to determine a muon position vector, $\vec{x}^*$, and momentum vector, $\vec{p}^*$, (both in the top chamber) which generate a trajectory best characterizing the data. Here we use the notation

$$\vec{x}^* = [x^*, y^*, z^*] \tag{1}$$

$$\vec{p}^* = [p_x^*, p_y^*, p_z^*] \tag{2}$$

We prefer to transform the momentum vector to an equally good triple of numbers

$$(\theta_x^*, \theta_y^* , p^*) \tag{3}$$

where

$$\theta_x^* = \mathrm{TAN}^{-1}\left[\frac{p_z^*}{p_x^*}\right] \tag{4}$$

$$\theta_y^* = \mathrm{TAN}^{-1}\left[\frac{p_z^*}{p_y^*}\right] \tag{5}$$

$$p^* = [p_x^{*2} + p_y^{*2} + p_z^{*2}]^{1/2} \tag{6}$$

If we assume that the z-component of $\vec{x}^*$ (i.e. z^*) is a constant in the center plate of the top spark chamber then (1) and (2) may be written in terms of 5 parameters

$$(x^*, y^*, \theta_x^*, \theta_y^*, p^*) \qquad (7)$$

which we now write

$$\vec{A}^* = (x^*, y^*, \theta_x^*, \theta_y^*, 1/p^*) \qquad (8)$$

where we have used $1/p^*$ rather than p^* because $1/p^*$ has errors which are gaussian distributed (a prime requirement of the χ^2-fit technique). In general we shall use as fit parameters the 5-component vector

$$\vec{A} = (x_T, y_T, \theta_{xT}, \theta_{yT}, 1/p_T) \qquad (9)$$

where the subscript "T" denotes that all variables are in the top chamber. Given suitable initial values for the components of $\vec{A}$ one can approach arbitrarily close to $\vec{A}^*$ by applying the χ^2-fit to the measured data. We assume the measured parameter vector, $\vec{x}_M$, to be

$$\vec{x}_M = (x_3, y_3, \theta_{x3}, \theta_{y3}, x_2, y_2, \theta_{x2}, \theta_{y2}, x_1, y_1, \theta_{x1}, \theta_{y1}) \qquad (10)$$

where

x_i, y_i are the x and y coordinates of the muon in the ith chamber (i=1,2,3 for the bottom, middle, and top chambers respectively)

θ_{xi}, θ_{yi} are the projected angles of the muon track in the x_s-z_s and y_s-z_s planes respectively for the ith spark chamber.

From (10) it is seen that a suitable initial value of $\vec{A}$ is

$$\vec{A}^{(1)} = (x_3, y_3, \theta_{x3}, \theta_{y3}, 1/p_3) \qquad (11)$$

where

$$p_3 = \frac{.3B_0S}{\phi_B} \qquad (12)$$

Here B_0 is the magnetic field in gauss, S is the path length in cm and ϕ_B is the effective bending angle of the muon as measured in the field view. Thus, in summary, we are making an initial guess for the "state" of the muon as it enters the spectrometer, $\vec{A}^{(1)}$, and subsequently hope to find some χ^2-fitted initial muon state, $\vec{A}^*$, which best characterizes the data, eq. (10). Since there are 5 fit parameters in $\vec{A}$ and 12 measured parameters in $\vec{x}_M$ there are 7 degrees of freedom in the χ^2-fit.

We have assumed that the parameters of $\vec{x}_M$ are directly measured; however this is not strictly true. The components of $\vec{x}_M$ are "real space" variables found by reconstructing other measured variables into the spectrometer frame by the methods of Sec. 3.4. However we expect the errors in the components of $\vec{x}_M$ to be gaussian distributed. This is because coordinate variables used in the reconstruction process are measured in planes nearly parallel to the spectrometer x_s-z_s and y_s-z_s planes. However the errors in $\vec{x}_M$ include not only measurement error but also errors in the reconstruction process itself.

The fitting procedure, by which we determine $\vec{A}^*$, has been computer programmed. An outline of this program follows:

(1) Reconstruct the muon event into real space

(2) Determine the charge on the muon

(3) Make an initial guess of the muon momentum by

$$p_3 = \frac{.3B_0S}{\phi_B}$$

(4) Form the initial state of the muon in the top chamber

$$\vec{A}^{(1)} = (x_3, y_3, \theta_{x3}, \theta_{y3}, 1/p_3)$$

(5) Given the initial state of the muon, $\vec{A}^{(1)}$, integrate the muon motion through the spectrometer and subsequently obtain a calculated parameter vector

$$\vec{x}_c = (x_3, y_3, \theta_{x3}, \theta_{y3}, x_2, y_2, \theta_{x2}, \theta_{y2}, x_1, y_1, \theta_{x1}, \theta_{y1})_c$$

Here the subscript "c" on the brackets indicates that all the included variables were calculated via a trajectory algorithm (discussed in the next section).

(6) Numerically calculate derivatives of $\vec{x}_c$ with respect to $(x_3, y_3, \theta_{x3}, \theta_{y3}, 1/p_3)$ by means of the trajectory algorithm.

(7) Estimate a better value of $\vec{A}$ via the χ^2-fit method and return to step (5) if another iteration is desired (i.e. if $\vec{A}$ is not sufficiently close to $\vec{A}^*$).

We see that the heart of the muon momentum determination program is the trajectory algorithm by which the muon motion is numerically integrated through a computer model of the spectrometer. This trajectory algorithm is discussed in the following section.

3.5.2.1 NUMERICAL INTEGRATION OF THE MUON TRAJECTORY THROUGH THE SPECTROMETER

A typical trajectory of a muon passing through the spectrometer is shown in Fig. 3.14. Neglecting multiple scattering it is possible to completely generate such a trajectory if the incoming state $(\vec{x}_T, \vec{p}_T)$ of the muon is known. Given $(\vec{x}_T, \vec{p}_T)$ the computer program TRAJEC is designed to calculate the muon trajectory through the spectrometer. Fig. 3.15 is a flowchart of this program which saves the muon state vector $(\vec{x}, \vec{p})$ for 5 points inside the spectrometer:

1) $\vec{x}_T, \vec{p}_T$ top spark chamber
2) $\vec{x}_{s1}, \vec{x}_{s1}$ top scintillator
3) $\vec{x}_m, \vec{p}_m$ middle spark chamber
4) $\vec{x}_{s2}, \vec{x}_{s2}$ bottom scintillator
5) $\vec{x}_B, \vec{p}_B$ bottom spark chamber

From Fig. 3.15 we see that TRAJEC requires (a) an extrapolator (translates the muon along the momentum vector to a desired z_s-plane in the absence of magnetic iron), and (b) an integrator (which integrates the relativistic equation of motion of the muon in iron). Before examining (a) and (b) we need to be able to transform the muon

FIG. 3.14 TYPICAL MUON TRAJECTORY IN THE SPECTROMETER

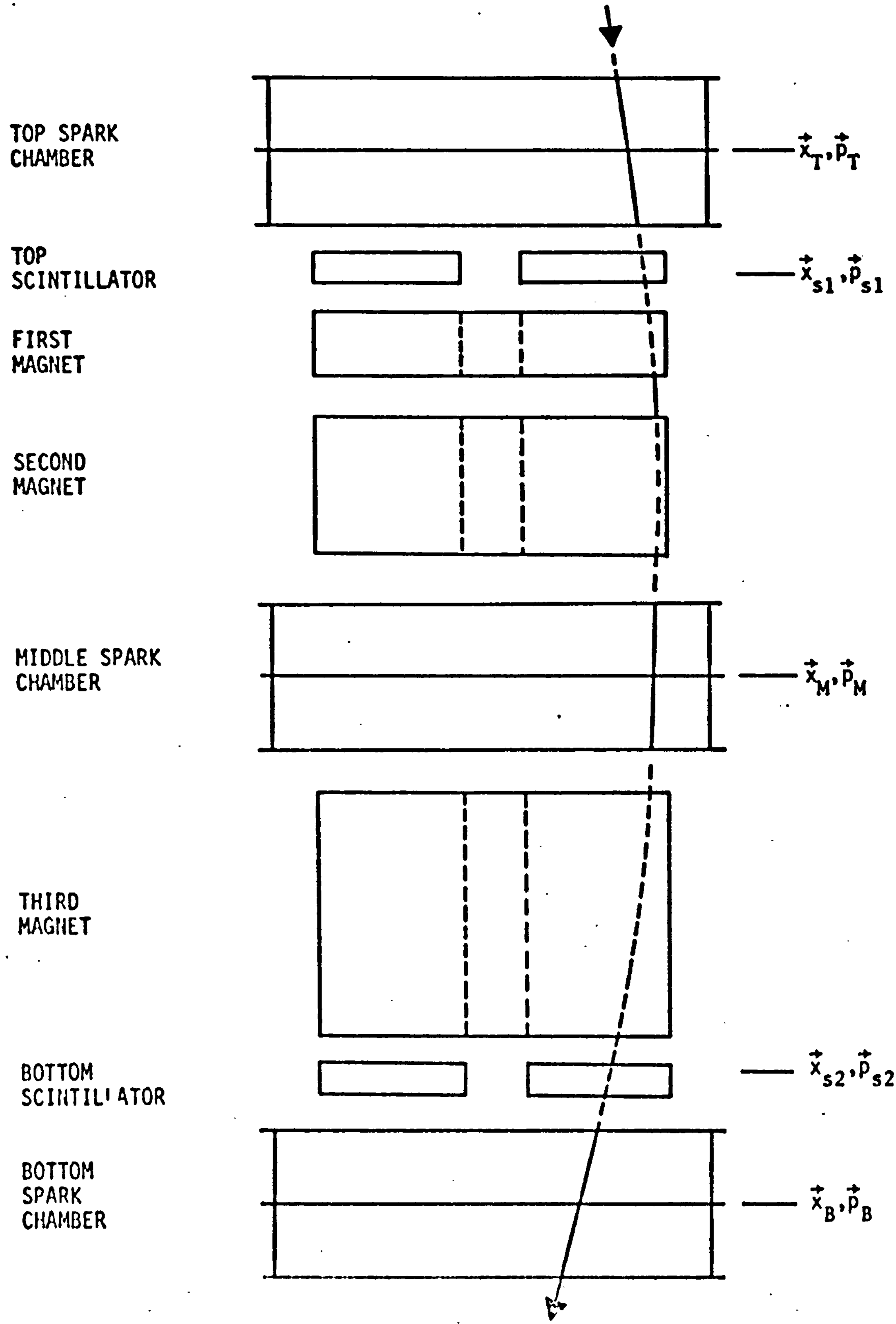
TOP SPARK CHAMBER
$\vec{x}_T, \vec{p}_T$
TOP SCINTILLATOR
$\vec{x}_{s1}, \vec{p}_{s1}$
FIRST MAGNET
SECOND MAGNET
MIDDLE SPARK CHAMBER
$\vec{x}_M, \vec{p}_M$
THIRD MAGNET
BOTTOM SCINTILLATOR
$\vec{x}_{s2}, \vec{p}_{s2}$
BOTTOM SPARK CHAMBER
$\vec{x}_B, \vec{p}_B$

FIG. 3.15 FLOWCHART OF THE PROGRAM 'TRAJEC'

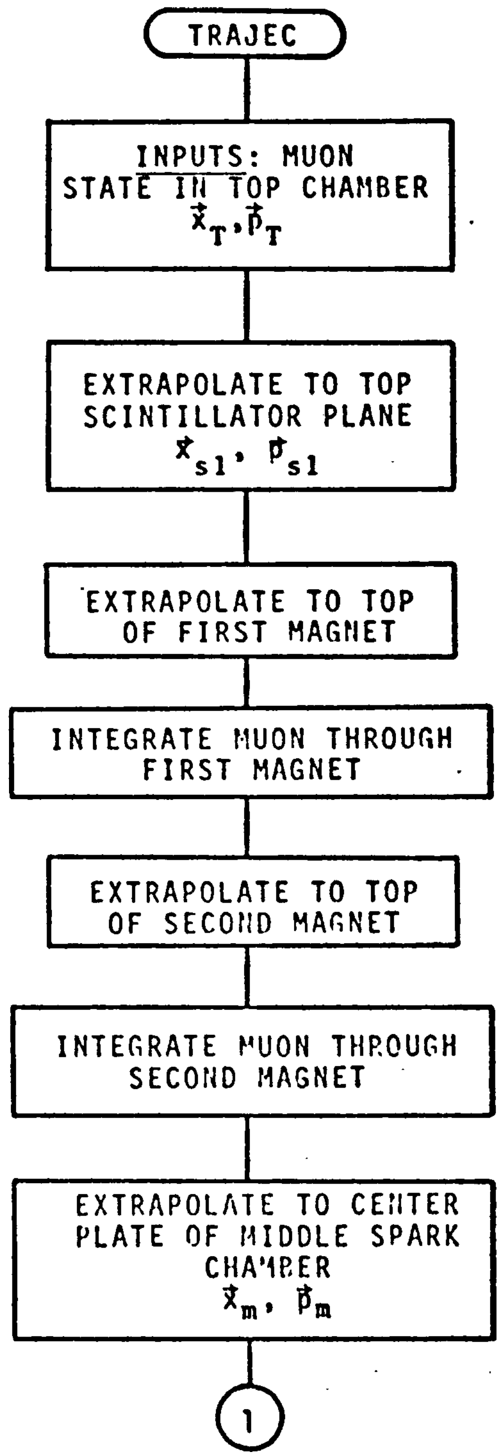
TRAJEC
INPUTS: MUON STATE IN TOP CHAMBER $\vec{x}_T, \vec{p}_T$
EXTRAPOLATE TO TOP SCINTILLATOR PLANE $\vec{x}_{s1}, \vec{p}_{s1}$
EXTRAPOLATE TO TOP OF FIRST MAGNET
INTEGRATE MUON THROUGH FIRST MAGNET
EXTRAPOLATE TO TOP OF SECOND MAGNET
INTEGRATE MUON THROUGH SECOND MAGNET
EXTRAPOLATE TO CENTER PLATE OF MIDDLE SPARK CHAMBER $\vec{x}_m, \vec{p}_m$
1

FIG. 3.15 FLOWCHART OF THE PROGRAM 'TRAJEC' (CONT.)

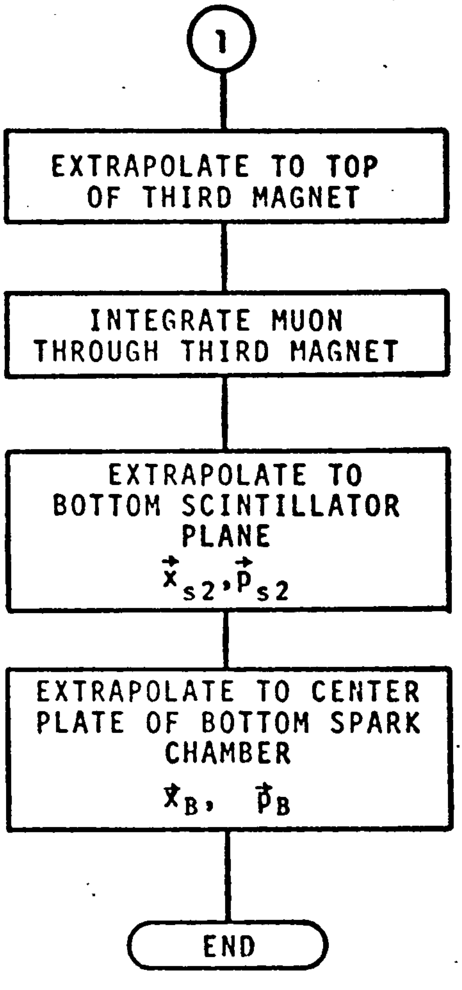
1
EXTRAPOLATE TO TOP OF THIRD MAGNET
INTEGRATE MUON THROUGH THIRD MAGNET
EXTRAPOLATE TO BOTTOM SCINTILLATOR PLANE
$\vec{x}_{s2}, \vec{p}_{s2}$
EXTRAPOLATE TO CENTER PLATE OF BOTTOM SPARK CHAMBER
$\vec{x}_B, \vec{p}_B$
END

state $\vec{A}$ in the top chamber into a position vector, $\vec{x}_T$, and momentum vector, $\vec{p}_T$. For the position vector, since $\vec{A} = (x, y, \theta_x, \theta_y, 1/p)$, we find

$$\vec{x}_T = (x, y, z_T) \tag{1}$$

where z_T is the z_s-coordinate of the top spark chamber. The momentum vector is obtained by noticing that $\vec{p}$ is the intersection of the plane ABO and BCO in Fig. 3.16.a. The cross product of the normals to these planes is in the direction of $\vec{p}$:

$$\frac{\vec{p}}{p} = \frac{n_x X\ \hat{n}_y}{|\hat{n}_x x\ \hat{n}_y|} \tag{2}$$

where $\hat{n}_x$ is normal to plane ABO and $\hat{n}_y$ is normal to plane BCO. From Fig. 3.16.b we see that

$$\hat{n}_x = [-\mathrm{SIN}\ \theta_x,\ 0,\ \mathrm{COS}\ \theta_x] \tag{3}$$

$$\hat{n}_y = [0,\ -\mathrm{SIN}\ \theta_y,\ \mathrm{COS}\ \theta_y] \tag{4}$$

Thus eq. (2) becomes

$$\frac{\vec{p}}{p} = \frac{-[\mathrm{COS}\,\theta_x \mathrm{SIN}\theta_y,\ \mathrm{SIN}\theta_x \mathrm{COS}\theta_y,\ \mathrm{SIN}\theta_x \mathrm{SIN}\theta_y]}{[\mathrm{SIN}^2\theta_y + \mathrm{SIN}^2\theta_x \mathrm{COS}^2\theta_y]^{1/2}} \tag{5}$$

Eq. (5) is the unit momentum vector of the muon; the momentum vector itself can be found by using the fact that $A_5 = 1/p$. The minus sign in (5) insures that $\vec{p}$ will always point downward into the spectrometer.

In order to extrapolate the muon position to some desired z -coordinate, z', we write the unit momentum

FIG. 3.16.a PROJECTED ANGLES OF THE MUON MOMENTUM VECTOR

FIG. 3.16.b DETERMINATION OF THE NORMAL VECTORS $\hat{n}_x$ AND $\hat{n}_y$

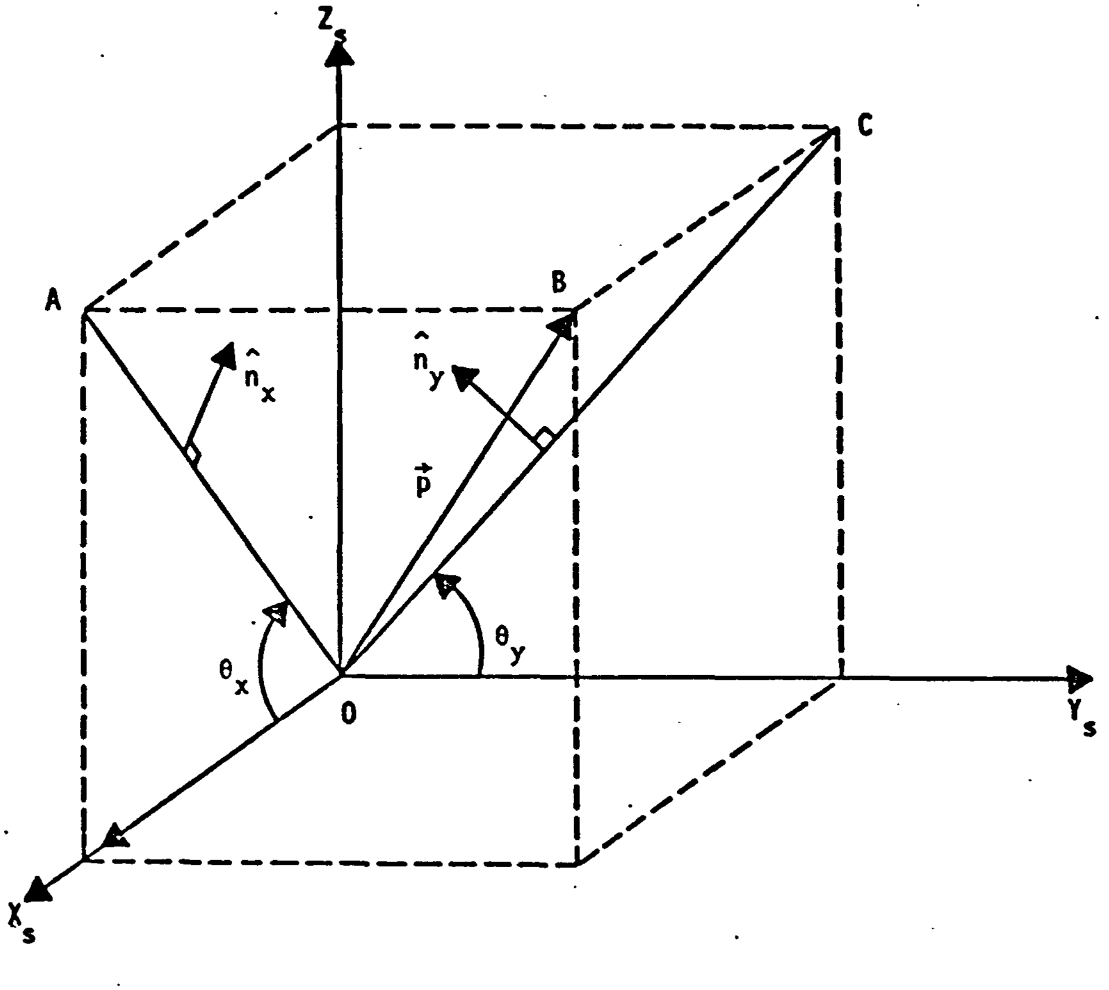

Z_s
A
B
C
$\hat{n}_x$
$\hat{n}_y$
$\vec{p}$
θ_x
θ_y
0
Y_s
X_s

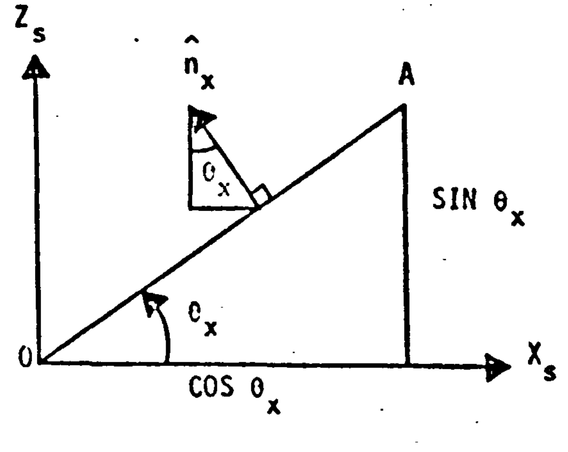

Z_s
$\hat{n}_x$
A
θ_x
SIN θ_x
θ_x
0
X_s
COS θ_x

vector as

$$\hat{u} = \frac{\vec{p}}{p} = [u_x, u_y, u_z] \qquad (6)$$

Now define the desired z_s-axis position delta to be

$$\Delta z = z' - z \qquad (7)$$

where z is the present z-axis position, and z' is the desired z-axis position. Then the extrapolated position vector $\vec{x}'$ is just

$$\vec{x}' = \vec{x} + \Delta z \frac{\hat{u}}{u_z} \qquad (8)$$

We now turn our attention to the muon motion in magnetic iron. Since the motion is relativistic we shall need the following

<u>FOUR-POSITION</u>

$$r_\mu = [\vec{r}, ict] \qquad (9)$$

<u>FOUR-VELOCITY</u>

$$u_\mu = \gamma[\vec{v}, ic] \quad ; \gamma = 1/(1-\beta^2)^{1/2} \ ; \ \beta = \frac{v}{c} \qquad (10)$$

<u>FOUR-MOMENTUM</u>

$$p_\mu = [\gamma m_0 \vec{v}, \frac{i\gamma m_0 c^2}{c}] \qquad (11)$$

$$p_\mu = [\vec{p}, iE/c] \qquad (12)$$

where

$$p = \gamma m_0 \vec{v} \qquad (13)$$

$$E = \gamma m_0 c^2 = \sqrt{E_0{}^2 + p^2 c^2} \ ; \ E_0 = m_0 c^2 \qquad (14)$$

Here all the usual definitions hold

$\vec{r}$ = position

t = time

$\vec{v}$ = velocity

p = momentum

E = energy

The equation of motion of a charged particle in a B-field is given by

$$\left.\frac{d\vec{p}}{dt}\right|_B = \frac{q}{c}\vec{v} \times \vec{B} \tag{15}$$

From (13) we can show that

$$\vec{v} = \frac{c^2\vec{p}}{E} \tag{16}$$

so that (15) becomes

$$\left.\frac{dp}{dt}\right|_B = \frac{qc}{E}\,\vec{p} \times \vec{B} \tag{17}$$

Because of collisions inside the iron we expect the charged particle to undergo momentum loss, hence we write

$$\left.\frac{dp}{dt}\right|_{COL} = \left[-\frac{dp}{ds}\right]\frac{d\vec{s}}{dt} = -\rho\,\frac{dp}{dx}\,\vec{v} \tag{18}$$

where ρ is the density of iron. Use (16) in (18) to get

$$\left.\frac{d\vec{p}}{dt}\right|_{COL} = -\rho\left(\frac{dp}{dx}\right)\frac{c^2}{E}\vec{p} \tag{19}$$

Finally the equation of motion of the muon in iron is

$$\frac{d\vec{p}}{dt} = \left.\frac{d\vec{p}}{dt}\right|_B + \left.\frac{d\vec{p}}{dt}\right|_{COL} \tag{20}$$

$$\frac{d\vec{p}}{dt} = \frac{qc}{E}\,\vec{p} \times \vec{B} - \rho\left(\frac{dp}{dx}\right)\frac{c^2}{E}\,\vec{p} \qquad (21)$$

where

$$E = p^2c^2 + m_o^2c^4 \qquad (21)'$$

Thus (21) accounts for magnetic bending and momentum loss (due to Coulomb collisions) but does not account for multiple scattering. Since multiple scattering is a random process we cannot predict how it will affect a single trajectory and we will therefore not attempt to correct for it here.

The muon relativistic equation of motion (21) is integrated numerically by the Adams-Moulton[10] scheme which we write in terms of our own notation

$$x_{n+1} = x_n + \frac{\Delta t}{24}(55\dot{x}_n - 59\dot{x}_{n-1} + 37\dot{x}_{n-2} - 9\dot{x}_{n-3}) \qquad (22)$$

$$x_{n+1} = x_n + \frac{\Delta t}{24}(9\dot{x}_{n+1} + 19\dot{x}_n - 5\dot{x}_{n-1} + \dot{x}_{n-2}) \qquad (23)$$

Here the subscript "n" denotes "nth past value"; thus n = 1 corresponds to the first past value, n = 2 the second, etc. We execute eqs. (22) and (23) iteratively with some arbitrary time step Δt between iterations. Eq. (22) is called a "predictor" while (23) is a "corrector". Thus (22) may be used to estimate x_{n+1} and (23) applies a smaller final correction. However the true value of x_{n+1} lies somewhere between (22) and (23). By reducing the step size one finds that the results of (22) and (23) become arbitrarily close; hence if Δt is sufficiently small we do not need to use (23) at all. Thus by reducing Δt one can use the Adams-Moulton scheme to estimate the error in the resultant integration. Further, if Δt is small enough, one can reduce the computer time by a factor of 2 by not executing (23) since (22) is sufficiently accurate.

A single iteration in the integration of the muon equation of motion (21) is executed thus by:

$$\vec{p} = \int \dot{\vec{p}}\,dt + \vec{p}_0 \tag{24}$$

$$\vec{v} = \frac{c^2}{E}\,\vec{p} \tag{25}$$

$$\vec{x} = \int \vec{v}\,dt + \vec{x}_0 \tag{26}$$

where the integrations are performed by (22) and (23). The iteration of (24) - (26) is repeated until the bottom of a magnet section is reached.

In order to integrate eq. (21) a knowledge of the momentum loss for muons in iron is required. Fig. 3.16 shows the dependence of the energy loss rate on energy. Values of energy loss were taken from Barkus and Berger[11] for $E < 5$ GeV/c, while values above 5 GeV/c were found by extrapolating the above data according to the equation[12]

FIG. 3.17 MUON ENERGY LOSS RATE IN IRON

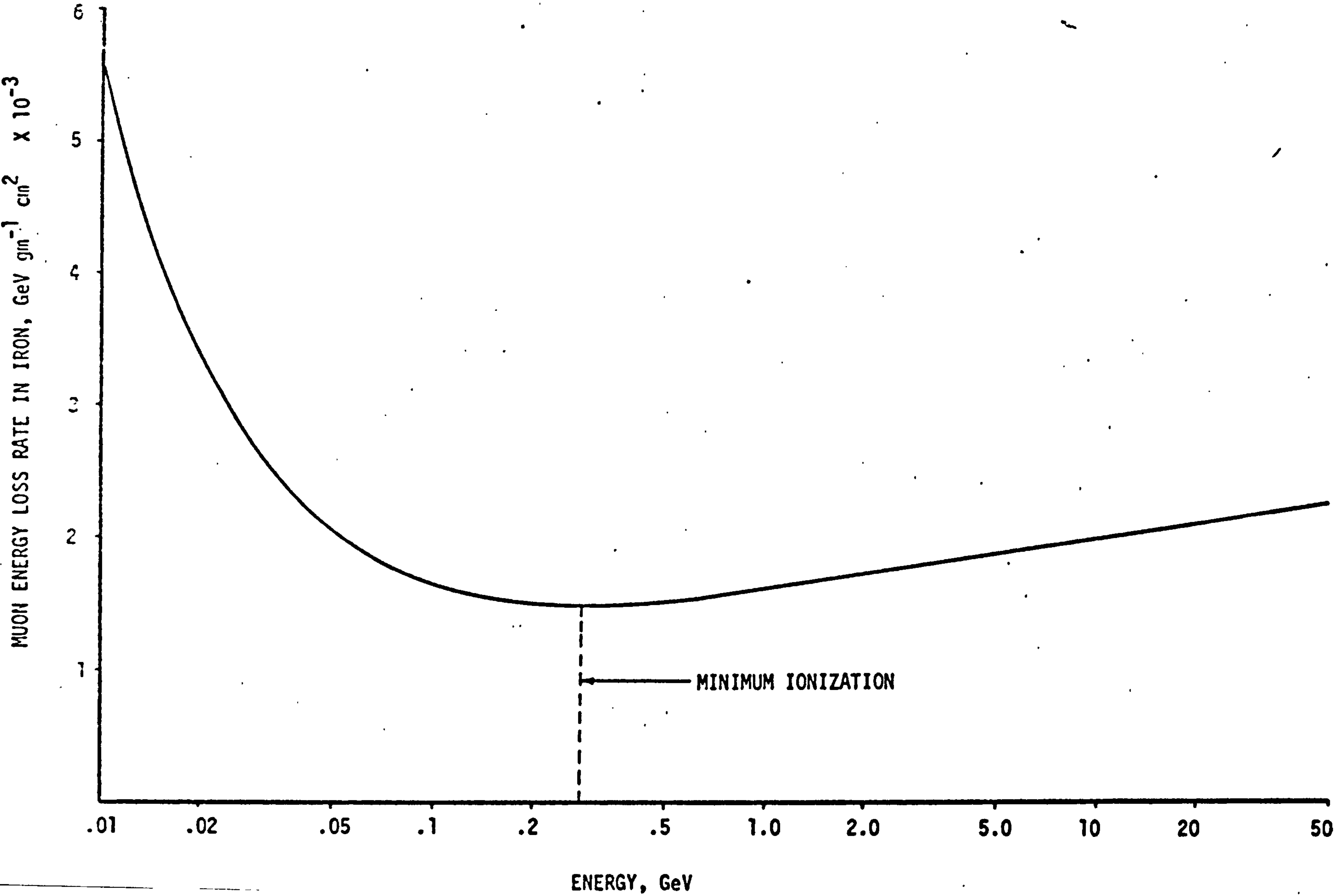
MUON ENERGY LOSS RATE IN IRON, GeV gm⁻¹ cm² x 10⁻³
6
5
4
3
2
1
MINIMUM IONIZATION
.01
.02
.05
.1
.2
.5
1.0
2.0
5.0
10
20
50
ENERGY, GeV

$$-\frac{dE}{dx} = a+bE + c \;\ell n \left[\frac{E_m}{m_\mu c^2}\right] \text{ MeV/gm-cm}^{-2} \tag{27}$$

where

$$E_m = \frac{p^2c^2}{E + m_\mu{}^2c^2/2m_e} \tag{28}$$

The momentum loss rate is then found by

$$\frac{d(pc)}{dx} = \frac{E}{(pc)}\,\frac{dE}{dx} \tag{29}$$

CHAPTER IV

MOLIÈRE'S THEORY OF MULTIPLE SCATTERING

4.1 INTRODUCTION

In this chapter we develop the small angle theory of multiple scattering due to Molière.[13] However we first discuss some basic assumptions of multiple scattering theory in general.

It is assumed that a fast charged particle will undergo many small angular deflections while traversing a target material. The deflections are due to collisions with atoms of the material and are described by the single scattering probability density, $W(\theta,\beta,x)$, such that

$W(\theta,\beta,x)\ \mathrm{SIN}\theta d\theta d\beta dx$ = the probability of the incident particle being deflected by a single collision into a spatial angle between θ and $\theta + d\theta$ and an azimuthal angle between β and $\beta + d\beta$ (see Fig. 4.1) during traversal of a target of thickness dx. (1)

While penetrating the target material there occur n collisions resulting in the total angular displacements,

$$\theta = \theta_1 + \theta_2 + \dots + \theta_n \tag{2}$$
$$\beta = \beta_1 + \beta_2 + \dots + \beta_n$$

The probability density in the total deflection angles given by (2) is called the multiple scattering density,

$F(\theta,\beta,x)\ SIN\theta d\theta d\beta dx$ = the probability of the particle being multiply scattered into $(\theta,\ \theta + d\theta)$ and $(\beta,\beta + d\beta)$ after n collisions in a target of thickness, x. (3)

Given the single scattering function, $W(\theta,\beta,x)$, the goal of multiple scattering theory, in general, is to calculate the multiple scattering density, $F(\theta,\beta,x)$, from the following assumptions:

(1) The single scattering function is independent of the azimuth angle, β, (in the absence of spin) hence $W(\theta,\beta,x) = W(\theta,x)$.

(2) Successive single scatterings in the target material are statistically independent.

(3) The small angle approximation can be used, i.e. $SIN\ \theta \simeq \theta$ and $COS\ \theta \simeq 1$.

Molière makes further assumptions about the physics of single scattering which we will discuss in a later section.

Due to the assumptions made above we write:

$2\pi W(\theta,x)\theta d\theta dx$ = the probability of only one scattering occurring in dx at x through an angle between θ and $\theta + d\theta$.

If, further, we suppress the dependence on x, (which is equivalent to ignoring ionization momentum loss in the target) then we seek the density in

$$\theta = \theta_1 + \theta_2 + \dots + \theta_n \tag{4}$$

where the θ_i are described by the density $W(\theta_i)$ and also the θ_i are statistically independent. This allows the use of the limiting form of the central limit theorem (for the special case $\langle\theta_i^2\rangle = \langle\theta_j^2\rangle$ for $i,j = 1,2, \dots n$) which gives[14]

$$F(\theta) = \frac{1}{\sqrt{2\pi}} e^{-\frac{\theta^2}{2}} \Big[1 - \frac{s}{3!\sqrt{n}} H_3(\theta) + \frac{\gamma}{4!n} H_4(\theta) + \frac{s^2}{2\cdot 3!3!n} H_6(\theta) + \dots\Big] \tag{5}$$

where the skewness coefficient, s, is given by

$$s = \frac{M_3}{\sqrt{M_2^3}} \tag{6}$$

The coefficient of excess, γ, is

$$\gamma = \frac{M_4}{M_2^2} - 3 \tag{7}$$

Here the kth moment of the single scattering law is

$$M_k = 2\pi \int_0^\infty W(\theta)\theta^{k+1}\, d\theta \tag{8}$$

Finally the Hermite polynomials, $H_k(\theta)$, are

$$H_k(\theta) = (-1)^k\, e^{\frac{\theta^2}{2}} \frac{d^k}{d\theta^k}\left(e^{-\frac{\theta^2}{2}}\right) \tag{9}$$

$$
\begin{aligned}
H_o(\theta) &= 1 \\
H_1(\theta) &= \theta \\
H_2(\theta) &= \theta^2-1 \\
H_3(\theta) &= \theta^3-3\theta \\
H_4(\theta) &= \theta^4-6\theta^2+3 \\
H_{k+1}(\theta) &= \theta H_k(\theta) - kH_{k-1}(\theta)
\end{aligned}
\tag{10}
$$

From eq. (5) we see that for sufficiently large n:

$$\lim_{n\to\infty} F(\theta) = \frac{1}{\sqrt{2\pi}}\, e^{-\frac{\theta^2}{2}} \tag{11}$$

Since the number of collisions, n, is proportional to the target thickness, t, then (11) is the limiting multiple scattering density for an infinitely thick target. Thus we have shown that, from mathematical considerations, the multiple scattering density is gaussian with correction terms, eq. (5). Moliere uses physical arguments to develop correction terms which are considerably simpler than those in eq. (5).

4.2 THE PROJECTED ANGLE DENSITY

We shall ultimately be interested in the projected angle densities $f(\phi_x,x)$ and $f(\phi_y,x)$ where ϕ_x and ϕ_y are the projected angles defined in Fig. 4.1 and are given by

$$\mathrm{TAN}\ \phi_x = \mathrm{TAN}\ \theta\ \mathrm{COS}\ \beta \tag{1}$$

$$\mathrm{TAN}\ \phi_y = \mathrm{TAN}\ \theta\ \mathrm{SIN}\ \beta \tag{2}$$

In the small angle approximation these become

$$\phi_x = \theta \cos \beta \tag{3}$$

$$\phi_y = \theta \sin \beta \tag{4}$$

Thus a deflection (θ,β) can be described as a vector

$$\vec{\theta} = [\phi_x,\phi_y] \ ; \ \theta = [\phi_x^2 + \phi_y^2]^{1/2} \tag{5}$$

The functions $F(\theta,x)$ and $f(\phi_x,x)$ are normalized according to

$$2\pi \int_0^\infty \theta d\theta F(\theta,x) = 1 \tag{6}$$

and

$$\int_{-\infty}^\infty f(\phi_x,x) d\phi_x = 1 \tag{7}$$

One may calculate the projected angle density by

$$f(\phi_x,x) = \int_{-\infty}^\infty d\phi_y F[(\phi_x^2 + \phi_y^2)^{1/2}, x] \tag{8}$$

Molière introduces the zeroth order infinite Hankel transform of the multiple scattering density

$$\tilde{F}(\xi,x) = 2\pi \int_0^\infty \theta d\theta J_0(\xi\theta) F(\theta,x) \tag{9}$$

and its inverse

$$F(\theta,x) = \frac{1}{2\pi} \int_0^\infty \xi d\xi J_0(\xi\theta) \tilde{F}(\xi,x) \tag{10}$$

A useful property of this transform can be developed if we consider two successive scatterings θ_1 and θ_2 such that the total scattering angle is

$$\theta = \theta_1 + \theta_2$$

FIG. 4.1 GEOMETRY OF THE SPATIAL ANGLE θ, AND THE PROJECTED ANGLES ϕ_x AND ϕ_y

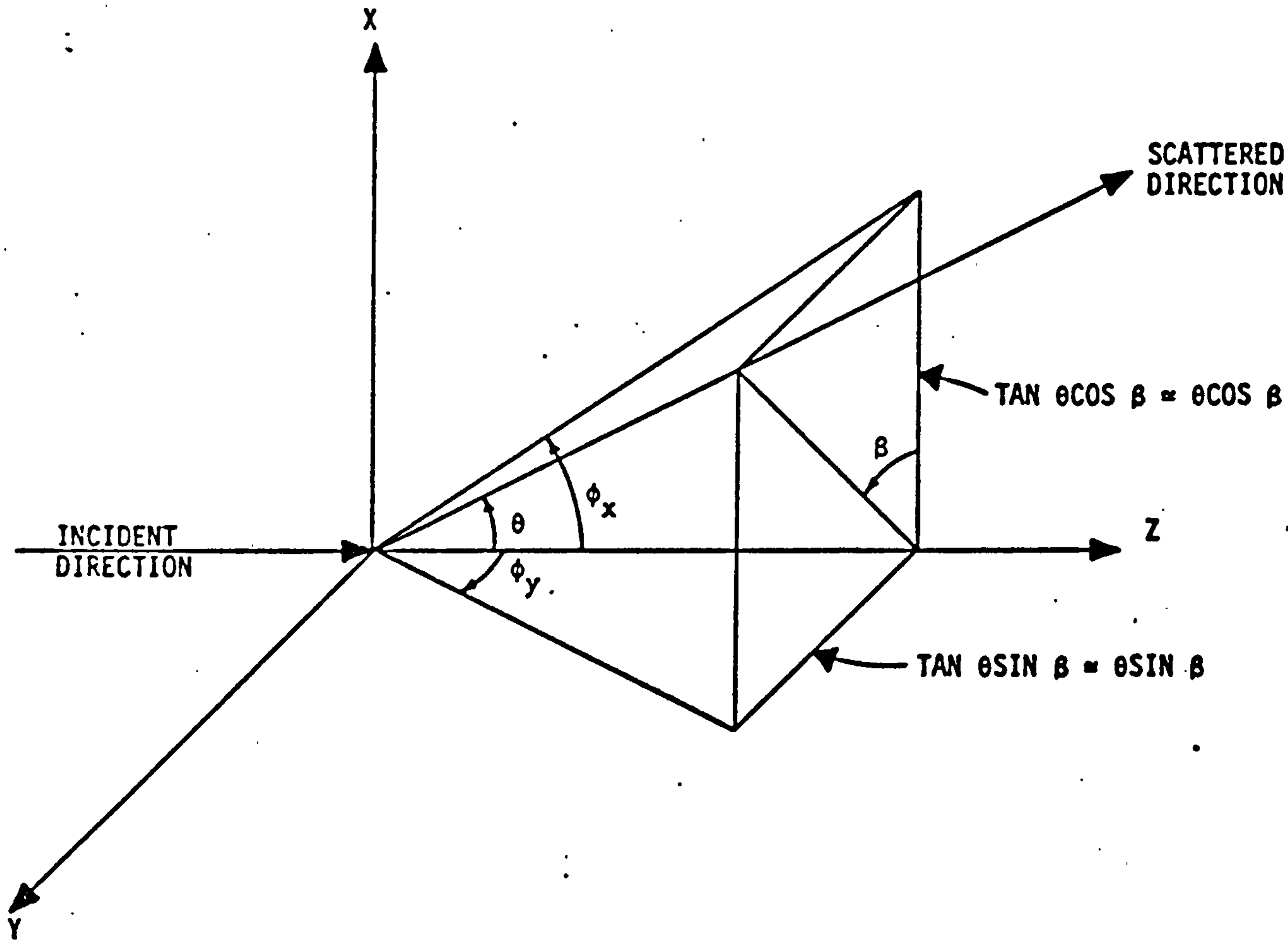
X
SCATTERED DIRECTION
TAN θCOS β ≃ θCOS β
β
ϕ_x
θ
INCIDENT DIRECTION
Z
ϕ_y
TAN θSIN β ≃ θSIN β
Y

we then find

$$\tilde{F}(\xi,x) = \tilde{F}_1(\xi,x)\ \tilde{F}_2(\xi,x) \qquad (11)$$

In fact for n collisions

$$\tilde{F}(\xi,x) = \tilde{F}_1(\xi,x)\ \tilde{F}_2(\xi,x)\ \ldots\ \tilde{F}_n(\xi,x) \qquad (12)$$

Molière then proceeds to use (9) - (12) to discover the multiple scattering density $F(\theta,x)$. Cooper and Rainwater[15] have shown that the multiple scattering density in projected angle can be derived using Fourier transforms. We shall, however, follow the method of Molière, and thus neglect the projected angle density until a later section. There we will derive $f(\phi_x,x)$ directly from $F(\theta,x)$.

4.3 THE WENTZEL SUMMATION METHOD

Here we develop a general expression for the multiple scattering density after the method of Wentzel.[16] To this end we assume that a beam of like particles is incident on a homogeneous target of thickness, x. We assume that the incident beam is a delta function

$$F(\theta,0) = \delta_s(0) \qquad (1)$$

such that

$$2\pi dx\int_0^\infty \theta d\theta\, \delta_s(\theta) = 1 \qquad (2)$$

We now seek to find the density for the beam after n scatterings. We write

$$2\pi dx\int_0^\infty \theta d\theta W(\theta) = \omega_0 dx$$

which is the probability that one scattering will occur in dx. Here we have assumed that

$$W(\theta,x) = W(\theta), \tag{3}$$

i.e. that there is no momentum loss in the target. The probability that no scatterings will occur in a thickness, Δx, is

$$P_0(\Delta x) = e^{-\omega_0 \Delta x} \tag{4}$$

Now the probability that exactly n scatterings occur of (θ_1,β_1) in $\theta_1 d\theta_1 d\beta_1$, (θ_2,β_2) in $\theta_2 d\theta_2 d\beta_2$, ... (θ_n,β_n) in $\theta_n d\theta_n d\beta_n$ at depths in (x_1,x_1+dx_1), (x_2,x_2+dx_2), ...(x_n,x_n+dx_n) is just the product

$$[W(\theta_1)\theta_1 d\theta_1 d\beta_1 dx_1][W(\theta_2)\theta_2 d\theta_2 d\beta_2 dx_2]\ldots \times [W(\theta_n)\theta_n d\theta_n d\beta_n dx_n] \tag{5}$$

From (4) we see that the probability that no scatterings occur in x is just

$$\lim_{\Delta x \to 0} e^{-\omega_0(x-\Delta x_1-\Delta x_2 - \ldots - \Delta x_n)} = e^{-\omega_0 x} \tag{6}$$

Here $x-\Delta x_1-\Delta x_2 - \ldots \Delta x_n$ is just the total space between the Δx's in the limit of the integral over x. Finally the probability of exactly n scatterings is given by the product of (5) and (6)

$$e^{-\omega_0 x}[W(\theta_1)\theta_1 d\theta_1 d\beta_1 dx_1][W(\theta_2)\theta_2 d\theta_2 d\beta_2 dx_2] \ldots \times [W(\theta_n)\theta_n d\theta_n d\beta_n dx_n] \tag{7}$$

Integrating over the x's and β's we get the probability of exactly n scatterings in x:

$$\frac{(2\pi x)^n}{n!} e^{-\omega_0 x} [W(\theta_1)\theta_1 d\theta_1][W(\theta_2)\theta_2 d\theta_2]\ldots[W(\theta_n)\theta_n d\theta_n]$$

or

$$\frac{(2\pi x)^n}{n!} e^{-\omega_0 x} \prod_{i=1}^{n} W(\theta_i)\theta_i d\theta_i \tag{8}$$

where n! removes all the extra permutations obtained in the integrations over the x's. If we introduce the Hankel transform

$$\omega(\xi) = 2\pi \int_0^\infty \chi d\chi J_0(\xi\chi) W(\chi) \tag{9}$$

then the transform of the density in θ after n scatterings is

$$\tilde{F}_n(\xi,x) = e^{-\omega_0 x} \frac{[\omega(\xi)x]^n}{n!} \tag{10}$$

The final distribution is just the sum over all n so that

$$\tilde{F}_n(\xi, x) = e^{\omega(\xi)x-\omega_0 x} \tag{11}$$

Finally the multiple scattering density we seek is found by (4.2.10)

$$F(\theta,x) = \frac{1}{2\pi} \int_0^\infty \xi d\xi J_0(\xi\theta) e^{\omega(\xi)x-\omega_0 x} \tag{12}$$

If we had assumed the single scattering law to be a function of target thickness then a more general result is

$$F(\theta,x) = \frac{1}{2\pi}\int_0^\infty y\,dy\,J_0(y\theta)e^{\Omega(y,x)-\Omega_0 x} \qquad (13)$$

where

$$\Omega(y,x) = \int_0^x \omega(y,x')dx' = 2\pi \int_0^\infty \chi d\chi \int_0^x dx' J_0(y\chi)W(\chi,x') \qquad (14)$$

Also

$$\Omega_0(x) = \Omega(0,x) = 2\pi \int_0^\infty \chi d\chi \int_0^x dx' W(\chi,x') \qquad (15)$$

When $W(\chi,x)$ is independent of target thickness we find from (13) and (14) that, as we saw before:

$$\Omega(y,x) = \omega(y)x \qquad (16)$$

$$\Omega_0(x) = \omega_0 x \qquad (17)$$

We now investigate the single scattering law, $W(\theta,x)$, in preparation for the evaluation of (13).

4.4 THE SINGLE SCATTERING LAW

The scattering of fast charged particles by atoms is given, for the non-relativistic case, by the Rutherford formula

$$\sigma_{RU}(\theta) = \left(\frac{2zZe^2}{mv^2}\right)^2 \frac{1}{[2\ \mathrm{SIN}\ \frac{\theta}{2}]^4} \qquad (1)$$

Relativistic scattering is described by a simple modification to (1), i.e. if we use the relativistic mass, γm, then the Rutherford formula describes the scattering of relativistic particles. If we use the small angle approximation then the relativistic single scattering law becomes

$$W(\theta,x) = N(x)\sigma_{RU}(\theta) = 4N(x)\frac{a^2}{k^2\theta^4} \qquad (2)$$

where $N(x)$ is the number of scattering centers/cm^3. Here "a" is the Born parameter given by

$$a = \frac{zZ}{137\beta} = \frac{zZe^2}{\hbar v} \qquad (3)$$

where $\beta = v/c$ and

$$\frac{1}{k} = \lambda_o = \frac{\hbar}{p} \qquad (4)$$

is the particle wave number.

The basic single scattering law, eq. (2), is inaccurate for several physical reasons:

(1) The screening of the nuclear Coulomb field by the atomic electrons.

(2) The finite size of the nuclear charge distribution.

(3) The contribution due to particle spin.

(4) Scattering by the atomic electrons.

The single scattering law eq.(2) determines the scattering of a fast charged particle by a heavy point charge. Molière modifies (2) to take electron screening into account; he neglects all of the other contributions. A simple way to take screening into account is by use of the Yukawa potential

$$V(r) = zZe^2 \frac{e^{-\frac{r}{r_0}}}{r} \tag{5}$$

Here r_o is the so-called screening radius or the Thomas-Fermi radius, given by

$$r_o = .885 a_o Z^{-1/3} = .468 \times 10^{-8} Z^{-1/3} \text{cm} \tag{6}$$

where a_o is the Bohr radius

$$a_o = \frac{\hbar^2}{m_e e^2} = 5.292 \times 10^{-9} \text{ cm} \tag{7}$$

Using the potential (5) and the first Born approximation solution to the relativistic Schroedinger equation, one gets

$$W(\theta,x) = \frac{4N(x)a^2}{k^2[1/k^2 r_o{}^2 + 2\ \mathrm{SIN}^2(\theta/2)]^2} \tag{8}$$

In the small angle approximation one finds

$$W(\theta,x) = \frac{4N(x)a^2}{k^2(\theta^2 + \theta_o{}^2)^2} \tag{9}$$

where the Born screening angle, θ_o, is

$$\theta_o = \frac{1}{kr_o} = \frac{\hbar}{pr_o} = \frac{\lambda\!\!\!^{-}_{o}}{r_o} \tag{10}$$

From (6) and (7) we find for (10)

$$\theta_o = \frac{1.13}{137} Z^{1/3} \left[\frac{m_e c^2}{pc}\right] \text{ radians} \tag{11}$$

When the momentum of the particle greatly exceeds the rest energy of the electron we see that $\theta_o << 1$ (which is clearly the case for the present experiment, where $pc>2.5$ GeV).

Molière writes the single scattering law (9) in the following form

$$W(\theta,x) = \frac{4N(x)a^2}{k^2\theta^4}\, q(\theta) \tag{12}$$

where

$$q(\theta) = \frac{\theta^4}{(\theta^2 + \theta_0{}^2)^2} \tag{13}$$

We may view (13) as being the ratio of "actual" to Rutherford scattering; $q(\theta)$ is sometimes referred to as a screening factor. It is seen that

$$\lim_{\theta\to 0} q(\theta) = 0$$

which corresponds to small scattering angles that occur for passage of the fast particle far from the nucleus, i.e. outside the atomic electrons where screening is most effective. Likewise

$$\lim_{\theta\to\infty} q(\theta) = 1$$

corresponding to large scattering angles occurring for passage near the nucleus.

We defer, until the next section, a discussion of Molière's derivation of $q(\theta)$.

4.5 DERIVATION OF THE MULTIPLE SCATTERING DENSITY

Here we develop the multiple scattering density,

$F(\theta,x)$ by means of eqs. 4.3.13-15. Neglecting momentum loss and using the fact that

$$W(\theta,x)dx = N(x)\sigma(\theta,x)dx \qquad (1)$$

we find the multiple scattering function to be

$$F(\theta,x) = \int_0^\infty \eta d\eta J_0(\eta\theta)e^{-Nx\int_0^\infty \sigma(\chi)\chi d\chi[1-J_0(\eta\chi)]} \qquad (2)$$

where $\sigma(\chi)$ is the differential scattering cross section of a screened Coulomb potential. After Molière we write for (4.4.12)

$$Nx\sigma(\chi)\chi d\chi = 2\chi_c{}^2\chi d\chi q(\chi)/\chi^4 \qquad (3)$$

where $q(\chi)$ is the ratio of actual to Rutherford scattering and

$$\chi_c{}^2 = 4\pi Nxe^4(zZ)^2/(pv)^2 \qquad (4)$$

The characteristic angle, χ_c^2, has a physical meaning: the probability of single scattering through an angle greater than χ_c is exactly one. Conversely, no scattering angle less than χ_c is possible. Using (3) we now evaluate the exponent of (2):

$$\Omega_0 x-\Omega(\eta)x = 2\chi_c^2 \int_0^\infty \chi^{-3}d\chi[1-J_0(\chi\eta)]q(\chi) \qquad (5)$$

To evaluate this integral we use the method of Bethe,[17] which is simpler and more physically transparent than that of Molière. Bethe selects an angle, k, with the property

$$\chi_o << k << \frac{1}{\eta} \sim \chi_c \tag{6}$$

Then the integral (5) is split at the angle k so that for the part of the integral from k to infinity the function q (χ) can be replaced by 1. Further, in the integral from 0 to k, the argument of the Bessel function is sufficiently small so that we may write

$$1 - J_o(\chi\eta) = \frac{(\chi\eta)^2}{4} \tag{7}$$

Hence for (5) we get

$$\Omega_o x - \Omega(\eta)x = 2\chi_c^2\left[\int_o^k \chi^{-3}d\chi[1 - J_o(\chi\eta)]q(\chi) + \right.$$

$$\left. + \int_k^\infty \chi^{-3}d\chi[1-J_o(\chi\eta)]q(\chi)\right].$$

$$\Omega_o x - \Omega(\eta)x = 2\chi_c^2\{\frac{\eta^2}{4}[I_1(k\eta) + I_2(k)]\} \tag{8}$$

where

$$I_2(Z) = 4\int_Z^\infty \frac{dt}{t^3}[1-J_o(t)] = \frac{2}{Z^2}[1-J_o(Z)] + \frac{J_1(Z)}{Z} + \int_Z^\infty dt\,\frac{J_o(t)}{t} \tag{9}$$

$$I_2(Z) = 1 - \ln Z + \ln 2 - c + O(Z^2) + \ldots \tag{10}$$

where c = .577... is Euler's constant. Furthermore for

I_1 we have

$$I_1 = \int_0^k q(\chi)d\chi/\chi \tag{11}$$

If we use (10) and (11) in (8):

$$\Omega_0 x - \Omega(\eta)x = \frac{(\chi_c\tau)^2}{2}\left[\int_0^k q(\chi)d\chi/\chi + 1 - \ell nk + \ell n2 - c\right] \tag{12}$$

Following Molière it is instructive to investigate the quantity

$$I = \int_0^k \frac{q(\chi)d\chi}{\chi} + \frac{1}{2} - \ell nk \tag{13}$$

We shall evaluate (13) for the Yukawa potential, for which

$$q(\chi) = \frac{\chi^4}{(\chi^2 + \chi_0^2)^2} \tag{14}$$

where $\chi_0 \equiv \theta_0$, the Born screening angle. Using (14) in (13) we find, upon evaluating the integral:

$$I = \frac{1}{2}\ell n(k^2 + \chi_0^2) - \frac{1}{2}\ell n\chi_0^2 + \frac{\chi_0^2}{2(k^2 + \chi_0^2)} - \frac{1}{2} + \frac{1}{2} - \ell nk \tag{15}$$

Using the condition (6) we get

$$I = -\ell n\chi_0 \tag{16}$$

This leads to Molière's definition of a screening angle, χ_a, which is used when $q(\chi)$ is <u>not</u> given by the Yukawa potential:

$$-\ell n\ \chi_a \equiv \lim_{k\to\infty}\left[\int_0^k \frac{q(\chi)d\chi}{\chi} + \frac{1}{2} - \ell nk\right] \tag{17}$$

The limit as $k \to \infty$ is consistent with (6). If we use (17) in (12) we get

$$\Omega_0 x - \Omega(\eta)x = \frac{(\chi_c \eta)^2}{2}\left[-\ln(\chi_a y) + \frac{1}{2} + \ln 2 - c\right] \tag{18}$$

Now let $\chi_c \eta = y$ to get

$$\Omega_0 x - \Omega(\eta)x = \frac{y^2}{4}\left[b - \ln\left(\frac{y^2}{4}\right)\right] \tag{19}$$

$$\text{where } b = \ln\left(\frac{\chi_c}{\chi_a}\right)^2 + 1 - 2c \equiv \ln\left(\frac{\chi_c}{\chi_a'}\right)^2 \tag{20}$$

The new screening parameter, χ_a', is given by

$$-\ln \chi_a' = -\ln \chi_a + \frac{1}{2} - c \tag{21}$$

After Molière, we introduce a new parameter B by the transcendental equation

$$B - \ln B = b$$

We obtain, finally, for the multiple scattering function, eq. (4.3.12):

$$f(\theta)\theta d\theta = \frac{\theta d\theta}{\chi_c^2 B}\int_0^{y_{max}} y dy\, J_0\left(\frac{\theta\, y}{\chi_c\sqrt{B}}\right) e^{-\frac{y^2}{4} + \frac{y^2}{4B}\ln\frac{y^2}{4}} \tag{22}$$

If we let

$$s = \frac{\theta}{\chi_c\sqrt{B}} \tag{23}$$

$$f(s)sds = sds\int_0^{y_{max}} y dy\, J_0(sy) e^{-\frac{y^2}{4} + \frac{y^2}{4B}\ln\frac{y^2}{4}} \tag{24}$$

The upper limit, y_{max}, is required to prevent (22) or (23) from being divergent. In fact y_{max} can be estimated from (6). Since the evaluation of (5) depends on the approximation (6), our derivation will fail if $\eta \sim 1/\chi_0$ or y is of order $\chi_c/\chi_0 \sim e^{b/2}$. Since the exponent in (23) has a minimum at $y = y_{max} = 2e^{1/2(b-1)}$ we shall use this as the upper limit of (23).

Due to the fact that B is reasonably large eq. (23) may be expanded in a series:

$$f(s)sds = sds[2e^{-s^2} + \frac{f^{(1)}(s)}{B} + \frac{f^{(2)}(s)}{B^2} + \ldots] \qquad (25)$$

where

$$f^{(n)}(s) = \frac{1}{n!}\int_0^\infty ydy\ J_o(sy)e^{-\frac{y^2}{4}}\left[\frac{y^2}{4}\ \ell n\ \frac{y^2}{4}\right]^n \qquad (26)$$

Where now we let the upper limit $\to \infty$ since the integrand of (26) is convergent. Eqs. (25) and (26) are the basic Molière formulae and show that the multiple scattering density is a Gaussian density with correction terms.

We now emphasize the single most important result of Moliere's theory: it does not depend upon the shape of the single scattering cross section, only on the screening parameter, χ_a, calculated by eq. (17). In order to see the explicit dependence on χ_a we use a result from Scott[18] who wrote an approximation for B:

$$B = 11.32 + 2.48 \log\left[\frac{X_o{}^2 Z^{4/3}\ A^{-1}x}{\beta^2\ \chi_a^2}\right] \qquad (27)$$

where A is the target atomic weight. Because $\chi_a{}^2$ is in the argument of a logarithm small variations in χ_a will not affect the value of B to an appreciable extent. Nevertheless, Molière calculates his own value of $q(\chi)$ for single scattering by a Thomas-Fermi potential which he numerically fits to the form

$$V(r) = \frac{zZe^2}{r} \ \omega_M(r/r_0) \tag{28}$$

where

$$\omega_M(r/r_0) = 0.01\ e^{-.6r/r_0} + .55e^{-1.2r/r_0} + .35e^{-.3r/r_0} \tag{29}$$

Using (28) and (29) Molière accomplished a numerical solution to the Schroedinger equation by the WKB method, for which he obtained

$$q(\chi) \approx 1 - 8.85\left(\frac{\chi_0}{\chi}\right)^2 \left[1 + a^2\ \ln \frac{7.1 \times 10^{-4}(\chi/\chi_0)^4}{(a^4 + a^2/3 + .13)}\right] \tag{30}$$

Assuming a linear relation between χ_a^2 and a^2 Molière obtained, after numerical integration of (17),

$$\chi_a^2 = \chi_0^2\ (1.13 + 3.76a^2) \tag{31}$$

When "a" is small (as it is for $\beta \sim 1$ and with Z for moderately dense elements) then χ_a differs from χ_0 by only a few percent; for iron $\chi_a \approx 1.12\ \chi_0$.

Experimentally, we shall be interested in the projected angle density. This may be derived directly from eq. (22) by the use of

$$J_o(xy) = \frac{1}{2\pi}\int_o^{2\pi} e^{iyx\cos\rho}d\rho \qquad (32)$$

If we let

$$g(y^2) = e^{-\frac{y^2}{4} + \frac{y^2}{4B}\ln\frac{y^2}{4}} \qquad y \le y_{max} \qquad (33)$$

$$g(y^2) = 0 \qquad y > y_{max} \qquad (34)$$

then eq. (22) becomes

$$f(\theta)\theta d\theta = \frac{\theta d\theta}{\chi_c^2 B}\int_o^{\infty} y dy\left[\frac{1}{2\pi}\int_o^{2\pi} e^{i\frac{y\theta\cos\rho}{\chi_c\sqrt{B}}}d\rho\right] g(y^2) \qquad (35)$$

Since the variable of integration, ρ, is arbitrary we let

$$y\theta\cos\rho = \vec{y}\cdot\vec{\theta} = y_1\phi_x + y_2\phi_y \qquad (36)$$

where the vectors $\vec{y}$, $\vec{\theta}$ are given by

$$\vec{y} = [y_1, y_2] \qquad (37)$$

$$\vec{\theta} = [\phi_x, \phi_y] \qquad (38)$$

which are consistent with the small angle approximation. Also use

$$2\pi\theta d\theta = d\phi_x d\phi_y \qquad (39)$$

$$y dy d\rho = dy_1 dy_2 \qquad (40)$$

Get for 35:

$$f(\phi_x,\phi_y)d\phi_x d\phi_y = \frac{d\phi_x d\phi_y}{(2\pi)^2\chi_c^2 B}\int\int_{-\infty}^{\infty} dy_1 dy_2 e^{\frac{iy_1\phi_x}{\chi_c\sqrt{B}} + \frac{iy_2\phi_y}{\chi_c\sqrt{B}}} g(y_1^2+y_2^2) \qquad (41)$$

Subsequent integration over ϕ_y and use of the delta function,

$$\delta(y_2) = \frac{1}{2\pi}\int_{-\infty}^{\infty} d\phi_y\, e^{iy_2\phi_y} \tag{42}$$

gives

$$f(\phi)d\phi = \frac{d\phi}{\pi\chi_c\sqrt{B}}\int_0^{y_{max}} dy\ \cos\left[\frac{\phi y}{\chi_c\sqrt{B}}\right]\ e^{-\frac{y^2}{4} + \frac{y^2}{4B}\ \ell n\ \frac{y^2}{4}} \tag{43}$$

We prefer a multiple scattering density in the parameter α:

$$\alpha = \frac{\sqrt{2}\phi}{\chi_c\sqrt{B}} \equiv \frac{\phi}{\sigma_\phi}\ ;\ \sigma_\phi = \frac{\chi_c\sqrt{B}}{\sqrt{2}} \tag{44}$$

where σ_ϕ will be called the "width" of the multiple scattering density. Hence (43) becomes

$$f(\alpha)d\alpha = \frac{d\alpha}{\sqrt{2}\pi}\int_0^{y_{max}} dy\ \cos\left[\frac{\alpha y}{\sqrt{2}}\right] e^{-\frac{y^2}{4} + \frac{y^2}{4B}\ \ell n\ \frac{y^2}{4}} \tag{45}$$

A series expansion about 1/B gives

$$f(\alpha) = \frac{1}{\sqrt{2\pi}}\ e^{-\frac{\alpha^2}{2}} + \frac{f^{(1)}(\alpha)}{B} + \frac{f^{(2)}(\alpha)}{B^2} + \ldots \tag{46}$$

where

$$f^{(n)} = \frac{1}{\sqrt{2}\ \pi n!}\int_0^{\infty} dy\ \cos\left[\frac{\alpha y}{\sqrt{2}}\right] e^{-\frac{y^2}{4}}\left[\frac{y^2}{4}\ell n\frac{y^2}{4}\right]^n \tag{47}$$

Thus the dimensionless projected angle density in α is a gaussian with correction terms.

In order to take ionization energy loss into account integrations over target thickness, x, must be carried out in χ_c and χ_a. We now sum up the equations of the Molière theory (which include energy loss):

$$\alpha = \frac{\phi}{\sigma_\phi} \qquad \text{(DIMENSIONLESS SCATTERING PARAMETER)} \qquad (48)$$

$$\sigma_\phi = \chi_c\sqrt{B}/\sqrt{2} \qquad \text{(WIDTH OF SCATTERING DENSITY)} \qquad (49)$$

$$B = 1.153 + 1.122 \ln \Omega_o \qquad (49')$$

$$\Omega_o = \chi_c{}^2/\chi_a{}^2 \qquad \text{(MEAN NUMBER OF COLLISIONS)} \qquad (50)$$

$$\chi_{ao}^2 = \chi_0^2\,(1.13 + 3.76a^2) \qquad \text{(MOLIÈRE SCREENING ANGLE)} \qquad (51)$$

$$\chi_0 = \hbar/pr_o = \lambda_0/r_o \qquad \text{(BOHR SCREENING ANGLE)} \qquad (52)$$

$$r_o = .468 \times 10^{-8}\, Z^{-1/3} \qquad \text{(FERMI-THOMAS RADIUS)} \qquad (53)$$

$$a = \frac{zZ}{137\,\beta} \qquad \text{(BORN PARAMETER)} \qquad (54)$$

$$\chi_{co}^2 = 4\pi\frac{N}{A}\left(\frac{zZe^2}{pc\beta}\right)^2 = \frac{(.396zZ)^2}{A}\,\frac{1}{(p\beta)^2} \qquad (55)$$

$$\chi_c^2 = \int_{p_o}^{p_1} \chi_{co}^2\,(p')\;\frac{dp'}{(-dp'/dx)} \qquad (56)$$

$$\ln \chi_a^2 = \frac{1}{\chi_c^2}\int_{p_o}^{p_1} \chi_{co}^2\,(p')\;\ln \chi_{ao}^2\,(p')\;\frac{dp'}{(-dp'/dx)} \qquad (57)$$

Equations (48) to (57) have been used to generate multiple scattering curves for muons in iron, (Fig. 4.2). The parameter B = 18.45 for 95 cm (725 gm/cm^2) of iron; since B varies by less than .5% for momenta > 2.5 GeV/c we take B to be a constant and assume the curves of Fig. 4.2 are good for all momenta above 2.5 GeV/c.

FIG. 4.2 MOLIÈRE MULTIPLE SCATTERING DENSITY

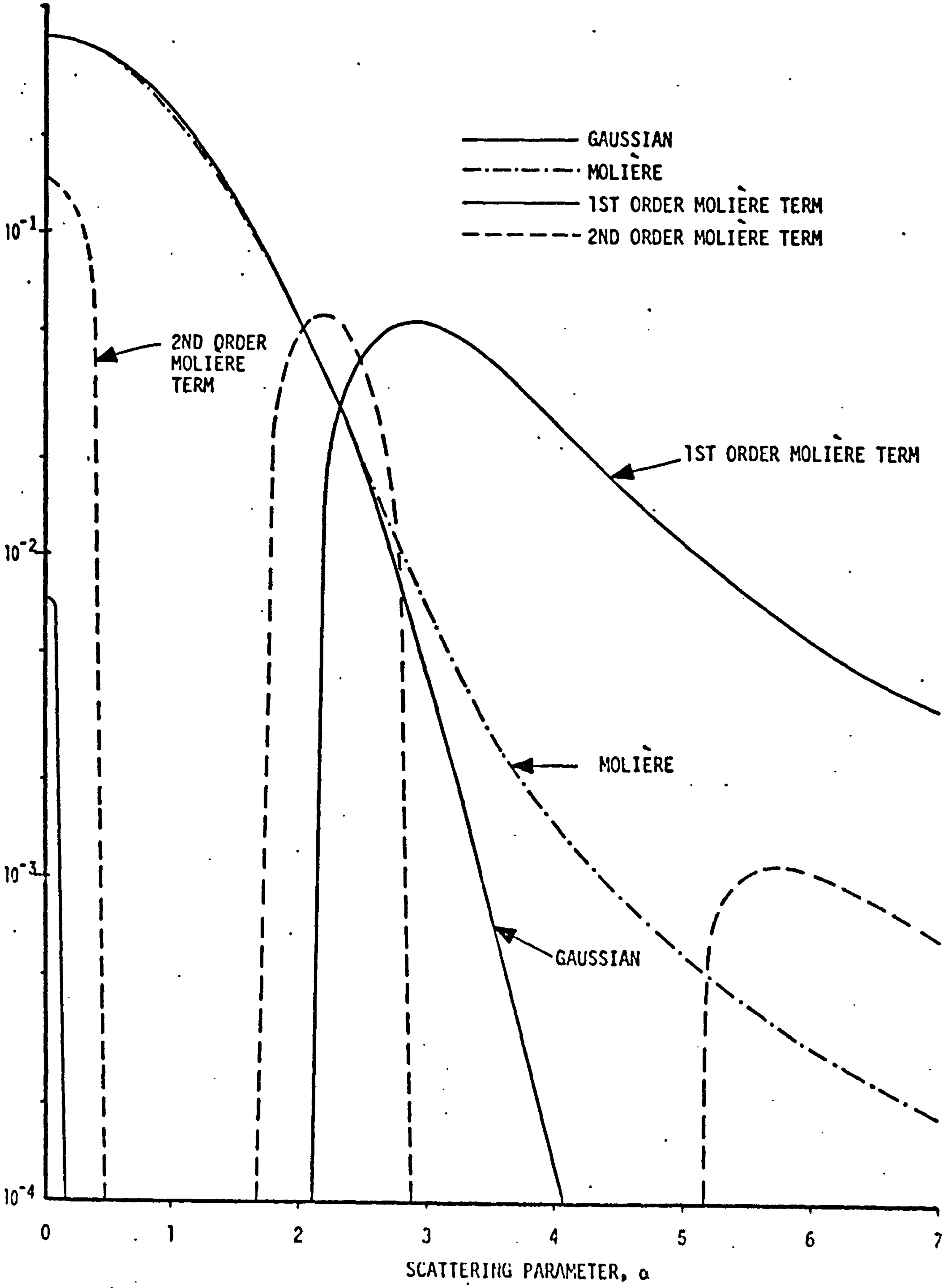
GAUSSIAN
MOLIÈRE
1ST ORDER MOLIÈRE TERM
2ND ORDER MOLIÈRE TERM
2ND ORDER MOLIERE TERM
1ST ORDER MOLIÈRE TERM
MOLIÈRE
GAUSSIAN
10^{-1}
10^{-2}
10^{-3}
10^{-4}
0
1
2
3
4
5
6
7
SCATTERING PARAMETER, α

4.6 WIDTH OF THE MULTIPLE SCATTERING PROBABILITY DENSITY

We have previously defined the width of the multiple scattering density to be

$$\sigma_\phi = \sqrt{\frac{B}{2}}\chi_c \tag{1}$$

which we now write

$$\sigma_\phi = \frac{1}{f(p,x)p} \tag{2}$$

so that

$$f(p,x) = \sqrt{\frac{2}{B}}\ \frac{1}{p\chi_c} \tag{3}$$

Motivation for introducing the function f(p,x) comes from the well known equation for σ_ϕ when momentum loss is negligible

$$\sigma_\phi = \frac{15}{p\beta}\sqrt{\frac{x}{x_o}} \tag{4}$$

where x_o is the radiation length of the target material and x is the target thickness in gm/cm². Comparing (2) with (4) we find

$$f(p,x) = \frac{\beta}{15}\sqrt{\frac{x}{x_o}} \tag{5}$$

Thus when momentum loss is not important f(p,x) is independent of the particle momentum.

For linear momentum loss Eyges[19] has shown that

$$\sigma_\phi = \frac{15}{\sqrt{p_o p_1}}\sqrt{\frac{x}{x_o}} \tag{6}$$

where p_0 and p_1 are the entry and exit momenta of the particle. For this case we have

$$f(p_0,x) = \frac{1}{15}\sqrt{\frac{p_1}{p_0}}\sqrt{\frac{x_0}{x}} \qquad (7)$$

For high momenta $p_0 \approx p_1$ and (7) becomes independent of momentum.

CHAPTER V

MODIFICATION TO THE THEORY OF MULTIPLE SCATTERING

5.1 STATEMENT OF THE PROBLEM

The ideal multiple scattering experiment, nominally conducted with a particle accelerator, consists of a collimated beam of high energy particles of well defined momentum, p_0, traversing a target of thickness, x. The projected multiple scattering angle, ϕ_s, is experimentally measured for each incident particle (see Fig. 5.1). The relative multiple scattering parameter α_0, for each event can then be formed by

$$\alpha_0 = \frac{\phi_s}{\sigma_\phi} \quad ; \quad \sigma_\phi = \sigma_\phi(p_0, x) \qquad (1)$$

where the root-mean-square multiple scattering angle, σ_ϕ, varies approximately as the square root of x and inversely as p_0. The parameter α_0 in eq. (1) has a Molière probability density that is a gaussian with correction terms:

$$f(\alpha_0) = \frac{1}{\sqrt{2\pi}}\, e^{-\frac{\alpha_0^2}{2}} + \frac{f^{(1)}(\alpha_0)}{B} + \frac{f^{(2)}(\alpha_0)}{B^2} + \ldots \qquad (2)$$

The exact expressions for σ_ϕ, B and $f^{(n)}(\alpha_0)$ have been derived in Chapter IV. Typically in an experiment one measures the scattering angle, ϕ_s, and then calculates the corresponding value of α_0 by eq. (1). A histogram of the

FIG. 5.1 IDEAL MULTIPLE SCATTERING EXPERIMENT USING A PARTICLE ACCELERATOR

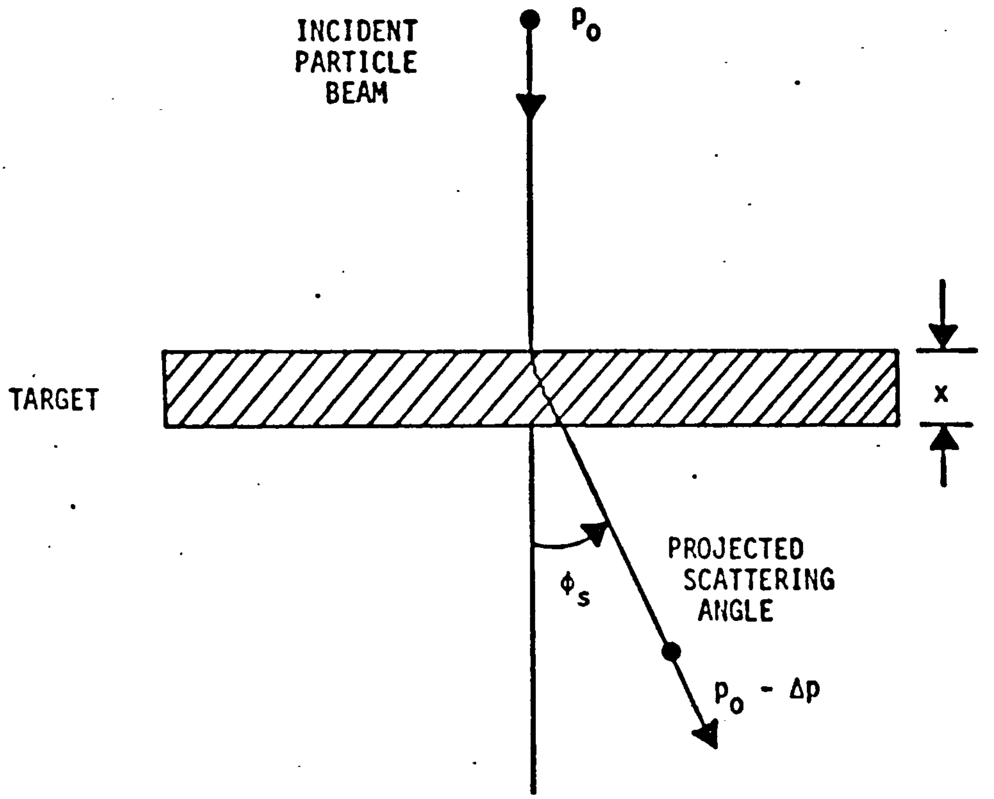

INCIDENT PARTICLE BEAM
p_o
TARGET
x
PROJECTED SCATTERING ANGLE
ϕ_s
$p_o - \Delta p$

values of α_0 can then be directly compared to the theory, eq. (2).

We now turn our attention to the present cosmic ray experiment which is considerably different from particle accelerator experiments. Our intention is to delineate how this experiment differs from a conventional multiple scattering experiment, what the difficulties encountered are, and what a course of action for removing these difficulties might be. Fig. 5.2 shows how multiple scattering can be investigated with the magnetic spectrometer. Recall that two cameras photograph orthogonal projections of the muon sparks. One film plane is parallel, the other is perpendicular to the magnetic field. Hence we observe the muon trajectory as projected onto a plane perpendicular to the magnetic field (which we have labeled the "field view") and also as projected onto a plane parallel to the magnetic field (the "no-field view"). It is clear that one observes magnetic bending of the muon in the field view. However, (in the absence of multiple scattering) the projection of the particle trajectory onto the no-field view is nearly a straight line, i.e. the projection of a trajectory which is approximately a helix of large radius. We realize of course that the effects of multiple scattering and ionization energy loss are observed in both views.

In later sections we will show the following results:

FIG. 5.2 MEASUREMENT OF MULTIPLE SCATTERING VARIABLES

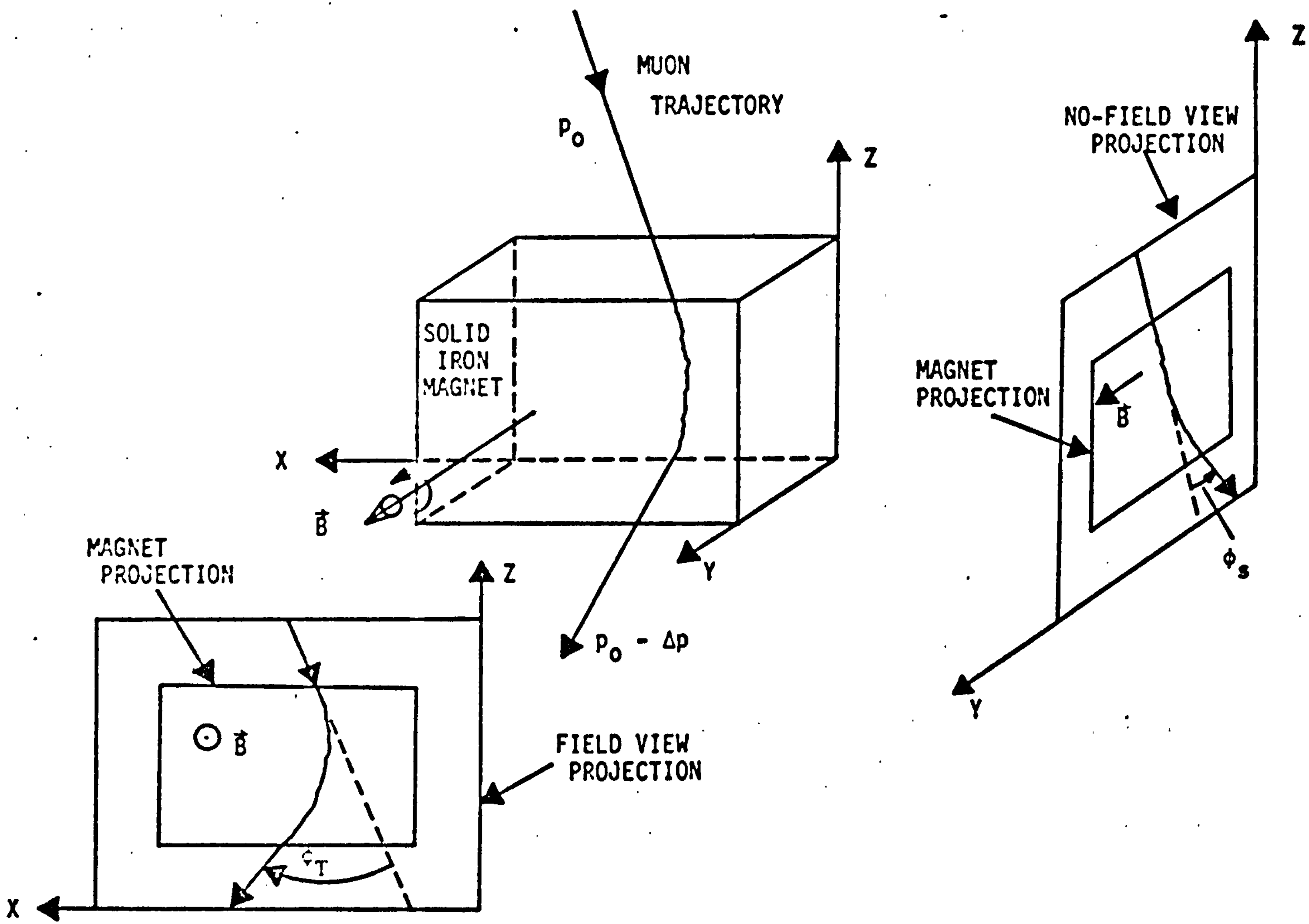

MUON
TRAJECTORY
p_o
Z
SOLID
IRON
MAGNET
X
$\vec{B}$
Y
$p_o - \Delta p$
MAGNET
PROJECTION
Z
$\vec{B}$
ϕ_T
X
FIELD VIEW
PROJECTION
Z
NO-FIELD VIEW
PROJECTION
MAGNET
PROJECTION
$\vec{B}$
ϕ_s
Y

(1) The muon momentum can be determined from the field view projection. However, because of multiple scattering, the momentum determined by the spectrometer is a random variable, p, statistically distributed about the real momentum, p_0. It will be shown that the experimentally measured momentum has an uncertainty of about 20% due to multiple scattering and that a direct determination of the real momentum, p_0, cannot be made.

(2) The projected multiple scattering angle, ϕ_s, can be measured from the no-field view projection of the muon trajectory.

(3) Since the momentum determined by the spectrometer, p, is <u>not</u> the real momentum, p_0, we conclude that the relative scattering angle, $\alpha_0 = \alpha_0(p)$, calculated by eq. (1) does not have the probability density of eq. (2). We shall seek to derive the correct density.

The purpose of this chapter is to ultimately modify the Molière theory to take into account the fact that (due to multiple scattering) the experimentally determined momentum, p, is statistically distributed about the (unknown) real momentum, p_0, with an uncertainty of about 20%. However, we shall first modify the simpler Gaussian theory because (1) the results are necessary in the modification of Molière's theory and (2) a great deal of physical insight is obtained in the mathematically simpler derivation.

5.2 MODIFICATION OF THE SIMPLE GAUSSIAN THEORY

5.2.1 INTRODUCTION

In this section we shall derive the probability density for the relative scattering parameter, α:

$$\alpha = \frac{\phi_s}{\sigma_\phi} \quad ; \quad \sigma_\phi = \frac{1}{f(p,x)p} \tag{1}$$

where p is the experimentally determined momentum (not the real momentum, p_o) and $f(p,x)$ is a slowly varying function of p given by eq. (4.6.3). We may write eq. (1) as

$$\alpha = f(p,x)p\phi_s \tag{2}$$

For high momentum we find that $f(p,x) = f(x) = \text{CONST}$ and α is proportional to the product of momentum and scattering angle.

We already know that ϕ_s has a probability density given by eq. (5.1.2). The following sections will be devoted to: (1) discovering a probability density function for the experimentally determined momentum, p, and finally (2) to deriving the probability density for the random variable $\alpha = f(p)p\phi_s$.

5.2.2 UNCERTAINTY IN MOMENTUM

Here we derive the uncertainty in the experimentally determined momentum. If we assume that there is no momentum loss or multiple scattering then the real momentum, p_o, is given by

$$p_o = \frac{.3B_oS}{\phi_B} = \frac{.3B_o x}{\rho\phi_B} \tag{1}$$

where

p_o = momentum in MeV/c.

ϕ_B = magnetic bending angle in radians.

B_o = magnetic field in kilogauss.

S = path length in cm.

x = path length in gm/cm^2.

ρ = target density in gm/cm^3.

From eq. (1) we find

$$\frac{dp_o}{p_o} = \left|\frac{d\phi_B}{\phi_B}\right| \tag{2}$$

If it is assumed that the uncertainty in bending angle, $\Delta\phi_B$, is due only to multiple scattering then we may define the relative momentum uncertainty, $\Delta p_o/p_o$, to be

$$\sigma \equiv \frac{\Delta\phi_B}{\phi_B} = \frac{\sigma_\phi}{\phi_B} \tag{3}$$

When momentum loss is not important $\sigma_\phi = \frac{15}{p_o\beta}\sqrt{\frac{S}{S_o}}$, hence using eq. (1) we get

$$\sigma = \left(\frac{50}{\beta\sqrt{S_o}}\right) \frac{1}{B_o\sqrt{S}} \tag{4}$$

where β is the particle velocity in units of the speed of light and S_o is the radiation length of the target material in cm. For high momenta $\beta \sim 1$ and the momentum uncertainty,

σ, is independent of particle momentum. Additionally this uncertainty can be seen to decrease with increasing magnetic field, B_0, and the square root of the path length, S. Here we have seen that σ is independent of momentum when ionization energy loss is not important. However, we shall later show that σ is nearly independent of momentum even when momentum loss is substantial. For the magnetic spectrometer with an iron target of thickness 725 gm/cm^2 and magnetic field 17.5 kilogauss we find $\sigma \approx .2$, hence the experimentally determined momentum is uncertain by about 20% due to multiple scattering in the iron.

5.2.3 THE MOMENTUM AND TOTAL ANGLE PROBABILITY DENSITIES

Given a muon beam incident on an iron target with zero magnetic field the multiple scattering probability density in total scattering angle, θ, is approximately

$$f(\theta)\theta d\theta = \frac{1}{\sigma_\phi{}^2}\, e^{-\frac{1}{2}\left(\frac{\theta}{\sigma_\phi}\right)^2} \theta d\theta \;;\; \langle\theta^2\rangle = 2\sigma_\phi \tag{1}$$

The projection of (1) onto the X-Z and Y-Z planes respectively (see FIG. 5.3.a) gives

$$f(\phi_x) = \frac{1}{\sqrt{2\pi}\;\sigma_\phi}\, e^{-\frac{1}{2}\frac{\phi_x{}^2}{\sigma_\phi{}^2}} \;;\; \langle\phi_x^2\rangle = \sigma_\phi{}^2 \tag{2}$$

$$f(\phi_y) = \frac{1}{\sqrt{2\pi}\;\sigma_\phi}\, e^{-\frac{1}{2}\frac{\phi_y{}^2}{\sigma_\phi{}^2}} \;;\; \langle\phi_y^2\rangle = \sigma_\phi{}^2 \tag{3}$$

5.2.3.2

FIG. 5.3.a PROJECTED MULTIPLE SCATTERING ANGLES FOR NO MAGNETIC FIELD

FIG. 5.3.b PROJECTED ANGLES WHEN A MAGNETIC FIELD IS PRESENT

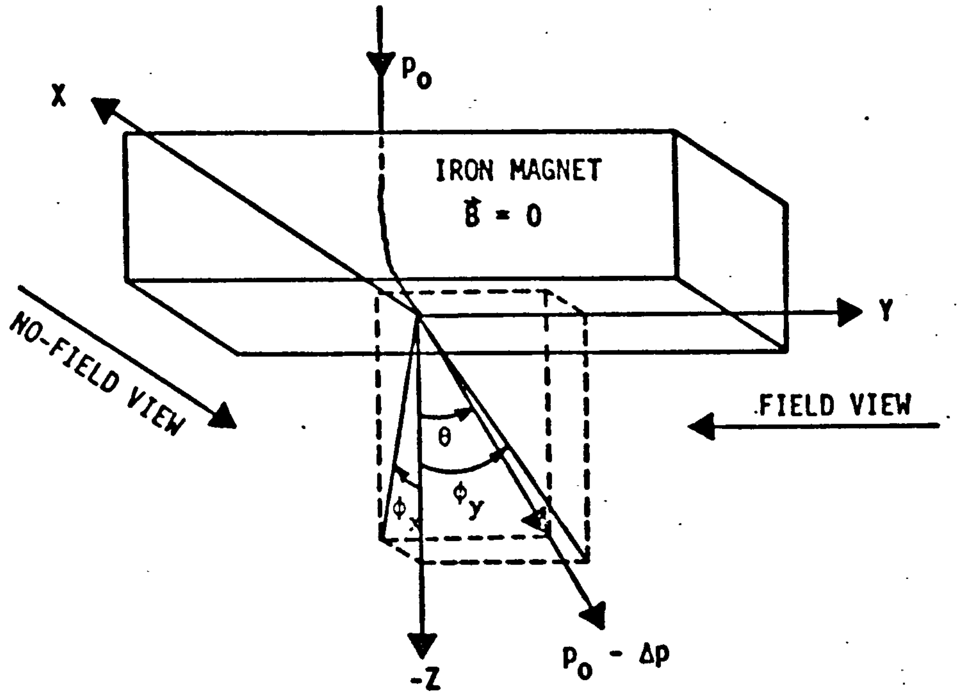

p_o
X
IRON MAGNET
$\vec{B} = 0$
Y
NO-FIELD VIEW
FIELD VIEW
θ
ϕ_y
ϕ_x
-Z
$p_o - \Delta p$

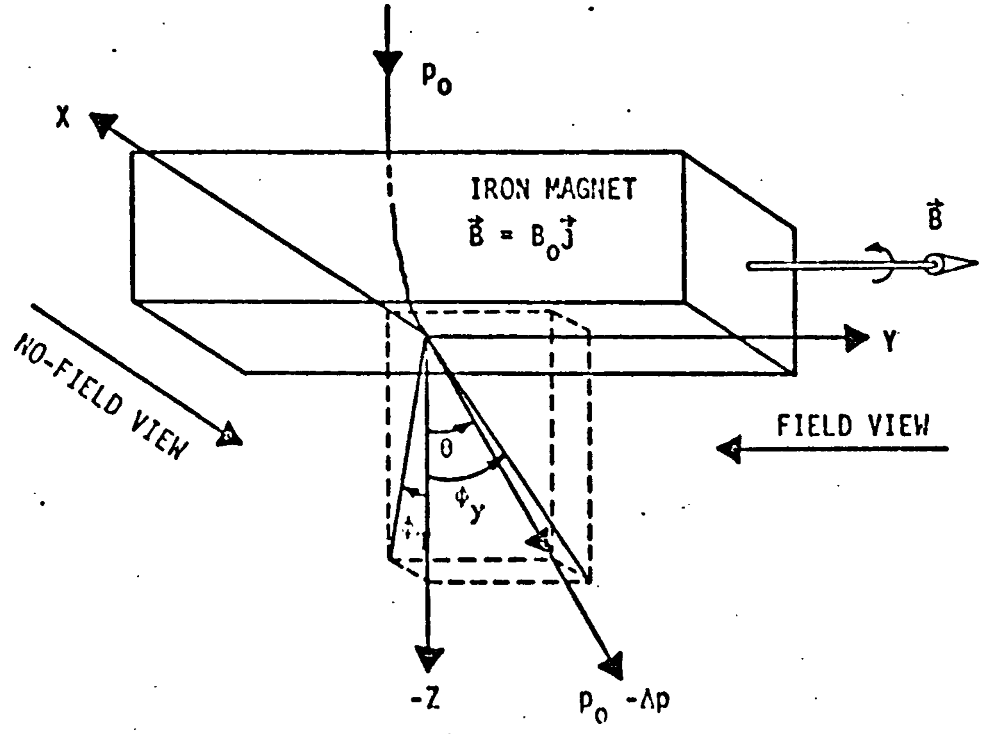

p_o
X
IRON MAGNET
$\vec{B} = B_o\vec{J}$
$\vec{B}$
Y
NO-FIELD VIEW
FIELD VIEW
θ
ϕ_y
-Z
$p_o - \Delta p$

where

$$\langle\theta^2\rangle = 2\langle\phi^2\rangle \tag{4}$$

The random variables ϕ_x and ϕ_y are the projected multiple scattering angles and are statistically uncorrelated. In the gaussian approximation used here ϕ_x and ϕ_y are also statistically independent. If we now assume that a magnetic field is present in the iron then the ratio, σ, of rms scattering, σ_ϕ, to bending, ϕ_B, yields

$$\sigma_\phi = \sigma\phi_B \tag{5}$$

Thus for (2) and (3) we get

$$f(\phi_x) = \frac{1}{\sqrt{2\pi}\ \sigma\phi_B}\, e^{-\frac{1}{2\sigma^2}\left(\frac{\phi_x}{\phi_B}\right)^2} \tag{6}$$

$$f(\phi_y) = \frac{1}{\sqrt{2\pi}\ \sigma\phi_B}\, e^{-\frac{1}{2\sigma^2}\left(\frac{\phi_y}{\phi_B}\right)^2} \tag{7}$$

Here we have traded the particle momentum, p_0, for the bending angle, ϕ_B, and written multiple scattering in terms of the "noise", σ. We now have three different ways to write the relative scattering parameter

$$\alpha_0 = \frac{\phi_s}{\sigma_\phi} = f(p_0)p_0\phi_s = \frac{1}{\sigma}\,\frac{\phi_s}{\phi_B} \tag{8}$$

from which either (6) or (7) becomes

$$f(\alpha_0) = \frac{1}{\sqrt{2\pi}}\, e^{-\frac{\alpha_0^2}{2}} \tag{9}$$

5.2.3.1 APPROXIMATE FORMS FOR THE MOMENTUM AND TOTAL ANGLE DENSITIES

In this section we examine how multiple scattering affects a muon trajectory in an iron magnet. In particular we will derive the momentum probability density which is caused by the randomizing process of multiple scattering. In Fig. 5.4 we see how a fast charged particle enters a solid iron magnet and is subjected to multiple scattering, magnetic bending, and ionization energy loss. If no energy loss or multiple scattering were to take place then the muon would be bent through only the projected magnetic bending angle ϕ_B. Because of multiple scattering however the particle undergoes a total angular displacement, $\phi_B + \phi_x$. If we ignore energy loss for the present results, we know that the real particle momentum is found by

$$p_o = \frac{.3B_0S}{\phi_B} \qquad \text{(REAL MOMENTUM)} \qquad (1)$$

The experimentally measured momentum, due to the total deflection angle, is

$$p = \frac{.3B_0S}{|\phi_B + \phi_x|} \qquad \text{(MEASURED MOMENTUM)} \qquad (2)$$

Eq. (2) is graphed in Fig. 5.5. Only when the scattering angle, ϕ_x , is zero is the momentum determination correct. If $\phi_x = \phi_B$ then $p = \frac{p_o}{2}$; however, when $\phi_x = -\phi_B$, then $p \to \infty$. Thus the determined momentum is very asymmetric in ϕ_x. We

FIG. 5.4. BENDING AND SCATTERING ANGLES

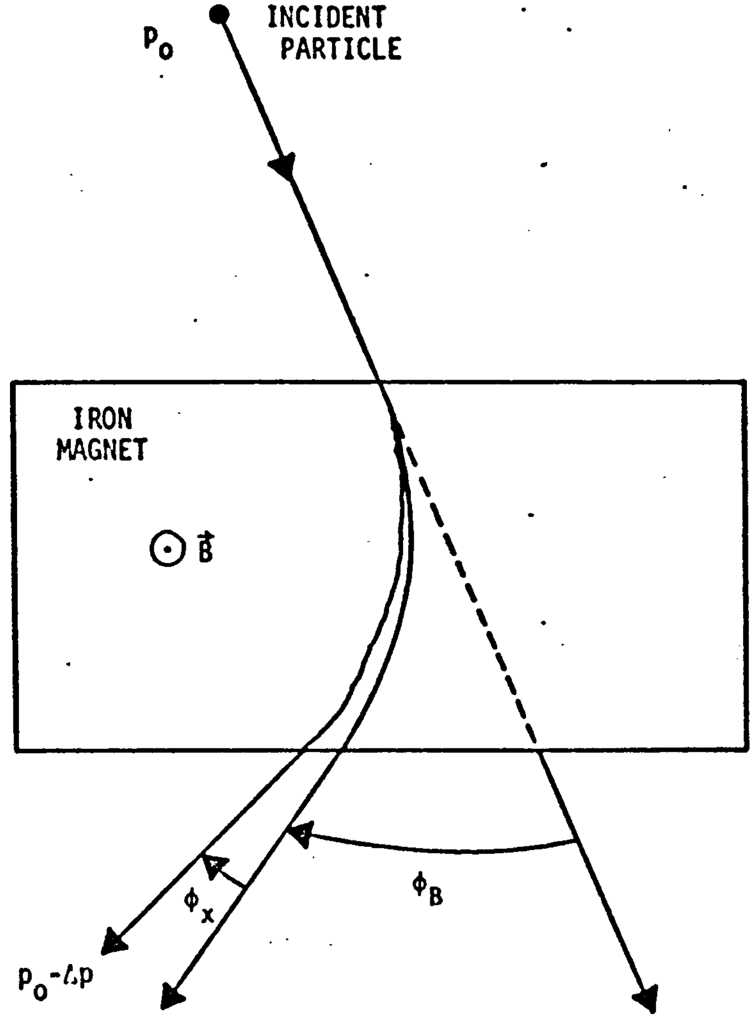

INCIDENT
PARTICLE
p_o
IRON
MAGNET
$\vec{B}$
ϕ_B
ϕ_x
$p_o-\Delta p$

already know that the rms scattering angle is σ times the magnetic bending angle. Hence most values of ϕ_x fall in or near the range

$$-3\sigma\phi_B \lesssim \phi_x \lesssim 3\sigma\phi_B \ ; \ \sigma \simeq .2 \tag{3}$$

We have stated that the probability density for the scattering angle, ϕ_x, is nearly gaussian and given by (5.2.3.6). We now seek the corresponding probability density for the measured momentum, p. Clearly such a density exists, for if we randomly choose values of ϕ_x from eq. (5.2.3.6) and calculate corresponding values of p (for some particular value of ϕ_B) using (2), then for a sufficiently large number of values of p we could simulate the probability density of p (this procedure is a straightforward application of the Monte Carlo technique). To develop an analytical expression for the density of p, we use a result from probability theory[20]

$$f(p) = f(\phi_x) \left|\frac{d\phi_x}{dp}\right| \ ; \ \phi_x = g^{-1}(p) \tag{4}$$

where it is understood that

$$p = g(\phi_x) \tag{5}$$

is a monotonically increasing or decreasing function in the region of interest. From Fig. 5.5 this must be the region centered around $\phi_x = 0$, namely

$$-\phi_B \leq \phi_x \leq \phi_B \tag{6}$$

5.2.3.1.4

FIG. 5.5 EXPERIMENTALLY DETERMINED MOMENTUM

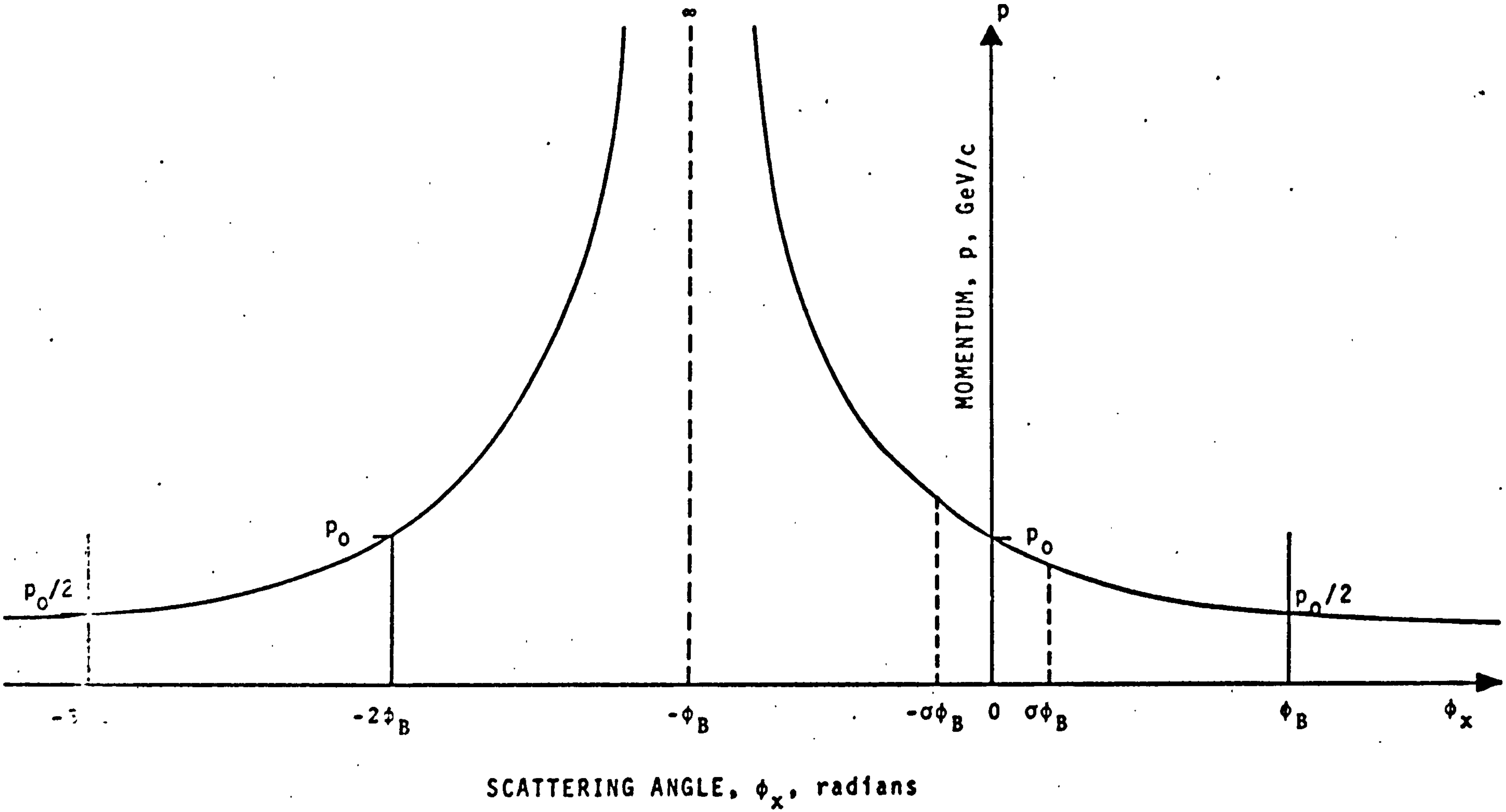

∞
p
MOMENTUM, p, GeV/c
p_o
p_o
p_o/2
p_o/2
-2φ_B
-φ_B
-σφ_B
0
σφ_B
φ_B
φ_x
SCATTERING ANGLE, φ_x, radians

But we know that the width of the multiple scattering density is $\sigma\phi_B$. Hence the above range, (6), corresponds to the 5-sigma point for a gaussian density. Notice that we have neglected the regions less than $-\phi_B$ and greater than ϕ_B; we will investigate these regions in Sec.5.2.3.2. Even though we have confined ourselves to region (6) in order to use (4), we have not significantly affected the normalization of the resultant probability density, f(p).

At this point it can be noted that the probability densities used here have the usual definitions, i.e.

$f(p)dp$ = probability that a particle of initial momentum p_0 will be measured to have a momentum between p and p+dp after traversing an iron magnet of "noise" σ.

$f(\phi_x)d\phi_x$ = probability that a particle incident at angle $\phi_x = 0$ will be multiply scattered into an angle between ϕ_x and $\phi_x + d\phi_x$ after traversing an iron target of "noise" σ.

Also we require $f(\phi_x) \geq 0$ and $f(p) \geq 0$ for all values of ϕ_x and p. Likewise we require the normalizations

$$\int_{-\phi_B}^{\phi_B} f(\phi_x)\, d\phi_x = 1 \qquad (7)$$

$$\int_{\frac{p_0}{2}}^{\infty} f(p)\, dp = 1 \qquad (8)$$

where the limits on (7) and (8) can be taken directly from Fig. 5.5. Notice once again that the normalizations of (7) and (8) are little affected by the restrictions on the range of ϕ_x.

Eq. (2) can now be written without the absolute value sign since $\phi_B + \phi_x \geq 0$ in the region (6):

$$p = \frac{k_0}{\phi_B + \phi_x} \tag{9}$$

and

$$p_0 = \frac{k_0}{\phi_B} \tag{10}$$

where we have let

$$k_0 = .3B_0S \tag{11}$$

If we use (5.2.3.6), (9) and (10) in (4) we get the momentum probability density

$$f(p|p_0) = \frac{1}{\sqrt{2\pi}\,\sigma}\frac{p_0}{p^2}\, e^{-\frac{1}{2}\left(\frac{p_0}{\sigma}\right)^2\left(\frac{1}{p} - \frac{1}{p_0}\right)^2} \tag{12}$$

Fig. 5.6 shows the shape of the momentum density, which is an asymmetric function about the real momentum, p_0. The density f(p) has a long tail in the region of high momentum indicating a high probability of measuring momenta much greater than the real momentum, p_0.

If the relative momentum is defined by

$$a \equiv \frac{p}{p_0} \tag{13}$$

FIG. 5.6 MOMENTUM DISTRIBUTION DUE TO MULTIPLE SCATTERING, $\sigma = .2$

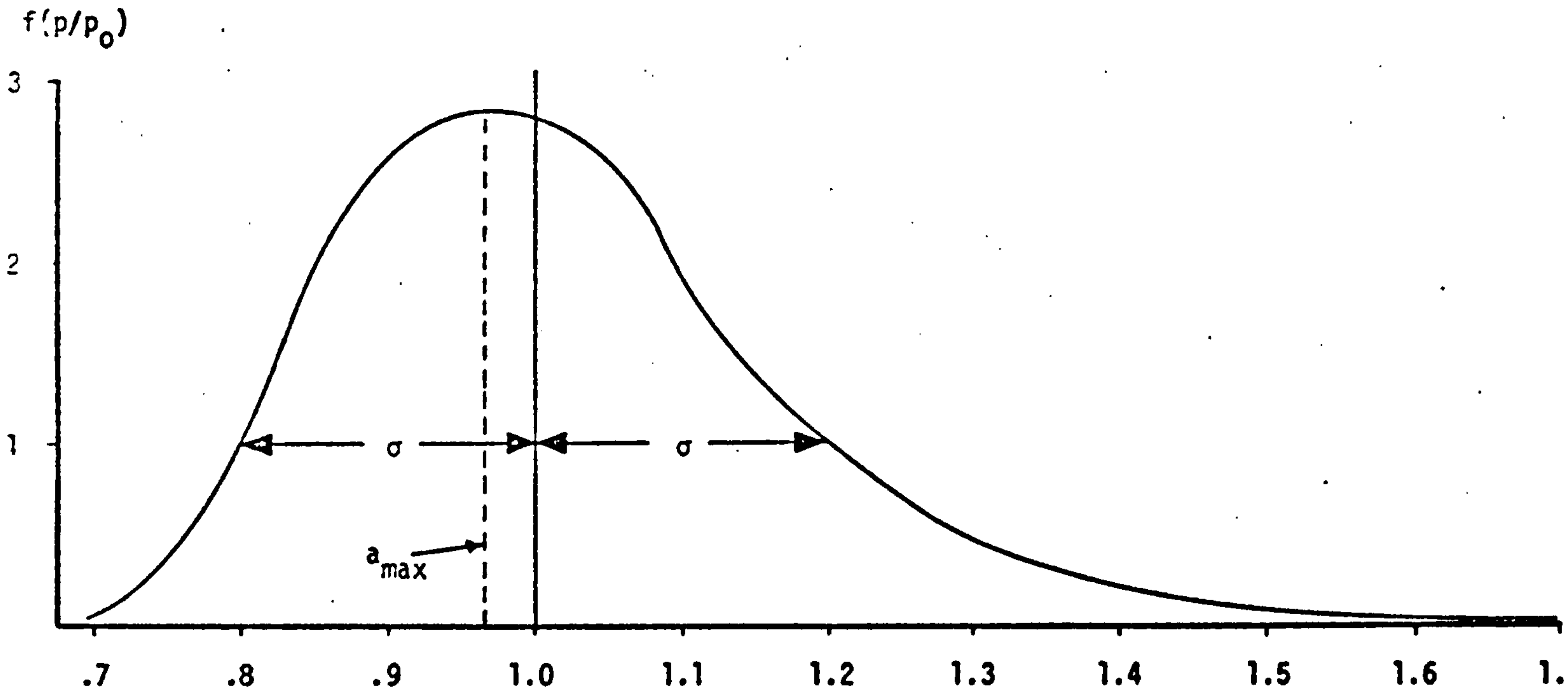

RELATIVE MOMENTUM, $a = p/p_o$

then the relative momentum density is found to be

$$f(a) = \frac{1}{\sqrt{2\pi}\,\sigma}\,\frac{e}{a^2}^{-\frac{1}{2\sigma^2}\left(\frac{a-1}{a}\right)^2} ; \quad \frac{1}{2} < a < \infty \tag{14}$$

The maximum value of f(a) is easily evaluated and gives

$$a_{max} = \frac{1}{4\sigma^2}\,[\sqrt{1+8\sigma^2} - 1] \tag{15}$$

Since $8\sigma^2$ is reasonably small we may write approximately

$$a_{max} \approx 1 - 2\sigma^2 + 4\sigma^2 + \ldots \approx .96 \tag{16}$$

The $n^{\underline{th}}$ moment of the relative momentum, a, can be found by:

$$\langle a^n \rangle = \frac{1}{\sqrt{2\pi}\,\sigma} \int_{\frac{1}{2}}^{\infty} a^{n-2} \quad e^{-\frac{1}{2\sigma^2}\left(\frac{a-1}{a}\right)^2} da \tag{17}$$

If we let

$$y = \frac{a-1}{a}$$

then (17) becomes

$$\langle a^n \rangle = \frac{1}{\sqrt{2\pi}\,\sigma} \int_{-\infty}^{\infty} \frac{e^{-\frac{1}{2}\left(\frac{y}{\sigma}\right)^2}}{(1-y)^n}\,dy \tag{18}$$

where we have let $1/\sigma \to \infty$ in the limits of the integral. Without evaluating (18) directly it is intuitive that

$$\langle p \rangle \gtrsim p_0 \tag{19}$$

$$\langle p^2 \rangle^{1/2} \simeq \sigma p_0 \tag{20}$$

If we define the <u>total-angle</u> to be

$$\phi_T = |\phi_B + \phi_x| \tag{21}$$

then the experimentally determined momentum, p, is found from ϕ_T by where we include only the region of eq. (6):

$$p = \frac{.3B_0S}{\phi_T} \tag{22}$$

Finally the total-angle probability density is easily found to be:

$$f(\phi_T) = \frac{1}{\sqrt{2\pi}\ \sigma\phi_B} e^{-\frac{1}{2\sigma^2}\left(\frac{\phi_T - \phi_B}{\phi_B}\right)^2} \tag{23}$$

Thus while the total-angle, ϕ_T, has a gaussian density, the corresponding momentum, p, is distributed by the more complicated equation (12).

We have developed expressions for momentum and total-angle probability densities f(p) and $f(\phi_T)$ by assuming that contributions from the region $-\infty < \phi_x < -\phi_B$ are negligible. In the next section we will include this region and calculate exact expressions for (12) and (23).

5.2.3.2 EXACT FORMS FOR THE MOMENTUM AND TOTAL-ANGLE DENSITIES

We may write the total-angle, eq. (5.2.3.1.21) as

$$\begin{aligned} \phi_T &= \phi_B + \phi_X \;; \quad -\phi_B < \phi_X < \infty \quad \text{REGION 1} \\ \phi_T &= -(\phi_B + \phi_X) \;; \quad -\infty < \phi_X < -\phi_B \quad \text{REGION 2} \end{aligned} \tag{1}$$

where we have separated the ϕ_X domain into two regions (see FIG. 5.7). We see that the total-angle is monotonically increasing in region 1 and monotonically decreasing in region 2. This allows one to write for the total-angle probability density[21]

$$f(\phi_T) = f_1(\phi_X)\left|\frac{d\phi_X}{d\phi_T}\right|_1 + f_2(\phi_X)\left|\frac{d\phi_X}{d\phi_T}\right|_2 \tag{2}$$

Using the above we may easily find the exact total-angle density, i.e. we include effects in the region $-\infty<\phi_X<-\phi_B$. The second term in (2) is given by (5.2.3.1.23) while the first is obtained by changing the sign of ϕ_T in (5.2.3.1.23), hence the exact total-angle density is

$$f(\phi_T|\sigma,\phi_B) = \frac{1}{\sqrt{2\pi}\,\sigma\phi_B} e^{-\frac{1}{2\sigma^2}\left(\frac{\phi_T-\phi_B}{\phi_B}\right)^2} + \frac{1}{\sqrt{2\pi}\,\sigma\phi_B} e^{-\frac{1}{2\sigma^2}\left(\frac{\phi_T+\phi_B}{\phi_B}\right)^2} \tag{3}$$

5.2.3.2.2

FIG. 5.7 THE MULTIPLE SCATTERING DENSITY AND TOTAL ANGLE AS A FUNCTION OF PROJECTED SCATTERING ANGLE

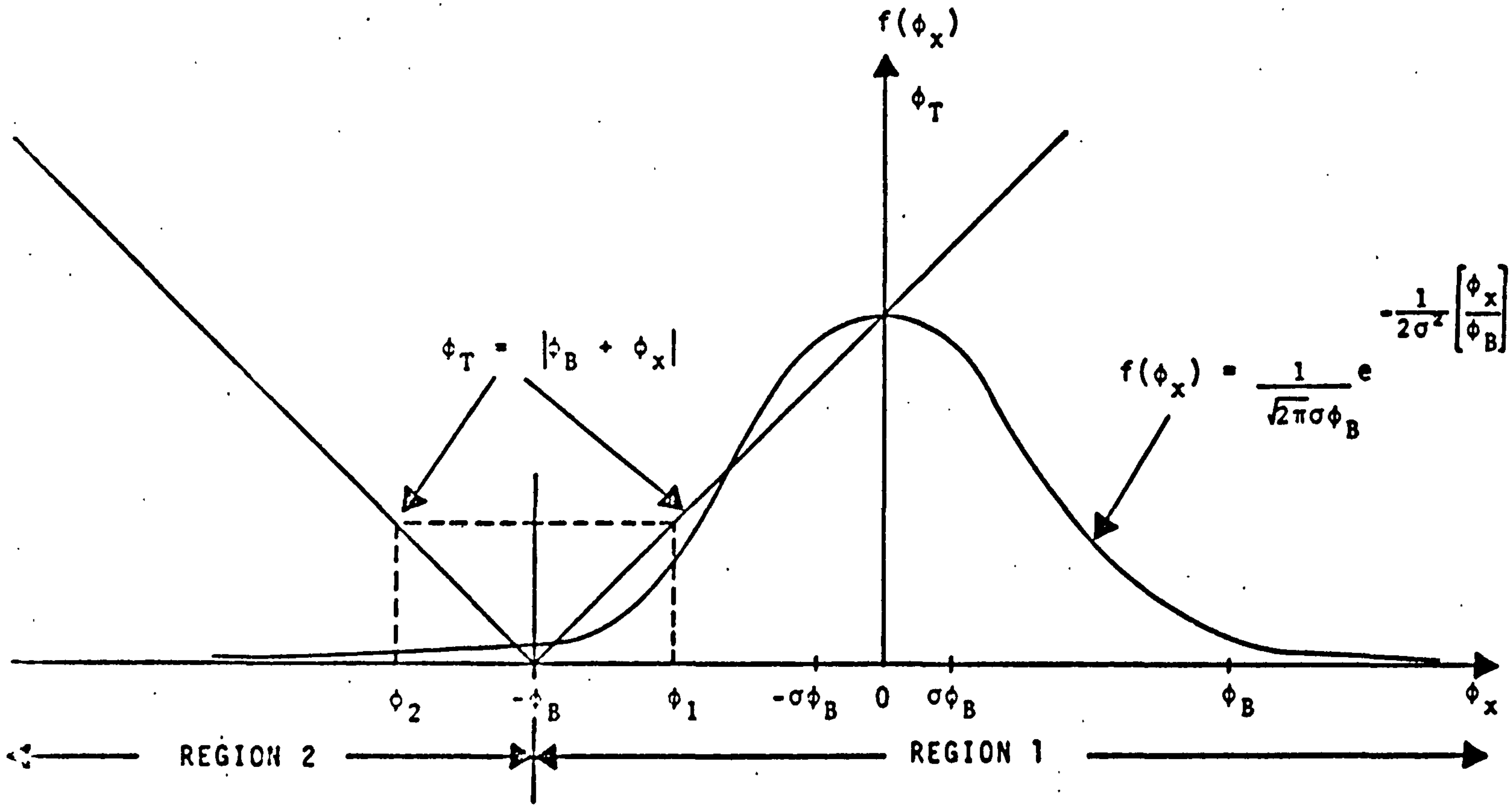

$f(\phi_x)$
ϕ_T
$\phi_T = |\phi_B + \phi_x|$
$f(\phi_x) = \frac{1}{\sqrt{2\pi}\sigma\phi_B} e^{-\frac{1}{2\sigma^2}\left[\frac{\phi_x}{\phi_B}\right]^2}$
ϕ_2
$-\phi_B$
ϕ_1
$-\sigma\phi_B$
0
$\sigma\phi_B$
ϕ_B
ϕ_x
REGION 2
REGION 1

where $0 < \phi_T < \infty$. Eq. (3) is graphed in FIG. 5.8. The first term is a gaussian of width $\sigma\phi_B$ centered at ϕ_B, while the second term also has width $\sigma\phi_B$, but is centered at $-\phi_B$. We see that $f(\phi_T)$ is just the sum of the two curves in the region $0 < \phi_T < \infty$; thus no negative values of ϕ_T are allowed since, experimentally, one assumes the total-angle to be positive to insure that the corresponding momentum is positive. If σ is sufficiently small we may neglect the second term of (3) to obtain

$$f(\phi_T|\sigma,\phi_B) \simeq \frac{1}{\sqrt{2\pi}\ \sigma\phi_B}\, e^{-\frac{1}{2\sigma^2}\left(\frac{\phi_T-\phi_B}{\phi_B}\right)^2} \ ; \ \sigma \ll 1 \ ; \ 0 < \phi_T < \infty \qquad (4)$$

which is the approximate result obtained before, (5.2.3.1.23).
Using the fact that $p = k_0/\phi_T$ we find directly from (3)

$$f(p|\sigma,p_0) = \frac{1}{\sqrt{2\pi}\sigma}\frac{p_0}{p^2}\, e^{-\frac{1}{2}\left(\frac{p_0}{\sigma}\right)^2\left(\frac{1}{p}-\frac{1}{p_0}\right)^2} + \frac{1}{\sqrt{2\pi}\sigma}\frac{p_0}{p^2}\, e^{-\frac{1}{2}\left(\frac{p_0}{\sigma}\right)^2\left(\frac{1}{p}+\frac{1}{p_0}\right)^2} \qquad (5)$$

for $0<p<\infty$.

Again, when $\sigma \ll 1$ we get

$$f(p|\sigma,p_0) = \frac{1}{\sqrt{2\pi}\sigma}\frac{p_0}{p^2}\, e^{-\frac{1}{2}\left(\frac{p_0}{\sigma}\right)^2\left(\frac{1}{p}-\frac{1}{p_0}\right)^2} \ ; \ \sigma \ll 1 \ ; \ 0<p<\infty \qquad (6)$$

which we obtained earlier in (5.2.3.1.12)

FIG. 5.8 TOTAL-ANGLE DENSITY: THE SUM OF TWO GAUSSIAN DENSITIES

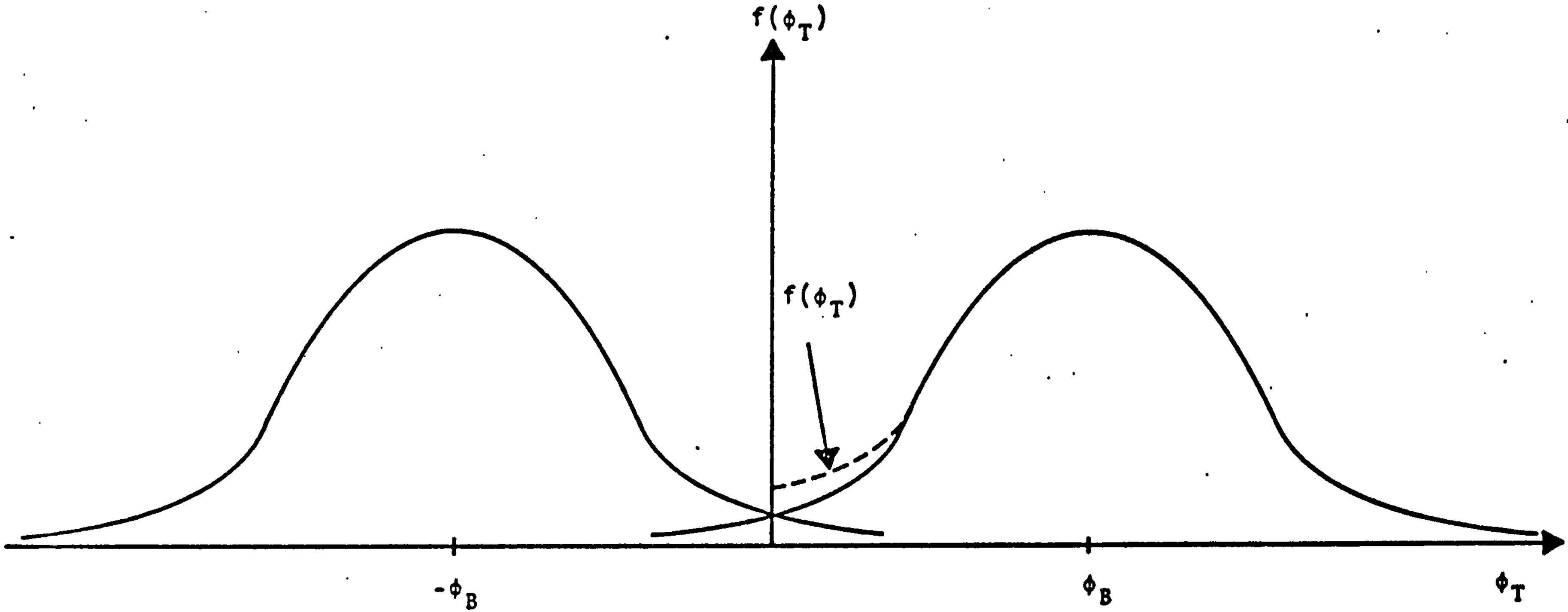

f(ϕT)
f(ϕT)
-ϕB
ϕB
ϕT

Before continuing to the next section we recall the relationships between the following variables:

p_o = real momentum of the incident particle.

ϕ_B = bending angle of the incident particle neglecting multiple scattering and hence corresponds to p_o.

p = experimentally determined momentum.

ϕ_T = experimentally measured deflection angle (due to bending plus scattering) of the incident particle and corresponds to momentum p.

Therefore

$$p_o = \frac{k_o}{\phi_B} \; ; \; p = \frac{k_o}{\phi_T}$$

While we can measure ϕ_T and hence calculate p, we have as yet no knowledge about ϕ_B and p_o. Equations (3) and (5) can only be used if particular values of ϕ_B and p_o are assumed. Thus, ultimately, we must fold the probability density in ϕ_B (or p_o) with the density in ϕ_T (or p). This will require knowledge of the momentum spectrum of the incoming cosmic ray muon flux. However, we delay these considerations until a later section.

5.2.4 THE EFFECTS OF MOMENTUM LOSS

Previously we have ignored ionization energy loss. Here we examine how the relative momentum uncertainty, σ, varies as the incident muon loses energy in the magnet iron. To this end we first determine how the magnetic deflection angle is affected by momentum loss.

For a differential thickness of target material, ds, the particle undergoes a net magnetic deflection, $d\phi_B$:

$$d\phi_B = \frac{.3B_0 ds}{p} \qquad (1)$$

If energy loss occurs then we expect $p = p(s)$. Integrating eq. (1) leads to

$$\phi_B = \frac{k(s,p_0)}{p_0} \qquad (2)$$

where

$$k(s,p_0) = k_0 I(s,p_0) \qquad (3)$$

$$k_0 = .3B_0 s \qquad (4)$$

$$I(s,p_0) = \frac{p_0}{s}\int_0^s \frac{ds'}{p(s';p_0)} \qquad (5)$$

Here

ϕ_B = net magnetic deflection angle.

s = target thickness in cm.

p_0 = entry momentum of the particle, MeV/c.

From eq. (5) we see that if no momentum loss occurs $I(s,p_0) = 1$ and

$$\phi_B = \frac{k_0}{p_0} \qquad (6)$$

which is the expression that we have used before for no momentum loss.

For constant momentum loss we have

$$p(s) = p_o - \frac{dp}{ds} s \quad ; \quad \frac{dp}{ds} = \text{CONSTANT} \tag{7}$$

Thus for eq. (5) we get

$$I(s,p_o) = \frac{p_o}{s} \int_0^s \frac{ds'}{p_o - cs'} \tag{8}$$

where we have let $c = dp/ds$.

Integration of (8) leads to

$$I(s,p_o) = \frac{k(s,p_o)}{k_o} = \frac{1}{\varepsilon} \ln(1-\varepsilon)^{-1} \tag{9}$$

where

$$\varepsilon = \frac{\Delta p_o}{p_o}$$

is the fractional momentum loss of the particle and Δp_o is the total momentum loss:

$$\Delta p_o = \frac{dp}{ds} s \tag{11}$$

If the fractional momentum loss is small we may expand (9) in a Taylor series to obtain

$$I(s,p_o) = \frac{k(s,p_o)}{k_o} = 1 + \frac{\varepsilon}{2} + \frac{\varepsilon^2}{3} + \ldots \tag{12}$$

For constant momentum loss we have finally for the magnetic bending angle

$$\phi_B = \frac{k_o}{p_o}\left[\frac{1}{\varepsilon} \ln(1-\varepsilon)^{-1}\right] \tag{13}$$

which, for $\varepsilon \ll 1$, reduces to

$$\phi_B = \frac{k_o}{p_o}\left[1 + \frac{\varepsilon}{2} + \frac{\varepsilon^2}{3} + \ldots\right] \tag{14}$$

If the momentum loss is linear

$$-\frac{dp}{ds} = a + bp,$$

(where a and b are constants) then to an excellent degree of approximation eqs. (13) and (14) are still true if we let

$$\Delta p_o \cong (a+bp_o)s \tag{15}$$

Next we examine how the rms multiple scattering angle, σ_ϕ, varies as a function of momentum loss. Recall that σ_ϕ, for constant momentum loss, was found by Eyges[11] to be:

$$\sigma_\phi = \frac{15}{\sqrt{p_o p_1}}\sqrt{\frac{s}{s_o}} \tag{16}$$

The momentum p_o is the entry momentum and p_1 is the exit momentum of the particle after traversing a target of thickness, s, and radiation length, s_o. We may write p_1, for constant momentum loss, as

$$p_1 = p_o(1-\varepsilon). \tag{17}$$

Hence (16) becomes

$$\sigma_\phi = \sigma_{\phi o}(1-\varepsilon)^{-1/2} \tag{18}$$

where

$$\sigma_{\phi o} = \frac{15}{p_o}\sqrt{\frac{s}{s_o}} \tag{19}$$

is the rms multiple scattering angle for no momentum loss.

For small ε we expand (19) in a series:

$$\sigma_\phi = \sigma_{\phi 0}[1 + \frac{\varepsilon}{2} + \frac{3\varepsilon^2}{8} + \ldots]. \qquad (20)$$

Finally, we are able to determine the relative momentum uncertainty due to multiple scattering from (13) and (18)

$$\sigma(p) = \frac{\sigma_\phi}{\phi_B} = \sigma_0 \frac{\varepsilon}{\sqrt{1-\varepsilon}\,\ell n(1-\varepsilon)^{-1}} \qquad (21)$$

where

$$\sigma_0 = \frac{50}{\sqrt{s_0}} \; \frac{1}{B_0\sqrt{s}} \qquad (22)$$

is the relative momentum uncertainty for no momentum loss. When the fractional momentum loss, ε, is small we obtain from (14) and (20)

$$\sigma(p) = \sigma_0[1 + \frac{\varepsilon}{2} + \frac{3\varepsilon^2}{8} + \ldots]/[1 + \frac{\varepsilon}{2} + \frac{\varepsilon^2}{3} + \ldots] \qquad (23)$$

Thus for small ε we do not expect $\sigma(p)$ to be very momentum dependent. In fact for the AMH magnetic spectrometer (with a target thickness of about 725 gm/cm^2, sufficient to stop a 1.2 GeV/c muon) we find for an incident momentum of 2.4 GeV/c that $\sigma/\sigma_0 \sim 1.02$. Thus even at this low momentum σ does not vary by more than 2%. We conclude that $\sigma(p)$ can be assumed to be constant over the momentum range of interest 2.5 GeV/c $\leq p_0 < \infty$.

We now investigate how the momentum and total angle densities (eqs. (5.2.3.2.6) and (5.2.3.2.4) are altered by momentum loss. First, since $\sigma(p)$ = constant, we see that the total angle density remains unchanged. However we must determine the momentum density from

$$\phi_T = \frac{k(s,p)}{p} \tag{24}$$

where now $k(s,p) \neq$ constant. Taking the derivative we get

$$\left|\frac{d\phi_T}{dp}\right| = \frac{k}{p^2}\left[1 - \frac{p}{k}\frac{dk}{dp}\right] \tag{25}$$

where

$$k(s,p) = k_o I(s,p) \tag{26}$$

$$I(s,p) = \frac{p}{s}\int_0^s \frac{ds'}{p'(s')} \tag{27}$$

This leads to a momentum density (when $\sigma \ll 1$) of

$$f(p) = \frac{1}{\sqrt{2\pi}\,\sigma}\, I(s,p)\left[1 - \frac{p}{I}\frac{dI}{dp}\right]\frac{p_o}{p^2}\, e^{-\frac{1}{2}\left(\frac{p_o}{\sigma}\right)^2\left(\frac{I}{p} - \frac{1}{p_o}\right)^2} \tag{28}$$

This may be compared to the previously derived result, eq. (5.2.3.2.6), which was developed for no momentum loss.

Eq. (28) may be greatly simplified if we assume that momentum loss is constant. We find that

$$k(s,p) = \frac{k_o}{\varepsilon}\,\ell n(1-\varepsilon)^{-1} \tag{29}$$

$$I(s,p) \simeq 1 + \frac{\varepsilon}{2} \tag{30}$$

$$\left|\frac{d\phi_T}{dp}\right| = \frac{k_0}{p^2}(1-\varepsilon)^{-1} \approx \frac{k_0}{p^2}(1+\varepsilon) \qquad (31)$$

The momentum density for constant momentum loss is then, approximately,

$$f(p|p_0) \cong \frac{1}{\sqrt{2\pi}\,\sigma}\frac{p_0}{p^2}\frac{e^{-\frac{1}{2}\left(\frac{p_0}{\sigma}\right)^2\left[\frac{1+\varepsilon/2}{p}-\frac{1}{p_0}\right]^2}}{(1-\varepsilon)} \qquad (32)$$

It is easy to see that eq. (32) becomes the simpler form used previously when $\varepsilon \to 0$.

In order to verify the utility of (32) a Monte Carlo investigation of multiple scattering in the AMH magnetic spectrometer was made. A total of 1000 muon trajectories of momentum 10 GeV/c were calculated by numerical integration of the muon relativistic equation of motion. The computer simulation included the effects of magnetic bending, ionization energy loss and multiple scattering. After each step in the numerical integration the muon direction was randomly scattered according to eqs. (5.2.3.6-7). The trajectories generated in the above fashion were then submitted to the χ^2 momentum determination program described in Sec. 3.5.2. Finally, the momentum histogram for the 1000 simulated trajectories was fitted to the momentum probability density, eq. (32) using the χ^2 minimization technique. The result of this fit is shown in Fig. 5.9.

FIG. 5.9 MONTE CARLO MOMENTUM DISTRIBUTION FOR THE MAGNETIC SPECTROMETER

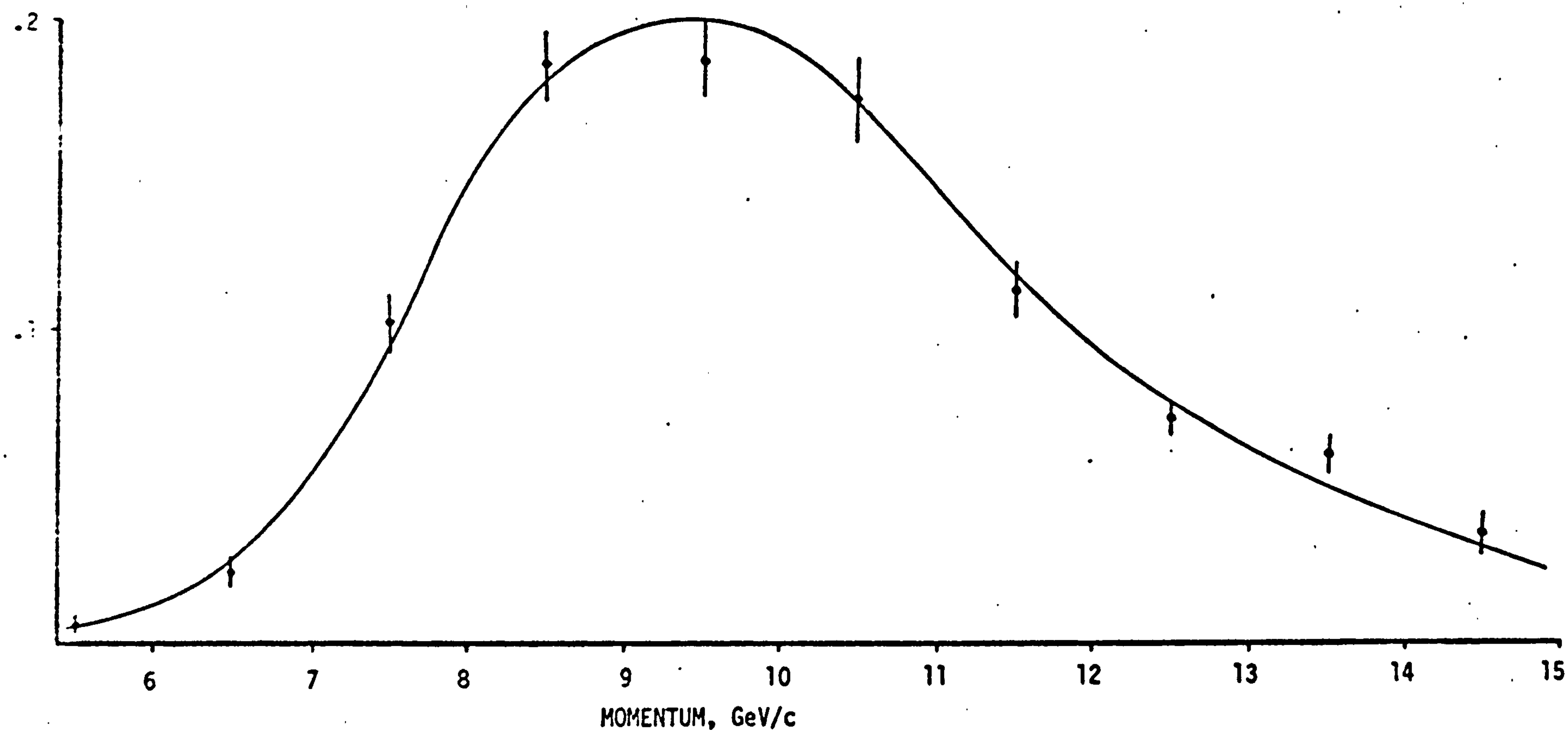
.2
.1
6
7
8
9
10
11
12
13
14
15
MOMENTUM, GeV/c

The fit parameters were taken to be the real momentum, p_0, and the momentum uncertainty, σ. The values resulting from the fit were $p_0 = 10.0 \pm .8$, $\sigma = .22 \pm .01$ with a reduced χ^2 of .89. The real values were $p_0 = 10.0$ and $\sigma = .217$.

In this section we have determined that, even when momentum loss is taken into consideration, the relative momentum uncertainty, σ, remains a constant. Furthermore

(1) the total-angle probability density remains unchanged, while

(2) the momentum density becomes much more complicated.

In fact the momentum probability density does not have an analytic form for the most generalized expressions of momentum loss. We shall therefore use the probability density in total-angle, rather than the probability density in momentum, in all future calculations.

5.2.5 MODIFICATION OF THE GAUSSIAN THEORY

Recall that the relative scattering parameter, α_0, can be written two ways

$$\alpha_0 = f(p_0)p_0\phi_x = \frac{1}{\sigma}\frac{\phi_x}{\phi_B} \tag{1}$$

where the first is in terms of the incident particle momentum, p_0, and the second is in terms of the corresponding bending angle, ϕ_B. Here we assume

$$p_o = \frac{k(s,p_o)}{\phi_B} \qquad (2)$$

which is a transcendental equation in p_o. We have discussed previously that ϕ_B and hence p_o are not measurable with the magnetic spectrometer. Only the "experimentally measured total-angle", ϕ_T can be determined and hence the "experimentally measured momentum", p, can then be found from

$$p = \frac{k(s,p)}{\phi_T} \qquad (3)$$

We have seen that p is a random variable given by a well defined probability density, eq. (5.2.4.28). This leads to a new definition for the relative scattering parameter:

$$\alpha = f(p)p\,\phi_y = \frac{1}{\sigma}\,\frac{\phi_y}{\phi_T} \qquad (4)$$

where we now use the experimentally determined value of momentum, p, and the total-angle, ϕ_T, rather than the assumed true values, p_o and ϕ_B. It is clear that the probability density in α is not a gaussian probability density, and thus it is our goal to discover this new density. We will assume that the new relative scattering parameter, α, does not have the same probability density as that for α_o, because the experimentally determined momentum, p, is a random variable distributed about the real momentum, p_o, or stated differently, because the experimentally determined total-angle, ϕ_T, is distributed about the real bending angle, ϕ_B. Thus in order to discover the new probability density in α we may use (1) $\alpha = f(p)p\phi_y$, so that knowledge of the densities of p and ϕ_y will allow $f(\alpha)d\alpha$ to be discovered, or (2) $\alpha = \frac{1}{\sigma}\frac{\phi_y}{\phi_T}$, and hence knowledge of the densities of ϕ_T and ϕ_y allows $f(\alpha)d\alpha$ to be calculated. Either of these methods is sufficient for our needs and both should yield the same resultant density in α. Since the second of the two methods is mathematically simpler, we shall pursue a determination of the density in terms of

$$\alpha = \frac{1}{\sigma}\frac{\phi_S}{\phi_T} \tag{5}$$

where we have let $\phi_S \equiv \phi_y$. Thus ϕ_S is the multiple scattering angle as measured in the spectrometer no-field view. ϕ_T is the total-angle (due to multiple scattering plus magnetic bending) measured in the spectrometer field-view. Hence the scattering parameter, α, is proportional to the ratio of the no-field view angle to the field view angle. The approximate no-field view density in scattering angle is

$$f(\phi_S|\phi_B) = \frac{1}{\sqrt{2\pi}\ \sigma\phi_B}\, e^{-\frac{1}{2\sigma^2}\left(\frac{\phi_S}{\phi_B}\right)^2} \tag{6}$$

while the field view density in total angle is

$$f(\phi_T|\phi_B) = \frac{1}{\sqrt{2\pi}\ \sigma\phi_B}\, e^{-\frac{1}{2\sigma^2}\left(\frac{\phi_T-\phi_B}{\phi_B}\right)^2} \tag{7}$$

The variables ϕ_S, ϕ_T and ϕ_B, can be seen in Fig. 5.10. Here we have defined:

$f(\phi_S|\phi_B)d\phi_S$ = probability of a muon of momentum $p_0(=k(s,p_0)/\phi_B)$ entering the spectrometer and being scattered into $(\phi_S, \phi_S + d\phi_S)$ in the no-field view.

$f(\phi_T|\phi_B)d\phi_T$ = probability of a muon of momentum p_0 $(=k(s,p_0)/\phi_B)$ entering the spectrometer and being scattered and magnetically bent into total angle $(\phi_T, \phi_T + d\phi_T)$ in the field view.

We may form the joint density in ϕ_S and ϕ_T by

$J(\phi_S,\phi_T|\phi_B)d\phi_S d\phi_T = f(\phi_T|\phi_B)f(\phi_S|\phi_B)d\phi_S d\phi_T$ = probability of a muon of momentum $p_0(=k(s,p_0)/\phi_B)$ entering the spectrometer and being scattered into $(\phi_S, \phi_S + d\phi_S)$ in the no-field view AND being scattered and magnetically bent into $(\phi_T, \phi_T + d\phi_T)$ in the field view.

Thus

$$J(\phi_S,\phi_T|\phi_B) = \frac{1}{2\pi(\sigma\phi_B)^2}\, e^{-\frac{1}{2\sigma^2}\left[\left(\frac{\phi_S}{\phi_B}\right)^2 + \left(\frac{\phi_T-\phi_B}{\phi_B}\right)^2\right]} \qquad (8)$$

We now seek the density in α (eq. (5)). To this end we write

$$\int_{-\infty}^{\alpha} f(\alpha')d\alpha' = \iint_R J(\phi_S,\phi_T|\phi_B)d\phi_S\, d\phi_T \qquad (9)$$

where $f(\alpha)$ is the density in α. The region R in ϕ_S-ϕ_T space corresponding to $(-\infty,\alpha)$ in α space can be seen in FIG. 5.11. Thus eq. (9) becomes

$$\int_{-\infty}^{\alpha} f(\alpha')d\alpha' = \int_{0}^{\phi_{T_{max}}} \int_{-\infty}^{\sigma\alpha\phi_T} J(\phi_S,\phi_T|\phi_B)d\phi_S d\phi_T \qquad (10)$$

Differentiation with respect to α yields

$$f(\alpha) = \sigma \int_{0}^{\phi_{T_{max}}} \phi_T J(\sigma\alpha\phi_T,\phi_T|\phi_B)d\phi_T \qquad (11)$$

The upper limit on the integral corresponds to the maximum total-angle possible, or the lowest measurable momentum. Because of momentum loss any muon which enters with $p \lesssim 1.2$ GeV/c is absorbed by the magnet iron. Thus a cutoff momentum, p_c, is defined by

$$p_c = \frac{k(s,p_c)}{\phi_{T_{max}}} \qquad (12)$$

such that no values of $\phi_T > \phi_{T_{max}}$ are allowed. These values of ϕ_T correspond to values of momentum $< p_c \simeq 1.2$ GeV/c. If we put (8) into (11) we get:

$$f(\alpha) = \frac{1}{2\pi\ \sigma\phi_B} \int_{0}^{\phi_{T_{max}}} \left(\frac{\phi_T}{\phi_B}\right) e^{-\frac{1}{2\sigma^2}\left(\frac{\phi_T-\phi_B}{\phi_B}\right)^2 - \frac{\alpha^2}{2}\left(\frac{\phi_T}{\phi_B}\right)^2} d\phi_T \qquad (13)$$

If we let $x = \phi_T/\phi_B$ eq. (13) becomes

$$f(\alpha) = \frac{1}{2\pi\sigma} \int_{0}^{X_{max}} x e^{-\frac{1}{2}\left(\frac{x-1}{\sigma}\right)^2 - \frac{\alpha^2 x^2}{2}} dx \qquad (14)$$

where

$$X_{max} = \frac{\phi_{T_{max}}}{\phi_B} = \frac{k(s,p_c)}{k(s,p_o)} \frac{p_o}{p_c} \tag{15}$$

For linear momentum loss

$$X_{max} = \frac{\Delta p_o}{\Delta p_c} \frac{\ln(1-\varepsilon_c)}{\ln(1-\varepsilon_o)} \tag{16}$$

$$\varepsilon_c = \frac{\Delta p_c}{p_c} \quad ; \quad \varepsilon_o = \frac{\Delta p_o}{p_o} \tag{17}$$

$$\begin{aligned} \Delta p_c &\simeq (a + bp_c)s \\ \Delta p_o &\simeq (a + bp_o)s \end{aligned} \tag{18}$$

When $p_o = p_c$, $X_{max} = 1$ and when $p_o \gg p_c$, $X_{max} \simeq p_o/p_c$, for small ε_c.

By completing the square in the exponent of eq. (14) we obtain

$$f(\alpha) = \frac{1}{2\pi\sigma} e^{-\frac{1}{2}\left(\frac{\alpha^2}{(1+\sigma^2\alpha^2)}\right)} \int_0^{X_{max}} x e^{-\frac{1}{2}\left(\frac{x - x_o}{2\sigma_1}\right)^2} dx \tag{19}$$

where

$$x_o = \frac{1}{1+\sigma^2\alpha^2} \quad ; \quad \sigma_1 = \frac{\sigma}{(1+\sigma^2\alpha^2)^{1/2}} \tag{20}$$

If we assume that X_{max} is sufficiently large and that σ is sufficiently small eq. (19) can be integrated exactly to obtain

FIG. 5.10 SPECTROMETER FIELD AND NO-FIELD VIEW SCATTERING VARIABLES

FIG. 5.11 DOMAIN OF (ϕ_S,ϕ_T) INTEGRATION

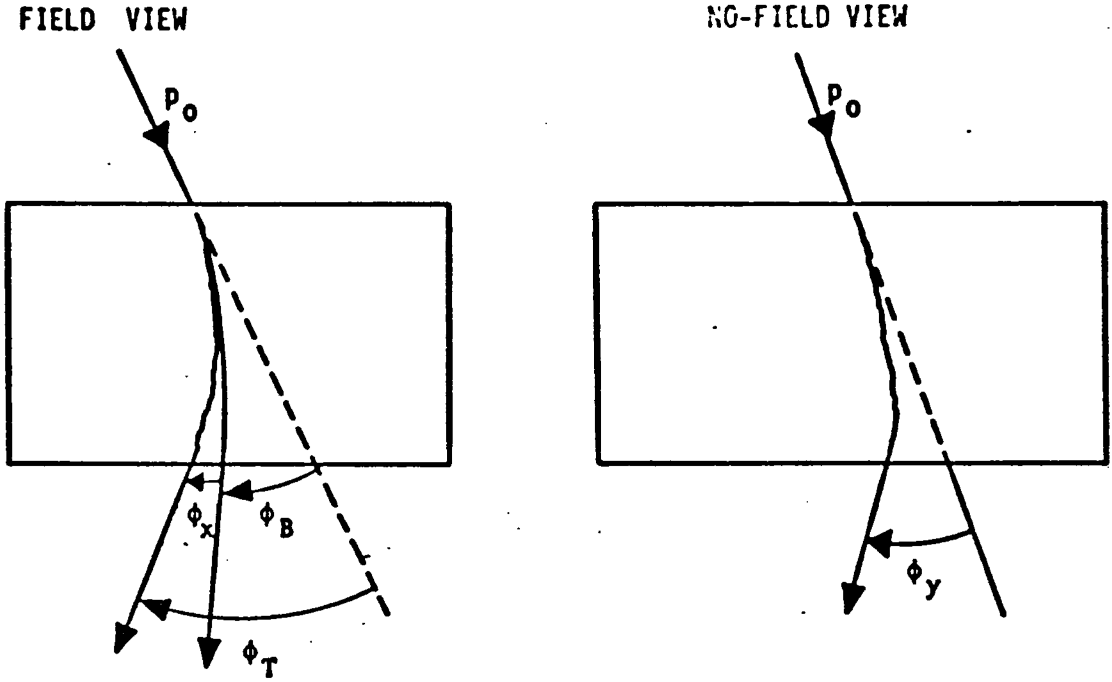
FIELD VIEW
NO-FIELD VIEW
p_o
p_o
ϕ_x
ϕ_B
ϕ_T
ϕ_y

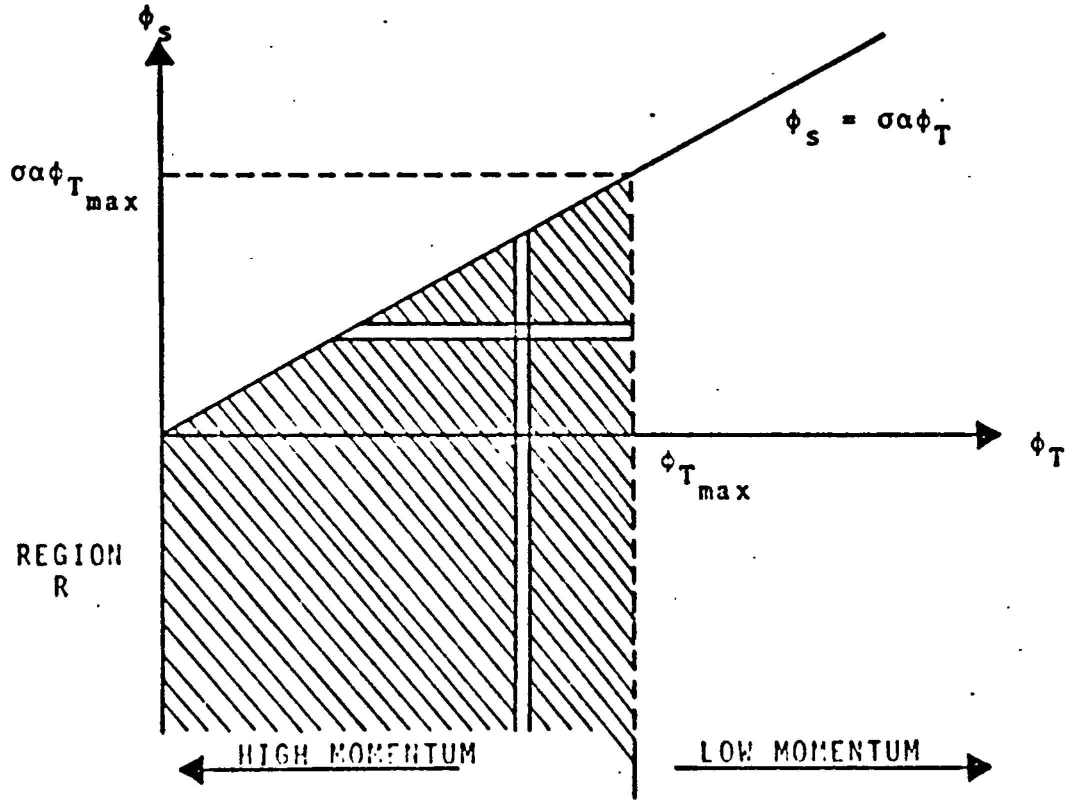
ϕ_s
$\sigma\alpha\phi_{T_{max}}$
$\phi_s = \sigma\alpha\phi_T$
ϕ_T
$\phi_{T_{max}}$
REGION R
HIGH MOMENTUM
LOW MOMENTUM

$$f(\alpha|\sigma) = \frac{1}{\sqrt{2\pi}} \frac{e^{-\frac{1}{2}\frac{\alpha^2}{(1+\sigma^2\alpha^2)}}}{(1+\sigma^2\alpha^2)^{3/2}} \tag{21}$$

If we examine momenta > 2 GeV and use $\sigma = .2$ we find that numerical integration of (19) gives results which compare favorably with (21). The error is found to increase with α but is found not to exceed .2% at $\alpha = 7$, i.e. approximately 7 standard deviations.

Fig. 5.12 compares the gaussian density in α_0 to the corrected density in α, eq. (21). We see that the corrected density is lower in the region near $\alpha = 1$ but is greater for $\alpha \gtrsim 2$. Thus the corrected density is characterized by a "tail" at large α. Notice also that if σ is set to zero in (21) we obtain the gaussian density in α_0. This is equivalent to removing the momentum uncertainty due to multiple scattering and is tantamount to replacing the momentum density, eq. (5.2.4.28) and the total-angle density, eq. (7), by Dirac delta functions and then evaluating eq. (11) as before. In fact we shall ultimately require

$$\lim_{\sigma \to 0} f(\alpha|\sigma) = f_{mol}(\alpha) \tag{22}$$

where $f_{mol}(\alpha)$ is the Molière density and $f(\alpha|\sigma)$ is the Molière density corrected for uncertainty in momentum determination. The corrected Molière density will be

FIG. 5.12 MODIFICATION TO THE SIMPLE GAUSSIAN THEORY, $\sigma = .2$

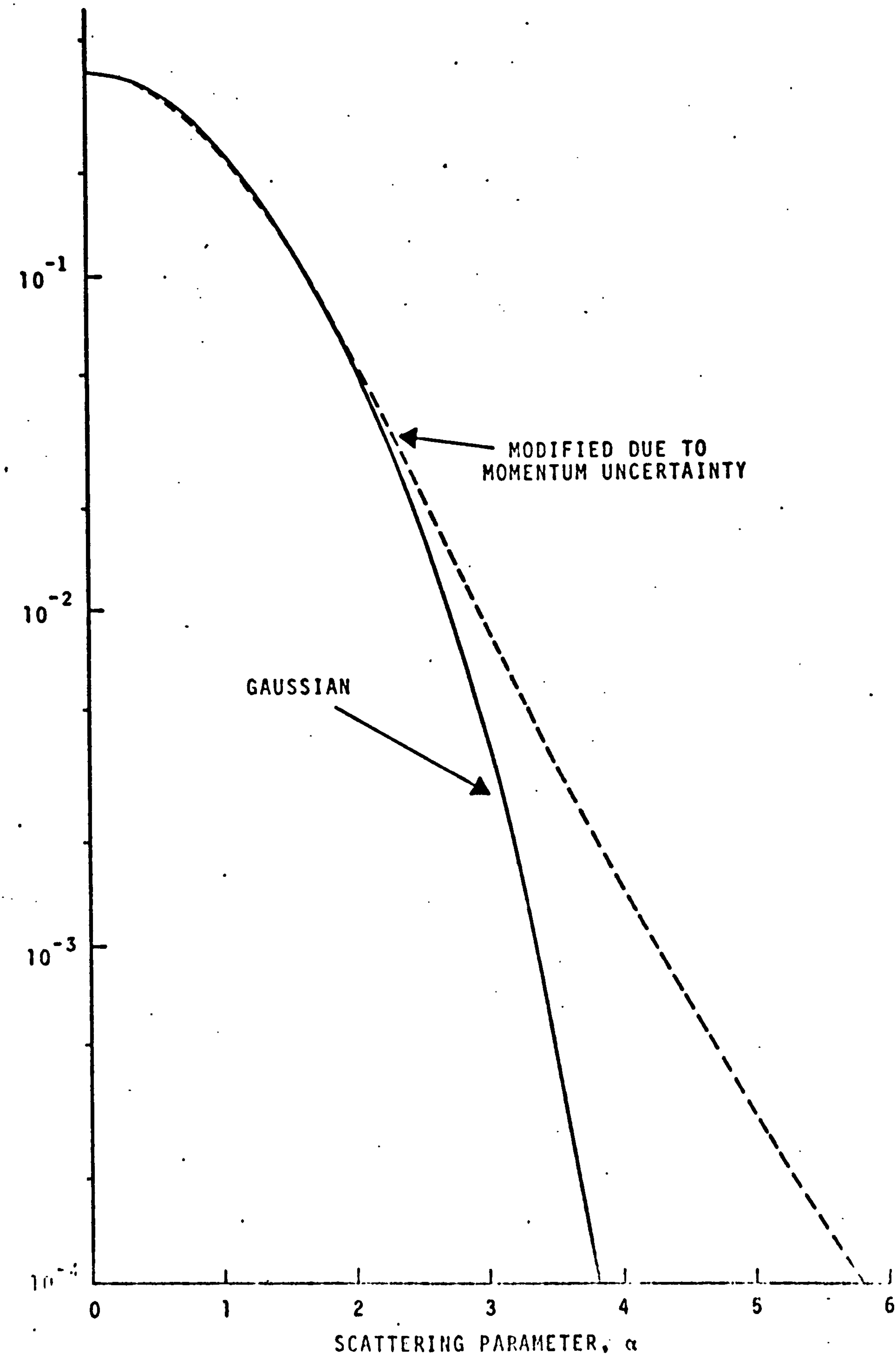

MODIFIED DUE TO MOMENTUM UNCERTAINTY
GAUSSIAN
10^{-1}
10^{-2}
10^{-3}
0
1
2
3
4
5
6
SCATTERING PARAMETER, α

developed in a later section.

Another feature of eq. (21) can be noted: it is not a function of ϕ_B (and thus not a function of p_0) and is therefore not a function of the cosmic ray muon momentum spectrum. This is a most fortunate circumstance (because an integration over the cosmic ray spectrum is not required) and will be investigated further in Sec. 5.2.7.

Before proceeding to the next section we examine what effect the approximation eq. (7) has caused in the development of $f(\alpha|\sigma)$. Recall that the exact form of (7) is given by (5.2.3.2.3). Thus our calculation of $f(\alpha|\sigma)$ has excluded scattering in the region $-\infty<\phi_x<-\phi_B$. Use of (5.2.3.2.3) allows $f(\alpha|\sigma)$ to be calculated exactly:

$$f(\alpha|\sigma) = f_-(\alpha|\sigma) + f_+(\alpha|\sigma) \tag{23}$$

where

$$f_{\mp}(\alpha|\sigma) = \frac{1}{2\pi\sigma} e^{-\frac{1}{2}\frac{\alpha^2}{(1+\sigma^2\alpha^2)}} \int_0^{X_{max}} x e^{-\frac{1}{2}\left(\frac{x \mp x_0}{\sigma_1}\right)^2} dx \tag{24}$$

Evaluation of the above leads to

$$f_{\mp}(\alpha|\sigma) = \frac{1}{\sqrt{2\pi}} \frac{e^{-\frac{1}{2}\frac{\alpha^2}{(1+\sigma^2\alpha^2)}}}{(1+\sigma^2\alpha^2)^{3/2}} \; g_{\mp}(\alpha|\sigma) \tag{25}$$

where

$$g_{\mp}(\alpha|\sigma) = \frac{1}{\sqrt{2\pi}}\left[\sigma(1+\sigma^2\alpha^2)\left(e^{-\frac{Z^2_{min}}{2}} - e^{-\frac{Z^2_{max}}{2}}\right) \mp \int_{Z_{min}}^{Z_{max}} e^{-\frac{Z^2}{2}}\, dZ\right] \tag{26}$$

$$Z_{min} = \pm \frac{x_o}{\sigma_1} \tag{27}$$

$$Z_{max} = \frac{X_{max} \pm x_o}{\sigma_1} \; ; \; X_{max} = \frac{\phi_{T\ max}}{\phi_B} \tag{28}$$

Notice that there is a slight dependence upon ϕ_B in (25) through (28); however, this effect is small. Numerical integration of eqs. (25) - (28) yields results consistent with (21) to within 2% (at α=7) for different values of ϕ_B. The total error in eq. (21), due to all of the sources mentioned, does not exceed 3% for values of α>5. These errors are considered negligible because (1) the data in this region has errors ~50%, and (2) the Molière correction terms for $\alpha \geq 3$ completely dominate the tail region of eq. (21). These points will be considered in greater detail in later sections.

5.2.6 THE EFFECTS OF UNCERTAINTY IN ANGLE MEASUREMENT

In this section we consider the effect that angle measurement uncertainty has on the multiple scattering density, $f(\alpha)$. First we shall assume that there is some measurement error in the total-angle, ϕ_T, say $\Delta\phi$. Then the measured total angle, ϕ_{TM}, is distributed by

$$f(\phi_{TM}|\phi_T) = \frac{1}{\sqrt{2\pi}\,\Delta\phi}\, e^{-\frac{1}{2}\left(\frac{\phi_{TM}-\phi_T}{\Delta\phi}\right)^2} \tag{1}$$

Recall that the total angle density in the spectrometer field-view is given by

$$f(\phi_T|\phi_B) = \frac{1}{\sqrt{2\pi}\,\sigma\phi_B}\, e^{-\frac{1}{2}\left(\frac{\phi_T-\phi_B}{\sigma\phi_B}\right)^2} \tag{2}$$

All of the variables of (1) and (2) are shown in Fig. 5.13. We now seek the density in the measured total-angle, which is obtained by integrating the product of (1) and (2) over the total-angle, ϕ_T, to obtain

$$f(\phi_{TM}|\phi_B) = \frac{1}{\sqrt{2\pi}\,\sigma_n\phi_B}\, e^{-\frac{1}{2}\left(\frac{\phi_{TM}-\phi_B}{\sigma_n\phi_B}\right)^2} \tag{3}$$

where

$$\sigma_n^2 = \sigma^2 + \left(\frac{\Delta\phi}{\phi_B}\right)^2 \tag{4}$$

5.2.6.2

FIG. 5.13 FIELD VIEW AND NO-FIELD VIEW ANGLE VARIABLES

FIELD VIEW

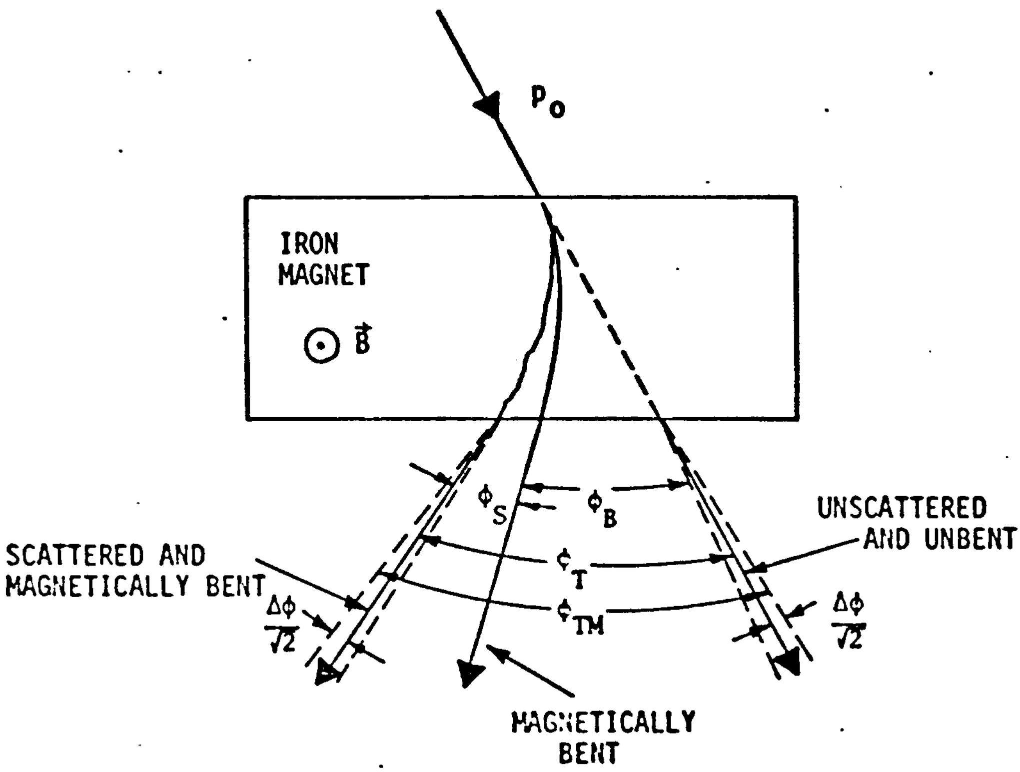

NO-FIELD VIEW

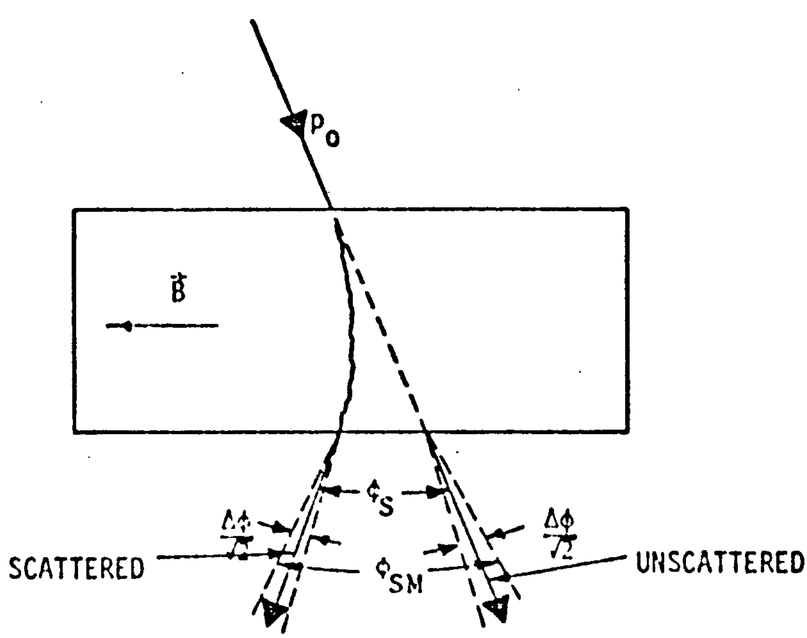

or

$$\sigma_n = \sigma'\sigma \tag{5}$$

for which

$$\sigma' = \left[1 + \left(\frac{1}{\sigma}\,\frac{\Delta\phi}{\phi_B}\right)^2\right]^{1/2} \tag{6}$$

Thus the density in the measured total-angle, ϕ_{TM}, is the same as that for the total-angle, ϕ_T, except that $f(\phi_{TM})$ has a new standard deviation given by eqs. (5) and (6). Notice that $\sigma_n = \sigma$ only if the uncertainty in angle measurement, $\Delta\phi$, is zero.

Multiple scattering in the spectrometer no-field view is given by

$$f(\phi_S) = \frac{1}{\sqrt{2\pi}\,\sigma\phi_B}\, e^{-\frac{1}{2}\left(\frac{1}{\sigma}\,\frac{\phi_S}{\phi_B}\right)^2} \tag{7}$$

Due to measurement error we introduce a measured scattering angle, ϕ_{SM}, distributed by

$$f(\phi_{SM}|\phi_S) = \frac{1}{\sqrt{2\pi}\,\Delta\phi}\, e^{-\frac{1}{2}\left(\frac{\phi_{SM}-\phi_S}{\Delta\phi}\right)} \tag{8}$$

where we have assumed the angle uncertainty, $\Delta\phi$, to be the same for the no-field view as for the field view. We seek the density in the measured scattering angle which we obtain by integrating the product of (7) and (8) over the scattering angle, ϕ_S:

$$f(\phi_{SM}) = \frac{1}{\sqrt{2\pi}\,\sigma_n\phi_B}\, e^{-\frac{1}{2}\left(\frac{1}{\sigma_n}\;\frac{\phi_{SM}}{\phi_B}\right)^2} \qquad (9)$$

where σ_n is again given by (5) and (6). Fig. 5.13 shows the no-field view scattering variables of eqs. (7) and (8). The probability density for ϕ_{SM}, eq. (9), differs from that for ϕ_S only in that the standard deviation is now given by σ_n rather than σ.

We now form the joint density in ϕ_{TM} and ϕ_{SM} from the product of (4) and (9):

$$J(\phi_{SM},\phi_{TM}|\phi_S) = \frac{1}{2\pi(\sigma_n\phi_B)^2}\, e^{-\frac{1}{2\sigma_n^2}\left[\left(\frac{\phi_{SM}}{\phi_B}\right)^2 + \left(\frac{\phi_{TM}-\phi_B}{\phi_B}\right)^2\right]} \qquad (10)$$

Comparison of this result with eq. (5.2.5.8) shows that the following changes of variable have taken place

$$\phi_S \longrightarrow \phi_{SM}$$
$$\phi_T \longrightarrow \phi_{TM}$$
$$\sigma \longrightarrow \sigma_n$$

Thus the exact values of ϕ_S and ϕ_T have been replaced by their measured values ϕ_{SM} , ϕ_{TM} and the uncertainty σ has been replaced by σ_n. Hence we can rewrite eq. (5.2.5.21) with the above changes of variable to obtain a new multiple scattering density

$$f(\alpha_n|\sigma_n) = \frac{1}{\sqrt{2\pi}} \frac{e^{-\frac{1}{2}\frac{\alpha_n{}^2}{(1+\sigma_n{}^2\alpha_n{}^2)}}}{(1+\sigma_n{}^2\alpha_n{}^2)^{3/2}} \tag{11}$$

where

$$\sigma_n{}^2 = \sigma^2 + \left(\frac{\Delta\phi}{\phi_B}\right)^2 \tag{12}$$

$$\alpha_n = \frac{1}{\sigma_n}\left(\frac{\phi_{SM}}{\phi_{TM}}\right) \tag{13}$$

The new scattering density eq. (11) has a characteristic "width", σ_n, which is a function of multiple scattering "noise", σ, and of measurement uncertainty, $\Delta\phi$. If it is possible to reduce measurement error to a negligible level then the uncertainty, σ_n, is due only to the noise, σ. However, for a sufficiently thick target and/or a sufficiently great magnetic field the parameter σ becomes arbitrarily small and σ_n is due only to measurement error. When both sources of uncertainty approach zero the probability density $f(\alpha_n|\sigma_n)$ becomes the Dirac delta function.

From eq. (13) we see that the new value of α_n is not useful since it is a function of ϕ_B and hence of the real momentum p_o. Since we cannot experimentally determine p_o, eq. (13) cannot be used. A more useful scattering parameter for the evaluation of experimental results is

$$\alpha = \frac{1}{\sigma}\frac{\phi_{SM}}{\phi_{TM}}, \tag{14}$$

because now α can be experimentally measured. Comparing (13) to (14) yields

$$\sigma_n \alpha_n = \sigma\alpha \tag{15}$$

Also let

$$\sigma_n = \sigma\sigma' \quad ; \quad \sigma' = \left[1 + \left(\frac{\Delta\phi}{\sigma\phi_B}\right)^2\right]^{1/2} \tag{16}$$

so that

$$\alpha_n = \frac{\alpha}{\sigma'} \tag{17}$$

Transforming (11) by (15)-(17) we get

$$f(\alpha|\sigma,\phi_B) = \frac{1}{\sqrt{2\pi}\ \sigma'} \ \frac{e^{-\frac{1}{2}\frac{\alpha^2}{\sigma'^2(1 + \sigma^2\alpha^2)}}}{(1 + \sigma^2\alpha^2)^{3/2}} \tag{18}$$

where

$$\sigma' = \left[1 + \left(\frac{\Delta\phi}{\sigma\phi_B}\right)^2\right]^{1/2} \tag{19}$$

$$\alpha = \frac{1}{\sigma}\left(\frac{\phi_{SM}}{\phi_{TM}}\right)$$

From (19) it is easy to see that $\sigma' = 1$ only when the measurement error is zero. In this limit (18) is equal to eq. (5.2.5.21). Eq. (18) is the corrected gaussian density which we originally sought to discover; unfortunately it cannot be compared directly to experimental results because of the conditional dependence on ϕ_B and hence on the real particle momentum, p_0. Integration of (18) over the cosmic ray muon momentum spectrum allows a momentum independent multiple scattering density to be calculated. This problem will be treated in the next section.

5.2.7 INTEGRATION OVER THE COSMIC RAY SPECTRUM

In order to see the explicit dependence of the corrected multiple scattering density, eq. (5.2.6.18), on the cosmic ray muon momentum spectrum we must make a change of variable in eq. (5.2.6.19) from angle to momentum coordinates. First we define

$$p_{CDM} = \frac{k(s, p_{CDM})}{\Delta\phi} \tag{1}$$

to be the "characteristically determined momentum" (CDM) of the spectrometer. This is the value of momentum for which the uncertainty due to measurement error is approximately 100%. This relationship for p_{CDM} is analogous to similar relations which have been introduced, i.e. it can be recalled that the "real muon momentum" is given by

$$p_o = \frac{k(s, p_o)}{\phi_B} \tag{2}$$

and that the "experimentally determined momentum" is found from

$$p = \frac{k(s, p)}{\phi_T} \tag{3}$$

In the high momentum limit we use eq. (5.2.4.12) to show that

$$k(s,p) = k(s,p_o) = k(s,p_{CDM}) = k_o = .3B_o s \qquad (4)$$

One can then easily transform the measured total angle density, eq. (5.2.6.3), to a momentum density which includes measurement error:

$$f(p|p_o) = \frac{1}{\sqrt{2\pi}\ \sigma_n} \frac{p_o}{p^2} e^{-\frac{1}{2}\left(\frac{p_o}{\sigma_n}\right)^2 \left(\frac{1}{p} - \frac{1}{p_o}\right)^2} \qquad (5)$$

This is the same density which we have seen previously except that the relative momentum uncertainty, σ, has been replaced by σ_n. Thus σ_n is a measure of momentum uncertainty which not only includes the effects of multiple scattering but also the effects of measurement error.

The expression for σ_n, eq. (5.2.6.12), can be transformed from angle to momentum variables by use of (1) and (2).

$$\sigma_n^2 = \sigma^2 + \left(\frac{k(s,p_M)}{k(s,p_o)} \frac{p_o}{p_{CDM}}\right)^2 \qquad (6)$$

From eq. (4) we find that at high momentum eq. (3) becomes, approximately,

$$\sigma_n^2 \simeq \sigma^2 + \left(\frac{p_o}{p_{CDM}}\right)^2 \qquad (7)$$

If σ^2 is assumed small then when $p_o = p_{CDM}$ the uncertainty is nearly 100% (actually the figure is about 102% if $\sigma = .2$).

In the same way we are led to a new expression for

σ', eq. (5.2.6.19)

$$\sigma' = \left[1 + \left(\frac{\eta}{\sigma}\right)^2\right]^{1/2} \tag{8}$$

where

$$\eta = \frac{k(s, p_{CDM}) p_o}{k(s, p_o)\, p_{CDM}} \tag{9}$$

$$k(s, p_{CDM}) = \frac{k_o\ p}{s} \int_0^s \frac{ds'}{p(s', p_{CDM})} \tag{10}$$

$$k(s, p_o) = \frac{k_o p_o}{s} \int_0^s \frac{ds'}{p(s', p_o)} \tag{11}$$

For linear momentum loss we obtain

$$\eta = \int_0^s \frac{ds'}{p(s', p_{CDM})} \Bigg/ \int_0^s \frac{ds'}{p(s', p_o)} \simeq \frac{\Delta p_o}{\Delta p_{CDM}} \frac{\ln(1 - \Delta p_{CDM}/p_{CDM})}{\ln(1 - \Delta p_o/p_o)} \simeq \frac{p_o}{p_{CDM}} \tag{12}$$

$$\Delta p_{CDM} = (a + b p_{CDM}) \tag{13}$$

$$\Delta p_o = (a + b p_o) s \tag{14}$$

The last approximation of eq. (12) is obtained only when momentum loss is assumed to be small.

We are finally able to write the expression for the corrected gaussian multiple scattering density

$$f(\alpha|\sigma, p_o) = \frac{1}{\sqrt{2\pi}\ \sigma'} \frac{e^{-\frac{1}{2\sigma'^2} \frac{\alpha^2}{(1 + \sigma^2\alpha^2)}}}{(1 + \sigma^2\alpha^2)^{3/2}} \tag{15}$$

where

$$\sigma' \approx \left[1 + \frac{1}{\sigma^2}\left(\frac{p_0}{p_{CDM}}\right)^2\right]^{\frac{1}{2}} \tag{16}$$

$$\alpha = \frac{1}{\sigma}\frac{\phi_{SM}}{\phi_{TM}} \tag{17}$$

Here we have used only an approximate expression for σ', however, it is sufficient for the arguments which follow.

From (16) we see that if the CDM is finite, then $\sigma' = \sigma'(p_0)$, a relation which forces (15) to have a "width" which is dependent on the real momentum, p_0, of the muon. The probability density for p_0 is governed by the cosmic ray muon momentum spectrum, $I(p_0|\gamma)$. Knowing the functional form for the spectrum allows one to calculate a multiple scattering density independent of p_0:

$$f(\alpha|\sigma,\gamma) = \int_{p_c}^{\infty} f(\alpha|\sigma,p_0)I(p_0|\gamma)\,dp_0 \tag{18}$$

It is this expression which must ultimately be compared to experimental results. The form for the spectrum, $I(p_0|\gamma)$, is discussed in Appendix I.

5.3 MODIFICATION OF THE MOLIÈRE THEORY

5.3.1 INTRODUCTION

In Section 5.2 the simple gaussian theory of multiple scattering was modified to take into account the random nature of the momentum measured by a muon magnetic spectrometer. In this section we use the same techniques to modify the more complete theory of Molière. It will be seen that all of the results of Section 5.2 are applicable here. Only one previous assumption will be invalidated; in the Molière theory the projected angles ϕ_x and ϕ_y are not statistically independent. The consequences of this one change will be investigated in subsequent sections.

5.3.2 MOMENTUM UNCERTAINTY DUE TO MULTIPLE SCATTERING

Here we determine the momentum dependence of the multiple scattering noise, σ, in a rigorous way. In particular we calculate σ using Moliere's theory, which includes the effect of ionization energy loss. Recall that σ is the ratio of rms multiple scattering, σ_ϕ, to magnetic bending, ϕ_B:

$$\sigma = \frac{\sigma_\phi}{\phi_B} \tag{1}$$

From eqs. (5.2.4.2-5) we find an integral expression for ϕ_B:

$$\phi_B = .3B_0 \int_0^s \frac{ds'}{p(s',p_0)}. \tag{2}$$

where s is the target thickness and p_0 is the momentum of the muon as it enters the solid iron magnet. Because of the complicated behavior of ionization energy loss eq. (2) must be integrated numerically. To this end we rewrite eq. (2):

$$\phi_B = \frac{.3B_0}{\rho} \int_{p_0}^{p_1} \frac{dp}{p(-dp/dx)} \qquad (3)$$

where the rate of momentum loss (-dp/dx) is a tabularized function and is described in Sec. 3.5; ρ is the density of the iron and p_1 is the particle momentum as it exits from the magnet iron. Before integrating eq. (3) the exit momentum, p_1, must be calculated from

$$x = \int_{p_0}^{p_1} \frac{dp}{(-dp/dx)} \qquad (4)$$

Here p_0 and x are known and p_1 is determined numerically. This task is easily accomplished by the Newton-Rhapson[10] method which yields an iterative equation:

$$p_1^{n+1} = p_1^n - [f(p_1^n)-x]\left[-\frac{dp}{dx}(p_1^n)\right] \qquad (5)$$

where

$$f(p_1^n) = \int_{p}^{p_1^n} \frac{dp}{(-dp/dx)} \qquad (6)$$

and p_1^n is the n^{th} value of the exit momentum. Typically one guesses an initial value of p_1 (based upon constant momentum loss) and then uses (5) and (6) to iteratively converge on the actual value of p_1. No more than three iterations are necessary to obtain p_1 to an accuracy of .1% or better.

In chapter IV we found that the root mean square multiple scattering angle of Molière is given by

$$\sigma_\phi = \left[\frac{2\pi BN}{A}\right] \frac{ze^2}{c} \left(\int_{p_o}^{p_1} \frac{dp}{(p\beta)^2(-dp/dx)} \right)^{1/2} \qquad (7)$$

Numerical integration of (7) is of course necessary.

A computer program was written to calculate the momentum uncertainty using equations (1)-(7). The program requires for input the target thickness, x, and the particle entry momentum, p_o. The exit momentum, p_1, is then determined by eqs. (5) and (6). The magnetic bending angle, ϕ_B, is found by numerical integration of eq. (3), and the rms scattering angle, σ_ϕ, is determined by numerical integration of eq. (7). (All numerical integrations in this program are performed by a fifth-order Runga-Kutta[10] algorithm.) Finally a value of σ is calculated from eq. (1). Values of σ, determined from the above program, were used to plot the curve of Fig. 5.14 for a magnet target thickness of 95 cm. We see that σ = .228 for entry momenta $\tilde{>}$ 5 GeV/c but rapidly increases to .247 at 1.5 GeV/c. While σ is not constant below 5 GeV/c we see that the deviation from constancy is only 1.7% down to 2.5 GeV/c. The uncertainty for momenta > 2.5 GeV/c is considered negligible and is justification for assuming

5.3.2.4

FIG. 5.14 SPECTROMETER NOISE AS A FUNCTION OF MOMENTUM

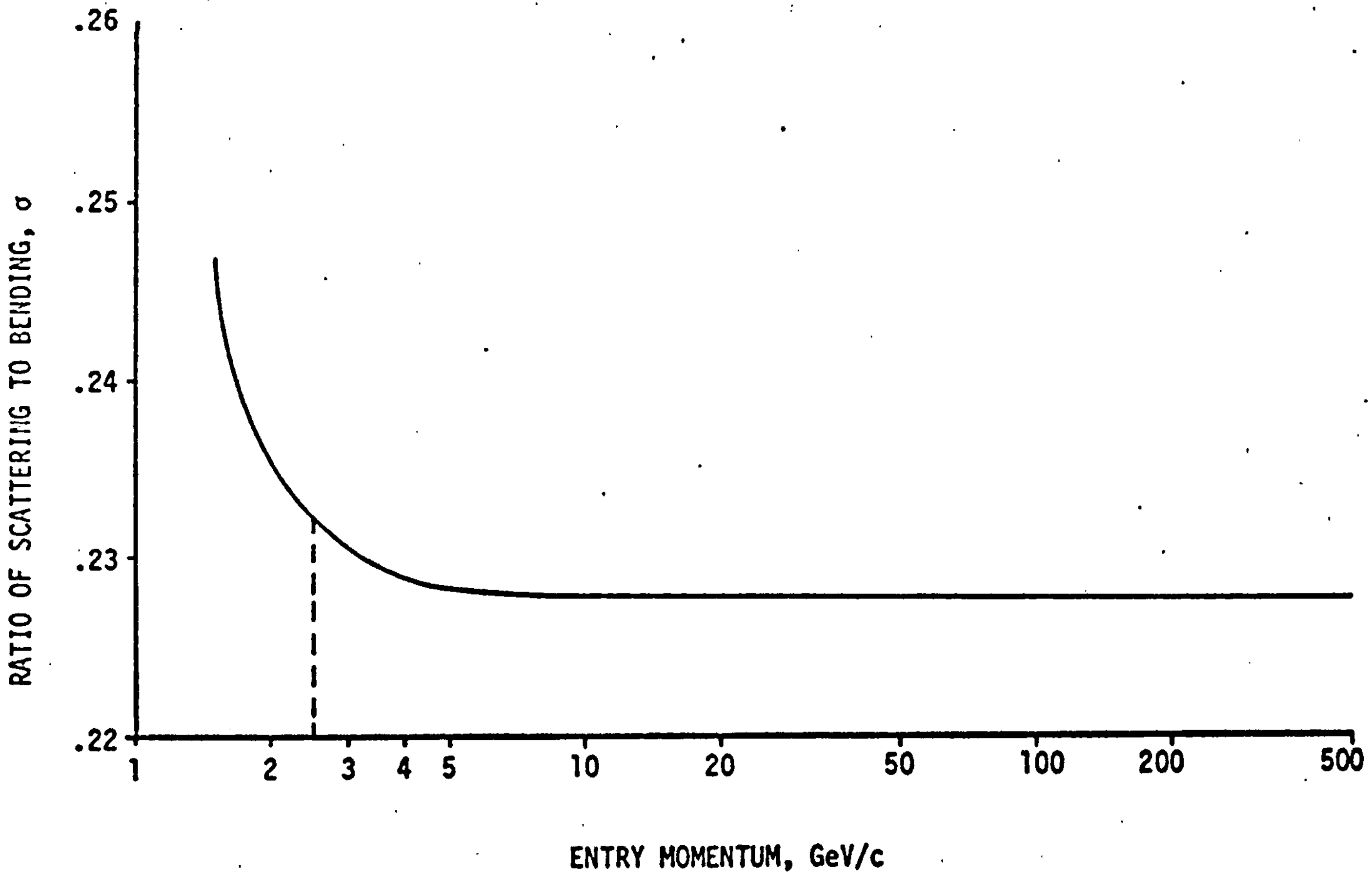

RATIO OF SCATTERING TO BENDING, σ
.26
.25
.24
.23
.22
1
2
3
4
5
10
20
50
100
200
500
ENTRY MOMENTUM, GeV/c

σ to be constant above 2.5 GeV/c. Thus all data below 2.5 GeV/c are neglected in the data analysis.

5.3.3 THE TOTAL ANGLE DENSITY

We have seen that Molière's joint density in the projected multiple scattering angles ϕ_x, ϕ_y (see eq. (4.5.41) is given by:

$$J(\phi_x,\phi_y)d\phi_x d\phi_y = \frac{d\phi_x d\phi_y}{2(2\pi\sigma\phi_B)^2}\int\limits_{-\infty}^{\infty}\int\limits_{-\infty}^{\infty} dy_1 dy_2 e^{\frac{iy_1}{\sqrt{2}}\left(\frac{\phi_x}{\sigma\phi_B}\right)+i\frac{y_2}{\sqrt{2}}\left(\frac{\phi_y}{\sigma\phi_B}\right)} g(y_1^2+y_2^2) \qquad (1)$$

where

$$g(y_1^2+y_2^2) = e^{-\left(\frac{y_1^2+y_2^2}{4}\right) + \left(\frac{y_1^2+y_2^2}{4B}\right)\ln\left(\frac{y_1^2+y_2^2}{4}\right)} \qquad (2)$$

Eq. (1) represents the probability that a particle incident on a target will be multiply scattered into projected angle intervals $(\phi_x, \phi_x+d\phi_x)$ and $(\phi_y, \phi_y+d\phi_y)$ during traversal of the target.

Recalling the definition of the "total" angle (the muon angular deflection due to multiple scattering and magnetic bending as observed in the spectrometer field view), we write

$$\phi_T = \phi_x + \phi_B \qquad (3)$$

This allows the density (1) to be transformed into:

$$J(\phi_y,\phi_T)d\phi_T d\phi_y = \frac{d\phi_T d\phi_y}{2(2\pi\sigma\phi_B)^2}\int\limits_{-\infty}^{\infty}\int\limits_{-\infty}^{\infty} dy_1 dy_2 e^{\frac{iy_1}{\sqrt{2}}\left(\frac{\phi_T-\phi_B}{\sigma\phi_B}\right)+\frac{iy_2}{\sqrt{2}}\left(\frac{\phi_y}{\sigma\phi_B}\right)} g(y_1^2+y_2^2) \qquad (4)$$

Thus in complete analogy to eq. (5.2.5.8) we know that eq. (4) represents the joint probability that a charged particle of momentum p_0 (corresponding to a bending angle, ϕ_B) enters the spectrometer and (1) is multiply scattered into $(\phi_y, \phi_y + d\phi_y)$ in the no-field view and (2) is multiply scattered and magnetically bent into $(\phi_T, \phi_T + d\phi_T)$ in the field view.

If we integrate eq. (4) over ϕ_T we immediately obtain the density in scattering angle, $f(\phi_y)$,

$$f(\phi_y)d\phi_y = \frac{d\phi_y}{\sqrt{2}\pi\sigma\phi_B} \int_0^\infty dy \cos\left[\frac{\phi_y y}{\sqrt{2}\sigma\phi_B}\right] e^{-\frac{y^2}{4} + \frac{y^2}{4B} \ln \frac{y^2}{4}} \qquad (5)$$

Using the fact that B is reasonably large (B ≈ 18) we may expand (5) about 1/B to obtain:

$$f(\phi_y|\sigma,\phi_B) = \frac{1}{\sqrt{2\pi}\sigma\phi_B} e^{-\frac{1}{2}\left(\frac{\phi_y}{\sigma\phi_B}\right)^2} + \frac{f_y^{(1)}}{B}(\phi_y) + \frac{f_2^{(2)}}{B^2}(\phi_y) + \ldots \qquad (6)$$

where

$$f^{(n)}(\phi_y) = \frac{1}{\sqrt{2}\pi\sigma\phi\ n!} \int_0^\infty dy \cos\left[\frac{\phi_y y}{\sqrt{2}\sigma\phi}\right] e^{-\frac{y^2}{4}} \left[\frac{y^2}{4} \ln \frac{y^2}{4}\right]^n \qquad (7)$$

If we now integrate eq. (4) over ϕ_y we obtain the density in total-angle, $f(\phi_T)$:

$$f(\phi_T)d\phi_T = \frac{d\phi_T}{\sqrt{2}\pi\sigma\phi_B} \int_0^\infty dy \cos\left[\frac{(\phi_T - \phi_B)y}{\sqrt{2}\sigma\phi_B}\right] e^{-\frac{y^2}{4} + \frac{y^2}{4B} \ln \frac{y^2}{4}} \qquad (8)$$

Expanding about 1/B gives

$$f(\phi_T|\sigma,\phi_T) = \frac{1}{\sqrt{2\pi}\sigma\phi_B} e^{-\frac{1}{2}\left(\frac{\phi_T-\phi_B}{\sigma\phi_B}\right)^2} + \frac{f_T^{(1)}}{B}(\phi_T) + \frac{f_T^{(2)}}{B^2}(\phi_T) + \ldots \quad (9)$$

where

$$f_T^{(n)}(\phi_T) = \frac{1}{\sqrt{2\pi}\sigma\phi_B n!} \int_0^\infty dy \cos\left[\frac{(\phi_T-\phi_B)y}{\sqrt{2}\sigma\phi_B}\right] e^{-\frac{y^2}{4}} \left[\frac{y^2}{4} \ell n \frac{y^2}{4}\right]^n \quad (10)$$

We shall later have need to reference the series expansions above, i.e. eqs. (6) and (9).

One can easily see that the product of eqs. (5) and (8), does not yield a joint density in ϕ_T and ϕ_y equal to eq. (4). This implies that ϕ_T and ϕ_y are <u>not</u> statistically independent (since $J(\phi_y,\phi_T) \neq J(\phi_T)J(\phi_y)$). Thus we are forced to use eq. (4) rather than the product of (5) and (8) to modify the Molière theory of multiple scattering. How the statistical dependence of ϕ_x and ϕ_y effects our results will be seen in the following section.

5.3.4 MODIFICATION TO THE MOLIÈRE DENSITY

5.3.4.1 INTEGRAL FORMULATION

In order to modify Molière's theory we use equation (5.2.5.11) together with (5.3.3.4) to obtain the density in α, $f(\alpha)$:

$$f(\alpha) = \frac{1}{2(2\pi)^2\sigma} \int_0^\infty dx\ x \int_{-\infty}^{\infty}\int_{-\infty}^{\infty} dy_1 dy_2\ e^{iy_1\left(\frac{x-1}{\sqrt{2}\sigma}\right) + \frac{iy_2\,\alpha\,x}{\sqrt{2}}}\ g(y_1^2 + y_2^2) \quad (1)$$

Here we have let $x = \phi_T/\phi_B$ in order to simplify the equation. Notice that eq. (1) is <u>not</u> a function of ϕ_B and hence not a function of the cosmic ray muon momentum spectrum (this is exactly what we found in Section 5.2.5 when the gaussian theory was modified). Notice also that the upper limit of eq. (5.2.5.11) has been set to infinity in eq. (1). This has been done because numerical integra- of (1) yields results which show that all possible values for this upper limit are consistent with infinity. This is due to the rapid convergence of the two inner integrals over y_1 and y_2.

Now recall the arguments in Sec. 5.2.3.2 which led to an examination of the scattering angle ϕ_x in the region $-\infty < \phi_x < -\phi_B$ (REGION 2 of Fig. 5.7) and which subsequently led to a correction of the total angle density as given by eq. (5.2.3.2.2). We now apply eq. (5.2.3.2.2) to the joint density $J(\phi_T, \phi_y)$, eq. (5.3.3.4), and obtain the exact form of the joint density:

$$J(\phi_T, \phi_y) = J_+(\phi_T, \phi_y) + J_-(\phi_T, \phi_y) \tag{2}$$

where

$$J_\pm(\phi_T, \phi_y) = \frac{1}{2(2\pi\sigma\phi_B)^2} \int\limits_{-\infty}^{\infty}\int\limits_{-\infty}^{\infty} dy_1 dy_2 \, e^{\frac{iy}{\sqrt{2}}\left(\frac{\phi_T \mp \phi_B}{\sigma\phi_B}\right) + \frac{iy}{\sqrt{2}}\left(\frac{\phi_y}{\sigma\phi_B}\right)} g(y_1^2 + y_2^2) \tag{3}$$

We have formed eqs. (2) and (3) in exactly the same way as we formed eq. (5.2.3.2.3). If we use eq. (2) (rather than 5.3.3.4) to form the density in $f(\alpha)$ we obtain:

$$f(\alpha) = f_+(\alpha) + f_-(\alpha) \tag{4}$$

where

$$f_\pm(\alpha) = \frac{1}{2(2\pi)^2\sigma} \int_0^\infty dx \; x \int\limits_{-\infty}^{\infty}\int\limits_{-\infty}^{\infty} dy_1 dy_2 \, e^{iy\left(\frac{x \mp 1}{\sqrt{2}\sigma}\right) + \frac{iy_2 \alpha x}{\sqrt{2}}} g(y_1^2 + y_2^2) \tag{5}$$

Notice the similarity of (4) and (5) compared to eqs. (5.2.5.23) and (5.2.5.24) which were derived in analogous fashion. Numerical integration of $f_\pm(\alpha)$ shows that $f_+(\alpha)$ may be neglected, i.e. that $f(\alpha) \approx f_-(\alpha)$ to a sufficient degree of accuracy. It is found that $f_+(\alpha)$ amounts to, at most, a 5% correction to $f(\alpha)$ at $\alpha = 7$ (7 standard deviations).

Before proceeding further we point out that a simple change of variable in eq. (1) was made in order to facilitate its numerical integration. This change of variable was accomplished by

$$z = \frac{x-1}{\sigma}\ ; \quad x_1 = \frac{y_1}{\sqrt{2}}\ ; \ x_2 = \frac{y_2}{\sqrt{2}}$$

and led to

$$f(\alpha) = \frac{1}{\pi^2}\int_{-\frac{1}{\sigma}}^{\infty} dz(\sigma z+1)\int_0^{\infty} dx_1 \cos zx_1\, e^{-\frac{x_1^2}{2}}\int_0^{\infty} dx_2 \cos[\alpha(\sigma z+1)x_2]e^{-\frac{x_2^2}{2}} \tag{6}$$

$$X\, e^{\left(\frac{x_1^2+x_2^2}{2}\right)} \ln\left(\frac{x_1^2+x_2^2}{2}\right)$$

Here we have taken the real part of eq. (1). This result is very well behaved (much more so than eq. (1)) and can be easily integrated on the computer.

5.3.4.2 SEMI-ANALYTIC FORMULATION

We now proceed to the direct integration of eq. (5.3.4.1.1). To this end we write

$$e^{iy_1\left(\frac{x-1}{\sqrt{2}\sigma}\right)+\frac{iy_2\alpha x}{\sqrt{2}}} = \cos\left[\frac{(x-1)}{\sqrt{2}\sigma}y_1 + \frac{\alpha x y_2}{\sqrt{2}}\right] + i\sin\left[\frac{(x-1)}{\sqrt{2}\sigma}y_1 + \frac{\alpha x y_2}{\sqrt{2}}\right] \tag{1}$$

$$= \cos\left[\frac{(x-1)}{\sqrt{2}\sigma}y_1\right]\cos\left[\frac{\alpha x y_2}{\sqrt{2}}\right] - \sin\left[\frac{(x-1)}{\sqrt{2}\sigma}y_1\right]\sin\left[\frac{\alpha x y_2}{2}\right] \tag{2}$$

where only the real part has been retained in eq. (2). Now use (2) in eq. (5.3.4.1.1) to obtain

$$f(\alpha) = \frac{1}{2\pi^2\sigma}\int_0^{\infty} dx x \int_0^{\infty}\int_0^{\infty} dy_1 dy_2 \cos\left[\frac{(x-1)}{\sqrt{2}\sigma}y_1\right]\cos\left[\frac{\alpha x y_2}{\sqrt{2}}\right]\ g(y_1^2+y_2^2) \tag{3}$$

where $g(y_1^2 + y_2^2)$ is given by (5.3.3.2).

If we expand (3) in a series about 1/B we obtain

$$f(\alpha) = \frac{1}{2\pi^2\sigma}\int_0^\infty dx\, x \iint_{00}^{\infty\infty} dy_1 dy_2 \cos\left[\frac{(x-1)}{\sqrt{2}\sigma}y_1\right]\cos\left[\frac{\alpha x y_2}{\sqrt{2}}\right] e^{-\left(\frac{y_1^2+y_2^2}{4}\right)}$$

$$+ \frac{1}{2\pi^2\sigma B}\int_0^\infty dx\, x \iint_{00}^{\infty\infty} dy_1 dy_2 \cos\left[\frac{(x-1)}{\sqrt{2}\sigma}\, y_1\right] \cos\left[\frac{\alpha x y_2}{\sqrt{2}}\right] G(y_1^2+y_2^2) + \ldots \qquad (4)$$

where

$$G(y_1^2+y_2^2) = e^{-\left(\frac{y_1^2+y_2^2}{4}\right)}\left[\frac{y_1^2 + y_2^2}{4}\right]\ln\left[\frac{y_1^2 + y_2^2}{4}\right] \qquad (5)$$

In eq. (4) we have neglected terms of order $(1/B)^2$ and greater. We shall designate the first integral of (4) as $f_0(\alpha)$ and rewrite it:

$$f_0(\alpha) = \frac{1}{2\pi^2\sigma}\int_0^\infty dx\, x \left(\int_0^\infty dy_1 \cos\left[\frac{(x-1)}{\sqrt{2}\sigma}\, y_1\right] e^{-\frac{y_1^2}{4}}\right)\left(\int_0^\infty dy_2 \cos\left[\frac{\alpha x y_2}{\sqrt{2}}\right] e^{-\frac{y_2^2}{4}}\right) \qquad (6)$$

The integrals in brackets are easily evaluated

$$\int_0^\infty dy_1 \cos\left[\frac{(x-1)}{\sqrt{2}\,\sigma}y_1\right] e^{-\frac{y_1^2}{4}} = \sqrt{\pi}\; e^{-\frac{1}{2}\left(\frac{x-1}{\sigma}\right)^2} \qquad (7)$$

$$\int_0^\infty dy_2 \cos\left[\frac{\alpha x y_2}{\sqrt{2}}\right] e^{-\frac{y_2^2}{4}} = \sqrt{\pi}\, e^{-\frac{\alpha^2 x^2}{2}} \qquad (8)$$

Put (7) and (8) into (6) to get

$$f_o(\alpha) = \frac{1}{2\pi\sigma}\int_0^\infty x e^{-\frac{1}{2}\left(\frac{x-1}{\sigma}\right)^2 - \frac{\alpha^2 x^2}{2}} dx \tag{9}$$

We have integrated eq. (9) before (see eq. (5.2.5.14)) in Sec. 5.2.5; our result was

$$f_o(\alpha) = \frac{1}{\sqrt{2\pi}} \frac{e^{-\frac{1}{2}\frac{\alpha^2}{1+\sigma^2\alpha^2}}}{(1+\sigma^2\alpha^2)^{3/2}} \tag{10}$$

Thus the zeroth order term in the corrected Molière density is exactly the result we obtained for the corrected gaussian density. Needless to say, this is an expected result. Eq. (4) can now be written

$$f(\alpha) = \frac{1}{\sqrt{2\pi}} \frac{e^{-\frac{1}{2}\frac{\alpha^2}{1+\sigma^2\alpha^2}}}{(1+\sigma^2\alpha^2)^{3/2}} + \frac{f^{(1)}(\alpha)}{B} + \ldots \tag{11}$$

where

$$f^{(1)}(\alpha) = \frac{1}{2\pi^2\sigma}\int_0^\infty dx\, x \int_0^\infty\int_0^\infty dy_1 dy_2 \cos\left[\frac{(x-1)y_1}{\sqrt{2}\sigma}\right] \cos\left[\frac{\alpha x y_2}{\sqrt{2}}\right] G\,(y_1^2+y_2^2) \tag{12}$$

For reasons which will soon become clear we prefer to rewrite $G(y_1^2+y_2^2)$ so that

$$G(y_1^2+y_2^2) = e^{-\left[\frac{y_1^2+y_2^2}{4}\right]}\left(\frac{y_1^2}{4}\,\ln\left[\frac{y_1^2+y_2^2}{4}\right] + \frac{y_2^2}{4}\,\ln\left[\frac{y_1^2+y_2^2}{4}\right]\right)$$

$$= e^{-\left(\frac{y_1^2+y_2^2}{4}\right)} \left(\frac{y_1^2}{4} \ln \frac{y_1^2}{4} \left(1+\frac{y_2^2}{y_1^2}\right) + \frac{y_2^2}{4} \ln \frac{y_2^2}{4} \left(1+\frac{y_1^2}{y_2^2}\right)\right)$$

$$= e^{-\left(\frac{y_1^2+y_2^2}{4}\right)} \left(\frac{y_1^2}{4} \ln \frac{y_1^2}{4} + \frac{y_2^2}{4} \ln \frac{y_2^2}{4} + \frac{y_1^2}{4} \ln\left(1+\frac{y_2^2}{y_1^2}\right) + \frac{y_2^2}{4} \ln \left(1+\frac{y_1^2}{y_2^2}\right)\right) \quad (13)$$

Put eq. (13) into (12) and get

$$f^{(1)}(\alpha) = \frac{1}{2\pi^2\sigma} \int_0^\infty\int_0^\infty\int_0^\infty dx\,dy_1\,dy_2\,x \cos\left[\frac{(x-1)y_1}{\sqrt{2}\sigma}\right] \cos\left[\frac{\alpha x y_2}{\sqrt{2}}\right] e^{-\left(\frac{y_1^2+y_2^2}{4}\right)} \left[\frac{y_1^2}{4} \ln \frac{y_1^2}{4}\right] \quad (14)$$

$$+ \frac{1}{2\pi^2\sigma} \int_0^\infty\int_0^\infty\int_0^\infty dx\,dy_1\,dy_2\,x \cos\left[\frac{(x-1)}{\sqrt{2}\sigma} y_1\right] \cos\left[\frac{\alpha x y_2}{\sqrt{2}}\right] e^{-\left(\frac{y_1^2+y_2^2}{4}\right)} \left[\frac{y_2^2}{4} \ln \frac{y_1^2}{4}\right]$$

$+ H(\alpha)$

where

$$H(\alpha) = \frac{1}{2\pi^2\sigma} \int_0^\infty\int_0^\infty\int_0^\infty dx\,dy_1\,dy_2\,x \cos\left[\frac{(x-1)}{\sqrt{2}\sigma} y_1\right] \cos\left[\frac{\alpha x y_2}{\sqrt{2}}\right] e^{-\left(\frac{y_1^2+y_2^2}{4}\right)} \left(\frac{y_1^2}{4} \ln\left(1+\frac{y_2^2}{y_1^2}\right)\right.$$

$$\left. + \frac{y_2^2}{4} \ln \left(1 + \frac{y_1^2}{y_2^2}\right)\right)$$

Now integrate the first integral of (14) over y_2 to get

$$\int_0^\infty dy_2 \cos \left|\frac{\alpha x y_2}{\sqrt{2}}\right| e^{-\frac{y_2^2}{4}} = \sqrt{\pi}\, e^{-\frac{\alpha^2 x^2}{2}} \quad (16)$$

Integrate the second integral of (14) over y_1 and get

$$\int_0^{\infty} dy_1 \cos\left[\frac{(x-1)y_1}{\sqrt{2}\sigma}\right] e^{-\frac{y_1^2}{4}} = \sqrt{\pi}\, e^{-\frac{1}{2}\left(\frac{x-1}{\sigma}\right)^2} \tag{17}$$

Put (16) and (17) back into (14):

$$f^{(1)}(\alpha) = \frac{1}{\sqrt{2\pi}} \int_0^{\infty} dy\, F(y,\alpha)\, e^{-\frac{y^2}{4}} \left[\frac{y^2}{4} \ln \frac{y^2}{4}\right] + H(\alpha) \tag{18}$$

where

$$F(y,\alpha) = \frac{1}{\sqrt{2\pi}\sigma} \int_0^{\infty} x\, e^{-\frac{\alpha^2 x^2}{2}} \cos\left[\frac{(x-1)}{\sqrt{2}\sigma}\, y\right] dx \tag{19}$$

$$+ \frac{1}{\sqrt{2\pi}\sigma} \int_0^{\infty} x\, e^{-\frac{1}{2}\left(\frac{x-1}{\sigma}\right)^2} \cos\left[\frac{\alpha x y}{\sqrt{2}}\right] dx \tag{20}$$

Eq. (19) (which we label I_1) may be written

$$I_1 = \frac{1}{\sqrt{2\pi}\sigma} \cos\left[\frac{y}{\sqrt{2}\sigma}\right] \int_0^{\infty} x\, e^{-\frac{\alpha^2 x^2}{2}} \cos\left[\frac{xy}{\sqrt{2}\sigma}\right] dx$$

$$+ \frac{1}{\sqrt{2\pi}\sigma} \sin\left[\frac{y}{\sqrt{2}\sigma}\right] \int_0^{\infty} x\, e^{-\frac{\alpha^2 x^2}{2}} \sin\left[\frac{xy}{\sqrt{2}\sigma}\right] dx \tag{21}$$

The second integral of (21) may be evaluated exactly and hence (21) becomes:

$$I_1 = \frac{1}{\sqrt{2\pi}\sigma\alpha^2} \left(h(y) \cos\left(\frac{y}{\sqrt{2}\sigma}\right) + \sqrt{\frac{\pi}{2}} \left(\frac{y}{\sqrt{2}\sigma|\alpha|}\right) \sin\left(\frac{y}{\sqrt{2}\sigma}\right) e^{-\frac{1}{4}\left(\frac{y}{\sigma\alpha}\right)^2}\right) \tag{22}$$

where

$$h(y) = \left(\frac{\sqrt{2}\sigma\alpha}{y}\right)^2 \int_0^\infty x\, e^{-\left(\frac{\sigma\alpha}{y}\right)^2 x^2} \text{COS } x dx \qquad (23)$$

Eq. (23) can be expressed in terms of an infinite series; likewise h(y) may be written in terms of other integrals of different form. However, for computational purposes, no other formulation has proved more useful than (23).

If in eq. (20) (which we lable I_2) we let

$$z = \frac{x-1}{\sigma} \qquad (24)$$

then

$$I_2 = \frac{1}{\sqrt{2\pi}} \int_{-\frac{1}{\sigma}}^{\infty} (\sigma z+1)\, e^{-\frac{z^2}{2}} \text{COS}\left[\frac{\alpha(\sigma z+1)y}{\sqrt{2}}\right] dz \qquad (25)$$

For σ sufficiently small the lower limit of (25) approaches infinity. This allows I_2 to be written

$$I_2 = \frac{\sigma}{\sqrt{2\pi}} \int_{-\infty}^{\infty} z e^{-\frac{z^2}{2}} \text{COS}(az+b) dz + \frac{1}{\sqrt{2\pi}} \int_{-\infty}^{\infty} e^{-\frac{z^2}{2}} \text{COS}(az+b) dz \qquad (26)$$

where

$$a = \frac{\alpha y \sigma}{\sqrt{2}} \quad ; \quad b = \frac{\alpha y}{\sqrt{2}} \qquad (27)$$

Expanding COS(az+b) in (26) leads directly to

$$I_2 = \frac{2}{\sqrt{2\pi}} \text{COS} b \int_0^\infty e^{-\frac{z^2}{2}} \text{COS} az dz - \frac{2\sigma}{\sqrt{2\pi}} \text{SIN} b \int_0^\infty z e^{-\frac{z^2}{2}} \text{SIN} az dz \qquad (28)$$

These integrals are readily evaluated to give

$$I_2 = e^{-\left(\frac{\sigma\alpha y}{2}\right)^2}\left[\cos\left(\frac{\alpha y}{\sqrt{2}}\right) - \sigma^2\left(\frac{\alpha y}{\sqrt{2}}\right)\sin\left(\frac{\alpha y}{\sqrt{2}}\right)\right] \tag{29}$$

Finally (19) and (20) become

$$F(y,\alpha) = e^{-\left(\frac{\sigma\alpha y}{2}\right)^2}\left[\cos\left(\frac{\alpha y}{\sqrt{2}}\right) - \sigma^2\left(\frac{\alpha y}{\sqrt{2}}\right)\sin\left(\frac{\alpha y}{\sqrt{2}}\right)\right]$$

$$+ \frac{1}{\sqrt{2\pi}\sigma\alpha^2}\left(h(y)\cos\left[\frac{y}{\sqrt{2}\sigma}\right] + \sqrt{\frac{\pi}{2}}\left(\frac{y}{\sqrt{2}\sigma\alpha}\right)\sin\left(\frac{y}{\sqrt{2}\sigma}\right)e^{-\frac{1}{4}\left(\frac{y}{\sigma\alpha}\right)^2}\right) \tag{30}$$

We now return to eq. (18) which is the first order correction term of the modified Molière theory. Notice that the integral over $F(y,\alpha)$ in eq. (18) has exactly the same form as the Molière integral given by eq. (5.3.3.7), i.e. the cosine function of (5.3.3.7) has been replaced by eq. (30). Thus the integral

$$H_0(\alpha) = \frac{1}{\sqrt{2\pi}}\int_0^\infty dy\ F(y,\alpha)e^{-\frac{y^2}{4}}\left[\frac{y^2}{4}\ \ln\ \frac{y^2}{4}\right] \tag{31}$$

looks like the Molière integral, where $F(y,\alpha)$ is given by (30). Using (31) in (18) allows the first order correction to be written

$$f^{(1)}(\alpha) = H_0(\alpha) + H(\alpha) \tag{32}$$

It is interesting to note the physical meanings of $H_0(\alpha)$ and $H(\alpha)$:

$H_0(\alpha)$ = Molière correction integral which is obtained by assuming that the projected scattering angles ϕ_x and ϕ_y are independent

$H(\alpha)$ = Additional Molière correction obtained when the statistical dependence of ϕ_x and ϕ_y is included.

The above meaning of $H_0(\alpha)$ can be shown by assuming that the joint density $J(\phi_y, \phi_T)$ is the product of the densities of ϕ_T and ϕ_y:

$$J(\phi_y, \phi_T) = f(\phi_T) f(\phi_y) \tag{33}$$

where $f(\phi_T)$ and $f(\phi_y)$ are given by eqs. (5.3.3.6) and (5.3.3.9) respectively. This leads to a density in α:

$$f(\alpha) = \frac{1}{\sqrt{2\pi}} \frac{e^{-\frac{1}{2}\frac{\alpha^2}{1+\sigma^2\alpha^2}}}{(1+\sigma^2\alpha^2)^{3/2}} + \frac{H_0(\alpha)}{B}$$

However when the joint density $J(\phi_y, \phi_T)$ includes the statistical dependence of ϕ_T and ϕ_y (i.e. when $J(\phi_y, \phi_T)$ is given by (5.3.3.4)) we obtain

$$f(\alpha) = \frac{1}{\sqrt{2\pi}} \frac{e^{-\frac{1}{2}\frac{\alpha^2}{1+\sigma^2\alpha^2}}}{(1+\sigma^2\alpha^2)^{3/2}} + \frac{H_0(\alpha)}{B} + \frac{H(\alpha)}{B} \tag{35}$$

Thus $H(\alpha)$ contains the contribution due to the statistical dependence of ϕ_T on ϕ_y. The direct integration of $H(\alpha)$ has not proven feasible. However the numerical integration of $H(\alpha)$ has shown that

$$H(\alpha) \ll H_0(\alpha) \tag{36}$$

At most $H(\alpha)$ amounts to a 5% correction to eq. (35) for $\alpha > 4$. This correction is not important because statistical errors in this region vary from 15% to 50%. Thus we shall neglect the function $H(\alpha)$ in our analysis; this is equivalent to neglecting the statistical dependence of ϕ_x(or ϕ_T) on ϕ_y. Finally we have the corrected Molière density which we originally sought, (see Fig. 5.15 where the Molière and modified Molière densities are compared):

$$f(\alpha) = \frac{1}{\sqrt{2\pi}} \frac{e^{-\frac{1}{2}\frac{\alpha^2}{1+\sigma^2\alpha^2}}}{(1+\sigma^2\alpha^2)^{3/2}} + \frac{f^{(1)}(\alpha)}{B} + \ldots \tag{37}$$

where

$$f^{(1)}(\alpha) = \frac{1}{\sqrt{2\pi}} \int_0^\infty dy\ F(y,\alpha) e^{-\frac{y^2}{4}} \left[\frac{y^2}{4} \ln \frac{y^2}{4}\right] \tag{38}$$

and

$$F(y,\alpha) = e^{-\left(\frac{\sigma\alpha y}{2}\right)^2} \left[\cos\left(\frac{\alpha y}{\sqrt{2}}\right) - \sigma^2 \left(\frac{\alpha y}{\sqrt{2}}\right) \sin\left(\frac{\alpha y}{\sqrt{2}}\right)\right] + \frac{1}{\sqrt{2\pi}\,\sigma\alpha^2}\left[h(y)\cos\left(\frac{y}{\sqrt{2}\sigma}\right) + \sqrt{\frac{\pi}{2}} \left(\frac{y}{\sqrt{2}\sigma\alpha}\right) \sin\left(\frac{y}{\sqrt{2}\sigma}\right) e^{-\frac{1}{4}\left(\frac{y}{\sigma\alpha}\right)^2}\right] \tag{39}$$

$$h(y) = \left(\frac{\sqrt{2}\sigma\alpha}{y}\right)^2 \int_0^\infty x e^{-\left(\frac{\sigma\alpha x}{y}\right)^2} \cos x\, dx \tag{40}$$

When eq. (37) is compared directly to numerical integration of (5.3.4.1.4) the total error due to <u>all</u> sources

5.3.4.2.10

FIG. 5.15 COMPARISON OF MOLIÈRE AND CORRECTED MOLIÈRE DENSITIES

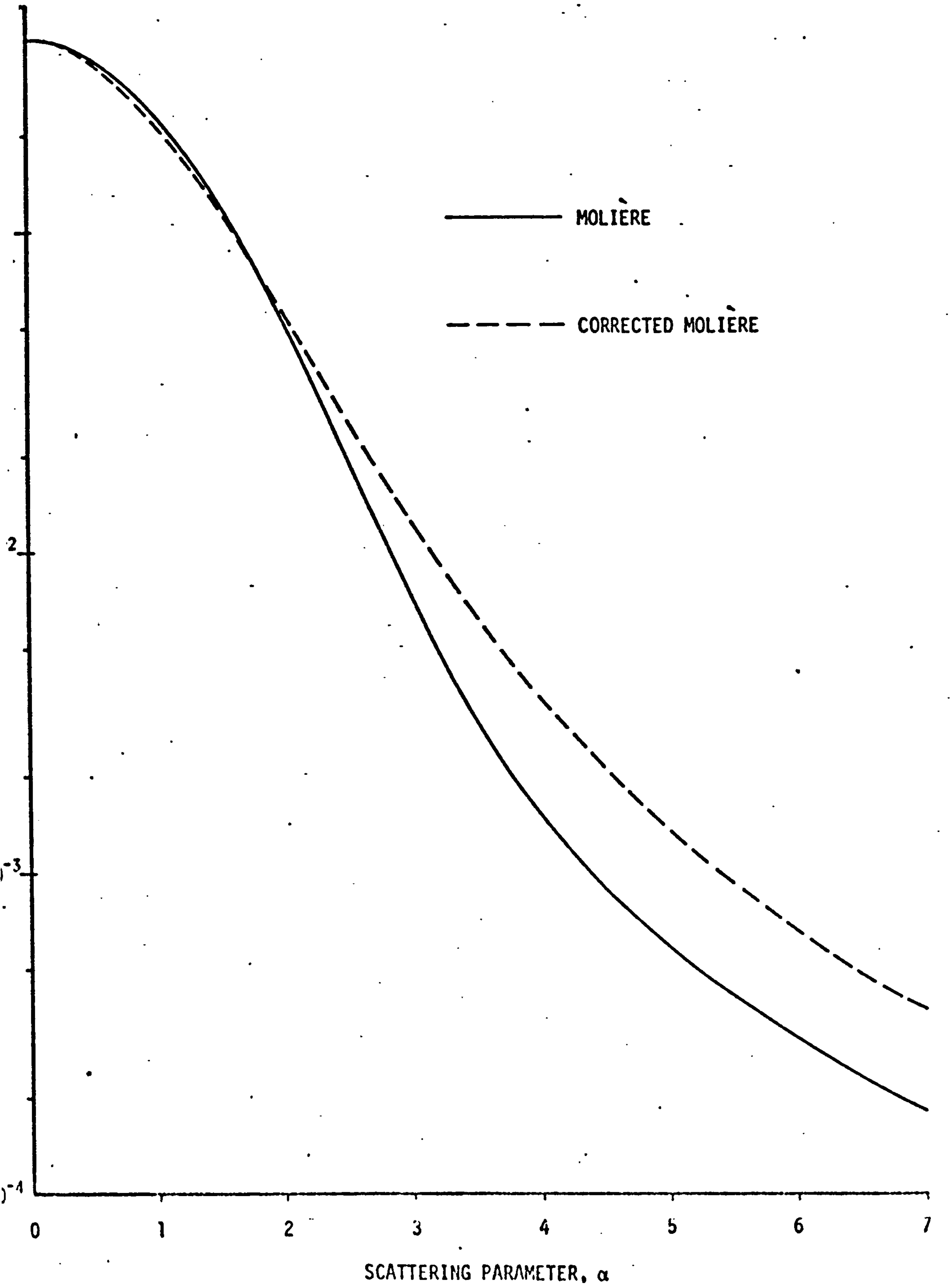

MOLIÈRE
CORRECTED MOLIÈRE
2
-3
-4
0
1
2
3
4
5
6
7
SCATTERING PARAMETER, α

of error does not exceed 6% as $\alpha \to 7$ (see Fig. 5.16).

As we shall see eq. (37) cannot be directly compared to experiment when angular measurement error is appreciable. Further modification of (37) to take measurement error into account will be developed in the following section.

5.3.5 THE EFFECTS OF UNCERTAINTY IN ANGLE MEASUREMENT

In this section we modify the corrected Molière density to include measurement error. To this end we first modify the joint density in projected angles, $J(\phi_x,\phi_y)$, to include measurement error. From eq. (5.3.3.1) we have the Molière joint density

$$J(\phi_x,\phi_y)d\phi_x d\phi_y = \frac{d\phi_x d\phi_y}{2(2\pi\sigma\phi_B)^2}\int_{-\infty}^{\infty}\int_{-\infty}^{\infty} dy_1 dy_2 \cos\left[\frac{y_1\phi_x}{\sqrt{2}\sigma\phi_B}\right] \cos\left[\frac{y_2\phi_y}{\sqrt{2}\sigma\phi_B}\right] g(y_1^2+y_2^2) \quad (1)$$

We now assume measured projected angles ϕ_{xM} and ϕ_{yM} which are described by

$$f(\phi_{xM}|\phi_x) = \frac{1}{\sqrt{2\pi}\Delta\phi}\, e^{-\frac{1}{2}\left(\frac{\phi_{xM}-\phi_x}{\Delta\phi}\right)^2} \quad (2)$$

$$f(\phi_{yM}|\phi_y) = \frac{1}{\sqrt{2\pi}\Delta\phi}\, e^{-\frac{1}{2}\left(\frac{\phi_{yM}-\phi_y}{\Delta\phi}\right)^2} \quad (3)$$

Thus the measured projected angles are assumed to be gaussian distributed with uncertainty $\Delta\phi$. The mean

FIG. 5.16 CORRECTED MOLIÈRE DENSITIES:
SEMI-ANALYTIC VS. NUMERICALLY INTEGRATED

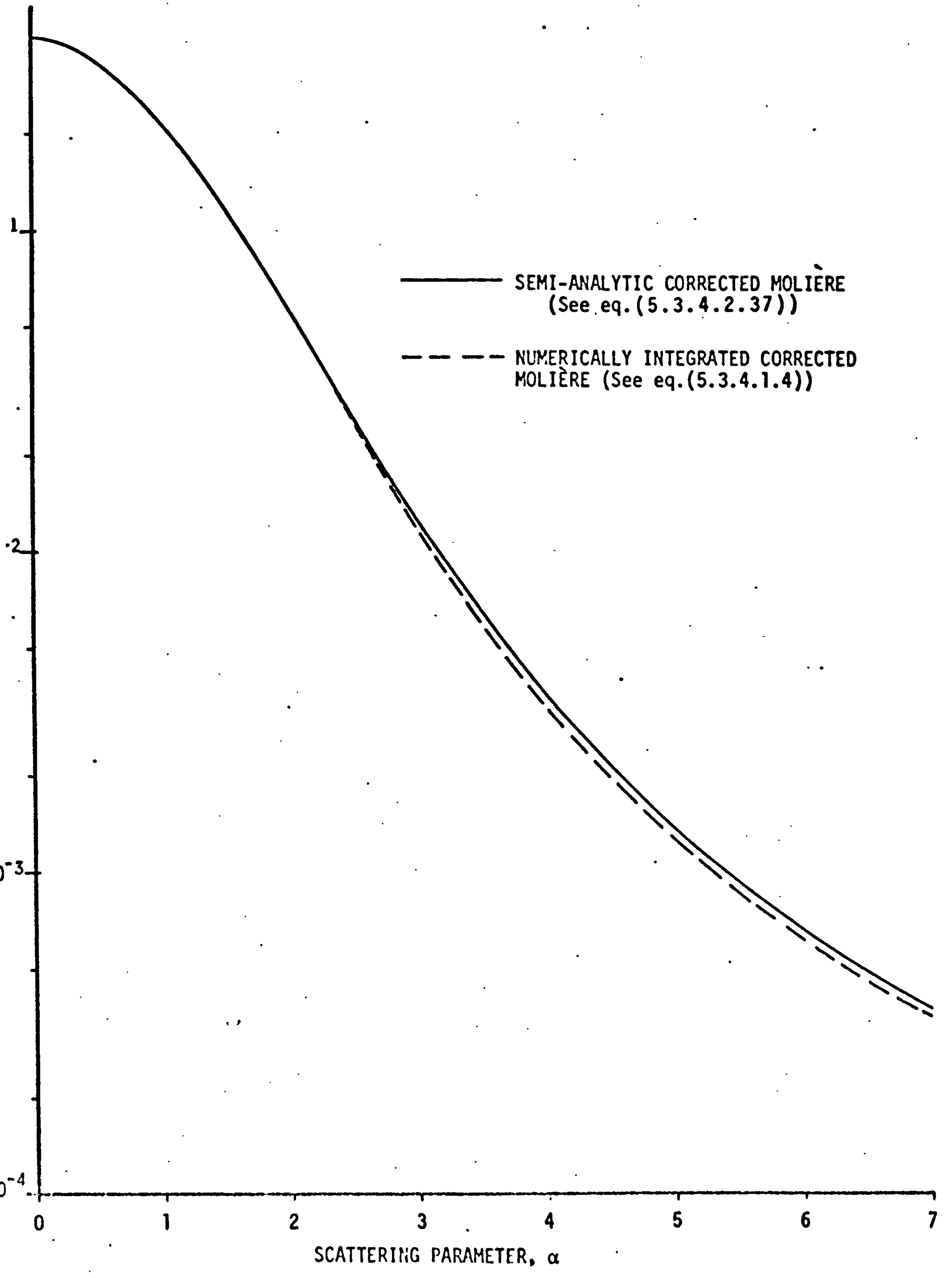

SEMI-ANALYTIC CORRECTED MOLIÈRE (See eq.(5.3.4.2.37))
NUMERICALLY INTEGRATED CORRECTED MOLIÈRE (See eq.(5.3.4.1.4))
1
-2
-3
-4
0
1
2
3
4
5
6
7
SCATTERING PARAMETER, α

values of the measured angles ϕ_{xM}, ϕ_{yM} are taken to be the real values of ϕ_x, ϕ_y.

If we take the product of (2) with (1) and integrate over ϕ_x we obtain

$$J(\phi_{xM},\phi_y)d\phi_{xM}d\phi_y = \frac{d\phi_{xM}d\phi_y}{2(2\pi\sigma\phi_B)^2}\int_{-\infty}^{\infty}\int_{-\infty}^{\infty} dy_1 dy_2 g(\phi_{xM},y_1)\cos\left[\frac{y_2}{\sqrt{2}}\left(\frac{\phi_y}{\sigma\phi_B}\right)\right] g(y_1^2+y_2^2) \quad (4)$$

where

$$g(\phi_{xM},y_1) = \frac{1}{\sqrt{2\pi}\Delta\phi}\int_{-\infty}^{\infty} \cos\left[\frac{y_1\phi_x}{\sqrt{2}\sigma\phi_B}\right] e^{-\frac{1}{2}\left(\frac{\phi_{xM}-\phi_x}{\Delta\phi}\right)^2} d\phi_y \quad (5)$$

Now let

$$z = \frac{\phi_{xM}-\phi_x}{\Delta\phi} \quad (6)$$

Thus eq. (5) becomes

$$g(\phi_{xM},y_1) = \frac{1}{\sqrt{2\pi}}\cos\left[\frac{y_1\phi_{xM}}{\sqrt{2}\sigma\phi_B}\right]\int_{-\infty}^{\infty}\cos\left[\frac{y_1\Delta\phi}{\sqrt{2}\sigma\phi_B}\right] e^{-\frac{z^2}{2}} dz \quad (7)$$

Finally

$$g(\phi_{xM},y_1) = \cos\left[\frac{y_1\phi_{xM}}{\sqrt{2}\sigma\phi_B}\right] e^{-\frac{y_1^2}{4}\left(\frac{\Delta\phi}{\sigma\phi_B}\right)^2} \quad (8)$$

Now take the product of (4) with (3), integrate over ϕ_y to obtain

$$J(\phi_{xM},\phi_{yM})d\phi_{xM}d\phi_{yM} = \frac{d\phi_{xM}d\phi_{yM}}{2(2\pi\sigma\phi_B)^2}\int_{-\infty}^{\infty}\int_{-\infty}^{\infty} dy_1 dy_2 g(\phi_{xM},y_1)g(\phi_{yM},y_2)g(y_1^2+y_2^2) \quad (9)$$

where

$$g(\phi_{yM},y_2) = \frac{1}{\sqrt{2\pi}\Delta\phi}\int_{-\infty}^{\infty} \cos\left[\frac{y_2\phi_y}{\sqrt{2}\sigma\phi_B}\right] e^{-\frac{1}{2}\left(\frac{\phi_{yM}-\phi_y}{\Delta\phi}\right)^2} d\phi_y \tag{10}$$

which leads to

$$g(\phi_{yM},y_2) = \cos\left[\frac{y_2}{\sqrt{2}}\left(\frac{\phi_{yM}}{\sigma\phi_B}\right)\right] e^{-\frac{y_2^2}{4}\left(\frac{\Delta\phi}{\sigma\phi_B}\right)} \tag{11}$$

We can now write the integrand of (9) as

$$g(\phi_{xM},y_1)g(\phi_{yM},y_2)g(y_1^2+y_2^2) =$$

$$\cos\left[\frac{y_1}{\sqrt{2}}\left(\frac{\phi_{xM}}{\sigma\phi_B}\right)\right] \cos\left[\frac{y_2}{\sqrt{2}}\left(\frac{\phi_{yM}}{\sigma\phi_B}\right)\right] e^{-\frac{y_1^2}{4}-\frac{y_1^2}{4}\left(\frac{\Delta\phi}{\sigma\phi_B}\right)} e^{-\frac{y_2^2}{4}-\frac{y_2^2}{4}\left(\frac{\Delta\phi}{\sigma\phi_B}\right)} \tag{12}$$

$$\times\, e^{-\left(\frac{y_1^2+y_2^2}{4B}\right)\ell n\left(\frac{y_1^2+y_2^2}{4}\right)}$$

If we let

$$\sigma'^2 = 1 + \left(\frac{\Delta\phi}{\sigma\phi_B}\right)^2 \tag{13}$$

we get for (9)

$$J(\phi_{xM},\phi_{yM})d\phi_{xM}d\phi_{yM} =$$

$$\frac{d\phi_{xM}d\phi_{yM}}{2(2\pi\sigma\phi_B)^2}\int_{-\infty}^{\infty}\int_{-\infty}^{\infty} dy_1 dy_2 \cos\left[\frac{y_1\phi_{xM}}{\sqrt{2}\sigma\phi_B}\right]\cos\left[\frac{y_2\phi_{yM}}{\sqrt{2}\sigma\phi_B}\right] e^{-\frac{(\sigma' y_1)^2}{4}-\frac{(\sigma' y_2)^2}{4}-\left(\frac{y_1^2+y_2^2}{4B}\right)\ell n\left(\frac{y_1^2+y_2^2}{4}\right)} \tag{14}$$

Now let

$$y_1 \Leftarrow \sigma' y_1 \quad ; \quad y_2 \Leftarrow \sigma' y_2$$

and hence (14) yields

$$J(\phi_{xM},\phi_{yM}) =$$

$$\frac{2}{(2\pi\sigma\sigma'\phi_B)^2}\int_0^{\infty}\int_0^{\infty} dy_1 dy_2 \cos\left[\frac{y_1}{\sqrt{2}}\left(\frac{\phi_{xM}}{\sigma\sigma'\phi_B}\right)\right]\cos\left[\frac{y_2}{\sqrt{2}}\left(\frac{\phi_{yM}}{\sigma\sigma'\phi_B}\right)\right] e^{-\left(\frac{y_1^2+y_2^2}{4}\right)+\left(\frac{y_1^2+y_2^2}{4B\sigma'^2}\right)\ln\left(\frac{y_1^2+y_2^2}{4\sigma'^2}\right)} \quad (15)$$

Furthermore since the measured total-angle is given by

$$\phi_{TM} = \phi_{xM} + \phi_B$$

eq. (15) becomes

$$J(\phi_{TM},\phi_{yM}) =$$

$$\frac{2}{(2\pi\sigma\sigma'\phi_B)^2}\int_0^{\infty}\int_0^{\infty} dy_1 dy_2 \cos\left[\frac{y_1}{\sqrt{2}}\left(\frac{\phi_{TM}-\phi_B}{\sigma\sigma'\phi_B}\right)\right]\cos\left[\frac{y_2}{\sqrt{2}}\left(\frac{\phi_{yM}}{\sigma\sigma'\phi_B}\right)\right] e^{-\left(\frac{y_1^2+y_2^2}{4}\right)+\left(\frac{y_1^2+y_2^2}{4B\sigma'^2}\right)\ln\left(\frac{y_1^2+y_2^2}{4\sigma'^2}\right)} \quad (16)$$

We introduce (as we previously did for the gaussian modification) the relative scattering parameter

$$\alpha = \frac{1}{\sigma}\frac{\phi_{yM}}{\phi_{TM}} \quad (17)$$

From (17) we have $\phi_{yM} = \sigma\alpha\phi_{TM}$; substitution of this equation into (16) and subsequent integration over ϕ_{TM} yields

$$f(\alpha|\sigma,\phi_B) = \sigma\int_0^{\infty}\phi_{TM} J(\phi_{TM},\sigma\alpha\phi_{TM})\,d\phi_{TM} \quad (18)$$

Put (16) into (18) and let $x = \phi_{TM}/\phi_B$ to get

$$f(\alpha|\sigma,\phi_B) =$$

$$\frac{1}{2(\pi\sigma')^2\sigma}\int_0^{\infty}dx\; x\int_0^{\infty}\int_0^{\infty}dy_1 dy_2 \cos\left[\frac{y_1}{\sqrt{2}}\left(\frac{x-1}{\sigma'}\right)\right]\cos\left[\frac{y_2}{\sqrt{2}}\left(\frac{\alpha x}{\sigma'}\right)\right] e^{-\left(\frac{y_1^2+y_2^2}{4}\right)+\left(\frac{y_1^2+y_2^2}{4B\sigma'^2}\right)\ln\left(\frac{y_1^2+y_2^2}{4\sigma'^2}\right)} \quad (19$$

where

$$\sigma' = \left[1 + \left(\frac{\Delta\phi}{\sigma\phi_B}\right)^2\right]^{1/2} \tag{20}$$

Eq. (19) is the integral formulation of the modified Molière density corrected for uncertainty in angle measurement. If the uncertainty in angle measurement, $\Delta\phi$, approaches zero then $\sigma' \to 1$ and eq. 19 approaches eq. (5.3.4.2.3), in the limit.

It is easy to verify that

$$\alpha \to \frac{\alpha}{\sigma'}$$

$$\sigma \to \sigma'\sigma$$

transforms (5.3.4.2.3) into (19) <u>except</u> for the additional factors of σ' in the 1/B term of the exponent. This allows the semi-analytic form of the modified Moliere density, eq. (5.3.4.2.37), to be corrected for measurement error by inspection. The final result is easily verified by series expansion and subsequent integration of eq. (19). We now present the final result

$$f(\alpha|\sigma,\phi_B) = \frac{1}{\sqrt{2\pi}} \frac{e^{-\frac{1}{2}\left(\frac{\alpha^2}{\sigma'^2(1+\sigma^2\alpha^2)}\right)}}{\sigma'(1+\sigma^2\alpha^2)^{3/2}} + \frac{f^{(1)}(\alpha|\sigma,\phi_B)}{B} \tag{21}$$

where

$$f^{(1)}(\alpha|\sigma,\phi_B) = \frac{1}{\sqrt{2}\,\pi} \int_0^\infty dy\, F(y,\alpha)\, e^{-\frac{y^2}{4}} \left[\frac{y^2}{4\sigma'^2} \ln \frac{y^2}{4\sigma'^2}\right] \tag{22}$$

$$F(y,\alpha) = \frac{e}{\sigma^{T}}^{-\left(\frac{\sigma\alpha y}{2}\right)^2}\left[\text{COS}\left(\frac{\alpha y}{\sqrt{2}\sigma'}\right) - (\sigma\sigma')^2\left(\frac{\alpha y}{\sqrt{2}\sigma'}\right)\ \text{SIN}\ \left(\frac{\alpha y}{\sqrt{2}\sigma'}\right)\right] \tag{23}$$

$$+ \frac{1}{\sqrt{2\pi}\sigma\alpha^2}\left[g(y)\ \text{COS}\left(\frac{y}{\sqrt{2}\sigma\sigma'}\right) + \sqrt{\frac{\pi}{2}}\frac{\sigma'}{|\alpha|}\left(\frac{y}{\sqrt{2}\sigma\sigma'}\right)\ \text{SIN}\ \left(\frac{y}{\sqrt{2}\sigma\sigma'}\right)\ e^{-\frac{1}{4}\left(\frac{y}{\sigma\alpha}\right)^2}\right]$$

Where

$$g(y) = 2\left(\frac{\sigma\alpha}{y}\right)^2 \int_0^\infty x e^{-\left(\frac{\sigma\alpha}{y}\right)^2 x^2}\ \text{COS}\ x dx \tag{24}$$

and

$$\sigma' = \left[1 + \frac{1}{\sigma^2}\left(\frac{\Delta\phi}{\phi_B}\right)^2\right]^{1/2} \tag{25}$$

5.3.6 INTEGRATION OVER THE COSMIC RAY SPECTRUM

Eq. (5.3.5.21) must be integrated over the cosmic ray spectrum in order to remove the dependence on the bending angle, ϕ_B. This is accomplished by

$$f(\alpha|\sigma,\gamma) = \int_{p_c}^{\infty} f(\alpha|\sigma,p_0)\ I(p_0|\gamma_0)dp_0 \tag{1}$$

where $f(\alpha|\sigma,p_0)$ is given by (5.3.5.21), p_0 is the momentum corresponding to ϕ_B and $I(p_0|\gamma_0)$ is the cosmic ray differential intensity discussed in Appendix I. The dependence on the momentum p_0 is due to

$$\sigma' \approx \left[1 + \frac{1}{\sigma^2}\left(\frac{p_0}{p_{CDM}}\right)^2\right]^{1/2} \tag{2}$$

where p_{CDM} is the CDM (characteristically determined momentum) of the spectrometer. Thus p_{CDM} plays the role of a free parameter which may be (1) calculated by independent means, or (2) fitted to the data. Here we determine p_{CDM} by fitting the experimental data to the theory.

Fig. 5.17 shows multiple scattering curves calculat·· by eq. (1) for p_{CDM} = 100 GeV/c and 50 GeV/c. Also sho.. in the figure is the corrected Molière density calculated by eq. (5.3.5.21) for $\sigma' = 1$. This corresponds to $p_{CDM} \to \infty$. Thus as $p_{CDM} \to o$ the multiple scattering density increases its width and "flattens out" until, in the limit, the density merges with the α-axis.

Fig. 5.18 shows most of the multiple scattering densities which have been encountered in our development; thus the reader can compare the various corrections which have been accounted for in this chapter.

5.3.6.2

FIG. 5.17 MULTIPLE SCATTERING CURVES AT CHARACTERISTICALLY DETERMINED MOMENTA OF 50 GeV/c, 100 GeV/c, ∞

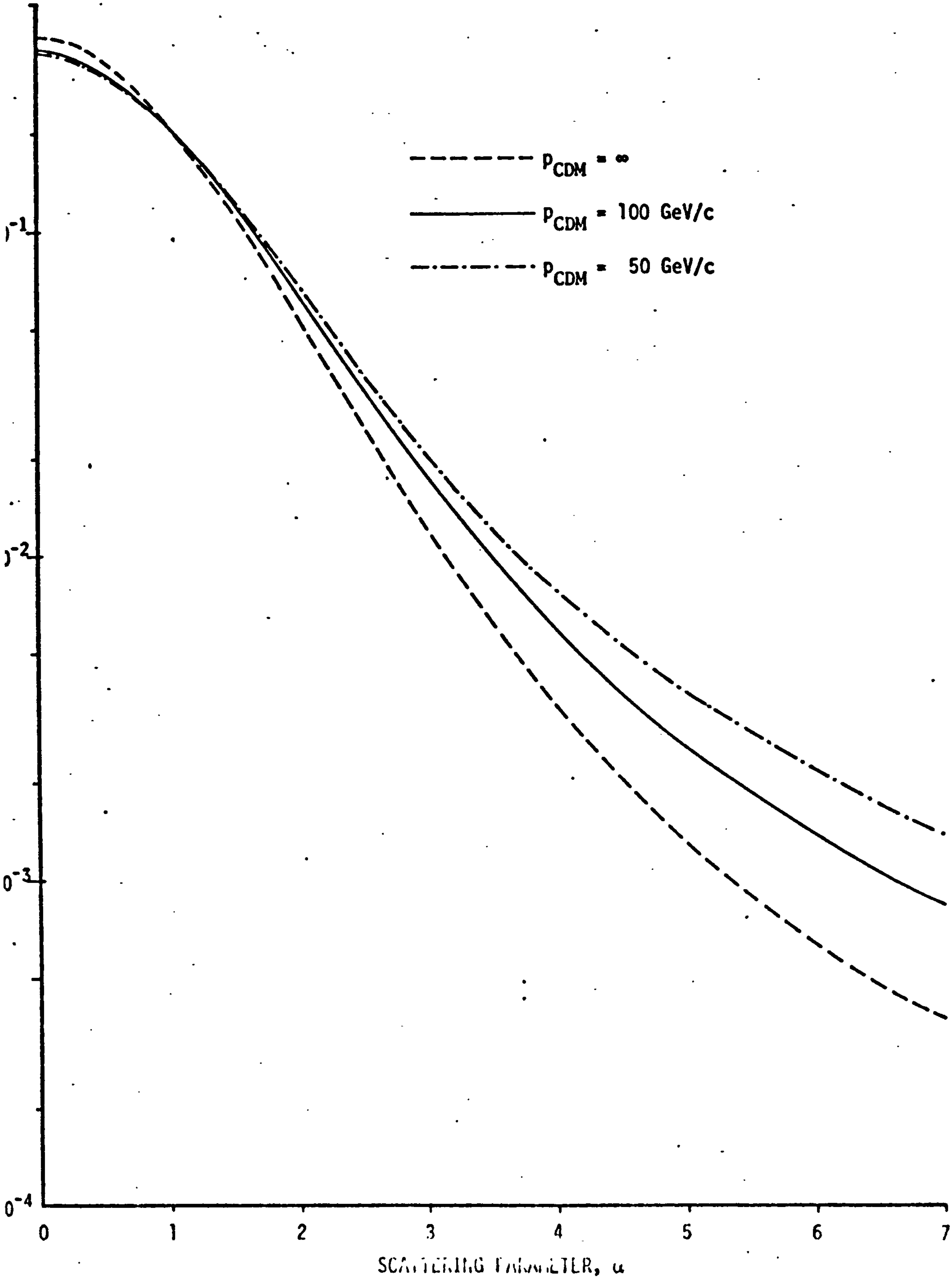

$p_{CDM} = \infty$
$p_{CDM} = 100$ GeV/c
$p_{CDM} = 50$ GeV/c
0
1
2
3
4
5
6
7

5.3.6.3

FIG. 5.18 MULTIPLE SCATTERING CURVES

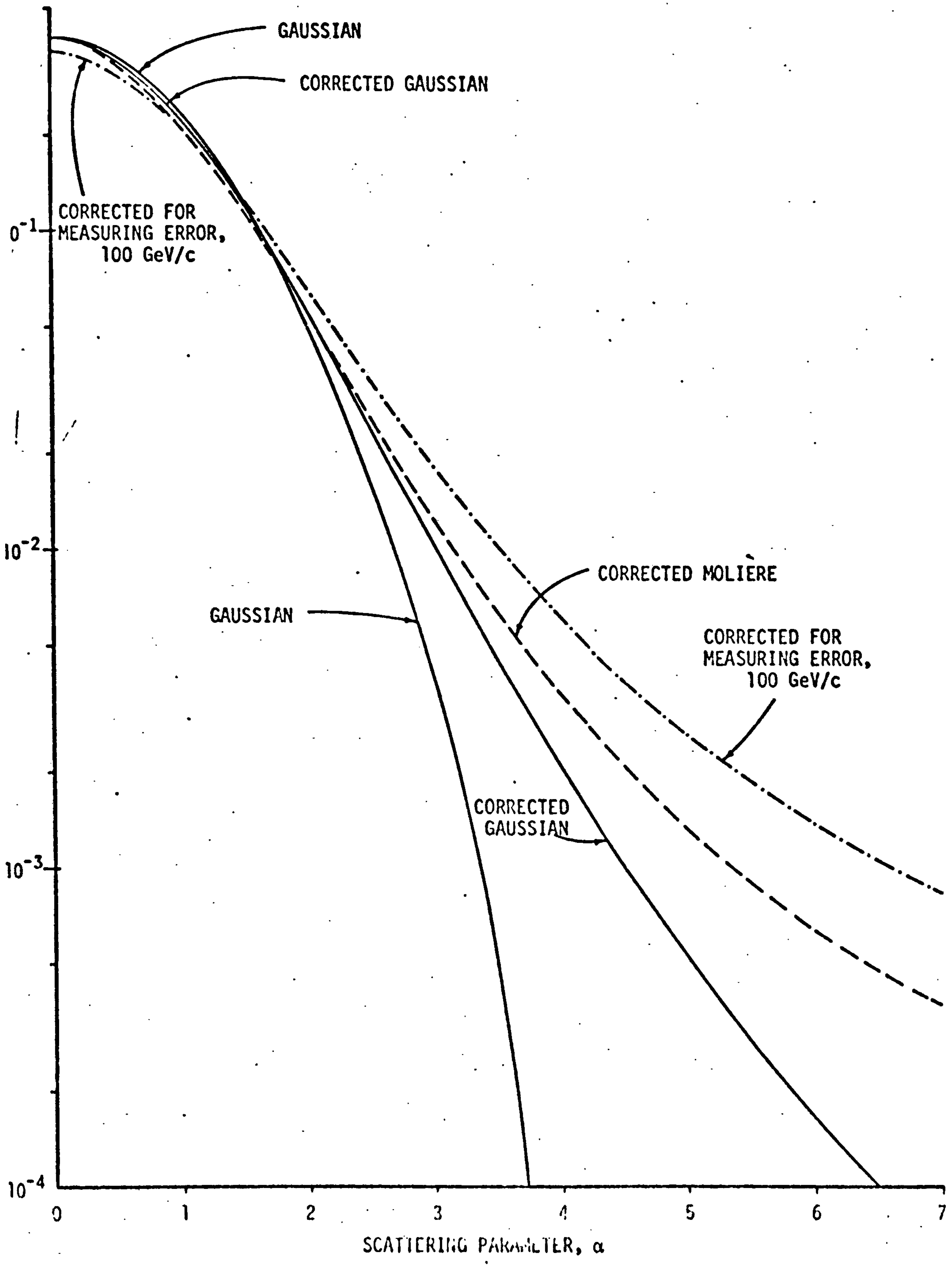
GAUSSIAN
CORRECTED GAUSSIAN
CORRECTED FOR MEASURING ERROR, 100 GeV/c
CORRECTED MOLIERE
GAUSSIAN
CORRECTED FOR MEASURING ERROR, 100 GeV/c
CORRECTED GAUSSIAN
0^-1
10^-2
10^-3
10^-4
0
1
2
3
4
5
6
7
SCATTERING PARAMETER, α

CHAPTER VI

EXPERIMENTAL RESULTS

6.1 INTRODUCTION

In this chapter we briefly review the physics of multiple scattering and then describe the analysis of the data from the AMH magnetic spectrometer. In particular we discuss: (1) the Molière theory and its basic assumptions, (2) the modification to the Molière theory (as presented in Ch. V) and the corresponding assumptions made, (3) the need for folding in the cosmic ray muon momentum spectrum in order to account for measurement error, (4) preparation of the data for analysis, and finally (5) comparison of the data to the theory and interpretation of the results.

6.2 ASSUMPTIONS OF THE MOLIÈRE THEORY

The multiple scattering of a fast charged particle is due to the many successive collisions of the particle with atoms of some target material. Molière, in the development of his theory, made two assumptions which were independent of the single scattering (collision) law:

1) Successive single scatterings in the target material are statistically independent.

2) The small angle approximation can be used, i.e. SIN $\theta \approx \theta$ and COS $\theta \approx 1$.

Further assumptions, made by Molière, about the single scattering law are:

(1) The single scattering cross section is independent of the azimuthal angle in the absence of spin effects.

(2) The single scattering law includes scattering due to a nuclear Coulomb field as screened by a cloud of atomic electrons.

Using the above assumptions, Molière developed a multiple scattering density which consisted of a gaussian with correction terms (as we have seen in Ch. IV).

Molière did not include the following physical processes in his results:

(1) The finite size of the nuclear charge distribution.

(2) Effects due to inelastic collisions in the nucleus.

(3) Multiple scattering by atomic electrons.

The effects of finite nuclear size and inelastic collisions in the nucleus have been developed by Cooper and Rainwater.[14] The scattering by atomic electrons is discussed by Scott.[17] We have, with Molière, ignored the above effects in our analysis.

6.3 ASSUMPTIONS MADE IN THE MODIFICATION TO THE MOLIÈRE THEORY

Molière's theory has been modified in Ch. V for use with magnetic spectrometers. Certain approximations were made in the development of the resultant semi-analytic multiple scattering function, eq. (5.3.4.2.37):

1) The statistical dependence of the projected angles ϕ_x and ϕ_y is ignored.

2) Whenever $\frac{1}{\sigma}$ appears in the limit of a rapidly converging integral the limit is assumed to be ∞.

3) Field view scattering angles in the region $-\infty < \phi_x < -\phi_B$ are neglected, thus simplifying the resultant multiple scattering density, $f(\alpha)$.

4) The spectrometer noise, σ, is a constant.

We have shown (see Fig. 5.16) that the above approximations introduce an error in the multiple scattering density of no more than 6% in the region $\alpha>3$.

We have also shown that the dimensionless scattering parameter, α, of the modified multiple scattering density, $f(\alpha)$, can be expressed in two ways:

(1) In terms of the experimentally determined momentum, p, the scattering angle, ϕ, and the target thickness, x,

$$\alpha = f(p,x)p\phi \qquad (1)$$

(2) In terms of the field-view total-angle, ϕ_T, the scattering angle, ϕ, and the "noise", σ,

$$\alpha = \frac{1}{\sigma} \frac{\phi}{\phi_T} \qquad (2)$$

In the analysis of the experimental data we shall bin the data according to values of α calculated for a single event by both (1) and (2). When eq. (1) is applied the procedure used is to χ^2-fit the momentum, p, by the technique discussed in Sec. 3.5.2. Briefly, this method generates the best muon trajectory through the measured muon position and unit momentum vectors in all three spark chambers. The resultant momentum, p, and path length in the iron, x, come from the χ^2-fit procedure. Using p and x together with the scattering angle, ϕ, (as measured in the no-field view) a value of the parameter α is calculated for a particular event. A histogram of the values of α for all of the events can then be compared to the theoretical results. In a similar way eq. (2) can be used to generate an α-histogram of the data. Here, however, the values of α are calculated much more simply by use of an average path length in the iron, $\langle x \rangle$, in order to determine an average value of σ (for the data $\langle x \rangle \cong 95$ cm iron, $\sigma \cong .23$). We will compare the data for eqs. (1) and (2) in a later section.

Before proceeding to the next section we point out that the semi-analytic multiple scattering density, $f(\alpha)$, (eq. (5.3.4.2.37)) can be used for any magnetic spectrometer experiment (provided it obtains both field view and no-field view data), and hence $f(\alpha)$ is a theoretical result useful for interpreting multiple scattering in magnetic spectrometers. However, each experiment has measurement error which must be accounted for. A technique for taking measurement error into account has been discussed in Sec. 5.3.5. This technique may or may not be applicable for other experimental apparatus; the assumptions made about experimental error for the AMH magnetic spectrometer may not hold true for other spectrometers. Thus other investigators may be unable to use the multiple scattering density which has been developed here to account for measurement error, i.e. eq. (5.3.5.21) but may, in fact, have to account for measurement error in a different way.

6.4 EXPERIMENTAL ERROR AND INSTRUMENT RESOLUTION

In Sec. 5.3.5 measurement error is taken into account by assuming that all measured angles have errors that are gaussian distributed. This leads to a new density in $f(\alpha)$ which is dependent upon the parameter σ', where

$$\sigma'^2 \cong \sigma^2 + \left[\frac{p_0}{p_{CDM}}\right]^2 \qquad (1)$$

Here σ is the spectrometer noise, p_0 is the "real" momentum of the muon, and p_{CDM} is the "characteristically determined momentum". Since $f(\alpha)$ is a function of p_0 we must now remove this dependence by integration over the cosmic ray muon momentum spectrum by eq. (5.3.6.1). As seen in Appendix I the cosmic ray spectrum is dependent upon two parameters: (1) N_0, which insures normalization, and (2) γ_0, the spectral exponent. For our purposes we require N_0 to be such that

$$\int_0^\infty I(p_o|N_\sigma\gamma_\sigma)dp_o = 1 \qquad (2)$$

Thus the dependence on the cosmic ray spectrum lies entirely in the spectral exponent, γ_o. The experimental determination of γ_o is discussed in Appendix II.

Eq. (1) depends on the parameter p_{CDM}. Thus, after integration over the cosmic ray spectrum, the multiple scattering density has the dependence:

$$f(\alpha|\sigma,p_{CDM})$$

Recall that p_{CDM} is the momentum corresponding to the uncertainty in an angle measurement, $\Delta\phi$, so that

$$p_{CDM} = \frac{k}{\Delta\phi}$$

In order to fit the multiple scattering data we shall use p_{CDM} as a fit parameter. We have assumed that p_{CDM} and $\Delta\phi$ are constants independent of the momentum. While we shall assume that this is the case we realize that p_{CDM} may not be constant, due to the following argument: High momentum events traversing the spectrometer generally pass nearly perpendicularly to the spark chamber plates, while low momentum events may be bent appreciably by the magnetic field, and therefore may traverse the chambers at angles as large as 35° from the perpendicular. The wide gap chambers are less efficient for these low energy events, i.e. the spark has less of a tendency to follow the ionized path, they become "s" shaped. Thus these events may be measured to less precision than the high momentum events. Such a dependence might be represented by

$$p_{CDM} = a_o + a_1 p + a_2 p^2 + \ldots \qquad (3)$$

Assuming that all the coefficients are positive then the characteristic momentum is greater for higher momentum. Since we do not know a_1, a_2 ... we shall assume that they are zero and fit a_o. If indeed p_{CDM} is given by (3) we expect an average $<p_{CDM}>$ over the muon momentum spectrum to be dominated by low momentum events, since 70% of the events are below 15 GeV/c. Thus the assumption that p_{CDM} is constant means that, when the multiple scattering data is fitted to theory, the resulting value of p_{CDM} will be dominated by low momentum events. We shall henceforth designate a constant value of p_{CDM} by p_{MDM}, the "maximum detectable momentum" of the spectrometer. $p_{CDM} = p_{MDM}$ only when the measurement error, $\Delta\phi$, is independent of momentum. We see that, in general

$$p_{CDM} < p_{MDM}$$

Now recall the definition of the "effective momentum", p_e: that momentum which corresponds to the error due to the optical reconstruction of a muon event and <u>excludes</u> measurement error incurred by use of the digitizing apparatus. We see that $p_e = p_{MDM}$ only when measurement error is zero. The relationship between the above three types of momentum is therefore

$$p_{CDM} \leq p_{MDM} \leq p_e$$

We have already estimated p_e in Ch. III. p_{CDM} will be obtained in a fit to the multiple scattering data, and we will have then obtained upper and lower limits on p_{MDM}.

6.5 PREPARATION OF THE DATA FOR ANALYSIS; THE DATA ANALYSIS

A certain percentage of the data is contaminated by "bad" events of various types. For this reason selection criteria are required in order that only the clean events be retained for analysis. To this end the χ^2 momentum determination program of Ch.III classifies bad events according to the following:

(1) CROSS OVER EVENT - an event which crosses from one channel of the spectrometer to the other. Such events undergo a magnetic field reversal, and therefore are not analyzable.

(2) INDETERMINANT CHARGE EVENT - an event which appears to have a different charge in the top and bottom magnets. This may be due to a badly scattered event or due to contamination by an accompanying particle.

(3) EVENT OUTSIDE THE SPECTROMETER - an event is judged to be "outside the spectrometer" if its position vector does not penetrate both the top and bottom scintillators of the same channel. Events of this type are frequently encountered when particle showers from the ceiling trigger the apparatus.

(4) SPURIOUS EVENT - an event is labelled "spurious" if one or more spark chambers do not fire for a single event.

All events, which were diagnosed as belonging to one of the above types, were not considered for multiple scattering analysis. Further, all events with a value of $\chi^2 > 16$ (from the momentum determination program) were considered as candidates for remeasurements. For a 7 degree-of-freedom fit this value of χ^2 corresponds to a 95% probability that, upon remeasurement, these events would yield a smaller value of χ^2.

After the above selection criteria were applied to 13,000 muon events approximately 8,000 remained. A χ^2-fit to this remaining data was made using eq. 5.3.6.1. The fit parameters used were

N_0 = normalization, used to scale the ordinate of the multiple scattering density.

σ_0 = a scale factor for α, the abscissa of the multiple scattering density.

p_{CDM} = the characteristically determined momentum.

The results of the fit are shown in Fig. 6.1. The resultant fit parameters were: N_0 = 1.01 ± .01, σ_0 = .97 ± .03 and p_{MDM} = 47.3 ± 6.6 GeV/c. This value of p_{CDM} is unexpectedly low, perhaps indicating that the data is still contaminated by some source yet to be accounted for. Further investigation indicated that a number of events contained knock-on electrons in one or more spark chamber. If, in the measuring process, a particle is judged to be a muon, but is in fact an electron, then a "bad" event results. We conclude that knock-on electrons are a source of contamination. An additional run was made with all knock-on events removed. The result of a fit to this data is shown in Fig. 6.2. Again N_0 and σ_0 fit sufficiently close to 1(as they theoretically should) and p_{MDM} increases to 98.9 ± 23.8 GeV/c. The data of Figs. 6.1 and 6.2 were histogramed using $\alpha = \frac{1}{\sigma}\frac{\phi}{\phi_T}$. However Fig. 6.3 shows the data histogramed by $\alpha = f(p)p\phi$. The data of Figs. 6.2 and 6.3 is the same except for the method of calculating α. It can be seen that there is very little difference in the histograms. The curve drawn through the data of Fig. 6.3 is the same as that fitted to the data of Fig. 6.2. Thus either method for calculating α appears to be just as good. However, we point out that the χ^2 momentum determination allows events to be selected on the basis of their value of χ^2. Thus $\alpha = f(p)p\phi$

FIG. 6.1 MULTIPLE SCATTERING FIT TO DATA CONTAMINATED BY KNOCK-ON ELECTRONS

$$\alpha = \frac{\phi}{\sigma\phi_T}$$

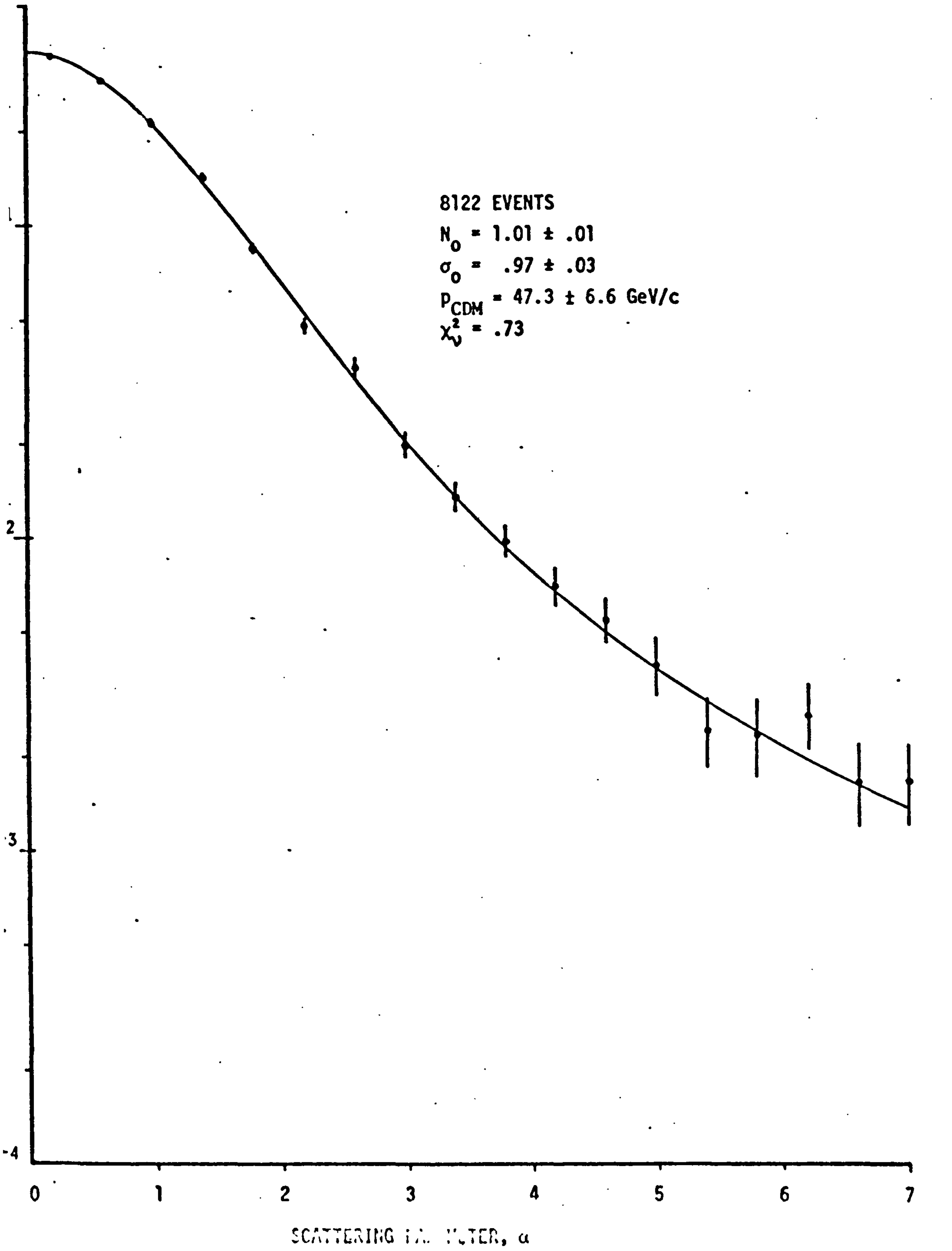
8122 EVENTS
N_o = 1.01 ± .01
σ_o = .97 ± .03
P_{CDM} = 47.3 ± 6.6 GeV/c
χ^2_ν = .73
1
2
3
-4
0
1
2
3
4
5
6
7

6.5.5

FIG. 6.2 MULTIPLE SCATTERING FIT WITH KNOCK-ON ELECTRONS REMOVED

$$\alpha = \frac{\phi}{\sigma\phi_T}$$

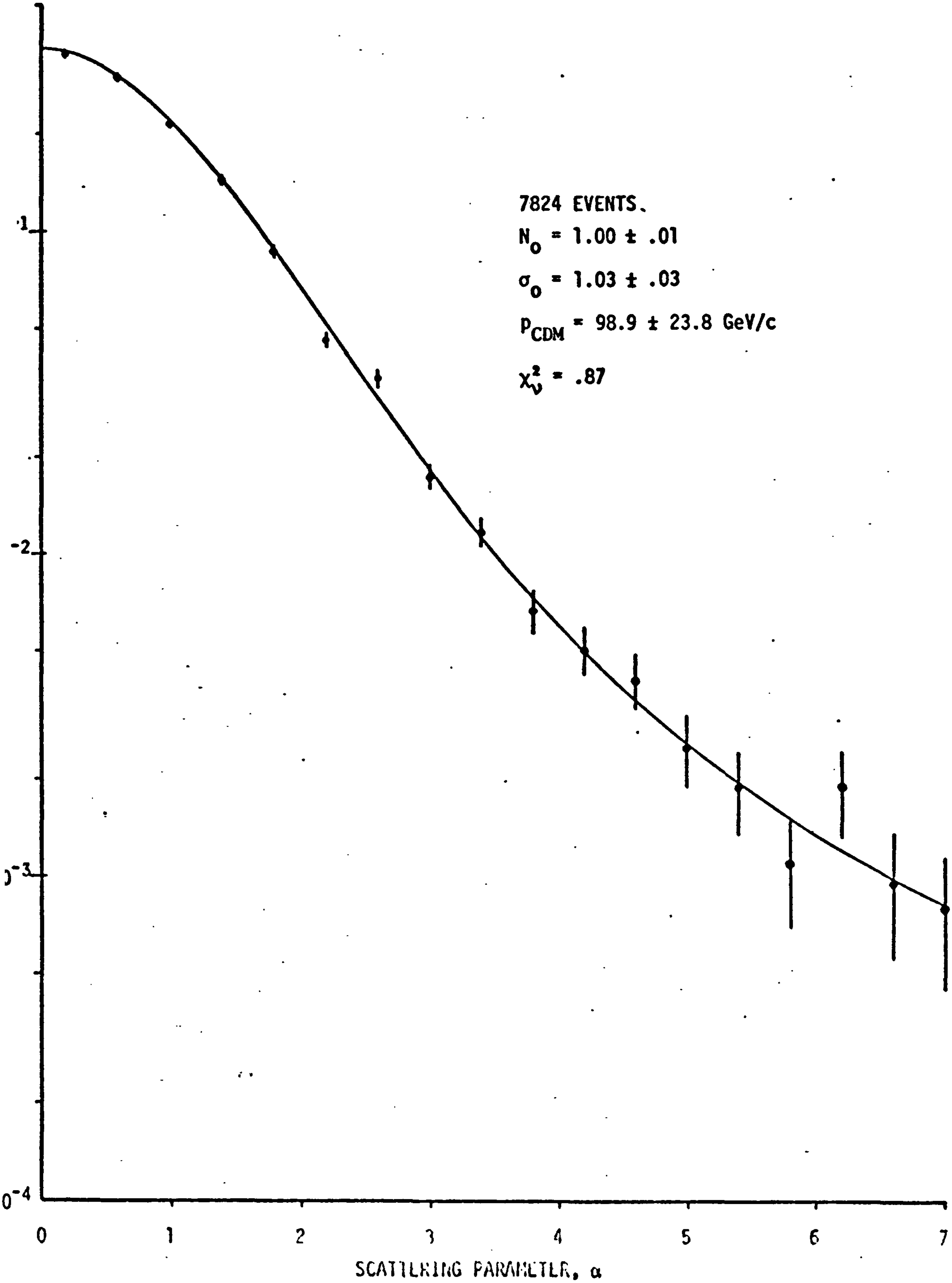
7824 EVENTS.
N_o = 1.00 ± .01
σ_o = 1.03 ± .03
P_{CDM} = 98.9 ± 23.8 GeV/c
χ^2_ν = .87
10^{-1}
10^{-2}
10^{-3}
10^{-4}
0
1
2
3
4
5
6
7
SCATTERING PARAMETER, α

6.5.6

FIG. 6.3 COMPARISON OF CURVE OF FIG. 6.2 WITH DATA HISTOGRAMED VIA

$$\alpha = f(p)p\phi$$

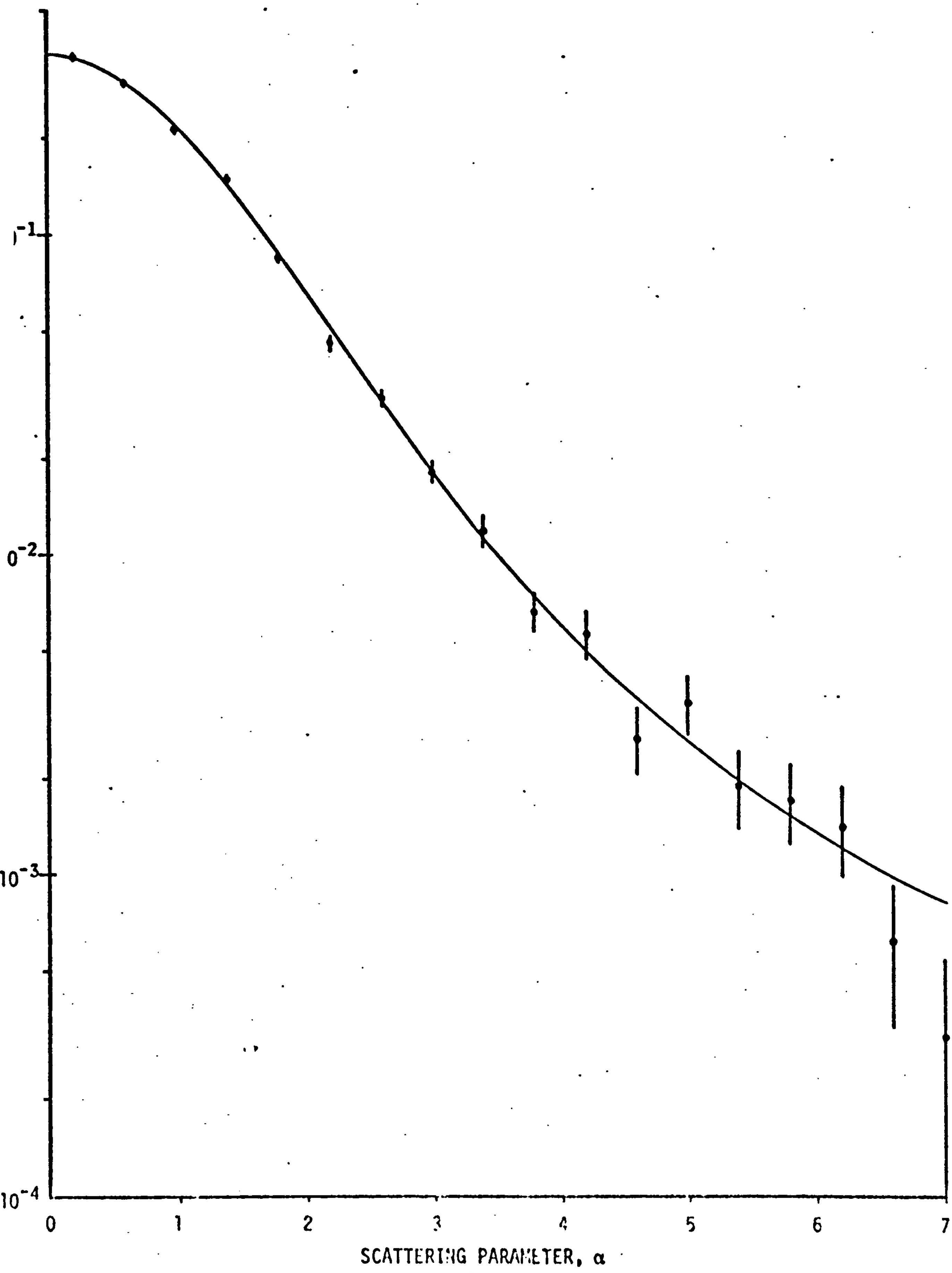

10^-1
10^-2
10^-3
10^-4
0
1
2
3
4
5
6
7
SCATTERING PARAMETER, α

appears to be the preferred method for calculating α.

In conclusion, we state that a χ^2 fit of the theoretical multiple scattering density to data from the AMH magnetic spectrometer has been accomplished. The resultant fit parameters were

$$N_0 = 1.00 \pm .01$$

$$\sigma_0 = 1.03 \pm .03$$

$$p_{CDM} = 98.9 \pm 23.8$$

with a reduced χ^2 of .87. Theoretically we expect $N_0 = 1$ and $\sigma_0 = 1$. The width of the experimentally determined multiple scattering density, σ_{EXP}, is given by

$$\sigma_{EXP} = \sigma_0 \sigma_\phi$$

We conclude that the width of the Moliere multiple scattering density, σ_ϕ, agrees well with the experimental result. Finally the determination of p_{CDM} sets a lower limit on the spectrometer MDM; taken together with the determination of the effective momentum, p_c, (see Sec. 3.3.5) we can set an upper limit on the MDM, resulting in

$$98.9 \text{ GeV/c} \leq p_{MDM} \leq 310 \text{ GeV/c}$$

Uncertainties in the behavior of measurement error as a function of momentum prevent a more precise determination of the spectrometer MDM.

We emphasize here the important role that measurement error plays in our results. Fig. 5.17 compares the corrected Molière density for no measurement error ($p_{CDM} = \infty$), to the corrected Molière density which includes measurement error ($p_{CDM} = 100$ GeV/c). We see that the introduction of measurement error spreads out the multiple scattering distribution, increasing its rms width. If measurement error is not included in our analysis anomalous results are encountered when theory is compared to the data, i.e. the rms width of the data is about 10% greater than what theory predicts. This increase in width is accounted for only when measurement error is included in our analysis. As we have seen before, the inclusion of measurement error results in an excellent fit to the data (Fig. 6.2). We conclude that the Molière theory accounts for the observations made with the AMH magnetic spectrometer.

Several observers have examined their data for the effects of finite nuclear size[2,6,8], which is accounted for theoretically by Cooper and Rainwater[15]. Bhattacharyya[2] and Meyer et al.[6] report good agreement with the theory of Cooper and Rainwater. Physically, finite nuclear size "cuts off" the single scattering cross section at large angles, resulting in a reduction in the height of the "tail" of the multiple scattering distribution. No attempt has been made to account for finite nuclear size in our analysis. The primary reasons for this omission are: 1) the relatively small number of events analyzed in the experiment, and 2) the lack of complete understanding of the momentum dependence in the measurement error, $\Delta\phi$. Thus, this uncertainty in the data in the region of large α means that a search for effects due to finite nuclear size may not be meaningful. Also, the large amount of computer time required for an additional analysis (40 hours of UNIVAC 1108 time were used for the analysis presented in this dissertation) precludes closer investigation of the data at this time.

A modification to the theory of Cooper and Rainwater (similar to the modification of the Molière theory in Ch. V), to account for magnetic spectrometer observations, has been accomplished and will be reported on in a later publication.

APPENDIX I

THE COSMIC RAY MUON MOMENTUM SPECTRUM

The maximum likelihood technique was used to fit cosmic ray muon momentum spectrum to a two parameter phenomenological model in N, γ[22]

$$I(p|N,\gamma) = N\, p_\mu(p)(p+\Delta p)^{-\gamma} \left[\frac{R_\pi^{\gamma-1} B_\pi}{p+\Delta p+B_\pi}\right] E(p) \qquad (1)$$

where

N = normalization parameter

p = observed muon momentum

γ = spectral exponent

B_π = 90 GeV/c

R_π = ratio of muon to pion mass, .76

Δp = ionization momentum loss of the muon in the earth's atmosphere

$E(p)$ = spectrometer efficiency function, the ratio of the geometrical factor at momentum p to the geometrical factor at $p = \infty$.

$p_\mu(p)$ = muon survival probability

APPENDIX II

CORRECTION OF THE COSMIC RAY MUON SPECTRUM FOR MULTIPLE SCATTERING

The cosmic ray muon spectrum described in the previous appendix must be corrected for the effects of multiple scattering. Thus we introduce the "total angle spectrum", $I(\phi_{TM}|N,\gamma)$, corresponding to the measured momentum spectrum $I(p|N,\gamma)$. Here as we have previously seen,

$$p = \frac{k}{\phi_{TM}} \tag{1}$$

Likewise we introduce the "magnetic bending angle spectrum", $I(\phi_B|N_o,\gamma_o)$, which corresponds to the actual momentum spectrum $I(p_o|N_o,\gamma_o)$. Also we have

$$p_o = \frac{k}{\phi_B} \tag{2}$$

The angular spectra are related by

$$I(\phi_{TM}|N,\gamma) = \int_0^\infty f_{TM}(\phi_{TM}|\phi_B) I_o(\phi_B|N_o,\gamma_o) d\phi_B \tag{3}$$

where $f_{TM}(\phi_{TM}|\phi_B)$ is the Molière total angle density given by

$$f(\phi_{TM}|\phi_B) = \frac{1}{\sqrt{2}\pi\sigma_n\phi_B} \int_0^\infty dy \cos\left[\frac{(\phi_{TM}-\phi_B)y}{\sqrt{2}\,\sigma_n\phi_B}\right] e^{-\frac{y^2}{4}+\frac{y^2}{4B\sigma_n^2}\ln\frac{y^2}{4\sigma_n^2}} \tag{4}$$

where

$$\sigma_n = \left[\sigma^2 + \left(\frac{\Delta\phi}{\phi_B}\right)^2\right]^{1/2}$$

The angle $\Delta\phi$ corresponds to the "characteristically determined momentum", p_{CDM}, of the spectrometer:

$$p_{CDM} = \frac{k}{\Delta\phi} \tag{5}$$

Thus the measured cosmic ray muon spectrum is a function of p_{CDM} just as the multiple scattering density is a function of p_{CDM}.

REFERENCES

1. E. V. Hungerford, G. S. Mutchler, G. C. Phillips and M. L. Scott (Rice University); J. C. Allred, L. Y. Lee, B. W. Mayes and Clark Goodman, Nuclear Physics A197(1972)515-528.

2. D. P. Bhattacharyya, Z. Physik 233 (1970) 445-451.

3. C. A. Ayre, M. A. Hamdan, C. J. Hume, B. C. Nandi, M. G. Thompson, S. C. Wells, M. R. Whalley and A. W. Wolfendale, J. Phys. A: Gen. Phys., Vol. 5, October 1972, 102-105.

4. J. J. Torsti, "Lateral Multiple Scattering Distributions of Muons in Cosmic Ray Spectrographs", Ph.D. Thesis, University of Turku, Turku, Finland, 1973.

5. W. L. Whittemore and R. P. Shutt, Phys. Rev. 88, 1312(1952).

6. M. A. Meyer, J. A. M. de Villiers, N. S. Wolmarans, J. W. Koen and I. J. Lessing, Journal of the Physical Society of Japan, Vol. 17, Supplement A-III, 1962, International Conference of Cosmic Rays and the Earth Storm, 350-352.

7. Hans Bichsel, Phys. Rev. 112, 182(1958).

8. J. L. Lloyd and A. W. Wolfendale, Proc. Phys. Soc. LXVIII, II-A, 1045-1065, 1955.

9. B. J. Bateman, Jr., "The Momentum and Zenithal Dependence of the Charge Ratio of Energetic Cosmic Ray Muons Near Sea Level", Ph.D. Thesis, Texas A&M University, 1970.

10. C. T. Gerald, "Applied Numerical Analysis", Addison-Wesley Pub. Co., 1970, p. 123.

11. Barkas and Berger, "Tables of Energy Losses and Ranges of Heavy Charged Particles, NASA SP-3013.

12. S. Hayakawa, "Cosmic Ray Physics", Wiley-Interscience, 1969, p. 393.

13. G. Molière, Z. Naturforschg, 2a, 133-145(1947).
G. Molière, Z. Naturforschg, 3a, 78-97(1948).
G. Molière, Z. Naturforschg, 10a, 177-211(1955).

14. P. Beckmann, "Elements of Applied Probability Theory", Harcourt, Brace & World, New York, 1968, p. 104.

15. L. N. Cooper and J. Rainwater, Phys. Rev. 97, 492(1955).

16. G. Wentzel, Ann. Physik 69, 335(1922).
G. Wentzel, Z. Physik 40, 590(1927).

17. H. A. Bethe, Phys. Rev. 89, 1256(1953).

18. W. T. Scott, Phys. Rev. 85, 245(1952).
W. T. Scott, Revs. Mod. Phy., 35, 231(1963).

19. L. Eyges, Phys. Rev. 75, 1534 (1948).

20. J. E. Freund, "Mathematical Statistics", Prentice-Hall (1971), p. 119.

21. P. Beckmann, "Elements of Applied Probability Theory", Harcourt, Brace & World, New York, 1968, p. 63.

22. M. S. Abdel-Monem, J. R. Benbrook, A. R. Osborne, and W. R. Sheldon, Department of Physics, University of Houston; N. M. Duller and P. J. Green, Department of Physics, Texas A&M University, Paper 118, Proceedings of the 13th International Cosmic Ray Conference, University of Denver, 1973.